

TURUN YLIOPISTON JULKAISUJA – ANNALES UNIVERSITATIS TURKUENSIS SARJA – SER. AI OSA – TOM. 751 | ASTRONOMICA – CHEMICA – PHYSICA – MATHEMATICA | TURKU 2025

Vadzim Krautsou



POLARIZED RADIATION FROM ACCRETING BLACK HOLES IN X-RAY BINARIES

Vadzim Krautsou

University of Turku

Faculty of Science
Department of Physics and Astronomy
Astronomy
Doctoral programme in Exact Sciences

Supervised by

Docent Alexandra Veledina University of Turku Turku, Finland

Professor Juri Poutanen University of Turku Turku, Finland Docent Andrei Berdyugin University of Turku Turku, Finland

Reviewed by

Professor Philip Allan Charles University of Southampton Southampton, United Kingdom Professor Felix Ryde KTH Royal Institute of Technology Stockholm, Sweden

Opponent

Professor Andrew Shearer University of Galway Galway, Ireland

The originality of this publication has been checked in accordance with the University of Turku quality assurance system using the Turnitin OriginalityCheck service.

Cover Image: Drawn by Vadzim Krautsou

ISBN 978-952-02-0452-5 (PRINT) ISBN 978-952-02-0453-2 (PDF) ISSN 0082-7002 (PRINT) ISSN 2343-3175 (ONLINE) Painosalama, Turku, Finland, 2025

"Nimaš, Bratki, bolšaho ščaścia na hetym świeci, jak kali čeławiek u halavie maje rozum i nawuku. Tahdy jon tolki može być u radzie, žyć u dastatkach i tahdy tolki pamaliŭšysia pa praŭdzie Bohu zasłužyć Niebo, bo zbahaciŭšy nawukaj rozum, razaŭje serce, i narod swoj ceły ščyra palubić"
"There is no greater happiness on this earth, brothers, than if a man has intellect and learning. Only then will he manage to live in counsel and in plenty and only when he has prayed properly to God, will he deserve Heaven, for once he has enriched his intellect with learning, he will develop his affection and sincerely love all his kinfolk"
Kastuś Kalinoŭski, 1864 Listy z-pad šybienicy Letters from Beneath the Gallows
To my homeland and its people – may knowledge always serve truth and freedom.

UNIVERSITY OF TURKU
Faculty of Science
Department of Physics and Astronomy
Astronomy
KRAUTSOU, VADZIM: Polarized radiation from accreting black holes in X-ray binaries
Doctoral dissertation, 172 pp.
Doctoral programme in Exact Sciences
December 2025

ABSTRACT

Accreting stellar-mass black holes are known to be one of the most efficient converters of gravitational energy into radiation in the Universe. They reside in binaries, where the normal type companion star supplies matter to the compact object. When spiraling into a black hole, matter forms an accretion disk around it, which exposes itself through a rich phenomenology across the electromagnetic spectrum: spectral state transitions, relativistic jet launching, and variability on timescales ranging from milliseconds to years.

This dissertation is devoted to the study of multiwavelength polarization from black hole X-ray binaries (BHXRBs), both low-mass and high-mass. Over the years of my work on this dissertation, I have carried out the most comprehensive survey to date of their optical polarization behavior: 12 black hole systems have been studied in total, for five of which the intrinsic optical polarization has been reliably detected, and for the rest it has been shown to be absent at the level better than 0.5%. In two of these sources, we discovered orbital variability of optical polarization and developed models to explain it. We showed that high-precision polarimetric observations can be used to independently estimate the orbital parameters of such systems, which is crucial when studying their physics, and provided models and tools for that.

Midway through my PhD journey, the IXPE satellite was successfully launched, naturally shifting the focus of my interests towards X-ray polarimetry. During the first months of its operation, I performed an optical polarimetric campaign, supporting the first IXPE observation of the black hole X-ray binary, Cyg X-1. The result of this joint observation was the first reliable detection of the X-ray polarization from BHXRB, which turned out to be unexpectedly high, with polarization angle aligned with the direction of the radio jet as well as with orbital axis, as evidenced by optical polarimetry. This discovery showed that the hot corona responsible for producing the hard X-ray spectrum is spatially extended in the plane perpendicular to the jet axis, rather than aligned with it, thereby ruling out models that place the corona along the jet direction. Later on, I organized simultaneous observations with IXPE, the Very Large Array (VLA), DIPol-2, and other facilities, which enabled the first detection of radio polarization in Cyg X-1 and led to the discovery of its X-ray polarization variability.

Together, these studies establish multiwavelength polarimetry as a unique tool for probing the geometry and dynamics of accreting black holes, laying the groundwork for future observational campaigns with next-generation polarimetric facilities.

TURUN YLIOPISTO

Matemaattis-luonnontieteellinen tiedekunta

Fysiikan ja tähtitieteen laitos

Oppiaine

KRAUTSOU, VADZIM: Polarized radiation from accreting black holes in X-ray

binaries

Väitöskirja, 172 s.

Eksaktien tieteiden tohtoriohjelma

Joulukuu 2025

TIIVISTELMÄ

Tähdenmassaiset kerryttävät mustat aukot tiedetään olevan yksi maailmankaikkeuden tehokkaimmista gravitaatioenergian muuntajista säteilyksi. Ne sijaitsevat kaksoistähtijärjestelmissä, joissa tavallisen tyypin kumppanitähti luovuttaa ainetta kompaktille kappaleelle.

Tämä väitöskirja on omistettu mustia aukkoja sisältävien röntgenkaksoistähtien (BHXRB), sekä pieni- että suurimassaisten, moniaaltopituuksisen polarisaation tutkimukselle. Työni aikana olen toteuttanut laajimman tähän mennessä tehdyn tutkimuksen niiden optisesta polarisaatiokäyttäytymisestä: yhteensä 12 mustaa aukkoa sisältävää järjestelmää tutkittiin, joista viidessä sisäinen optinen polarisaatio havaittiin luotettavasti, ja muissa sen osoitettiin puuttuvan paremmin kuin 0.5%:n tasolla. Kahdessa näistä kohteista havaitsimme optisen polarisaation kiertoratavaihtelua ja kehitimme malleja sen selittämiseksi. Näytimme, että tarkat polarimetriset havainnot tarjoavat riippumattoman keinon arvioida tällaisten järjestelmien kiertorataparametreja, mikä on olennaista niiden fysiikan ymmärtämisessä, ja tarjosimme tähän sopivia malleja ja työkaluja.

Väitöskirjatyöni puolivälissä IXPE-satelliitti laukaistiin onnistuneesti, mikä luonnollisesti siirsi kiinnostukseni painopisteen röntgenpolarimetriaan. Sen toiminnan ensimmäisinä kuukausina toteutin optisen polarimetrisen kampanjan tukeakseni IXPE:n ensimmäistä havaintoa mustaa aukkoa sisältävästä röntgenkaksoistähdestä, Cyg X-1:stä. Näiden yhteishavaintojen tuloksena saavutettiin ensimmäinen luotettava havainto röntgenpolarisaatiosta BHXRB-järjestelmässä, ja polarisaatio osoittautui odottamattoman voimakkaaksi. Polarisaatiokulma oli linjassa sekä radiosuihkun suunnan että kiertoradan akselin kanssa, kuten optinen polarimetria vahvisti. Tämä löytö osoitti, että kovan röntgenspektrin tuottava kuuma korona ulottuu laajalle kohtisuorassa tasossa suihkuakseliin nähden, näin sulkien pois mallit, joissa korona sijaitsee suihkun suunnassa. Myöhemmin järjestin samanaikaisia havaintoja IXPE:n, Very Large Arrayn (VLA), DIPol-2:n ja muiden laitosten kanssa, mikä mahdollisti ensimmäisen radiosäteiden polarisaation havainnon Cyg X-1:stä ja johti sen röntgenpolarisaation vaihtelun löytämiseen.

Yhdessä nämä tutkimukset vakiinnuttavat moniaaltopituuksisen polarimetrian ainutlaatuiseksi työkaluksi kerryttävien mustien aukkojen geometrian ja dynamiikan tutkimuksessa, ja ne osoittavat sen potentiaalin rajoittaa kiertorataparametreja, tutkia suihkun ja kiekon suunnan epäyhteneväisyyttä sekä tarkastella kertymävirtauksen sisimpiä alueita.

Acknowledgements

My journey to the doctoral degree turned out to be long and arduous – sometimes I can hardly understand how I ended up here. Reflecting on the past, it appears to be a string of carefully planned yet random coincidences.

At my entrance exams for elementary school, I was found to have perfect pitch, which, of course, defined my destiny as a violinist. Within the first academic year in the Art School, however, my violin teacher was promoted to vice principal, which meant they no longer had enough time to teach me. My pitch came in handy in the boys' choir, but I had already shifted my focus to drawing, which, this time, led me to choose a middle school for Architecture and Graphic Arts, where I spent five rough years. As it turned out, art classes were not about creative freedom, but rather endless hours and years of mastering the technique of drawing elementary geometric shapes. The only interesting classes were pottery, math, and physical (yes, physical) education. By the end of ninth grade, I had mastered drawing cubes at the cost of losing interest in art, had become a certified potter, knew mathematics quite well, and had developed a deep and lifelong hatred for the state ideology that was, and sadly continues to be, planted in most educational institutions of my homeland. My desire for changes supported and encouraged by my father pushed me to make the most important decision of my life – to try to enroll in the Physics and Math department of the Mahiliou State Regional Lyceum No 1, an island of freedom in an ocean of obedience and oppression, where I was fortunate enough to spend the two happiest years of my homeland life. Everything that happened afterwards appears to be a natural continuation of that decision, but nothing would have been possible without the numerous great people I met along the way, whom I would like to thank in these pages.

First of all, I want to express my sincere gratitude to my supervisors – docent Alexandra Veledina, docent Andrei Berdyugin, and Professor Juri Poutanen. This thesis work would not have been possible without the guidance and mentoring I received from you. In particular, I am grateful to Alexandra Veledina for introducing me to the field of High Energy Astrophysics (HEA) through many interesting projects, to Andrei Berdyugin for cultivating in me the neatness in working with data and instruments, and to Professor Juri Poutanen for showing by example how to be incredibly efficient while paying attention to even the tiniest details. I could not have hoped for better supervisors!

I would like to thank Professor Philip Allan Charles and Professor Felix Ryde for kindly agreeing to serve as my pre-examiners and for providing me with useful comments, which have improved the thesis. I wish to thank Professor Andrew Shearer for agreeing to come to Finland to serve as my esteemed opponent.

I would also like to thank my collaborators and colleagues with whom I had the pleasure of working and who warmly welcomed me during my research visits: thank you, Andrzej Zdziarski (CAMK), Michal Dovčiak (Astronomical Institute of the Czech Academy of Sciences), Cristina Baglio (INAF Osservatorio Astronomico di Brera), Alexander Mushtukov (University of Oxford), Adam Ingram (Newcastle University), and Joonas Nättilä (University of Helsinki).

My gratitude also goes to the current and previous members of the Turku HEA group, Pavel, Vladislav, Sergey, Sofia, Greg, Varpu, Anagha, Anna B., Anna C., Anastasiia B., Ilia K., Armin, Yasir, Juhani, Tuomo, Ale, Yannis, Alexander, who created a nice and welcoming atmosphere on the second floor of the Quantum building.

The path to the dissertation would not have been possible without my school teachers. I would like to thank my math teacher, NataÍlia Michajlaŭna Staravojtava, for showing me the beauty and order of mathematics amid the chaos of the art school. My warmest appreciation goes to the staff of Mahilioŭ State Regional Lyceum №1, in particular to my dear friend, the vice principal Nadzieja Ivanaŭna Savič, whose example taught me the true meaning of justice, humanity, and sincere kindness – it pains me deeply that I can no longer thank her in person. I thank Jury Uladzimiravič Sivajeŭ, who helped me turn my passion for astronomy into its systematic study and encouraged me to compete in the astronomy olympiads. I am grateful to Uladzimir Ivanavič Hrabcevič, who taught me not just physics, but also how to set and achieve goals without getting distracted by unnecessary things. Pieršy Liepšy!

I would not have been able to make it without the knowledge I gained at my alma mater. First of all, I would like to thank Peter Alexandrovich Tarakanov for allowing me to participate in the astronomy olympiad, the results of which earned me a place at the University. I am grateful to my undergraduate research supervisor, Professor Valeri Mikhailovich Larionov, who gave me my first research project on polarization, encouraged my desire to do science even in tough times, and sent me on an internship to the University of Turku. I will never forget our long conversations over a good cup of coffee... Finally, I would like to thank Sergey Savchenko, my mentor throughout my undergraduate studies, who showed me that programming is fun when you switch from Fortran to Python.

I am deeply grateful to my family – my mother Larisa, my father Viktar, and my brother Jaŭhien – for supporting me throughout all my endeavors and hobbies, which have always been many, from drawing and playing musical instruments to photography and astronomy. It is you who, in a good way, are responsible for the kind of person I have become in this life.

I would also like to thank my friends, with whom I was fortunate enough to share cozy Finnish evenings, long summer hikes, and sometimes just hours-long phone calls. Warm thanks to Andrii, Daria T., Arciom, Dzima, Raman, Daria Z., Faustine, Katja, Iulia, Ilia M., Maria, Taru, Hanna, to name a few.

I am grateful for the financial support of the Vilho, Yrjö and Kalle Väisälä rahasto, Suomen Kulttuurirahasto, and University of Turku.

Finally, and above all, I owe my deepest gratitude to my partner and the love of my life, Anastasiia. Your faith in me, your strength, and your love made this journey possible. None of this would have been possible without you.

Turku, November 2025 Vadzim Krautsou

Table of Contents

A	cknowi	edgem	ients	6
Ta	able of	Conter	nts	9
A	bbrevia	ations		11
Li	st of O	riginal	Publications	13
1	Road	to the	discovery of X-ray binaries	18
2	X-ray 2.1 2.2 2.3	Classif Accreti 2.2.1 2.2.2	ication of X-ray Binaries	20 20 21 22 24 25 25 27 28
3	Polari	ization	in X-ray binaries	30
J	3.1		ion of Polarization	30
	3.2		avelength Polarimetry	33
	0	3.2.1	Radio Polarimetry	33
		3.2.2	Optical Polarimetry	35
		3.2.3	X-ray Polarimetry	36
	3.3	Source	es of Polarization in BHXRBs	37
		3.3.1	Scattering	38
		3.3.2	Synchrotron Emission	40
		3.3.3	Interstellar Polarization	41
		3.3.4	Faraday Effect	42
4	Sumn	nary of	the original publications	44
	I	Variabi	ility of X-ray polarization of Cyg X-1	44

	II	optical polarimetry	44		
	III	Polarized x-rays constrain the disk-jet geometry in the black	44		
		hole x-ray binary Cygnus X-1	45		
	IV	Orbital variability of the optical linear polarization of the gamma	1 -		
		ray binary LS I +61 303 and new constraints on the orbital parameters	45		
	V	Optical and near-infrared polarization of the black hole X-ray	.0		
		binary A0620–00 in quiescence	46		
	VI	Optical polarization signatures of black hole X-ray binaries .	46		
	VII	Orbital variability of polarized X-ray radiation reflected from	40		
		a companion star in X-ray binaries	46		
	VIII	X-ray polarimetry as a tool to constrain orbital parameters in X-ray binaries	47		
	IX	Black hole spin—orbit misalignment in the X-ray binary MAXI	.,		
		J1820+070	47		
5	Future	e prospects	48		
Li	List of References				
0	Original Publications				

Abbreviations

2D two-dimensional

AGN active galactic nucleus

ALMA Atacama Large Millimeter Array

BH black hole

CCD charge-coupled device

co-I co-investigator

DIPol Double Image Polarimeter EHT Event Horizon Telescope

EM electro-magnetic

eROSITA extended ROentgen Survey with an Imaging Telescope Array

eXTP Enhanced X-ray Timing and Polarimetry mission

GPD gas pixel detector HF high frequency

HID hardness-intensity diagram HMXB high-mass X-ray binary

IAU International Astronomical Union ISCO innermost stable circular orbit

ISM interstellar medium

IXPE Imaging X-ray Polarimetry Explorer

LF low frequency

LMXB low-mass X-ray binary

MAXI Monitor of All-sky X-ray Image

NASA National Aeronautics and Space Agency

NIR near-infrared NS neutron star

OSO-8 Orbiting Solar Observatory 8

PA polarization angle
PD polarization degree
PI principal investigator
PSD power spectral density
SED spectral energy distribution
OPO quasi periodic oscillations

RM rotation measure

Vadzim Krautsou

RV radial velocity UV ultraviolet

VLA Very Large Array

VLBI Very Long Baseline Interferometry

XRB X-ray binary

List of Original Publications

This dissertation is based on the following original publications, which are referred to in the text by their Roman numerals:

I Variability of X-ray polarization of Cyg X-1,

Kravtsov V., Bocharova A., Veledina A., Poutanen J., Hughes A.K., Dovčiak M., Egron E., Muleri F., Podgorny J., Svoboda J., Forsblom S.V., Berdyugin A.V., Blinov D., Bright J.S., Carotenuto F., Green D.A., Ingram A., Liodakis I., Mandarakas N., Nitindala A.P., Rhodes L., Trushkin S.A., Tsygankov S.S., Brigitte M., Di Marco A., Iacolina N., La Monaca F., Loktev V., Mastroserio G., Petrucci P.-O., Pilia M., Tombesi F., Zdziarski A.A.

Astronomy & Astrophysics, 2025; 701: A115

II Peering into the tilted heart of Cyg X-1 with high-precision optical polarimetry,

Kravtsov V., Veledina A., Berdyugin A.V., Zdziarski A.A., Henson G.D., Piirola V., Sakanoi T., Kagitani M., Berdyugina S.V., Poutanen J. Astronomy & Astrophysics, 2023; 678: A58

III Polarized X-rays constrain the disk-jet geometry in the black hole X-ray binary Cygnus X-1,

Krawczynski H., Muleri F., Dovčiak M., Veledina A., Rodriguez Cavero N., Svoboda J., Ingram A., Matt G., Garcia J.A., Loktev V., Negro M., Poutanen J., Kitaguchi T., Podgorný J., Rankin J., Zhang W., Berdyugin A.V., Berdyugina S.V., Bianchi S., Blinov D., Capitanio F., Di Lalla N., Draghis P., Fabiani S., Kagitani M., *Kravtsov V.*, et al. Science, 2022; 378: 650

IV Orbital variability of the optical linear polarization of the γ -ray binary LS I +61 303 and new constraints on the orbital parameters,

Kravtsov V., Berdyugin A.V., Piirola V., Kosenkov I.A., Tsygankov S.S., Chernyakova M., Malyshev D., Sakanoi T., Kagitani M., Berdyugina S.V., Poutanen J.

Astronomy & Astrophysics, 2020; 643: A170

V Optical and near-infrared polarization of the black hole X-ray binary A0620–00 in quiescence,

Kravtsov V., Veledina A., Berdyugin A.V., Poutanen J., Tsygankov S.S., Shahbaz T., Torres M.A.P., Jermak H.E., McCall C., Steele I.A., Kajava J.J.E., Piirola V., Sakanoi T., Kagitani M., Berdyugina S.V. Astronomy & Astrophysics, 2025; 703: A14

VI Optical polarization signatures of black hole X-ray binaries,

Kravtsov V., Berdyugin A.V., Kosenkov I.A., Veledina A., Piirola V., Abdul Qadir Y., Berdyugina S.V., Sakanoi T., Kagitani M., Poutanen J. Monthly Notices of the Royal Astronomical Society, 2022; 514: 2479

VII Orbital variability of polarized X-ray radiation reflected from a companion star in X-ray binaries,

Ahlberg V., *Kravtsov V.*, Poutanen J. Astronomy & Astrophysics, 2024; 688: A220

VIII X-ray polarimetry as a tool to constrain orbital parameters in X-ray binaries,

Rankin J., *Kravtsov V.*, Muleri F., Poutanen J., Marin F., Capitanio F., Matt G., Costa E., Di Marco A., Fabiani S., La Monaca F., Marra L., Soffitta P. The Astrophysical Journal, 2024; 962: 34

IX Black hole spin-orbit misalignment in the x-ray binary MAXI J1820+070, Poutanen J., Veledina A., Berdyugin A.V., Berdyugina S.V., Jermak H., Jonker P.G., Kajava J.J.E., Kosenkov I.A., *Kravtsov V.*, Piirola V., Shrestha M., Torres M.A.P., Tsygankov S.S. Science, 2022; 375: 874

The original publications have been reproduced with the permission of the copyright holders.

List of Publications not Included in the Thesis

X Unveiling blazar synchrotron emission: a multiwavelength polarimetric study of HSP and LSP populations,

Capecchiacci S., ..., *Kravtsov V.*, et al. (IXPE collaboration), Astronomy & Astrophysics, 2025, accepted

XI A two-week IXPE monitoring campaign on Mrk 421,

Maksym W.P., ..., *Kravtsov V.*, et al. (IXPE collaboration), The Astrophysical Journal, 2025; 986: 230

XII Neutrino beaming in ultraluminous X-ray pulsars as a result of gravitational lensing by neutron stars,

Mushtukov A. A., Potekhin A., Markozov, I. D., Nallan S., Kornacka K., Ognev I. S., *Kravtsov V.*, Dobrynina A., Kaminker A. D. Monthly Notices of the Royal Astronomical Society, 2025; 538: 2396

XIII Studying geometry of the ultraluminous X-ray pulsar Swift J0243.6+6124 using X-ray and optical polarimetry,

Poutanen J., ..., *Kravtsov V.*, et al. (IXPE collaboration), Astronomy & Astrophysics, 2024; 691: A123

XIV X-ray and multiwavelength polarization of Mrk 501 from 2022 to 2023,

Chen C.-T. J., ..., *Kravtsov V.*, et al. (IXPE collaboration), The Astrophysical Journal, 2024; 974: 50

XV IXPE view of BH XRBs during the first 2.5 years of the mission,

Dovčiak M., Podgorny J., Svoboda J., Steiner J.F., Kaaret P., Krawczynski H., Ingram A., *Kravtsov V.*, Marra L., Muleri F., Garcia J.A., Mastroserio G., Mikušincová R., Ratheesh A., Rodriguez Cavero N., Galaxies, 2024; 12: 5

XVI Observations of low and intermediate spectral peak blazars with the IXPE.

Marshall H., ..., *Kravtsov V.*, et al. (IXPE collaboration), The Astrophysical Journal, 2024; 972: 74

XVII An IXPE-led X-ray spectropolarimetric campaign on the soft state of Cygnus X-1: X-ray polarimetric evidence for strong gravitational lensing,

Steiner J. F., ..., *Kravtsov V.*, et al. (IXPE collaboration), The Astrophysical Journal, 2024; 969: L30

XVIII Recovery of the X-ray polarisation of Swift J1727.8–1613 after the soft-to-hard spectral transition,

Podgorny J., ..., *Kravtsov V.*, et al. (IXPE collaboration), Astronomy & Astrophysics, 2024; 686: L12

XIX Tracking the X-ray polarization of the black hole transient Swift J1727.8–613 during a state transition,

Ingram A., ..., *Kravtsov V.*, et al. (IXPE collaboration), The Astrophysical Journal, 2024; 968: 76

XX X-ray polarized view on the accretion geometry in the X-ray binary Circinus X-1,

Rankin J., ..., *Kravtsov V.*, et al. (IXPE collaboration), The Astrophysical Journal Letters, 2024; 961: L8

XXI Discovery of X-ray polarization from the black hole transient Swift J1727.8–1613,

Veledina A., ..., *Kravtsov V.*, et al. (IXPE collaboration), The Astrophysical Journal Letters, 2023; 958: L16

XXII Complex variations of X-ray polarization in the X-ray pulsar LS V +44 17/ RX J0440.9+4431,

Doroshenko V., ..., *Kravtsov V.*, et al. (IXPE collaboration), Astronomy & Astrophysics, 2023; 677: A57

XXIII X-ray polarization observations of BL Lacertae,

Middei R., ..., *Kravtsov V.*, et al. (IXPE collaboration), The Astrophysical Journal, 2023; 942: L10

XXIV Polarized blazar X-rays imply particle acceleration in shocks,

Liodakis I., ..., *Kravtsov V.*, et al. (IXPE collaboration), Nature, 2022; 611: 677–681

XXV Disc and wind in black hole X-ray binary MAXI J1820+070 observed through polarized light during its 2018 outburst,

Kosenkov I.A., Veledina A., Berdyugin A.V., *Kravtsov V.*, Piirola V., Berdyugina S.V., Sakanoi T., Kagitani M., Poutanen J., Monthly Notices of the Royal Astronomical Society, 2020; 496: L96

XXVI Evolving optical polarisation of the black hole X-ray binary MAXI J1820+070,

Veledina A., Berdyugin A.V., Kosenkov I.A., Kajava J.J.E., Tsygankov S.S., Piirola V., Berdyugina S.V., Sakanoi T., Kagitani M., *Kravtsov V.*, Poutanen J.,

Astronomy & Astrophysics, 2019; 623: A75

1 Road to the discovery of X-ray binaries

Astronomers began exploring the potential of X-ray radiation for astronomical observations shortly after its discovery at the beginning of the 20th century. However, quantum theory and atomic physics at the time suggested that short-wavelength electromagnetic radiation, including X-rays, would be absorbed efficiently by gases like nitrogen and oxygen in the Earth's atmosphere, necessitating the deployment of any possible astronomical instruments into space, free from atmospheric absorption. Thus, the history of X-ray astronomy is closely tied to the history of near-space exploration.

The pioneering experiments of Robert H. Goddard (see Goddard 1948 for the overview), the father of modern rocketry, curiosity of the theoreticians studying the Earth's atmosphere (Breit & Tuve, 1925; Hulburt, 1928), and advances in X-ray detection techniques (Rutherford & Geiger, 1908; Geiger & Müller, 1928) gave birth to the conceptual idea of early X-ray telescopes: rockets or balloons equipped with proportional photon counters were proposed to be launched above the atmosphere for a short duration of time, during which the instruments would collect cosmic X-ray radiation.

The first astronomical observation of this kind was the detection of X-ray emission from the closest star to Earth — the Sun (Friedman et al., 1951). Early attempts to detect X-ray emission from other stars were unsuccessful, which, however, did not seem surprising at the time: indeed, if one assumes X-ray luminosity of other stars to be comparable to that of the Sun, the signal would be too weak to be detected by the available instruments. Nevertheless, the sensitivity of detectors improved rapidly as well as the efforts continued, leading to the discovery of the first extrasolar X-ray source in the constellation Scorpius, named Scorpius X-1 (Sco X-1, Giacconi et al., 1962). Subsequent rocket launches identified dozens more extrasolar and even extragalactic X-ray sources, although the omnidirectional nature of the first detectors limited the study of individual objects (Bowyer et al., 1965, 1970; Chodil et al., 1967; Gursky et al., 1967).

The solution to this problem came with technological advancements – the launch of the first artificial satellite, Sputnik 1, by the Soviet Union in 1957 demonstrated the feasibility of placing payloads into Earth's orbit. By the late 1960s, the first X-ray satellite telescope, UHURU, was developed and launched into orbit (Giacconi et al., 1971b). The data from UHURU revealed over a hundred bright X-ray sources,

including variable sources such as SMC X-1, Cyg X-1, Cyg X-3, and Cen X-3 (Schreier et al., 1972a; Tananbaum et al., 1972a; Parsignault et al., 1972; Schreier et al., 1972b). With angular resolutions better than 30 arcminutes, the telescope enabled ground-based observatories to associate X-ray sources with optical or radio counterparts. Her X-1 (Tananbaum et al., 1972b) was among the first such sources identified with an optical star, HZ Her (Bahcall & Bahcall, 1972). The X-ray flux from Her X-1 was found to pulse with a 1.24-second period and exhibit periodic eclipses with a period of 1.7 days, matching optical observations and indicating the binary nature of the system. This possible binary nature of the source has been additionally supported by the detection of periodic variations in the pulsation period with the orbital period, explained by the Doppler effect. Similar behavior was observed in other pulsating X-ray sources, such as e.g. Cen X-3 (Giacconi et al., 1971a).

Most of the newly identified bright X-ray sources shared common observational features: they had a companion star in a close orbit with a period of only a few days, while the periodic variations of X-ray emission on timescales of seconds pointed to the compact size of the X-ray-emitting body. Long-term studies showed that pulsation periods shortened with time, suggesting that rotation rates of the emitting objects were increasing. The only viable explanation for this behavior was found in a model in which matter with non-zero angular momentum falls onto a compact object, accelerating its rotation and producing X-rays as a result of the conversion of the matter's gravitational energy into radiation. This interpretation was further supported by distance measurements, which implied energy outputs far too large to be explained by conventional processes such as nuclear fusion. The compact emitting region was inferred to have temperatures of approximately 10⁸ K, making the accretion – a gravitational gathering of matter onto a central object – the only plausible mechanism for maintaining such high temperatures of plasmas.

Further multiwavelength observations, particularly the measurements of radial velocities of companion stars, made it possible to estimate the masses of compact objects. For some systems, such as Her X-1, Sco X-1, and Cen X-3, the compact object was found to have a mass of about 1–2 solar masses and a radius of approximately 10^6 cm, being consistent with predicted sizes and masses of neutron stars – the final evolutionary product of massive (9–25 M_{\odot}) stars (Baade & Zwicky, 1934; Tolman, 1939; Oppenheimer & Volkoff, 1939). In other systems, such as Cyg X-1, no periodic pulsations were detected, and the mass of the compact object was estimated to be > $6M_{\odot}$ (Gies & Bolton, 1986), which is far too high for a neutron star. This was the first indirect evidence supporting the existence of black holes (Schreier et al., 1971; Wade & Hjellming, 1972; Bardeen et al., 1972).

Thus, observations from the first space-based X-ray observatories in the 1970s led to the discovery of a new class of astrophysical objects – accreting binary systems with compact objects, or *X-ray binaries*.

2 X-ray binaries

An X-ray binary is a binary system in which a compact object (*accretor*) accretes matter from a companion (*donor*) star, producing X-ray emission. The physical conditions and underlying processes can vary drastically depending on the nature of the donor and the accretor. As a result, X-ray binaries are classified into distinct subclasses that capture these fundamental physical differences.

2.1 Classification of X-ray Binaries

To date, more than 500 X-ray binaries are known in our Galaxy (according to the most comprehensive catalog to date, XRBcats, Neumann et al., 2023; Avakyan et al., 2023). In modern classification, X-ray binaries are typically divided by the type of donor star into *low-mass* and *high-mass X-ray binaries*. By the type of accretor, these systems are classified into *neutron star*, and *black hole X-ray binaries*.

A low-mass X-ray binary (LMXB, Fig. 1) is a binary system with the mass of the donor not exceeding approximately $1M_{\odot}$. Currently, about 360 such systems are known in the Milky Way (LMXB Cat, Avakyan et al., 2023). For many of these systems, the nature of the compact objects remains uncertain, but population studies indicate that LMXBs with neutron stars are about twice as common as those with black holes. This finding aligns with predictions from evolutionary models of neutron stars and black holes (Kalogera & Webbink, 1998). The low mass of a companion star ensures its long life on the main sequence, which makes such stars common in the spherical subsystem of the Galaxy (Grimm et al., 2002).

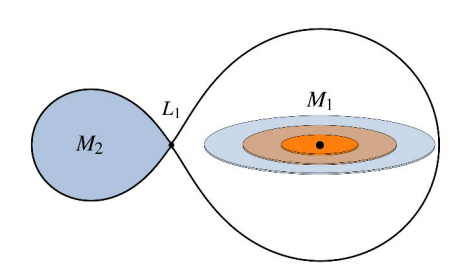


Figure 1. Sketch of LMXB with mass ratio $q = M_2/M_1 = 0.25$.

¹http://astro.uni-tuebingen.de/~xrbcat/

A high-mass X-ray binary (HMXB, Fig. 2) is a binary with the mass of the donor star $\geq 10 M_{\odot}$. According to the latest data, there are about 170 such systems in our Galaxy (HMXB Cat, Neumann et al., 2023). Stars with such masses do not live long, only a few million years, during which they, even those with a large natal kick, do not manage to fly far away from the place of their birth. Thus, most of the observed HMXBs spend their lives in the Galactic plane (Grimm et al., 2002). X-ray binaries with companion star masses between $1-10M_{\odot}$ are usually called Intermediate Mass X-ray Binaries, but may belong to either of the two classes mentioned above as well.

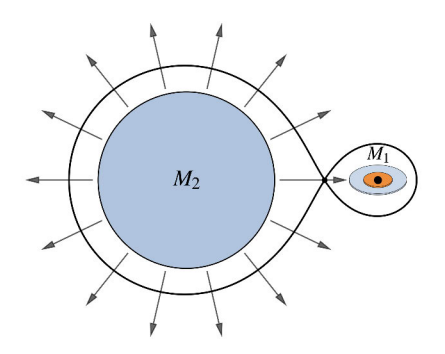


Figure 2. Sketch of HMXB with mass ratio $q = M_2/M_1 = 10$.

2.2 Accretion in X-ray Binaries

The primary source of radiative energy in X-ray binaries is accretion, the process in which the gravitational potential energy of matter falling onto a compact object is converted into heat and radiation. The energy released in this process can be roughly estimated as follows. Let us assume that probe mass m falls onto a body with mass M and radius R from infinity. The released potential energy will be equal to:

$$\Delta E_{\rm acc} = \frac{GMm}{R}.\tag{1}$$

For a compact object with a mass $M \approx M_{\odot}$ and a radius $R = 10^6$ cm (the order of magnitude values for a neutron star), the energy released by the accretion of 1 gram of matter is approximately $\Delta E_{\rm acc} \sim 1.3 \times 10^{20}$ erg, which is about 15% of its rest energy. This is more than an order of magnitude greater than the energy extracted from 1 gram of matter through nuclear reactions – the efficiency of hydrogen fusion $\eta_{\rm nuc} = E_{\rm nuc}/mc^2 \sim 0.7\%$ (Clayton, 1983). This high efficiency of accretion as an energy source is what makes the sky shine bright in the X-ray band (see Fig. 3).

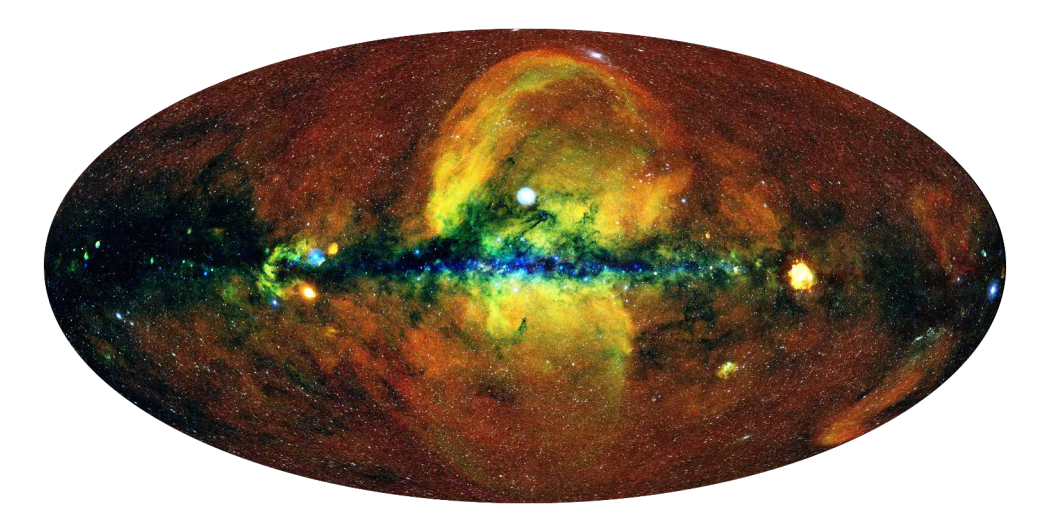


Figure 3. The universe in X-rays as seen with the eROSITA X-ray telescope. Credit: Jeremy Sanders, Hermann Brunner and the eSASS team (MPE); Eugene Churazov, Marat Gilfanov (IKI).

2.2.1 Eddington Luminosity

As seen from Eq. (1), accretion energy release is proportional to the compactness M/R of the accretor and the mass m of the infalling matter. Therefore, the luminosity L = dE/dt of an object with a fixed compactness M/R depends solely on the accretion rate, defined as $\dot{M} = dm/dt$. While the accretion rate depends on various system parameters such as the mass transfer mechanism, the binary separation, and the nature of the donor star, it is important to note that it cannot increase indefinitely. As the infalling matter releases

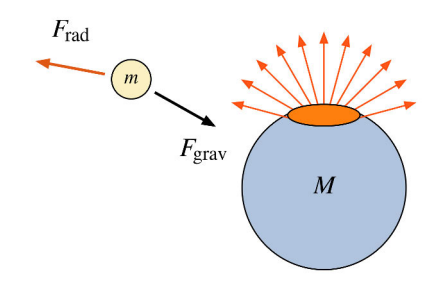


Figure 4. Sketch of the accretion of probe mass m onto a radiating body with mass M.

gravitational potential energy, it is converted into radiation. This radiation exerts an outward pressure that opposes further infall. When the outward radiation pressure balances the inward gravitational pull (see Fig. 4), a critical luminosity is reached, which sets an upper limit on the accretion rate, beyond which steady accretion is no longer sustainable.

The gravitational force acting on the infalling matter from the accretor is

$$F_{\rm grav} = \frac{GMm}{R^2},$$

and the radiation force is

$$F_{\rm rad} = P_{\rm rad} \kappa m$$
,

where $P_{\rm rad} = L/4\pi R^2 c$ is the radiation pressure and κ is the opacity. Their equality leads to

$$\frac{GMm}{R^2} = \frac{L_{\rm Edd}\kappa m}{4\pi R^2 c}.$$

Simplifying this gives:

$$L_{\rm Edd} = \frac{4\pi GMc}{\kappa}.$$

In most cases, we deal with ionized hydrogen, where the mass is primarily concentrated in protons m_p and the opacity κ is determined by Thomson scattering on electrons. In this case, $\kappa = \sigma_T/m_p$, which yields the Eddington limit:

$$L_{\rm Edd} = \frac{4\pi GMcm_{\rm p}}{\sigma_{\rm T}} \sim 1.3 \times 10^{38} \left(\frac{M}{M_{\odot}}\right) {\rm erg \, s^{-1}}.$$

If the luminosity exceeds this value, the radiation force surpasses the gravitational force, and accretion cannot continue, at least in the spherically-symmetric regime (see e.g. Abramowicz et al. 1980). It is important to note that $L_{\rm Edd}$ depends only on the mass of the accreting body.

If we assume that luminosity is produced by converting a fraction η of the rest mass energy of infalling matter into radiation near the surface of the object with radius R, then the luminosity of accretion is:

$$L_{\rm acc} = \eta \dot{M} c^2 \tag{2}$$

Equating $L_{acc} = L_{Edd}$ gives:

$$\eta \dot{M}_{\rm Edd} c^2 = \frac{4\pi G M c m_{\rm p}}{\sigma_{\rm T}},$$

which gives us the Eddington accretion rate:

$$\dot{M}_{\rm Edd} = \frac{2\pi R_{\rm s} c m_{\rm p}}{\eta \sigma_{\rm T}},$$

where $R_{\rm s}=2GM/c^2$ is the Schwarzschild radius for a black hole. Estimating the accretion efficiency for black holes that lack a solid surface is not trivial since the matter can fall under the event horizon without radiating energy. However, realistic estimates suggest that $\eta \sim 0.10-0.15$ of the rest energy of matter can be extracted

during accretion onto a black hole, yielding an order-of-magnitude estimate for the Eddington accretion rate of $\dot{M}_{\rm Edd} \sim 10^{18}\,{\rm g\,s^{-1}}$ (Shakura & Sunyaev, 1973; Frank et al., 2002).

2.2.2 Where Does the Accretion Disk Come From?

In an X-ray binary, the donor star supplies the matter that can be captured by a compact object. For accretion to proceed, however, specific conditions must be satisfied. First, the gravity of the compact object must be sufficiently strong to "strip" material away from the donor star. Second, for energy to be released, the infalling material must reach the surface of the compact object (or its effective boundary in the case of a black hole), which requires it to lose a significant fraction of its angular momentum. The dynamics of mass transfer in a binary system is governed by the effective gravitational potential in the co-rotating frame, which for the first time was studied over a century ago by

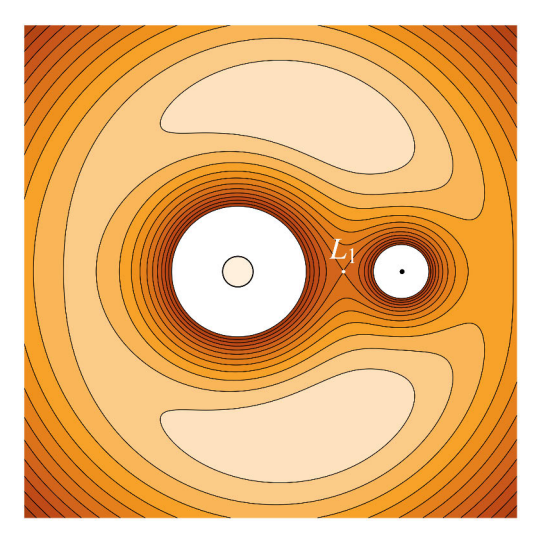


Figure 5. Roche potential for binary with mass ratio q = 0.25.

Édouard Roche (see Kopal 1989 for overview).

For a binary system consisting of two stars with masses M_1 and M_2 , the gravitational potential (or Roche potential) Ψ_R is given by

$$\Psi_{\rm R}(\vec{r}) = -\frac{GM_1}{|\vec{r} - \vec{r}_1|} - \frac{GM_2}{|\vec{r} - \vec{r}_2|} - \frac{1}{2}(\vec{\Omega} \times \vec{r})^2,\tag{3}$$

where $\vec{\Omega}$ is an angular velocity, \vec{r}_1 , \vec{r}_2 and \vec{r} are the position vectors of the M_1 , M_2 , and the probe mass respectively. The Roche potential defines regions around each star where material is gravitationally bound to that star. These regions are bounded by critical surfaces called Roche lobes. The inner Lagrange point L_1 (see Fig. 5), located between the two stars, is a point of gravitational equilibrium. If one star fills or overflows its Roche lobe, matter can flow through L_1 and be transferred to the compact object – a process known as Roche-lobe overflow. Since both bodies orbit a common center of mass, the material in the accretion stream has a velocity component perpendicular to the radial direction, $v_{\perp} \sim b\Omega$, where b is the distance from the compact object to L_1 . The radial velocity of the material is primarily determined by the gas pressure and is roughly comparable to the speed of sound in the gas, $v_{\parallel} \sim c_{\rm s}$

(Frank et al., 2002).

The infalling matter in the accretion stream has an initial nonzero tangential velocity, preventing it from falling directly onto a compact object; instead, the matter settles in an elliptical orbit around it. As new material continues to flow in, it interacts with previously accreted material in orbit. These interactions dissipate both energy and angular momentum, gradually circularizing the motion of the gas and leading to the formation of a ring of matter around the black hole. The angular velocity in the ring decreases with radius according to the Keplerian relation $\Omega_{\rm K}(r) = v/r = \sqrt{GM/r^3}$, while the angular momentum increases with radius as $l(r) = rv = r^2 \Omega_K = \sqrt{GMr}$. As the accretion proceeds, the differentially rotating gas rings interact through viscosity: the inner rings, rotating faster, exert a torque on their slower outer neighbors, transferring angular momentum outward. At the same time, rings interact viscously with their inner neighbors, slowing them down and causing them to spiral inward. This viscous transport spreads the disk in both directions, with mass accreting inward and angular momentum transported outward. As the matter moves through the disk, gravitational potential energy is converted into heat and radiation through viscous dissipation. This process results in the highenergy radiation observed in X-ray binaries. The high efficiency of this mechanism makes accretion disks among the most luminous structures in the Universe.

2.3 Phenomenology of X-ray Binaries

As the matter in the accretion disk heats up due to viscous dissipation, it emits X-rays with luminosities that can vary significantly on timescales ranging from milliseconds to weeks. This variability reflects instabilities in the accretion flow and dynamic processes in the innermost regions of the disk. Overall, the presence of an accretion disk gives rise to a wide range of observational effects. In this chapter, we will outline the main ones.

2.3.1 Long-term Activity and State Transitions

Since accretion is the primary energy source in X-ray binaries, the luminosity of these systems is directly tied to the accretion rate (see Eq. 2). Low-mass X-ray binaries undergo periods of *quiescence*, during which the accretion rate is low, and the viscosity within the disk is insufficient to allow the material to lose angular momentum and move toward the compact object.

The emission from LMXBs in quiescence is dominated by the donor star, which is typically a faint, approximately main-sequence star. As a result, these systems are extremely faint in the optical band and undetectable in X-rays. After an extended quiescent phase, lasting from years to decades (or potentially even hundreds of years), accretion resumes, leading to a dramatic increase in luminosity in all wavelengths.

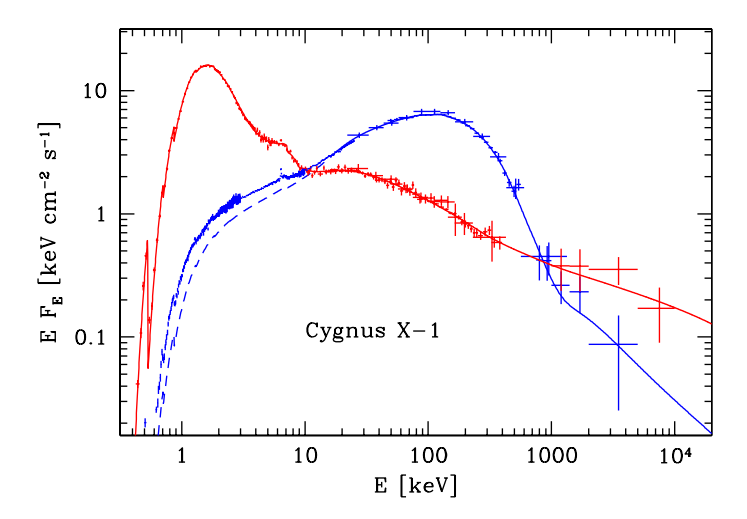


Figure 6. Hard (blue crosses) and soft (red crosses) spectra of Cyg X-1 (McConnell et al., 2002).

Such an event is called *an outburst*. The first LMXB of this kind was GX 339–4, discovered during its 1972 outburst (Markert et al., 1973) with Orbiting Solar Observatory 7 (OSO 7, Clark et al. 1973). The first dynamically confirmed black hole LMXB was A0620–00 (McClintock & Remillard, 1986), detected with British-American satellite Ariel V (Smith & Courtier, 1976) during an X-ray outburst in 1975 (Elvis et al., 1975; Boley et al., 1976), when its luminosity increased by a factor of a million, reaching the Eddington luminosity.

In addition to dramatic changes in luminosity, the spectral shape of X-ray binaries also changes drastically. One of the most prominent and well-studied examples is HMXB Cyg X-1, a persistent black hole X-ray binary which exhibits spectral state transitions (Gierliński et al., 1999). Based on differences in the spectral shape (see Fig. 6), the system's states are typically classified as "soft" and "hard" (Tananbaum et al., 1972a; Zdziarski & Gierliński, 2004; Done et al., 2007). The soft X-ray spectrum is generally attributed to thermal emission from a classical (optically thick and geometrically thin) accretion disk (Shakura & Sunyaev, 1973; Novikov & Thorne, 1973). In contrast, the hard state spectrum is believed to result from the Compton upscattering of seed photons by a hot medium surrounding the black hole, known as the X-ray corona (Sunyaev & Titarchuk, 1985; Poutanen & Svensson, 1996).

The spectral changes can be quantitatively described as the changes of the spectral hardness, usually defined as the ratio of flux in high-energy to low-energy X-ray band, e.g. F(10-20 keV)/F(2-6 keV). Because both spectral hardness and total luminosity evolve with time, it is customary to depict the state transitions of the X-ray binaries as 2D-evolution in the hardness-intensity diagram (HID, Mason et al. 1976; Makishima & Mitsuda 1985; Schulz et al. 1989). The evolution of an outburst on

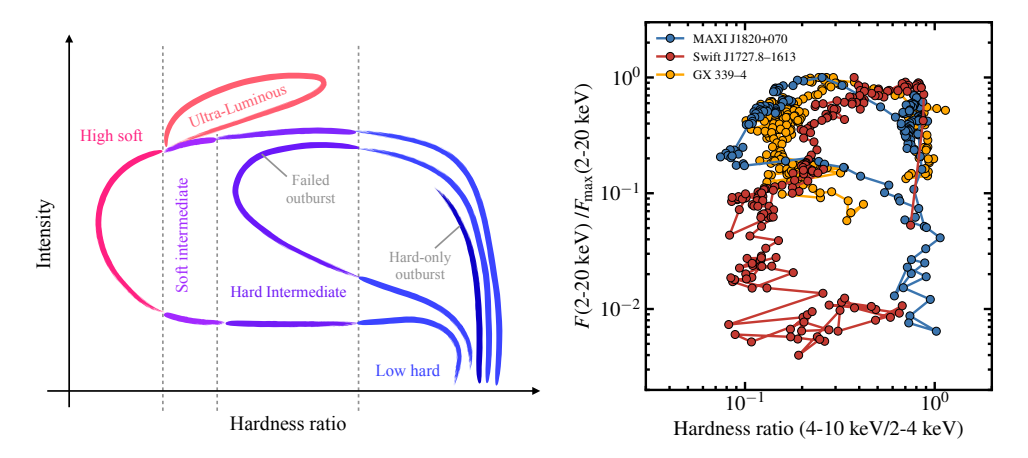


Figure 7. *Left:* A sketch of a typical hardness-intensity diagram (HID), Motta et al. 2021. *Right:* HID for MAXI J1820+070, Swift J1727.8–1613, GX 339–4 in their brightest outbursts as observed by MAXI satellite (Matsuoka et al., 2009). The flux is normalized to the peak flux.

HID is a closed hysteresis loop resembling the letter "q" (see Fig. 7), which is why HIDs are often referred to as q-diagrams.

A typical outburst begins in the bottom-right corner of the diagram, where the system only appears from quiescence and the X-ray spectrum is hard. The system then increases its luminosity by several orders of magnitude while maintaining a hard spectrum, moving to the top-right corner of the diagram. Next, at roughly constant luminosity, the system transitions to the soft spectral state. While residing in the soft state, the luminosity drops and the object makes reverse transition to the hard state, completing the outburst cycle. Examples of such behavior in real systems are shown in Fig 7. Although many phenomenological models exist to explain the observed spectra in different states (see Done et al. 2007; Belloni 2010 for an overview), no unified, widely accepted model yet provides a self-consistent explanation for both the spectral states and the transitions between them.

2.3.2 Orbital variability

X-ray binaries naturally exhibit variability at a distinct frequency set by their orbital period. In the optical band, XRBs show so-called "ellipsoidal variations" – periodic changes of the flux caused by the tidally distorted optical star (Avni & Bahcall, 1975; Morris, 1985; Sorabella et al., 2022): at different orbital phases, different surface areas of the star are visible to the observer, leading to variations in the observed flux. Additional, subtle modulations may arise from starspots or hot spots on the accretion disk, as well as from the disk itself, which can obscure the star during specific orbital

phases (Orosz & Bailyn, 1997; Orosz et al., 2007; Watarai & Fukue, 2010). An example of ellipsoidal variations of LMXB A0620–00 in quiescence is shown in Fig. 8 (Paper V).

X-ray emission of XRBs is also found to be modulated with the orbital period (Tananbaum et al., 1972a; Wen et al., 2006), which may be attributed to several mechanisms: an X-ray source may be eclipsed by the companion star, which is more common for HMXBs, or by the accretion flow or disk, usually in LMXBs (White & Swank, 1982); the wind from the companion star may cause phase-dependent absorption (Wen et al., 1999); the X-ray emission may be reprocessed in the vicinity or reflected by the companion star (Basko et al., 1974).

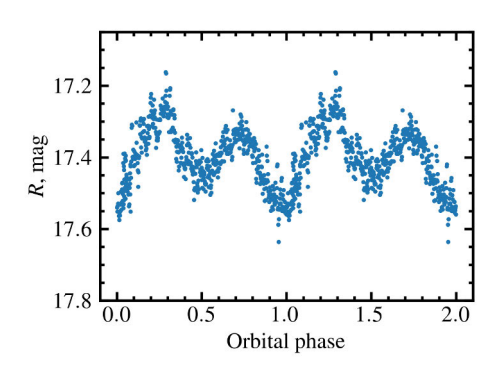


Figure 8. Optical light-curve of A0620-00 in quiescent state (Paper V).

Radial velocity (RV) variations, caused by the orbital motion of the companion star, produce periodic Doppler shifts in its spectral lines. By measuring these shifts over time and constructing a radial velocity curve, one can estimate the orbital parameters, which are crucial for understanding the physics of these systems. The RV method was first applied to a classical binary Algol by Vogel (1890), and a century later, for the first time to the optical companions of X-ray binaries by Bolton (1972) and Webster & Murdin (1972). In systems hosting pulsars, the Doppler effect is observed as periodic modulations in the pulsar period (Blandford & Teukolsky, 1975, 1976; Freire et al., 2001; Kramer et al., 2006). Additionally, polarization of X-ray binaries can vary periodically, as is discussed in Section 3.3.1.

2.3.3 Short-Term Variability

In addition to the long-term variability, XRBs exhibit variability on short time-scales (from milliseconds to seconds, Samimi et al. 1979; Motch et al. 1983; Miyamoto et al. 1991). To study short-period variability, Fourier analysis in general and power spectral density (PSD) analysis in particular are widely used (van der Klis, 1989). The PSDs of BHXRBs typically follow a broken power-law shape, corresponding to a broadband noise continuum, with distinct features at specific frequencies associated with so-called quasi-periodic oscillations (QPOs; Belloni & Hasinger, 1990; Belloni et al., 2002). QPOs are generally divided into two classes: low-frequency (LF) and high-frequency (HF), with centroid frequencies \leq 30 Hz and \geq 60 Hz, correspondingly. QPOs are thought to originate from instabilities and resonances in the

inner accretion flow or corona. LFQPOs are most likely caused by Lense–Thirring precession (Lense & Thirring, 1918) of a radially extended section of the hot inner accretion flow (Stella & Vietri, 1998; Fragile et al., 2007; Ingram et al., 2009). HFQPOs are rarely observed in black hole systems, appearing only in certain spectral states and luminosity ranges (Morgan et al., 1997; Remillard et al., 1999; Belloni et al., 2012). Consequently, no comprehensive theory has yet been developed to explain these oscillations. However, they are likely generated by processes occurring in the innermost regions of the accretion disk, near the innermost stable circular orbit (Remillard & McClintock, 2006; Belloni et al., 2012).

3 Polarization in X-ray binaries

Recent advances in X-ray polarimetry have opened a new observational window, enabling detailed tests of general relativity in the strong-field regime and improving our understanding of the interaction between matter, radiation, and gravity near black holes. This chapter defines polarization, describes the methods for its detection, and explores the processes through which it arises in XRBs.

3.1 Definition of Polarization

In most general terms, the polarization of light describes the orientation and behavior of its electric field vector as the light wave propagates. More specifically, polarization can be defined either for individual photons using Dirac notation (a formalism of modern quantum electrodynamics, see, e.g., Landau & Lifshitz 1991; Greiner & Reinhardt 2008) or for the electromagnetic field as a whole, as is customary in classical electrodynamics (Landau & Lifshitz, 1975).

In classical electrodynamics, the behavior of electromagnetic waves in vacuum is described by Maxwell's equations (Maxwell, 1865; Rybicki & Lightman, 1979):

$$\nabla E = 0,$$

$$\nabla B = 0,$$

$$\nabla \times E = -\frac{1}{c} \frac{\partial B}{\partial t},$$

$$\nabla \times B = \frac{1}{c} \frac{\partial E}{\partial t},$$
(4)

where E and B are electric and magnetic fields.

The solution of these equations is a transversal electromagnetic wave. In a Cartesian right-handed coordinate system constructed so the wave propagates along the z-axis, the solution for the electric field vector \vec{E} can be written as follows (Rybicki & Lightman, 1979):

$$E_x(t) = E_{0x} \cos(\varphi_x - \omega t), \tag{5}$$

$$E_{y}(t) = E_{0y}\cos(\varphi_{y} - \omega t). \tag{6}$$

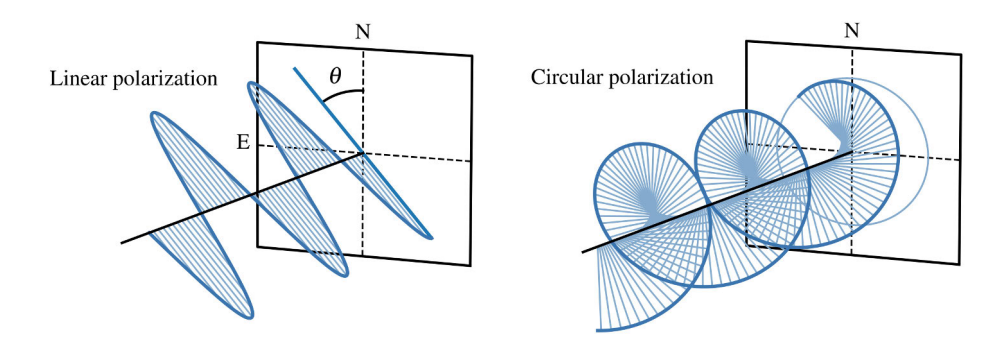


Figure 9. Illustration of electromagnetic field vector trajectory for linearly (left) and circularly (right) polarized light.

These equations describe the trajectory of the tip of the electric vector \vec{E} in the x-y plane. By expanding the cosine of the difference:

$$\frac{E_x}{E_{0x}} = \cos \varphi_x \cos (\omega t) + \sin \varphi_x \sin (\omega t), \tag{7}$$

$$\frac{E_y}{E_{0u}} = \cos \varphi_y \cos (\omega t) + \sin \varphi_y \sin (\omega t), \tag{8}$$

and by eliminating the ωt term using the Pythagorean identity $\sin^2(\omega t) + \cos^2(\omega t) = 1$, the system transforms into the general ellipse equation:

$$\frac{E_x^2}{E_{0x}^2} + \frac{E_y^2}{E_{0y}^2} - 2\frac{E_x E_y}{E_{0x} E_{0y}} \cos(\Delta \varphi) = \sin^2(\Delta \varphi), \tag{9}$$

where $\Delta \varphi = \varphi_{v} - \varphi_{x}$.

Equation (9) is the equation of an ellipse that describes the motion of the tip of the electric vector during a monochromatic electromagnetic wave propagation (see Fig. 9). The characteristic time of one revolution of this tip around z-axis is $1/\nu$, where ν is the wave frequency. The typical exposure time of astrophysical observations exceeds the latter by many orders of magnitude, meaning that the measured quantity is some average field $\langle E \rangle$:

$$\frac{\langle E_x^2 \rangle}{E_{0x}^2} + \frac{\langle E_y^2 \rangle}{E_{0y}^2} - 2 \frac{\langle E_x E_y \rangle}{E_{0x} E_{0y}} \cos(\Delta \varphi) = \sin^2(\Delta \varphi), \tag{10}$$

$$\langle E_x^2 \rangle = \frac{1}{2} E_{0x}^2, \quad \langle E_y^2 \rangle = \frac{1}{2} E_{0y}^2, \quad \langle E_x E_y \rangle = \frac{1}{2} E_{0x} E_{0y} \cos(\Delta \varphi). \tag{11}$$

Multiplying (10) by $4E_{0x}E_{0y}$, substituting (11) into (10) and regrouping terms yields the following equation:

$$(E_{0x}^2 + E_{0y}^2)^2 - (E_{0x}^2 - E_{0y}^2)^2 - (2E_{0x}E_{0y}\cos(\Delta\varphi))^2 = (2E_{0x}E_{0y}\sin(\Delta\varphi))^2, (12)$$

which can be simplified to just:

$$I^2 = Q^2 + U^2 + V^2, (13)$$

if we define

$$I = E_{0x}^2 + E_{0y}^2, (14)$$

$$Q = E_{0x}^2 - E_{0y}^2, (15)$$

$$U = 2E_{0x}E_{0y}\cos(\Delta\varphi),\tag{16}$$

$$V = 2E_{0x}E_{0y}\sin(\Delta\varphi). \tag{17}$$

The later four quantities, for the first time introduced in Stokes (1851), are commonly referred to as Stokes parameters of polarization for a plane electromagnetic wave. The parameter I is the total intensity of the light, Q describes the difference in intensities between x and y directions, U quantifies the difference between intensities of waves, oscillating along "diagonal" 45° and 135° directions, and V is the intensity of circularly polarized light. The Eq. (13) holds only for 100% polarized light: for unpolarized light, Q = U = V = 0, and for arbitrary polarized light, $I^2 \ge Q^2 + U^2 + V^2$. In observational astronomy, normalized Stokes parameters Q = Q/I, Q = U/I, and Q = V/I are often used. It can be shown that the Stokes parameters are additive: Stokes parameters of the superposition of two waves are the algebraic sum of those of the original waves (Chandrasekhar, 1960), which is an extremely useful property when considering light from several incoherent sources.

The fraction of the total intensity polarized along the predominant polarization plane is described by the polarization degree (PD):

$$p = \frac{\sqrt{Q^2 + U^2 + V^2}}{I}.$$

If the circular polarization is negligible in comparison to linear polarization, the degree of linear polarization is:

$$p = \frac{\sqrt{Q^2 + U^2}}{I}.$$

The direction of the dominant electric field oscillation of the linearly polarized light is given by the polarization angle (PA) χ :

$$\chi = \frac{1}{2}\arg(Q + iU) = \arctan\left(\frac{\sqrt{Q^2 + U^2} - Q}{U}\right)$$

To ensure that polarization measurements from different observatories and instruments are directly comparable, the polarization angle reference direction should be defined. According to the International Astronomical Union (IAU) convention, the polarization angle on the sky is measured from celestial north toward celestial east, in the plane perpendicular to the line of sight (i.e., the sky plane), and ranges from 0° to 180° (see Fig. 10).

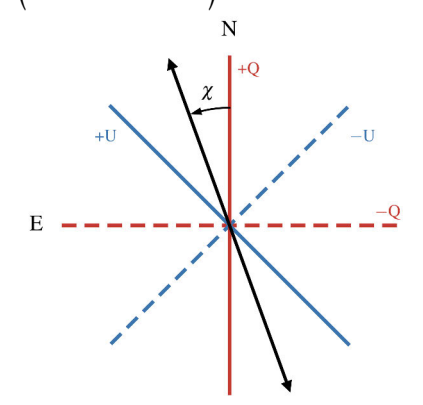


Figure 10. IAU convention on the polarization angle definition.

3.2 Multiwavelength Polarimetry

Soon after the polarization of light was discovered, astronomers began seeking ways to detect it from astrophysical objects. One of the first documented astronomical polarimetric observations was the discovery of the polarization from the comet C/1819 N1 in 1819 by François Arago (see Levasseur-Regourd 2019 for historical overview). Later in 1843, the first star was found to be intrinsically polarized – François Arago discovered the polarization of the solar corona (Arago, 1843), which was described later in a paper by Swedish physicist Erik Edlund titled "On the Polarisation of the Light of the Corona during Total Solar Eclipses" published in Astronomische Nachrichten in 1860 (Edlund, 1860). These observations marked the beginning of astrophysical polarimetric observations. In this section, we will discuss how astrophysical polarimetry has evolved over one and a half centuries and describe the tools now available for polarimetric observations across the entire electromagnetic spectrum, from radio to X-rays.

3.2.1 Radio Polarimetry

Radio receivers take full advantage of the wave nature of electromagnetic radiation, which allows them to nearly automatically detect the polarization of the observed radiation. This ability arises from the fact that radio receivers "see" radiation as waves with phase and amplitude, rather than as a superposition of waves with varying intensity, since the wavelength is comparable to the antenna size. The simplest radio

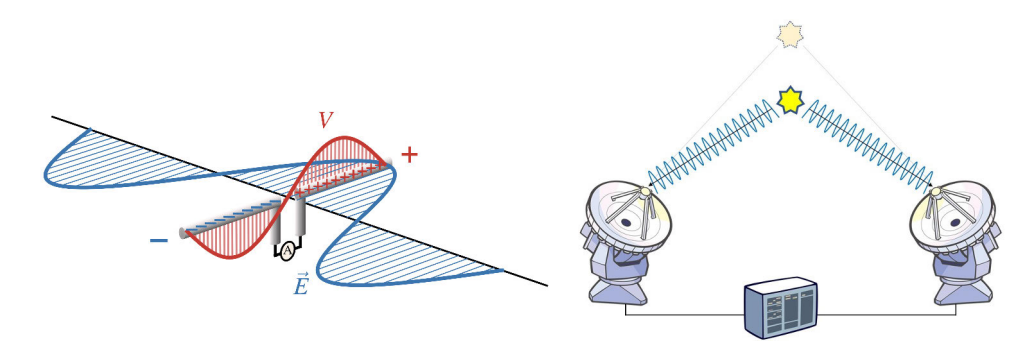


Figure 11. *Left:* Scheme of dipole radio antenna. *Right:* Scheme of interferometer. Image: ALMA (ESO/NAOJ/NRAO)

telescope is just a metal rod with the ammeter attached to it (see Fig. 11, left). As the electromagnetic wave passes through the rod, the electric field of the wave causes the electrons in the rod to oscillate back and forth, generating a current that flows through the ammeter. By measuring the current, one can infer the power of the received radiation. By rotating the antenna, one can also measure the polarization of the radiation.

Obviously, modern radio telescopes, such as the Karl G. Jansky Very Large Array (VLA) or Atacama Large Millimeter/submillimeter Array (ALMA), have advanced far beyond such a simple scheme. They utilize telescope array design (see Fig. 11, right) and radio interferometry, a technique where multiple radio telescopes are combined to act as a single, large telescope, to greatly increase the angular resolution and sensitivity of the instruments. By measuring the phase difference of radio waves arriving at each telescope, the system constructs an interference pattern that encodes spatial information about the source (McCready et al., 1947; Ryle, 1952). This pattern is then processed using techniques like Fourier transforms to produce highly detailed images of astrophysical objects, with the effective resolution limited by the maximum sep-

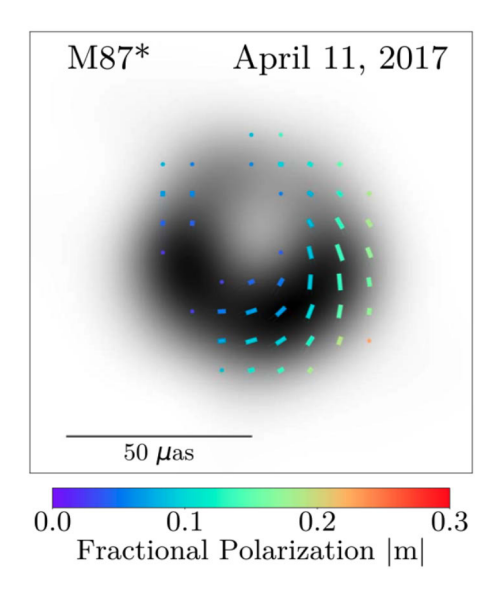


Figure 12. EHT polarimetric image of M87*. The intensity is shown in gray scale, and ticks illustrate the degree and direction of linear polarization (Event Horizon Telescope Collaboration et al., 2021).

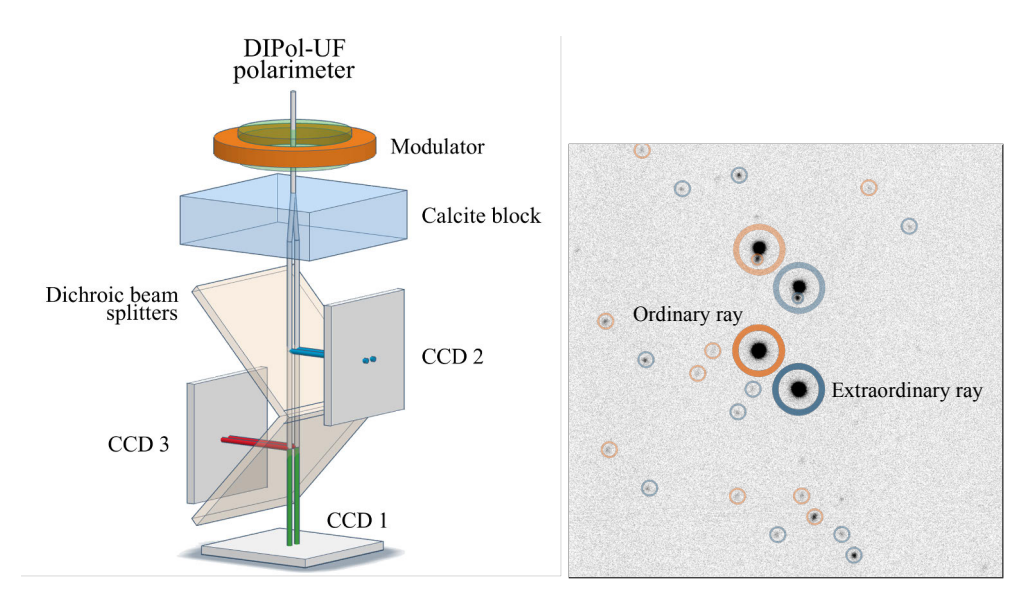


Figure 13. *Left*: Scheme of DIPol-2/UF polarimeter. *Right*: DIPol-2 image of Cyg X-1. All stars at the image are doubled due to the double-beam design of the instrument.

aration (baseline) between the telescopes. It makes radio interferometry computationally intensive, requiring precise calibration to correct for atmospheric distortions, instrumental imperfections, and variations in the array geometry. Additionally, the reconstruction of images from interference patterns involves solving complex inverse problems, often limited by noise, incomplete sampling, when use of advanced algorithms like CLEAN is needed to recover spatial information accurately (Högbom, 1974). In such cases, accurately measuring the polarization of radiation is an extremely complex task, the description of which goes beyond the scope of this thesis. However, it provides remarkable results such as the construction of a polarization map of the accretion disk around the black hole at the center of the M87 galaxy, obtained by the Event Horizon Telescope Collaboration et al. (2021), see Fig. 12.

3.2.2 Optical Polarimetry

Unlike the radio range, where instrument size is comparable to the wavelength of radiation, the size of optical instruments exceeds the wavelength by many orders of magnitude, requiring different methods for measuring the polarization. Most modern optical polarimeters employ a double-beam design, where the incoming radiation passes through a birefringent material before being detected. The phenomenon of birefringence in Iceland spar (a transparent form of calcite) was first documented by Danish physicist Erasmus Bartholin (1670), when he observed double refraction of light passing through the crystal. Centuries earlier, however, it is believed that

Viking navigators used Iceland spar as a "sunstone" to locate the Sun's position in overcast conditions by effectively measuring the polarization of the skylight (see Ropars et al. 2014 for historical overview). Materials like calcite have a refractive index that differs for rays polarized parallel and perpendicular to the optical axis of the crystal (Fresnel, 1821). This property of calcite and similar crystals is used to create an effective polarimeter for astrophysical observations.

A standard polarimeter comprises three main components: an analyzer, a modulator, and a detector (Serkowski, 1974; Berdyugin et al., 2019). The analyzer is an optical component that selectively transmits light with a specific polarization. This can either be a polarizer (single-beam analyzer) or a calcite crystal (double-beam analyzer). The modulator systematically alters the polarization of the incoming light, enabling the detection of its full polarization properties, including the polarization angle. Common modulators include half- and quarter-wave plates, which induce phase shifts of a half and a quarter of a wavelength, respectively, rotating the linear polarization or converting circular polarization into linear polarization. The final essential component of the polarimeter is a detector, which is most commonly a CCD camera.

In this thesis, we used DIPol-2 and DIPol-UF optical polarimeters (Piirola et al., 2014, 2021; Kosenkov, 2021). DIPol-family of polarimeters use a half-wave plate as the modulator and a plane-parallel calcite plate as a beam splitter (see Fig. 13, left). To measure the polarization with this instrument, one needs to capture at least four images of the object, with each image corresponding to a different orientation of the half-wave plate: 0° , 22.5° , 45° , and 67.5° . Next, an aperture photometry is used to determine the brightness ratio of ordinary and extraordinary rays $R = I_e/I_o$ for all four images. The normalized Stokes parameters are then computed as:

$$q = (R_0 - R_{45})/R_{\rm m}$$
 $u = (R_{22.5} - R_{67.5})/R_{\rm m}$, (18)

where $R_{\rm m} = R_0 + R_{22.5} + R_{45} + R_{67.5}$.

To determine the intrinsic polarization of the source, it is necessary to account for both instrumental and interstellar polarization. This is achieved by observing zero- and high-polarization standards, as well as the polarization of field stars. A more detailed description of the entire process of optical polarimetric observations is provided in Kosenkov (2021).

3.2.3 X-ray Polarimetry

X-ray polarimetric observations are generally more challenging compared to optical and radio observations due to several reasons. First, the Earth's atmosphere is completely opaque to X-rays, necessitating the deployment of X-ray polarimeters in space. Second, X-ray radiation has a very high frequency and, consequently, energy, which allows it to penetrate most materials rather than being reflected or re-

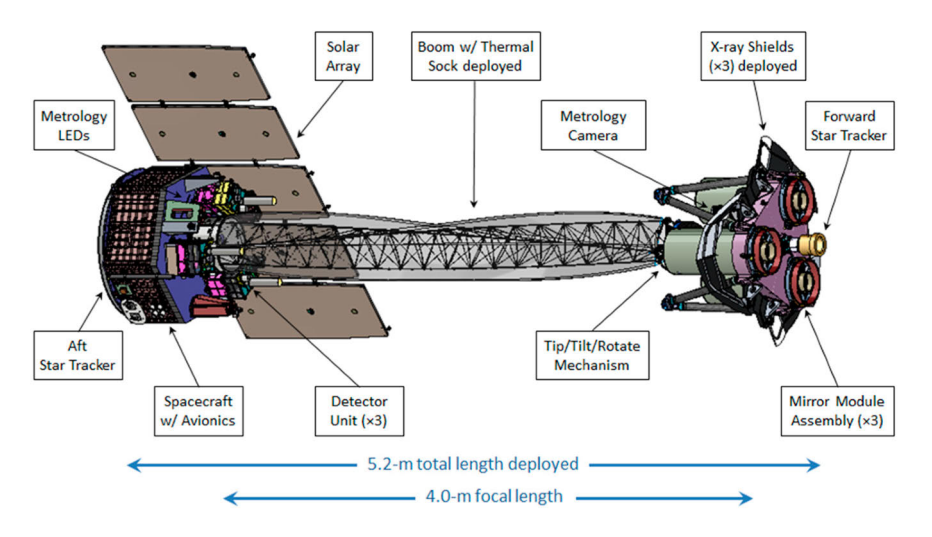


Figure 14. Scheme of IXPE satellite (Weisskopf, 2018).

fracted from them like visible light. These two factors make X-ray polarimetry technically challenging, which, despite numerous earlier attempts starting in the 1970s (e.g. Aerobee 350 rocket experiment, Novick et al. (1972), polarization experiment on NASA's 8th Orbiting Solar Observatory, OSO-8, in 1975, Weisskopf et al. 1976, 1978, Ariel V mission, Smith & Courtier 1976; Gowen et al. 1977), was accomplished to the point of reliable detection of polarization from dozens of XRBs only in 2022 with the launch of Imaging X-ray Polarimetry Explorer (IXPE) satellite (Weisskopf et al., 2022).

The detection principle of soft X-ray polarization by IXPE, that made two orders of magnitude leap in sensitivity (Costa et al., 2001), is the following: after the radiation from the source is focused using collimating telescopes, it is directed onto a gas pixel detector (GPD). The GPD records the photoelectron tracks produced when X-rays are absorbed in a specially chosen fill gas (Baldini et al., 2021). The initial emission direction of the photoelectron encodes the source polarization, while the position of the interaction point and the total charge deposited along the track provide the X-ray's location and energy, respectively (Weisskopf et al., 2022).

3.3 Sources of Polarization in BHXRBs

Most of the radiation observed from astrophysical sources has a thermal origin and generally carries little intrinsic polarization. However, various physical mechanisms can generate significant polarization or alter an existing one. This section will discuss astrophysical processes that generate or modify polarization, specifically in the context of BHXRBs.

3.3.1 Scattering

The most common physical mechanism that leads to polarization production is scattering. The radiation can be scattered by a wide range of particles: free electrons (Thomson or Compton scattering, Thomson 1907; Compton 1923), molecules (Rayleigh scattering, Strutt 1871; Rayleigh 1899), or dust particles (Mie scattering, Mie 1908). Due to the high temperatures, nearly all matter in the vicinity of black holes is ionized, making the most frequent type to be free-electron scattering.

A general case of such scattering is Compton scattering – a photon with initial 4-momentum $\underline{k} = h\nu/c\{1,\vec{n}\}$, where \vec{n} is a unit vector of photon propagation, scatters off an electron with the momentum $\underline{p} = \{mc, 0\}$ placed at the origin of the laboratory frame. After the scattering, the photon and electron 4-momenta are $\underline{k}' = h\nu'/c\{1, \vec{n}'\}$ and $\underline{p}' = \{E_e/c, \vec{p}_e\}$. The differential cross-section for Compton scattering is given by the Klein–Nishina formula:

$$\frac{d\sigma}{d\Omega} = \frac{1}{2}r_{\rm e}^2 \left(\frac{v'}{v}\right)^2 \left[\frac{v'}{v} + \frac{v}{v'} + \cos^2\theta - 1\right],$$

where $\cos \theta = \vec{n} \cdot \vec{n}'$ is the cosine of the scattering angle θ and r_e is a classical electron radius. The change in the photon frequency after scattering may be found from the momentum conservation law and has the following form, usually referred to as the Compton shift formula (Compton, 1923):

$$\frac{1}{\nu} + \frac{1}{\nu'} = \frac{h}{mc^2} (1 - \cos\theta).$$

The polarization degree of initially unpolarized light after scattering is given by:

$$p = \frac{\sin^2 \theta}{\frac{\nu}{\nu'} + \frac{\nu'}{\nu} - \sin^2 \theta}.$$
 (19)

When the energy of the incoming photon is much smaller than the rest energy of the electron ($h\nu \ll 511 \text{ keV}$), the interaction becomes quasi-elastic with negligible energy exchange. In this case, the frequency of the scattered radiation remains unchanged, and the expression for polarization takes the following (Thomson) form:

$$p = \frac{1 - \cos^2 \theta}{1 + \cos^2 \theta}.\tag{20}$$

In XRBs, Compton scattering is essential when describing the observed X-ray spectra. It is commonly assumed that in the hard state, "soft" thermal photons from the accretion disk undergo Comptonization – the energy gain as a result of scattering on the hot plasma known as the *corona*, leading to a harder X-ray spectrum. Since scattered radiation can be polarized (as indicated by Eq. 19), information about the geometry of the corona can be extracted from the degree of polarization and its spectrum. In Paper III, unexpectedly high X-ray polarization of Cyg X-1 with PA aligned

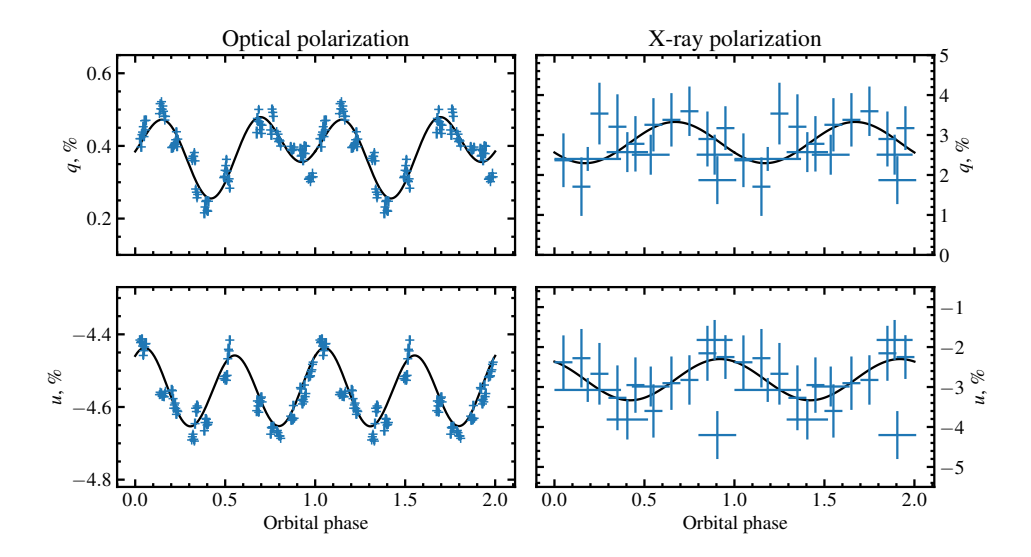


Figure 15. Orbital variability of Cyg X-1 in optical (left, Paper II) and X-ray (right, Paper I) polarization.

with that in the radio and optical, coming from Compton scattering in a hot black hole corona, significantly narrowed the range of plausible models for its geometry, favoring a model in which the X-ray emission region is extended perpendicular to the jet.

In the optical range, particularly in HMXBs, most of the radiation is produced by the donor star. This radiation can be scattered by the material that follows the compact object in its orbital motion. As seen from Eq. (20), polarization from Thomson scattering depends on the scattering angle – in this case, the angle between the direction from the companion star to the compact object and from the object to the observer. Due to the orbital motion, the scattering angle changes with the orbital phase ϕ , making the polarization variable with the period of the binary system (Brown et al. 1978, Paper IV). The orbital profiles of the Stokes parameters depend on how the scattering angle changes over time, which is determined mostly by the eccentricity e of the orbit and the orbital inclination i:

$$q = \frac{3f_0}{16} \left[\sin^2 i - \left(1 + \cos^2 i \right) \cos 2\lambda \right] \left[1 + e \cos \left(\lambda - \lambda_p \right) \right]^2,$$

$$u = \frac{3f_0}{8} \left[-\cos i \sin 2\lambda \right] \left[1 + e \cos \left(\lambda - \lambda_p \right) \right]^2,$$
(21)

where $\lambda = 2\pi\phi$ is the orbital longitude, λ_p is the longitude of periastron and f_0 is the fraction of scattered radiation.

By fitting Eqs. (21) to the observed orbital profiles of Stokes parameters, it is possible to estimate the orbital parameters of a binary system, such as eccentricity

and inclination. In Paper IV, we used this method to put independent constraints on the eccentricity of Be X-ray binary LS I +61 303, in which it is problematic to apply classical methods like Doppler spectroscopy due to complex gas dynamics in the decretion disk of the companion star. In Paper II, by applyting the method to the optical polarimetric observations of Cyg X-1 we were able to constrain the eccentricity and orbital inclination of the binary (see Fig. 15, left).

In the X-ray band, emission produced in the vicinity of the compact object can be reflected off the optical companion or scattered at some intrabinary structure (e.g. disk, stellar or disk wind, bow shock), leading to similar variability in X-ray polarization (see Fig. 15, right). In Paper VII, we developed a physical model of the reflection and used it to describe the observed variability in the X-ray polarization of the binary system GS 1826–238. We showed that the signal expected from such reflection is very weak, with a variability amplitude at the $\sim 1\%$ level. Such a low amplitude, combined with the current precision of X-ray polarimetric observations does not yet allow polarimetric determination of orbital parameters. Future, more precise observations may enable this analysis.

3.3.2 Synchrotron Emission

Synchrotron radiation is electromagnetic radiation emitted by relativistic charged particles spiraling around magnetic field lines (see Fig. 16). In XRBs, this radiation typically arises from relativistic jets or highly magnetized plasma structures within the corona. Synchrotron emission is intrinsically polarized, with both the polarization degree and polarization direction depending on the magnetic field configuration and the observer's viewing angle. An ensemble of electrons with an isotropic velocity distribution moving in an ordered magnetic field can generate linearly polarical direction and the polarization direction depending on the magnetic field can generate linearly polarical field can generate linearly polarical directions with an isotropic velocity distribution moving in an ordered magnetic field can generate linearly polarical directions.

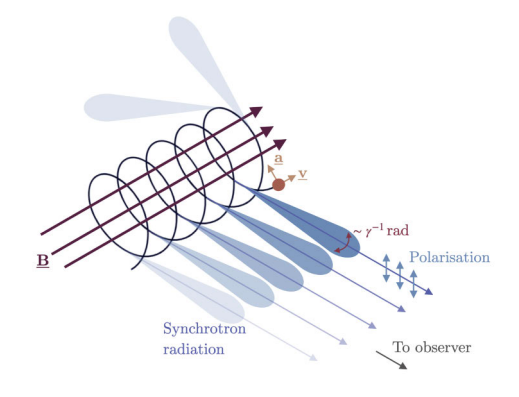


Figure 16. Schematic diagram of synchrotron emission. Image: Emma Alexander.

ized radiation with a PD of up to $\approx 75\%$ (Rybicki & Lightman, 1979). The maximum polarization for synchrotron radiation is given by

$$p = \frac{\alpha + 1}{\alpha + \frac{7}{3}},\tag{22}$$

where the electrons have a power-law energy distribution $dN/dE \propto E^{-\alpha}$ (Ginzburg & Syrovatskii, 1965; Legg & Westfold, 1968).

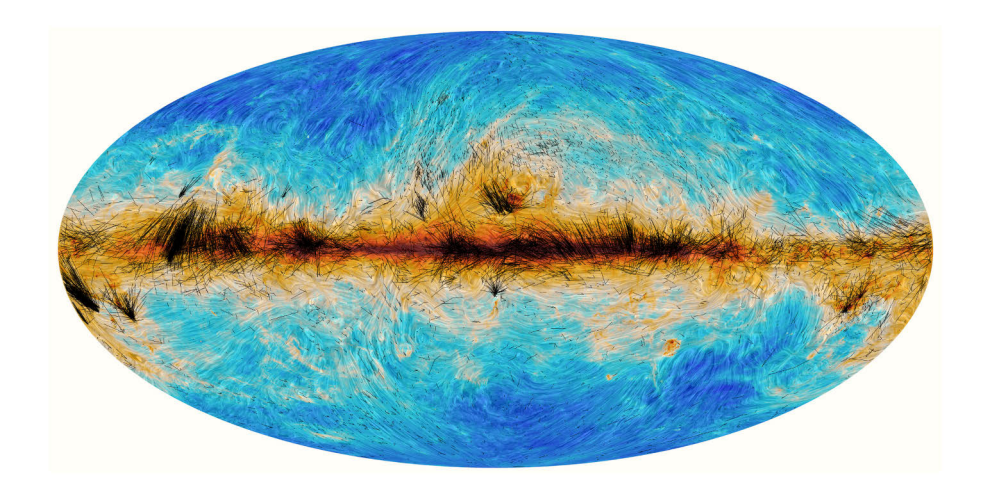


Figure 17. Polarization map of our Galaxy in submillimetre as observed by Planck Collaboration et al. (2020) combined with optical polarization measurements from Axon & Ellis (1976); Heiles (2000); Berdyugin et al. (2014) shown in black.

Despite this high expected PD, polarization from synchrotron emission is rarely observed in XRBs, unlike active galactic nuclei (AGNs). In the radio band, where most of the flux originates from the radio jet, polarization has only been detected in a few systems (Fender et al. 2003; Brocksopp et al. 2007, 2013; Koljonen & Hovatta 2021; Tian et al. 2023, Paper I). Radio polarization is often "washed out" by factors such as Faraday rotation (see Sect. 3.3.4), field inhomogeneities or the rotation of "blobs" producing the polarization. In the optical band, the contribution of synchrotron radiation to the total flux is typically small (a few per cent), making synchrotron polarization detection challenging (Paper VI). In the X-ray band, a significant polarization degree of 38%–77% has been detected from the "lobes" of the microquasar SS 433, with the polarization angle aligned with the jet direction, indicating synchrotron origin (Kaaret et al., 2024). Apart from that, no strong evidence of polarized X-rays from jet synchrotron emission have been found in black hole X-ray binaries (see discussion in Paper III; Dovčiak et al. 2024; Mastroserio et al. 2025).

3.3.3 Interstellar Polarization

As light from distant stars propagates through the interstellar medium (ISM), it becomes partially polarized due to interactions with dust particles, a phenomenon first observed independently by Hall (1949) and Hiltner (1949). The dust grains, which are not perfectly spherical, tend to align with the Galactic magnetic field. As the

scattering cross-section depends on the polarization of the incoming light, interstellar dust filters radiation polarized parallel to the dust grain alignment (i.e., along the Galactic magnetic field). As a result, light passing through the ISM becomes polarized, with its electric field vector oscillating in a direction aligned with the magnetic field (see Fig. 17).

The characteristic size of the dust grains determines the wavelength range affected by the ISM, which is primarily in the optical and ultraviolet bands. In the radio band, polarization measurements are often affected by Faraday rotation, whereas X-ray polarization is unaffected by the ISM. Accounting for interstellar polarization is a crucial step in optical astronomy for determining the intrinsic polarization of the observed objects. Due to the additivity of the Stokes parameters and under the assumption that $PD_{ism} \ll 1$, the intrinsic polarization of the source can be expressed as the difference between the observed and interstellar components:

$$q_{\text{int}} = q_{\text{obs}} - q_{\text{ism}}, \quad u_{\text{int}} = u_{\text{obs}} - u_{\text{ism}}.$$

Thus, to determine the intrinsic polarization of the source, the interstellar polarization must be measured and subtracted first. The most accurate method for estimating interstellar polarization involves measuring the polarization of the field stars, close both in the angular separation and in distance. Suitable stars can be identified using parallaxes from *Gaia* (Gaia Collaboration et al., 2021). Unlike interstellar extinction, interstellar polarization may decrease with distance if multiple dust clouds with different grain alignments are present along the line of sight. The combination of two polarizations with differing angles results in lower polarization with a different angle. This effect was observed in gamma-ray binary LS I +61 303 (Paper IV), located close to the Heart Nebula, dust grain orientations of which differ from the Galactic dust.

3.3.4 Faraday Effect

Magnetic fields and plasmas are common ingredients of astrophysical environments, especially near accreting black holes. When polarized radiation passes through a magnetized plasma, the plasma introduces a phase difference between the left- and right-handed circularly polarized components of radiation. As a result, the angle of linear polarization, which can always be decomposed into a superposition of two equal-amplitude circularly polarized components with opposite handedness, rotates with the wavelength λ as (see Fig. 18):

$$\theta(\lambda) = \theta_0 + RM \lambda^2, \tag{23}$$

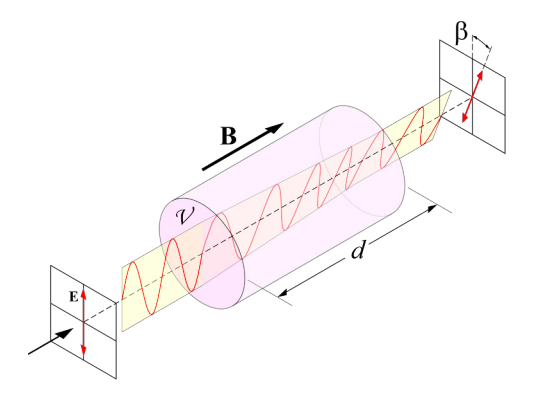


Figure 18. Scheme of Faraday rotation. Image: Bob Mellish.

where the rotation measure RM is defined as the integral along the line of sight

$$RM = \frac{e^3}{2\pi m_e^2 c^4} \int n_e(l) B_{||}(l) dl,$$
 (24)

where $n_{\rm e}$ is the electron number density, $B_{||}$ (in G) is the line of sight magnetic field strength, e is the elementary charge, $m_{\rm e}$ is the electron mass and c is the speed of light. If the magnetic field $B_{||}$ is constant, the RM can be expressed through the Thomson optical depth $\tau_{\rm T} = \int n_{\rm e}\sigma_{\rm T}dl$ as RM $\approx 0.4\tau_{\rm T}B_{||}$ rad $\mu{\rm m}^{-2}$. If the emitting region has a range of depths along the line of sight, different layers will experience different amounts of Faraday rotation. The superposition of polarized waves with varying polarization angles leads to the reduction of net polarization, the process often referred to as the Faraday depolarization.

Since the Faraday rotation scales with the square of wavelength, it is most significant at radio wavelengths. Even relatively weak Galactic magnetic fields on the order of a few μ G and low number densities of the interstellar medium can significantly alter the radio polarization, which necessitates its careful subtraction (Cooper & Price, 1962; Gardner & Whiteoak, 1963). However, Faraday rotation may also affect optical polarimetric observations. For instance, a magnetic field of ~ 5 G and a plasma optical depth of $\tau_T \sim 0.1$ are sufficient to noticeably rotate the optical polarization angle, which was proposed as one of the possible explanations for the observed polarization rotation in A0620–00 (Paper V). To significantly affect X-ray polarization, much stronger magnetic fields are required, typically on the order of 10^6-10^8 G. Such conditions, however, can still occur in X-ray binaries, pulsars, and magnetars (Barnier & Done, 2024; Taverna & Turolla, 2024).

4 Summary of the original publications

I Variability of X-ray polarization of Cyg X-1

In this manuscript, we report the results of a three-year X-ray, optical, and radio polarimetric monitoring campaign of the black hole X-ray binary Cyg X-1. We measured X-ray polarization of the source 13 times with IXPE, both in hard and soft states. We found the PD in the hard state to be $\approx 4\%$, roughly twice as high as in the soft state, where it was $\approx 2\%$. In both states, the PD increases with the photon energy, while the PA is independent of the spectral states and show no trend with energy. We also find that PD depends on spectral hardness, in a manner similar to what was observed in other black hole binaries both in slope and absolute value, suggesting consistency in the physical conditions in these systems during state transitions. Using VLA observations, we detect, for the first time, polarization of the radio emission of Cyg X-1, with the PA aligned with the jet direction, as well as with PA in both X-rays and optical. At the same time, we find clear orbital-phase modulation of X-ray polarization – the PD varies sinusoidally, gradually increasing from $\approx 3\%$ at orbital phase 0.1 to the maximum of $\approx 5\%$ at phase 0.5. The observed PA shows a swing with an amplitude of $\sim 10^{\circ}$ half-cycle out of phase with the PD. This behavior cannot be explained by either reflection from the companion star (Paper VII) or scattering in the spherical cloud (Papers IV and VIII), as both models produce two peaks per orbit instead of one, implying the asymmetry of the scattering matter relative to the orbital phase. Future high-precision X-ray polarimetric observations with instruments like eXTP are essential for further identification of this variability.

II Peering into the tilted heart of Cyg X-1 with highprecision optical polarimetry

In this paper, we present the results of high-precision optical polarimetric observations of black hole X-ray binary Cyg X-1, covering several cycles of its 5.6-day orbital period and carried out simultaneously with the first IXPE observation of the source in 2022. Week-long observations at two telescopes located in opposite hemispheres allowed us to follow the evolution of the polarization over a single orbital cycle with the highest temporal resolution achieved to date. We found that the optical polarization angle is aligned with the polarization angle in X-rays, as well as with

the direction of the radio jet. We have detected significant variability of the intrinsic optical polarization of Cyg X-1 with orbital period, caused by Thomson scattering of the companion star radiation by the matter that follows the black hole in its orbital motion. We found the asymmetry in the shapes of the orbital profiles of the Stokes parameters, which implies also an asymmetry of the distribution of scattering matter in the orbital plane, which may arise due to the inclination of the accretion disc. By extending the model from Paper IV to take into account precession of the accretion disc, we were able to model the polarization profiles and constrain the eccentricity and inclination of the orbit of the black hole X-ray binary.

III Polarized x-rays constrain the disk-jet geometry in the black hole x-ray binary Cygnus X-1

In this paper, we report the first reliable measurement of X-ray polarization of Cyg X-1. This was the first observation of a black hole X-ray binary with IXPE. The PD of X-ray polarization of Cyg X-1 in the hard state was found to be $\sim\!4\%$ with the PA aligned with the radio jet and the optical polarization PA measured simultaneously and described in Paper II, implying that the jet is launched from the inner X-ray emitting region. The observations reveal that the hot corona, which is needed to explain the hard X-ray spectrum of the source, is spatially extended in the plane perpendicular to the jet axis, not parallel to it, ruling out models in which the corona is extended along the jet axis.

IV Orbital variability of the optical linear polarization of the gamma-ray binary LS I +61 303 and new constraints on the orbital parameters

In this article, we present the results of 140 days of optical polarimetric observations of high-mass X-ray binary LS I +61 303, hosting Be-type star and a compact object of still unknown nature (either a BH or a NS). We detected for the first time a statistically significant orbital polarization variability in this source. We developed a simple toy model of Thomson scattering off a cloud of free electrons orbiting the central illuminating source to explain the observed variations. By fitting this model to the data, we derive constraints on the orbital parameters, including a small eccentricity e < 0.2 and a periastron phase $\varphi_p \sim 0.6$, which coincides with the peaks in radio, X-ray, and TeV emission. We argue that the apparent inconsistency between our and previous measurements of the orbital parameters from radial velocities is coming from the complex kinematics of the gas in the Be star circumstellar disk.

V Optical and near-infrared polarization of the black hole X-ray binary A0620–00 in quiescence

In Paper V, we present the results of high-precision optical polarimetric and NIR to UV photometric observations of a low-mass black hole X-ray binary A0620–00 in the quiescent state. By carefully measuring and subtracting the interstellar polarization, we show that the object has significant intrinsic polarization. We found that the intrinsic polarization of the source is variable with orbital period, which favors the fact that it is produced by scattering. In addition, we see the rotation of the intrinsic PA from 164° in R to 180° in B. The above, combined with historical polarimetric observations in NIR from Russell et al. (2016), shows about 53° rotation of the PA with wavelength, while PD of $\sim 1\%$ remains nearly constant throughout the whole spectral range. At the same time, photometric observations show a significant excess of UV photons in the SED of the binary. We propose two models that could explain the spectro-polarimetric properties of the object: a model with two polarized components (e.g., polarization from scattering at the intrabinary matter and polarization from the accretion disk) having different polarization angles, or Faraday rotation of the polarization plane in the surrounding magnetized plasma.

VI Optical polarization signatures of black hole X-ray binaries

In Paper VI, we present the results of the first comprehensive optical polarimetric survey of a sample of historical black hole X-ray binaries observed in quiescent (or near quiescent) state. We study both long- and short-period systems located at different galactic latitudes. We performed a thorough analysis of the interstellar polarization towards the sources to reliably estimate the intrinsic polarization. Our analysis showed that in most objects the intrinsic polarization is very small (with PD $\lesssim 0.2\%$), which imposes strong constraints on the physical processes that occur in such systems in quiescence. Namely, we show that the contribution of synchrotron radiation in the optical range cannot be large in quiescent X-ray binaries, since synchrotron radiation is expected to be highly polarized.

VII Orbital variability of polarized X-ray radiation reflected from a companion star in X-ray binaries

In this paper, we developed an analytical single-scattering model of the polarized reflection of the X-ray emission produced by a compact object from the companion star. Two cases were considered — reflection from a spherical star and a star filling its Roche lobe. We find that in both cases, polarized X-ray reflection from the companion star is weak because it is diluted by unpolarized direct emission from the

compact object. If diluted, the reflection cannot produce PD more than 1%, which makes the detection difficult for most sources. The polarized reflection is expected to be more pronounced in XRBs where the direct emission from the source is obscured. In the paper, we discuss the applicability of this model to the existing data and discuss future prospects.

VIII X-ray polarimetry as a tool to constrain orbital parameters in X-ray binaries

In X-ray binaries, the compact object that produces X-ray emission may illuminate the companion star. The X-ray emission scattered off this star gets polarized, with polarization depending on the scattering angle, which varies as the compact object rotates around the center of the mass of the system. In this paper, we adopted a model from Paper IV to describe such scattering in the first approximation. The potential of this technique has been probed with the specific case of the low-mass X-ray binary GS 1826–238 observed with IXPE satellite.

IX Black hole spin—orbit misalignment in the X-ray binary MAXI J1820+070

The assumption on the alignment of the black hole spin and orbital angular momentum is widely adopted when modeling the observational features of black hole X-ray binary systems. In the paper, we present the results of optical polarimetric observations of low-mass black hole X-ray binary MAXI J1820+070, from which the position angle of the orbit has been constrained. Combined with previous measurements of the radio jet orientation, we imposed a lower limit of 40° on the spin-orbit misalignment. Such misalignment may originate from the binary evolution as a result of a randomly directed natal kick of the black hole following the supernova explosion. If such spin-orbit misalignment is a common feature of X-ray binaries, it may introduce a bias in the black hole masses and spins derived from X-ray observations. This result dictates the need to treat the spin-orbit misalignment angle as a free parameter when modeling the X-ray data.

5 Future prospects

Multiwavelength polarimetry is a powerful technique helping us to probe the geometry of the emitting regions in accreting X-ray binaries. Combined with other methods, such as spectroscopy, timing, and imaging, it deepens our understanding of physics in the regions, where gravity warps the fabric of spacetime and changes the way time passes. Recent advancements in polarimetric instrumentation, such as the launch of IXPE (Weisskopf et al., 2022), capable of reliably measuring the X-ray polarization for the first time; DIPol-family of polarimeters (Piirola et al., 2014, 2021), setting the bar of 0.01% for optical polarimetric accuracy; or EHT (Event Horizon Telescope Collaboration et al., 2019), resolving the innermost regions of the black holes in radio, have added many missing pieces to the puzzle of black hole accretion, but the whole picture is yet to be understood. Several promising avenues can help fill this gap in our knowledge.

One perspective direction is the further advancement in astronomical instrumentation. The successful launch of IXPE has demonstrated the feasibility and scientific value of space-based X-ray polarimetry – out of about 80 known BHXRBs to date,² X-ray polarization has been detected in 12 out of about 15 observed – effectively in most of the persistent sources and sources that underwent bright outbursts. Although IXPE has secured its place of a pioneer, it has only outlined the picture in broad strokes, leaving substantial scope for future, more detailed studies. Even for the brightest sources like Cyg X-1 or Cyg X-3, temporal resolution is not yet enough to make a conclusion on the nature of their orbital polarization variability (Paper I, Veledina et al. 2024; Ahlberg et al. 2025). The upcoming eXTP mission (Zhou et al., 2025) will have five-fold larger effective area, allowing studies of rapid polarimetric variability. The narrow, 2–8 keV range of IXPE does not always allow to make an unambiguous link between X-ray polarization and broadband spectrum. Missions such as XL-Calibur (Abarr et al., 2021), operating at 15–80 keV, or REDSoX sounding rocket mission, working at 0.2–0.4 keV, will expand the spectral range of current polarimetric missions, at the same time expanding the capabilities of X-ray spectropolarimetry. A more detailed answer to the question "What after IXPE and why?" can be found in the eponymous section of Soffitta et al. (2024).

Another promising direction is an increase in the number of simultaneous multiwavelength polarimetric campaigns. Papers I, III, and V show that multi-telescope

²https://www.astro.puc.cl/BlackCAT

broadband polarimetric and photometric measurements may answer the questions that are beyond the reach of any single-instrument campaign. As an example, Paper V shows the presence of the UV excess in the spectrum of the BHXRB A0620–00, which can be associated with the Compton-upscattering of the disk photons in the hot accretion flow, and whose NIR-to-optical PA behavior suggests the presence of misalignment of the accretion disk relative to the orbital axis. However, only simultaneous, radio-to-UV (or even radio-to-X-ray in case the source goes to the outburst again) polarimetric campaign can provide unambiguous evidence on the nature of the broadband emission and geometry of the source. Such campaigns require advance scheduling of state-of-the-art instruments, such as VLA, VLT, and IXPE, not yet achieved for any of the BHXRBs.

Expanding the sample of objects surveyed is another possible option. For example, Paper I suggests the presence of the relation between PD and spectral hardness for BHXRBs with similar inclinations – the PD seems to grow as the sources go from the soft to the hard state (see Fig. 19). The consistency in both slope and absolute value for different sources suggests a consistency in the physical mechanisms producing polarization. To study the nature of this dependence in detail, larger sample of BHXRBs, covering the full range of inclinations is needed, which will require additional IXPE observations of sources as they move through the hardness-intensity diagram.

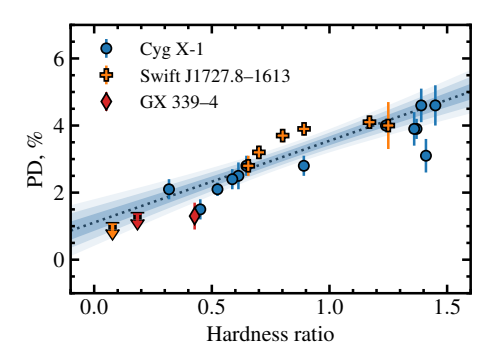


Figure 19. Dependence of X-ray PD on spectral hardness for Cyg X-1, Swift J1727.8–1613 and GX 339–4 (Paper I).

Optical polarimetric observations of BHXRBs, especially BH LMXBs, will also benefit from the expansion of the sample space. To date, statistically significant polarization detection has been made only in two quiescent sources – MAXI J1820+070 (Paper IX) and A0620–00 (Paper V), and in both cases polarimetry suggests complicated geometry of the emitting/scattering regions. A systematic survey, especially when combined with population synthesis models, could reveal trends in polarization behavior that reflect common physical processes or evolutionary pathways.

The author's contribution to the publications

Paper I:

The author obtained the data used in the paper as a PI of IXPE and co-I of VLA proposals, and organized a supporting observational campaign with other facilities. The author suggested the astrophysical implications of the results, wrote most of the text, and plotted most of the figures. Under the guidance of the author, A. Bocharova performed phase-resolved polarimetric analysis of the raw IXPE data, which is approximately 30% of the total amount of work, and wrote approximately 10% of the manuscript. The article will also be used in the doctoral thesis of A. Bocharova.

Paper II:

The author performed most of the theoretical and practical work, and carried out most of the analysis. The author suggested the astrophysical implications and wrote the first draft of the manuscript in consultation with co-authors.

Paper III:

The author planned and performed an optical observational campaign with DIPol-2 that supported the first IXPE observation of Cyg X-1. The author performed most of the DIPol-2 data acquisition, reduction, and interpretation, that helped to constrain the intrinsic polarization of Cyg X-1 in optical, which turned out to be aligned with PA in X-rays and with radio jet direction – an important result, used for interpretation of the X-ray polarization. The author plotted figures S11, S12, contributed to Table S4 and wrote about a half of "Optical polarimetry" section of the supplementary material.

Paper IV:

The author contributed to the research design of the paper, performed most of the practical work, and most of the data analysis. The formalism of the scattering model was proposed by J. Poutanen and implemented by the author. The author suggested the astrophysical implications of the findings and wrote the first draft of the manuscript in consultation with co-authors.

Paper V:

The author proposed the observing program, performed most of the theoretical and practical work, and most of the data analysis. The author proposed the astrophysical implications and wrote the first draft of the manuscript in consultation with co-authors.

Paper VI:

The author contributed to the research design of the paper and the data acquisition, and carried out most of the data analysis. The author suggested the astrophysical implications and wrote the first draft of the manuscript in consultation with co-authors.

Paper VII:

The author contributed to the research design of the paper, took part in the discussion of the reflection model, and performed most of the practical work related to its application to the IXPE data. The author's contribution covers approximately 20% of the total amount of work. The article will also be used in the doctoral thesis of V. Ahlberg.

Paper VIII:

The author contributed to the research design of the paper, took part in the discussion of the model and its constraining power, and performed part of the practical work. The author's contribution covers approximately 20% of the total amount of work.

Paper IX:

The author contributed to the acquisition, reduction, and analysis of optical photometric and polarimetric data used in the paper. The author took part in the discussion of the astrophysical implications of the results.

List of References

Abarr, Q., Awaki, H., Baring, M. G., et al. 2021, Astroparticle Physics, 126, 102529

Abramowicz, M. A., Calvani, M., & Nobili, L. 1980, ApJ, 242, 772

Ahlberg, V., Bocharova, A., & Veledina, A. 2025, arXiv e-prints, arXiv:2507.21708

Arago, F. 1843, Ann Philos Discov Month Report Progr Sci Art, 1, 209

Avakyan, A., Neumann, M., Zainab, A., et al. 2023, A&A, 675, A199

Avni, Y. & Bahcall, J. N. 1975, ApJ, 197, 675

Axon, D. J. & Ellis, R. S. 1976, MNRAS, 177, 499

Baade, W. & Zwicky, F. 1934, Proceedings of the National Academy of Science, 20, 254

Bahcall, J. N. & Bahcall, N. A. 1972, ApJL, 178, L1

Baldini, L., Barbanera, M., Bellazzini, R., et al. 2021, Astroparticle Physics, 133, 102628

Bardeen, J. M., Press, W. H., & Teukolsky, S. A. 1972, ApJ, 178, 347

Barnier, S. & Done, C. 2024, ApJ, 977, 201

Bartholin, E. 1670, Philosophical Transactions of the Royal Society of London Series I, 5, 2039

Basko, M. M., Sunyaev, R. A., & Titarchuk, L. G. 1974, A&A, 31, 249

Belloni, T. & Hasinger, G. 1990, A&A, 227, L33

Belloni, T., Psaltis, D., & van der Klis, M. 2002, ApJ, 572, 392

Belloni, T. M. 2010, in Lecture Notes in Physics, Vol. 794, The Jet Paradigm, ed. T. Belloni (Berlin Heidelberg: Springer Verlag), 53

Belloni, T. M., Sanna, A., & Méndez, M. 2012, MNRAS, 426, 1701

Berdyugin, A., Piirola, V., & Poutanen, J. 2019, in Astrophysics and Space Science Library, Vol. 460, Astronomical Polarisation from the Infrared to Gamma Rays, ed. R. Mignani, A. Shearer, A. Słowikowska, & S. Zane (Cambridge, UK: Springer Nature), 33

Berdyugin, A., Piirola, V., & Teerikorpi, P. 2014, A&A, 561, A24

Blandford, R. & Teukolsky, S. A. 1975, ApJL, 198, L27

Blandford, R. & Teukolsky, S. A. 1976, ApJ, 205, 580

Boley, F., Wolfson, R., Bradt, H., et al. 1976, ApJL, 203, L13

Bolton, C. T. 1972, Nature, 235, 271

Bowyer, C. S., Lampton, M., Mack, J., & de Mendonca, F. 1970, ApJL, 161, L1

Bowyer, S., Byram, E. T., Chubb, T. A., & Friedman, H. 1965, Science, 147, 394

Breit, G. & Tuve, M. A. 1925, Nature, 116, 357

Brocksopp, C., Corbel, S., Tzioumis, A., et al. 2013, MNRAS, 432, 931

Brocksopp, C., Miller-Jones, J. C. A., Fender, R. P., & Stappers, B. W. 2007, MNRAS, 378, 1111

Brown, J. C., McLean, I. S., & Emslie, A. G. 1978, A&A, 68, 415

Chandrasekhar, S. 1960, Radiative transfer (New York: Dover Publications, Inc.)

Chodil, G., Mark, H., Rodrigues, R., et al. 1967, Phys. Rev. Lett., 19, 681

Clark, G. W., Bradt, H. V., Lewin, W. H. G., et al. 1973, ApJ, 179, 263

Clayton, D. 1983, Principles of Stellar Evolution and Nucleosynthesis, Astronomy / Astrophysics (University of Chicago Press)

Compton, A. H. 1923, Phys. Rev., 21, 483

Cooper, B. F. C. & Price, R. M. 1962, Nature, 195, 1084

Costa, E., Soffitta, P., Bellazzini, R., et al. 2001, Nature, 411, 662

Done, C., Gierliński, M., & Kubota, A. 2007, A&AR, 15, 1

Dovčiak, M., Podgorný, J., Svoboda, J., et al. 2024, Galaxies, 12, 54

Edlund, E. 1860, Astronomische Nachrichten, 52, 305

Elvis, M., Page, C. G., Pounds, K. A., Ricketts, M. J., & Turner, M. J. L. 1975, Nature, 257, 656

Event Horizon Telescope Collaboration, Akiyama, K., Algaba, J. C., et al. 2021, ApJL, 910, L12

Event Horizon Telescope Collaboration et al. 2019, ApJ, 875, L1

Fender, R. P., Gallo, E., & Jonker, P. G. 2003, MNRAS, 343, L99

Fragile, P. C., Blaes, O. M., Anninos, P., & Salmonson, J. D. 2007, ApJ, 668, 417

Frank, J., King, A., & Raine, D. J. 2002, Accretion Power in Astrophysics: Third Edition (Cambridge, UK: Cambridge University Press), 398

Freire, P. C., Kramer, M., & Lyne, A. G. 2001, MNRAS, 322, 885

Fresnel, A.-J. 1821, Annales de Chimie et de Physique, 17, 102

Friedman, H., Lichtman, S. W., & Byram, E. T. 1951, Physical Review, 83, 1025

Gaia Collaboration, Brown, A. G. A., Vallenari, A., et al. 2021, A&A, 649, A1

Gardner, F. F. & Whiteoak, J. B. 1963, Nature, 197, 1162

Geiger, H. & Müller, W. 1928, Naturwissenschaften, 16, 617

Giacconi, R., Gursky, H., Kellogg, E., Schreier, E., & Tananbaum, H. 1971a, ApJL, 167, L67

Giacconi, R., Gursky, H., Paolini, F. R., & Rossi, B. B. 1962, Phys. Rev. Lett., 9, 439

Giacconi, R., Kellogg, E., Gorenstein, P., Gursky, H., & Tananbaum, H. 1971b, ApJL, 165, L27

Gierliński, M., Zdziarski, A. A., Poutanen, J., et al. 1999, MNRAS, 309, 496

Gies, D. R. & Bolton, C. T. 1986, ApJ, 304, 371

Ginzburg, V. L. & Syrovatskii, S. I. 1965, ARA&A, 3, 297

Goddard, R. H. 1948, Rocket Development: Liquid-Fuel Rocket Research, 1929–1941 (New-York: Prentice-Hall)

Gowen, R. A., Cooke, B. A., Griffiths, R. E., & Ricketts, M. J. 1977, MNRAS, 179, 303

Greiner, W. & Reinhardt, J. 2008, Quantum Electrodynamics, Physics and Astronomy (Springer Berlin Heidelberg)

Grimm, H. J., Gilfanov, M., & Sunyaev, R. 2002, A&A, 391, 923

Gursky, H., Gorenstein, P., & Giacconi, R. 1967, ApJL, 150, L75

Hall, J. S. 1949, Science, 109, 166

Heiles, C. 2000, AJ, 119, 923

Hiltner, W. A. 1949, Science, 109, 165

Högbom, J. A. 1974, A&AS, 15, 417

Hulburt, E. O. 1928, Phys. Rev., 31, 1018

Ingram, A., Done, C., & Fragile, P. C. 2009, MNRAS, 397, L101

Kaaret, P., Ferrazzoli, R., Silvestri, S., et al. 2024, ApJL, 961, L12

Kalogera, V. & Webbink, R. F. 1998, ApJ, 493, 351

Koljonen, K. I. I. & Hovatta, T. 2021, A&A, 647, A173

Kopal, Z. 1989, Astrophysics and Space Science Library, Vol. 152, The Roche Problem: And Its Significance for Double-Star Astronomy (Kluwer Academic Publisher)

Kosenkov, I. A. 2021, PhD thesis, University of Turku, Finland

Kramer, M., Stairs, I. H., Manchester, R. N., et al. 2006, Science, 314, 97

Landau, L. D. & Lifshitz, E. M. 1975, Course of Theoretical Physics, Vol. 2, The Classical Theory of Fields, 4th edn. (Oxford: Butterworth-Heinemann)

Landau, L. D. & Lifshitz, E. M. 1991, Course of Theoretical Physics, Vol. 3, Quantum Mechanics: Non-Relativistic Theory (Oxford: Butterworth-Heinemann)

Legg, M. P. C. & Westfold, K. C. 1968, ApJ, 154, 499

Lense, J. & Thirring, H. 1918, Physikalische Zeitschrift, 19, 156

Levasseur-Regourd, A. C. 2019, in EPSC-DPS Joint Meeting 2019, Vol. 2019, EPSC-DPS2019-1461

Makishima, K. & Mitsuda, K. 1985, in Galactic and Extra-Galactic Compact X-ray Sources, ed. Y. Tabaka & W. H. G. Lewin, 127

Markert, T. H., Canizares, C. R., Clark, G. W., et al. 1973, ApJ, 184, L67

Mason, K. O., Charles, P. A., White, N. E., et al. 1976, MNRAS, 177, 513

Mastroserio, G., De Marco, B., Baglio, M. C., et al. 2025, ApJL, 978, L19

Matsuoka, M., Kawasaki, K., Ueno, S., et al. 2009, PASJ, 61, 999

Maxwell, J. C. 1865, Philosophical Transactions of the Royal Society of London, 155, 459

McClintock, J. E. & Remillard, R. A. 1986, ApJ, 308, 110

McConnell, M. L., Zdziarski, A. A., Bennett, K., et al. 2002, ApJ, 572, 984

McCready, L. L., Pawsey, J. L., & Payne-Scott, R. 1947, Proceedings of the Royal Society of London Series A, 190, 357

Mie, G. 1908, Annalen der Physik, 330, 377

Miyamoto, S., Kimura, K., Kitamoto, S., Dotani, T., & Ebisawa, K. 1991, ApJ, 383, 784

Morgan, E. H., Remillard, R. A., & Greiner, J. 1997, ApJ, 482, 993

Morris, S. L. 1985, ApJ, 295, 143

Motch, C., Ricketts, M. J., Page, C. G., Ilovaisky, S. A., & Chevalier, C. 1983, A&A, 119, 171

Motta, S. E., Rodriguez, J., Jourdain, E., et al. 2021, New Astronomy Reviews, 93, 101618

Neumann, M., Avakyan, A., Doroshenko, V., & Santangelo, A. 2023, A&A, 677, A134

Novick, R., Weisskopf, M. C., Berthelsdorf, R., Linke, R., & Wolff, R. S. 1972, ApJL, 174, L1

Novikov, I. D. & Thorne, K. S. 1973, in Black Holes (Les Astres Occlus), ed. C. DeWitt & B. DeWitt (New York: Gordon and Breach), 343–450

Oppenheimer, J. R. & Volkoff, G. M. 1939, Physical Review, 55, 374

Orosz, J. A. & Bailyn, C. D. 1997, ApJ, 477, 876

Orosz, J. A., McClintock, J. E., Narayan, R., et al. 2007, Nature, 449, 872

Parsignault, D. R., Gursky, H., Kellogg, E. M., et al. 1972, Nature Physical Science, 239, 123

Piirola, V., Berdyugin, A., & Berdyugina, S. 2014, in Proc. SPIE, Vol. 9147, Ground-based and Airborne Instrumentation for Astronomy V, ed. S. K. Ramsay, I. S. McLean, & H. Takami, 91478I

Piirola, V., Kosenkov, I. A., Berdyugin, A. V., Berdyugina, S. V., & Poutanen, J. 2021, AJ, 161, 20

Planck Collaboration, Aghanim, N., Akrami, Y., et al. 2020, A&A, 641, A12

Poutanen, J. & Svensson, R. 1996, ApJ, 470, 249

Rayleigh, L. 1899, The London, Edinburgh, and Dublin Philosophical Magazine and Journal of Science, 47, 375

Remillard, R. A. & McClintock, J. E. 2006, ARA&A, 44, 49

Remillard, R. A., Morgan, E. H., McClintock, J. E., Bailyn, C. D., & Orosz, J. A. 1999, ApJ, 522, 397

Ropars, G., Lakshminarayanan, V., & Le Floch, A. 2014, Contemporary Physics, 55, 302

Russell, D. M., Shahbaz, T., Lewis, F., & Gallo, E. 2016, MNRAS, 463, 2680

Rutherford, E. & Geiger, H. 1908, Proceedings of the Royal Society of London, 81, 141

Rybicki, G. B. & Lightman, A. P. 1979, Radiative processes in astrophysics (New York: John Wiley & Sons, Ltd)

Ryle, M. 1952, Proceedings of the Royal Society of London Series A, 211, 351

Samimi, J., Share, G. H., Wood, K., et al. 1979, Nature, 278, 434

Schreier, E., Giacconi, R., Gursky, H., Kellogg, E., & Tananbaum, H. 1972a, ApJL, 178, L71

Schreier, E., Gursky, H., Kellogg, E., Tananbaum, H., & Giacconi, R. 1971, ApJ, 170, L21

Schreier, E., Levinson, R., Gursky, H., et al. 1972b, ApJL, 172, L79

Schulz, N. S., Hasinger, G., & Truemper, J. 1989, A&A, 225, 48

Serkowski, K. 1974, in Planets, Stars, and Nebulae: Studied with Photopolarimetry, ed. T. Gehrels, IAU Colloqium 23, 135

Shakura, N. I. & Sunyaev, R. A. 1973, A&A, 500, 33

Smith, J. F. & Courtier, G. M. 1976, Proceedings of the Royal Society of London Series A, 350, 421

Soffitta, P., Costa, E., De Angelis, N., et al. 2024, Galaxies, 12, 47

Sorabella, N. M., Bhattacharya, S., Laycock, S. G. T., Christodoulou, D. M., & Massarotti, A. 2022, ApJ, 936, 63

Stella, L. & Vietri, M. 1998, ApJL, 492, L59

Stokes, G. G. 1851, Transactions of the Cambridge Philosophical Society, 9, 399

Strutt, J. 1871, The London, Edinburgh, and Dublin Philosophical Magazine and Journal of Science, 41, 107

Sunyaev, R. A. & Titarchuk, L. G. 1985, A&A, 143, 374

Tananbaum, H., Gursky, H., Kellogg, E., Giacconi, R., & Jones, C. 1972a, ApJL, 177, L5

Tananbaum, H., Gursky, H., Kellogg, E. M., et al. 1972b, ApJL, 174, L143

Taverna, R. & Turolla, R. 2024, Galaxies, 12, 6

Thomson, J. 1907, The Corpuscular Theory of Matter, Marilee E. Thomas and Robert C. Thomas Science and Related Subjects Collection (Scribner's Sons)

Tian, P.-F., Zhang, P., Wang, W., et al. 2023, Journal of High Energy Astrophysics, 39, 43

Tolman, R. C. 1939, Physical Review, 55, 364

van der Klis, M. 1989, in NATO Advanced Study Institute (ASI) Series C, Vol. 262, Timing Neutron Stars, ed. H. Ögelman & E. P. J. van den Heuvel, 27

Veledina, A., Muleri, F., Poutanen, J., et al. 2024, Nature Astronomy, 8, 1031

Vogel, H. C. 1890, PASP, 2, 27

Wade, C. M. & Hjellming, R. M. 1972, Nature, 235, 271

Watarai, K.-Y. & Fukue, J. 2010, PASJ, 62, 467

Webster, B. L. & Murdin, P. 1972, Nature, 235, 37

Weisskopf, M. C. 2018, Galaxies, 6, 33

Weisskopf, M. C., Cohen, G. G., Kestenbaum, H. L., et al. 1976, in NASA Special Publication, ed. E. Boldt & Y. Kondo, Vol. 389, 81–96

Weisskopf, M. C., Silver, E. H., Kestenbaum, H. L., Long, K. S., & Novick, R. 1978, ApJL, 220, L117

Weisskopf, M. C., Soffitta, P., Baldini, L., et al. 2022, JATIS, 8, 026002

Wen, L., Cui, W., Levine, A. M., & Bradt, H. V. 1999, ApJ, 525, 968

Wen, L., Levine, A. M., Corbet, R. H. D., & Bradt, H. V. 2006, ApJS, 163, 372

White, N. E. & Swank, J. H. 1982, ApJL, 253, L61

Zdziarski, A. A. & Gierliński, M. 2004, Progress of Theoretical Physics Supplement, 155, 99

Zhou, P., Mao, J., Zhang, L., et al. 2025, arXiv e-prints, arXiv:2506.08367

Original Publications

Kravtsov V., Bocharova A., Veledina A., Poutanen J., Hughes A.K., Dovčiak M., Egron E., Muleri F., Podgorny J., Svoboda J., Forsblom S.V., Berdyugin A.V., Blinov D., Bright J.S., Carotenuto F., Green D.A., Ingram A., Liodakis I., Mandarakas N., Nitindala A.P., Rhodes L., Trushkin S.A., Tsygankov S.S., Brigitte M., Di Marco A., Iacolina N., La Monaca F., Loktev V., Mastroserio G., Petrucci P.-O., Pilia M., Tombesi F., Zdziarski A.A. Variability of X-ray polarization of Cyg X-1

Astronomy & Astrophysics, 2025; 701: A115

Variability of X-ray polarization of Cyg X-1

Vadim Kravtsov^{1,*}, Anastasiia Bocharova¹, Alexandra Veledina^{1,2}, Juri Poutanen¹, Andrew K. Hughes³, Michal Dovčiak⁴, Elise Egron⁵, Fabio Muleri⁶, Jakub Podgorny⁴, Jiři Svoboda⁴, Sofia V. Forsblom¹, Andrei V. Berdyugin¹, Dmitry Blinov^{7,8}, Joe S. Bright³, Francesco Carotenuto⁹, David A. Green¹⁰, Adam Ingram¹¹, Ioannis Liodakis⁷, Nikos Mandarakas^{7,8}, Anagha P. Nitindala¹, Lauren Rhodes³, Sergei A. Trushkin¹², Sergey S. Tsygankov¹, Maïmouna Brigitte^{4,13}, Alessandro Di Marco⁶, Noemi Iacolina¹⁴, Henric Krawczynski¹⁵, Fabio La Monaca^{6,16}, Vladislav Loktev^{1,17}, Guglielmo Mastroserio¹⁸, Pierre-Olivier Petrucci¹⁹, Maura Pilia⁵, Francesco Tombesi^{16,20,21}, and Andrzej A. Zdziarski²²

(Affiliations can be found after the references)

Received 6 May 2025 / Accepted 24 July 2025

ABSTRACT

We present the results of a three-year X-ray, optical, and radio polarimetric monitoring campaign of the prototypical black hole X-ray binary Cyg X-1, conducted from 2022 to 2024. The X-ray polarization of Cyg X-1 was measured 13 times with the Imaging X-ray Polarimetry Explorer (IXPE), covering both hard and soft spectral states. The X-ray polarization degree (PD) in the hard state was found to be \approx 4.0%, roughly twice as high as in the soft state, where it was around 2.2%. In both states, a statistically significant increase in PD with the energy was found. Moreover, a linear relation between PD and spectral hardness suggests a gradual and continuous evolution of the polarization properties, rather than an abrupt change of polarization production mechanism between states. The polarization angle (PA) was independent of the spectral state and showed no trend with the photon energy. The X-ray PA is well aligned with the orientation of the radio jet, as well as the optical and radio PAs. We find significant orbital changes of PA in the hard state, which we attribute to scattering of X-ray emission at the intrabinary structure. No significant superorbital variability in PD or PA was found at the period $P_{so} = 294$ d. We detect, for the first time in this source, polarization of the radio emission, with the PA aligned with the jet, and a strong increase of the PD at a transition to the soft state. We also find no correlation between the X-ray PD and the radio PD.

Key words. accretion, accretion disks - polarization - stars; black holes - stars; individual: Cyg X-1 - X-rays; binaries

1. Introduction

Accretion is an efficient mechanism for heating and extracting energy from matter as it falls toward a compact object. Energy can be released through various channels, producing distinct X-ray emission signatures (spectral states) observed in these systems. Black hole X-ray binaries (BHXRBs) are known to swing between two major spectral states, hard and soft, distinguished by the energies at which their emission peaks (Zdziarski & Gierliński 2004). The soft state is characterized by dominant thermal emission from the classical optically thick and geometrically thin accretion disk (Shakura & Sunyaev 1973; Novikov & Thorne 1973). Transition to the hard spectral state is marked by spectral shift to a power-law shape, peaking at ~100 keV. This emission is believed to be produced by multiple Compton upscatterings of soft seed photons, either from the disk or internally produced synchrotron photons, in a hot optically thin medium surrounding the black hole (Sunyaev & Titarchuk 1980; Gierliński et al. 1997; Poutanen & Vurm 2009; Veledina et al. 2013). Determining the size of the hot, rarefied plasma responsible for the bulk of X-ray emission, along with its shape and orientation with respect to the disk, remains one of the key open questions in high-energy astrophysics.

Similar X-ray spectra could be produced by various proposed configurations of the hot medium – such as slab, wedge, cone, or lamppost geometries – however, the polarization degree (PD), polarization angle (PA), and their spectral dependence differ significantly between these scenarios (Poutanen & Svensson

1996; Poutanen et al. 2018; Dovčiak et al. 2004; Krawczynski & Beheshtipour 2022). The launch of the Imaging X-ray Polarimetry Explorer (IXPE; Weisskopf et al. 2022) in December 2021 has opened a new window to probe the geometry of X-ray-emitting regions in accreting compact objects. Cygnus X-1 (Cyg X-1) was the first hard-state BHXRB studied with IXPE (Krawczynski et al. 2022).

Cyg X-1 is a bright persistent X-ray binary, harboring the first discovered (Bowyer et al. 1965) and possibly one of the most massive Galactic BHs with $M_{\rm BH} = 21.2 \pm 2.1 \, M_{\odot}$ (Miller-Jones et al. 2021), although most recent estimates favor a lower mass of $M_{\rm BH} \approx 14\,M_{\odot}$ (Ramachandran et al. 2025). It orbits a supergiant O-type donor star in a 5.6 d orbit. The donor star in this system nearly fills its Roche lobe and accretion proceeds via wind (Gies & Bolton 1986; Ramachandran et al. 2025). The accretion geometry, however, is not steady – this was first noticed as changes in the X-ray spectra of Cyg X-1, which gave rise to the soft/hard classification of the spectral states of X-ray binaries (Tananbaum et al. 1972; Zdziarski et al. 2004; Done et al. 2007). Recent estimates suggest the binary inclination is low, $i = 27^{\circ}.5 \pm 0^{\circ}.8$ (Orosz et al. 2011; Miller-Jones et al. 2021). The system inclination has a strong impact on the expected PD, which is highly sensitive to the presence of axial symmetry in the source. Sources with spherical symmetry, or those viewed face-on with circular symmetry, produce zero PD, whereas edge-on configurations yield a maximal PD as predicted by a specific model.

IXPE observations (Krawczynski et al. 2022) revealed an unexpectedly high polarization, PD = $4.0 \pm 0.2\%$, with the PA aligned with the direction of the radio jet (Miller-Jones et al.

^{*} Corresponding author: vakrau@utu.fi

2021). This finding significantly narrowed down the range of viable models, favoring a geometry in which the X-ray emission region is extended perpendicular to the jet, thereby being consistent with the hot flow models, and ruling out several alternatives, such as a vertically extended (jet-base) or lamppost corona. A similar PD of about 4%, with the PA again aligned with the jet, was detected in a BH transient Swift J1727.8–1613 during its hard state (Veledina et al. 2023; Ingram et al. 2024; Podgorný et al. 2024), providing further support to this shape of the X-ray emitting region.

The detected PD in Cyg X-1 is, however, too high for the known system inclination, and is hard to achieve in any scenario. Additional assumptions have been employed to achieve PD $\sim 4\%$ in the models: the inclination of the X-ray emitting region might be higher (by $15^{\circ}-30^{\circ}$) than the orbital one (Krawczynski et al. 2022), the hot medium may attain a significant outflow velocity (Poutanen et al. 2023), or the PD produced intrinsically in the source may be boosted by the scattering off the accretion disk wind at large radii (Nitindala et al. 2025).

The higher inclination may result either from a steady warp of the accretion flow caused by a misalignment between the BH spin and orbital axis (Bardeen et al. 1972) or from a particular phase of precession of the inner flow. Precession of the flow or an accretion disk has previously been considered in the source in the context of super-orbital variability of X-ray, optical and radio fluxes, as well as the X-ray hardness and optical polarization signatures (Kemp et al. 1983; Priedhorsky et al. 1983; Karitskaya et al. 2001; Lachowicz et al. 2006; Ibragimov et al. 2007; Poutanen et al. 2008; Zdziarski et al. 2011; Kravtsov et al. 2022). A substantial misalignment between the BH spin and the orbital axis can arise if the BH received a natal kick during its formation (Fragos et al. 2010). However, Cyg X-1 exhibits a small proper motion relative to the Cygnus OB3 stellar association (Rao et al. 2020), placing strong constraints on the natal kick velocity and limiting the maximum possible misalignment angle to ~10° (Miller-Jones et al. 2021). This upper limit is sufficient to account for the soft-state X-ray polarization signatures of Cyg X-1, PD = $2.0 \pm 0.1\%$ and an energy-independent PA aligned with the jet, assuming that returning radiation plays a dominant role in this state (Steiner et al. 2024). These findings disfavor the steady-warp scenario and instead support the case where the inner accretion flow undergoes precession on superorbital timescales. If true, this scenario predicts large variations of the PA with the amplitude exceeding 20° on the timescale of ~300 d, corresponding to the maximal reported super-orbital

In this paper, we present the results of thirteen IXPE observations of Cyg X-1 conducted between 2022 and 2024, covering its hard, intermediate, and soft spectral states. These include six observations analyzed here for the first time. Details of the IXPE observations, supporting multiwavelength data, and the data reduction procedures are provided in Sect. 2. The results of the comprehensive analysis are presented in Sect. 3. In Sect. 4, we discuss the implications of our findings in the context of the accretion geometry and polarization production mechanisms. We summarize our findings and outline future prospects in Sect. 5.

2. Observations and data reduction

21 IXPF

IXPE is the first satellite dedicated to polarimetric X-ray observations that operates in the 2-8 keV band (Weisskopf et al.

2022). It carries three X-ray telescopes, each consists of a Mirror Module Assembly and a polarization-sensitive gas-pixel detector unit (DU; Baldini et al. 2021; Soffitta et al. 2021; Di Marco et al. 2022), enabling imaging X-ray polarimetry of extended sources and a huge increase of sensitivity for point-like sources. IXPE provides angular resolution of ≤30" (half-power diameter, averaged over the three detectors). The overlap of the fields of view of the three DUs is circular with a diameter of 9'; the spectral resolution is better than 20% at 6 keV.

We consider the full set of IXPE observations of Cyg X-1, which consists of 13 individual pointings, conducted from 2022 to 2024 (see Table 1). We used Level 2 data downloaded from the IXPE archive at HEASARC and analyzed it using IXPEOB-SSIM package v31.0.1 (Baldini et al. 2022). In the case of the hard state observation in May 2022 we used post-reconstruction calibration of the energy scale1. The source region for all available observations was defined in SAOIMAGEDS9 v8.6 as a circle with radius 60" around the source and extracted using xpselect tool. The average polarization properties in the entire energy band for each observation were extracted using the xpbin tool with PCUBE algorithm in a single 2-8 keV energy bin. For phase-resolved polarimetric analysis, we utilized the xpphase tool with the orbital period of 5.599829 d and a zero point of JD 2441874.707 (Brocksopp et al. 1999a). We split Epoch 1 data into ten phase bins with xpselect and calculated the polarization properties in each phase bin with the same approach as for the whole observation. The hardness ratio was calculated as IXPE photon flux ratio in the energy ranges 4-8 and 2-4 keV. The main results are shown in Fig. 1. Spectra were extracted with the xpbin PHA1 algorithm, utilizing CalDB v13 response files. The superorbital phases were calculated with a period of 294.0 d and a zero point of JD 2440000.0 (Priedhorsky et al. 1983).

2.2. Multiwavelenath coverage

To support X-ray polarimetric observations with IXPE, the multiwavelength observational campaign was organized with optical and radio facilities. The high-precision optical polarimetric observations were performed with DIPol-2/UF instruments at 60 cm Tohoku telescope (T60) at Haleakala Observatory, Hawaii and at 2.56 m Nordic Optical Telescope (NOT), as well as with RoboPol at the Skinakas Observatory. Radio polarimetric observations were conducted with Karl G. Jansky Very Large Array (VLA) and where supported with RATAN-600 and the Arcminute Microkelvin Imager (AMI) monitoring.

2.2.1. Optical observations

Optical polarimetric observations of Cyg X-1 were carried out with the broad-band BVR polarimeters DIPol-2 (Piirola et al. 2014) and DIPol-UF (Piirola et al. 2021), mounted on the remotely controlled 60 cm Tohoku telescope (T60) at Haleakala Observatory, Hawaii and at the 2.56 m Nordic Optical Telescope (NOT), Observatorio del Roque de los Muchachos (ORM), La Palma, Spain, and with RoboPol polarimeter (Ramaprakash et al. 2019) in the focal plane of the 1.3 m telescope of the Skinakas observatory, Greece. DIPol-2 and DIPol-UF are high-precision double-image CCD polarimeters, capable of measuring polarization simultaneously in three

https://heasarc.gsfc.nasa.gov/FTP/ixpe/data/obs/01/
01002901/README

Table 1	IXPF	observing	log and	measured	X-ray no	larization

Epoch	Obs. ID		Date	Orbital Phase	IXPE Hardness 4–8 keV/2–4 keV	State	PD (%)	PA (deg)	Exposure Time (ks)
1	01002901	2022	May 15	0.00-1.00	0.569	Н	4.0 ± 0.2	-21 ± 2	241.5
2	01250101		June 18	0.00-0.37	0.610	Н	3.9 ± 0.3	-26 ± 3	86.0
3	02008201	2023	May 2	0.81-0.89	0.280	S	2.5 ± 0.4	-17 ± 5	20.8
4	02008301		May 9	0.97-0.09	0.271	S	2.4 ± 0.3	-23 ± 4	30.8
5	02008401		May 24	0.72 - 0.83	0.151	S	2.1 ± 0.3	-25 ± 4	24.6
6	02008501		June 13	0.31-0.43	0.210	S	1.5 ± 0.3	-26 ± 6	28.8
7	02008601		June 20	0.39-0.54	0.240	S	2.1 ± 0.2	-36 ± 3	34.2
8	03002201	2024	April 12	0.43-0.64	0.610	Н	3.9 ± 0.5	-25 ± 4	55.8
9	03003101		May 6	0.79-0.99	0.589	H	3.1 ± 0.5	-28 ± 5	53.8
10	03010001		May 26	0.29-0.52	0.620	H	4.6 ± 0.5	-28 ± 3	57.5
11	03010101		June 14	0.80-0.01	0.649	Н	4.6 ± 0.6	-33 ± 3	55.7
12	03002599^a		October 10	0.79-0.01	0.389	S	2.8 ± 0.3	-18 ± 3	55.1
13	03002599^a		December 12	0.19-0.42	0.280	S	2.8 ± 0.2	-25 ± 3	56.2

Notes. "Observations 12 and 13 were parts of one observation ID 03002599, which was then manually split into two parts.

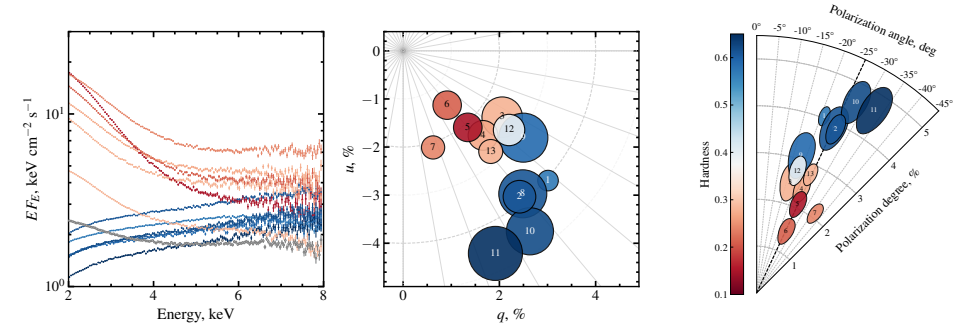


Fig. 1. Spectral and polarization properties of Cyg X-1 for each IXPE observation with hardness shown in color. Numbers represent the observation's epoch in accordance with Table 1. IXPE spectra, normalized Stokes parameters, and PD and PA of X-ray polarization are shown in left, middle, and right panels, respectively. Dashed black line in the right panel indicates the radio jet direction.

optical (BVR) bands. The instrumental polarization of both instruments is small (<10⁻⁴) and is well calibrated by observing 15-20 unpolarized standard stars. The polarization of the sky is optically eliminated by the design of the instruments. The zero point of the PA was determined by observing highly polarized standards HD 204827 and HD 161056. Each measurement of Stokes parameters took about 20 s and more than 200 individual measurements were obtained during the average observing night. In total, Cyg X-1 was observed for 90 nights in 2022-2024. Intrinsic polarization of the source has been extracted by subtracting the Stokes parameters of the interstellar polarization (Table 2 of Kravtsov et al. 2023) from the observed Stokes parameters of Cyg X-1. A more detailed description of the methods and calibrations can be found in Piirola et al. (2020) and Kravtsov et al. (2023). The RoboPol data was analyzed by the automatic pipeline described in Blinov et al. (2021) using both polarized and unpolarized standards to characterize the instrumental polarization. For the sources not in the central mask, used to account for the ISM polarization, we used the analysis procedure described in Panopoulou et al. (2015). For consistency, the ISM polarization is corrected using the same reference star for all three instruments.

2.2.2. The Karl G. Jansky Very Large Array

We obtained five radio observations with the Karl G. Jansky Very Large Array (VLA, Project Code: 24A-469) to track the evolution of the relativistic jets during the IXPE campaign. The observations were conducted on 2024 May 8 (MJD 60438), May 26 (MJD 60456), June 14 (MJD 60475), September 22 (MJD 60575), and December 16 (MJD 60660). The first three epochs were taken in the B configuration, the fourth in a hybrid $B \rightarrow A$ configuration, and the final epoch in the most extended A configuration. These configurations provided angular resolutions of <1", effectively eliminating concerns about source confusion. Each observation used the 3-bit C-band (4-8 GHz) and X-band (8-12 GHz) receivers, yielding approximately 8 GHz of contiguous bandwidth (prior to flagging). The X and C bands were observed consecutively, with X-band preceding C-band in each session. For calibration, we used 3C 286 as the bandpass, flux scale, and polarization angle (PA) calibrator; J2015+3710 as the complex gain calibrator; and J2355+4950 as the polarization leakage calibrator.

We calibrated and flagged the parallel-hand visibilities (i.e., Stokes I and V) using the automated VLA pipeline provided in

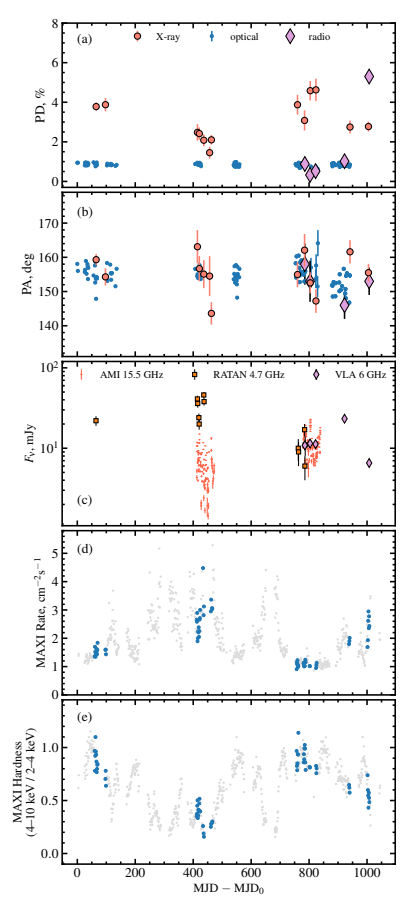


Fig. 2. Multiwavelength results on Cyg X-1. Panels (a) and (b): PD and PA of polarization in X-rays (IXPE), optical (DIPol) and radio (VLA), Panel (c): light curve in the radio as measured with AMI, VLA and RATAN 600. Panel (d): MAXI photon flux in 2–20 keV. Panel (e): MAXI hardness. In panels (d) and (e), we show all MAXI data in gray, highlighting in color only the data obtained simultaneously with IXPE. $MID_0 = 59653$ (2022 March 15).

CASA v6.5 (CASA Team et al. 2022). After each pipeline run, we manually inspected the resulting calibrated visibilities and removed any residual corrupted data that had not been caught by the automatic flagging routines. Because the pipeline does not include polarization calibration, we manually calibrated the cross-hand visibilities (i.e., Stokes *Q* and *U*), following the standard procedures outlined in the VLA calibration guides². Imaging was performed with WSCLEAN (Offringa et al. 2014), which generated, for each epoch, band, and Stokes parameter, a set of 32 frequency-resolved images (evenly spaced in frequency)

as well as a single integrated Multi-Frequency Synthesis (MFS) image to enhance sensitivity. To extract the full polarization flux densities of Cyg X-1, we used the imfit task in CASA to model the source in each image as an elliptical Gaussian. Since the source was unresolved, we fixed the Gaussian shape to match the synthesized beam. We estimated the uncertainty in the flux measurements as the root-mean-square (RMS) noise in a nearby, emission-free region covering an area of approximately 100 synthesized beams.

Finally, we extracted the key polarization properties — the PD, PA, and rotation measure (RM) — using the rotation measure synthesis software contained within the RM-TOOLS (Purcell et al. 2020); we direct interested readers to Brentjens & de Bruyn (2005) for a description of RM synthesis. Initially, we calculated the polarization properties of each band separately, and found no significant frequency-dependency on the measured RM or intrinsic PA0 (i.e., the PA corrected for the effects of Faraday rotation). Moreover, despite the non-simultaneity of our C- and X-band observations, we found that PA0 and RM did not exhibit intra-observation variability. As a result, our reported values of PA0 and RM combine the C- and X-band data to increase signal-to-noise and decrease the error on the inferred RMs³. We applied no further manipulation of our radio observations.

2.2.3. RATAN 600

We carried out monitoring of Cyg X-1 with the RATAN 600 radio telescope at 4.7 GHz and 11.2 GHz from 2022 May to 2024 June using the "Southern Sector and Flat mirror" antenna. The sensitivity of such measurements is about 3–10 mJy beam⁻¹. Thus, Cyg X-1 was undetected most of the time, with detections presented in Fig. 2. Previous monitoring observations of Cyg X-1 have shown typical flux variations in the vicinity of 10–30 mJy at 4.7 GHz. Calibration was performed using quasar 3C 48, adopting a brightness of 5.8 and 3.42 Jy at 4.7 and 8.2 GHz, respectively, according to the flux density scale by Ott et al. (1994).

224 AMI

Cyg X-1 was observed 98 times during May and June 2023 and May and June 2024 with the AMI Large Array (Zwart et al. 2008; Hickish et al. 2018) at 15.5 GHz. The observations were typically ~25 minutes, with two ten-minute scans of Cyg X-1 interleaved between short observations of a nearby compact source. The flux density scale of the observations was set by using daily short observations of 3C 286, and the interleaved calibrator observations were used to calibrate antenna-based amplitude and phase variations during the observations. The observations covered a 5 GHz bandwidth of a single linear polarization, Stokes I-Q.

3. Results

3.1. Long-term X-ray polarization changes

We first consider the long-term changes of X-ray polarization by averaging the polarization signatures within each observa-

https://casaguides.nrao.edu/index.php/Karl_G.
_Jansky_VLA_Tutorials

³ Cyg X-1 was not detected during our fourth observation on 2024 September 22, likely due to secular evolution of the source associated with the transition from C- to X-band. Consequently, we excluded it from the RM synthesis analysis, as its inclusion reduced the significance of the polarization detection.

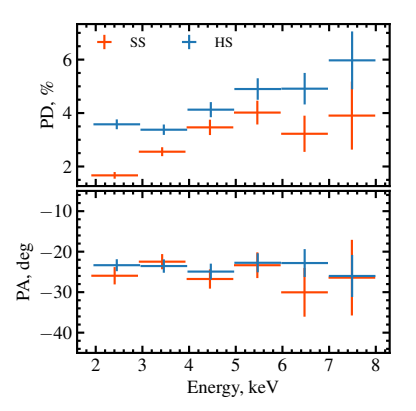


Fig. 3. Energy dependence of polarization properties of Cyg X-1 in the hard and soft states.

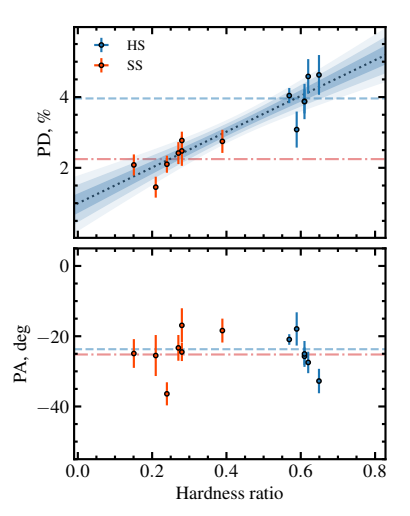


Fig. 4. Dependence of PD and PA of Cyg X-1 on spectral hardness. The dashed and dash-dotted horizontal lines show average values in the hard- and soft-states, respectively. The dotted line with 1, 2, and 3σ confidence intervals shows a linear fit to the PD.

tional epoch. The PCUBE-average polarization, along with IXPE hardness and assigned states are reported in Table 1. We adopt a hardness value of 0.4 as the threshold between the hard and soft spectral states; this simplified classification does not treat the intermediate state as a separate spectral state.

In Fig. 1 we show the spectra of individual epochs and their polarization in the (q, u)-plane and in the PD-PA plot, color-coded according to spectral hardness. The PA deviates from the jet position angle (of \sim -25°; Stirling et al. 2001; Miller-Jones et al. 2021) by no more than 10°. The PD is relatively stable within each state, yet clearly depends on the hardness, taking values between \approx 1.5% in the soft state to \approx 4.5% in the hard state.

The energy dependence of polarization, averaged separately over the hard and soft states, is shown in Fig. 3. The PD grows with energy in both states, as indicated by the highly statistically significant improvement of the fit with linearly increasing PD with energy comparing to the constant PD model: the χ^2 /d.o.f. value drops from 27.5/5 to 6.3/4 in the hard state and from 78/5 to 7/4 in the soft state. We further investigate the dependence of PD and PA on hardness in Fig. 4. We find that the X-ray PD shows strong positive correlation (Pearson correlation coefficient r=0.92) with spectral hardness, while PA is not sensitive to spectral changes – fit of the linear model to the PA gives χ^2 /d.o.f. = 13.6/11.

The X-ray PA shows small but significant variations around the average value; the fit with a constant to the observed PA values gives unacceptable fit with χ^2/d .o.f. = 33/12, suggesting that the spread of PA is higher than statistical noise. On the other hand, when considering the sample as a whole, there is no systematic trend of PA with hardness – soft- and hard-sate average PAs are consistent within the uncertainties ($-25^{\circ} \pm 1^{\circ}$ and $-24^{\circ} \pm 1^{\circ}$, respectively). The variations of PA might be related to one of the periods of the system: either orbital ($P_{\text{orb}} = 5.6 \,\text{d}$) or super-orbital ($P_{\text{so}} \sim 300 \,\text{d}$). Below we investigate variations of PA at these timescales in more detail.

3.2. Orbital variability

The orbital motion of an X-ray source in the presence of a companion star and circumstellar (intrabinary) matter can induce variations of the observed polarization on the orbital timescale (Brown et al. 1978; Kravtsov et al. 2020; Rankin et al. 2024; Ahlberg et al. 2024). To verify the presence of variability at the orbital period in IXPE observations of Cyg X-1, we performed a phase-resolved polarimetric analysis. The dependence of PD on the spectral hardness prevents us from combining the data in all spectral states. To minimize the influence of spectral hardness on polarization, we treated soft- and hard-state data separately.

We primarily focus on the hard-state data owing to repeating coverage of the same orbital phases over years and one complete orbital cycle (Epoch 1). We split the Epoch 1 data into 10 phase bins as described in Sect. 2.1, while the other, shorter observations were not subdivided. The results are shown in Figs. 5 and 6, where variations of the Stokes q and u are presented as function of the orbital phase and on the (q, u)-plane, and also through variation in PD and PA. The X-ray polarization of Cyg X-1 shows hints of orbital variability: the PD varies sinusoidally, gradually increasing from $\approx 3\%$ at orbital phase 0.1 to the maximum of $\approx 5\%$ at phase 0.5. The observed PA displays a swing with an amplitude of $\leq 10^\circ$, roughly half-cycle out of phase with the PD. This behavior can be interpreted as the tip of the polarization vector tracing a closed loop in the (q, u)-plane (see Fig. 5, left panel).

3.2.1. Constant versus sine-wave

To assess the statistical significance of the orbital variations, we used the F-test to compare two nested models. The null hypothesis, H_0 , assumes that the Stokes parameters q and u remain constant across all orbital phases. It has two free parameters: q_c and u_c . We find the χ_0^2/d .o.f. = 30.5/28 for the fit with this model (see dashed black line in Fig. 6).

This was tested against the alternative hypothesis, H_A , in which the Stokes parameters follow simple sinusoidal functions of the orbital phase. We notice that q and u have nearly the same amplitude and are out of phase. To keep the number of

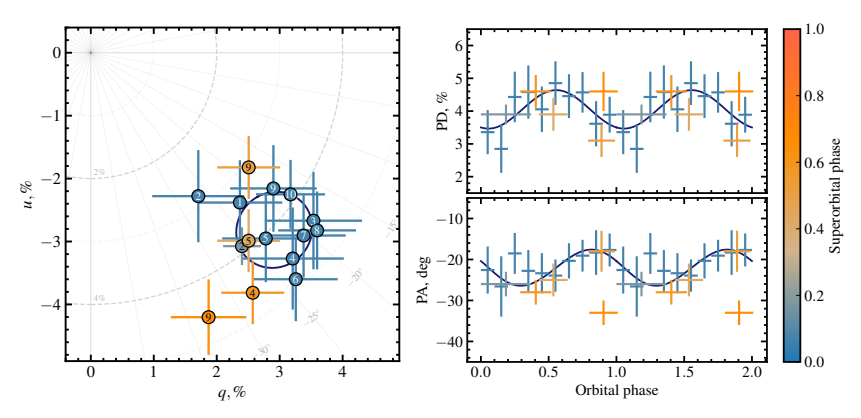


Fig. 5. Orbital phase-resolved polarization of Cyg X-1 in the hard state. Left panel: Variation of the normalized Stokes parameters. The numbers represent the orbital phase bins from 1 to 10 and the colors correspond to the superorbital phase (right color bar). Right panel: PD and PA as a function of orbital phase. Solid black lines in both panels correspond to the best-fit model described in Sect. 4.1.

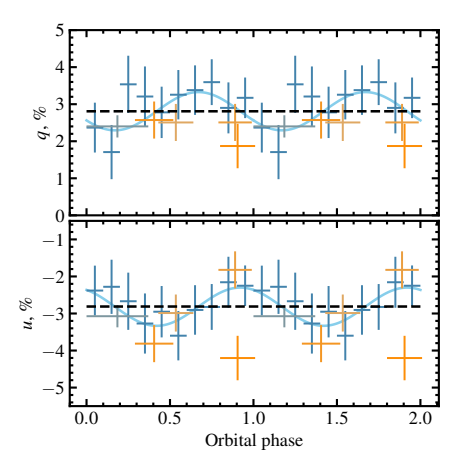


Fig. 6. Orbital phase-resolved normalized Stokes parameters of Cyg X-1 in the hard state. Dashed black and solid blue lines correspond to best-fit constant and sinusoidal models, respectively. See Sect. 3.2 for details.

parameters to minimum, we assume the same amplitude r_v of the sine wave and we fix the phase shift to $\pi/2$. This model can be expressed as follows:

$$q(\varphi) = q_{\rm c} + r_{\rm v} \cos(\varphi - \varphi_0),$$

$$u(\varphi) = u_{\rm c} + r_{\rm v} \sin(\varphi - \varphi_0),$$
(1)

where indices (c) and (v) denote constant and variable components, respectively, and φ_0 is the zero-phase angle. The model has four free parameters: q_c , u_c , r_v , and φ_0 . In this model, the trajectory the points track at the (q,u)-plane may be decomposed into the sum of two vectors: the first one, constant vector, links the origin with the average polarization (center of the circle), and another, varying vector, with constant length of r_v and with

the azimuthal angle being related to the orbital phase $(\varphi - \varphi_0)$, links the center of the circle with the instantaneous q, u parameters. Fig. 6 shows the best-fit model with the solid blue lines that gives $\chi_A^2/\text{d.o.f.} = 24.2/26$.

The resulting value of F-statistic, $F = [(\chi_0^2 - \chi_A^2)/(\text{d.o.f.}_0 - \text{d.o.f.}_A)]/[\chi_A^2/\text{d.o.f.}_A] = 3.4$, corresponds to the p-value, p = 1 - CDF(F) = 0.048, indicating 4.8% probability that the null hypothesis H_0 is correct. Hence, using this approach we find that orbital variations in the X-ray polarization of Cyg X-1 are marginally significant.

3.2.2. Rotating vector model

The rather low statistical significance in favor of the sinusoidal model may be related to our assumption that the amplitude of the variable component $r_{\rm v}$ remains constant throughout the orbit. However, a number of physical reasons may lead to its variations with orbital phase and over time, leading to the enhanced spread of data points around the average q,u values. For example, IXPE has detected well ordered variations of the PA with the spin phase in a number of X-ray pulsars, while the PD showed rather irregular behavior (see Poutanen et al. 2024a, for a recent review). In Cyg X-1 too, the dependence of $r_{\rm v}$ on the orbital phase may be complex and include random fluctuations leading to the loss of signal.

To account for this uncertainty, we adopted an alternative approach to test for the presence of orbital variability by leveraging the expectation that such variations should follow a coherent pattern, specifically, a closed loop in the (q, u)-plane, rather than appearing as random statistical fluctuations scattered around the mean. Below we consider only the orbital phase-dependent changes of PA of the variable component, which does not encompass the aforementioned uncertainty on its PD. This is similar to the application of the rotating vector model to X-ray pulsar polarimetric data (e.g., Suleimanov et al. 2023; Poutanen et al. 2024a,b; Forsblom et al. 2025) or searching for rotation of the X-ray PA with time in blazars (Di Gesu et al. 2023; Kim et al. 2024; Pacciani et al. 2025).

From the observed normalized Stokes parameters we subtracted the average values to obtain a new set of Stokes

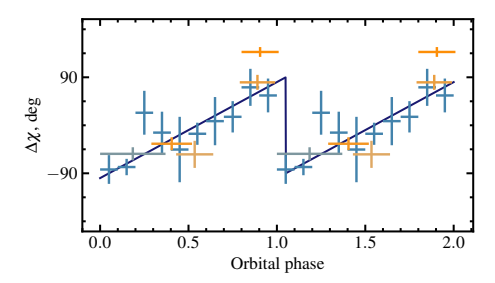


Fig. 7. Angle $\Delta \chi$ as a function of the orbital phase in Cyg X-1. The solid line shows the best fit to the Epoch 1 data with the linear model (7) described in Sect. 3.2.

parameters representing the variable component:

$$q_v = q - \langle q \rangle, \quad u_v = u - \langle u \rangle.$$
 (2)

We calculated $\langle q \rangle = 3.0 \pm 0.1\%$ and $\langle u \rangle = -2.7 \pm 0.1\%$ from the Epoch 1 data only (ten blue data points in Fig. 5), because it continuously covers the whole orbital period – this ensures that the center point of the loop will not be biased due to unequal orbital coverage. We then computed PD_v and PA_v of the variable component using standard formulae

PD =
$$\sqrt{q^2 + u^2}$$
, PA = $\frac{1}{2}$ atan2(u, q). (3)

The phase-resolved variations of PA $_{\rm v}$ are shown in Fig. 7. We see that PA $_{\rm v}$ shows pronounced, gradual 180° rotation along the orbit (corresponding to one full loop in the left panel of Fig. 5). Here, for the sake of an easier interpretation of the observed results, we show $\Delta\chi$, which is the difference between PA $_{\rm v}$ and the $\langle PA \rangle = -21^{\circ}$ of the constant component (obtained from $\langle q \rangle$ and $\langle u \rangle$ using Eq. (3))

$$\Delta \chi = PA_v - \langle PA \rangle. \tag{4}$$

One can think of $\Delta \chi$ as the deviations of the polarization orientation of the variable component from the average direction of polarization on the sky (i.e., relative to the position angle of the orbital axis, rather than relative to North).

When PD_v is comparable to its error, the PA_v is not normally distributed. To compare models to the data, we should use the probability density function of the PA_v , ψ , from Naghizadeh-Khouei & Clarke (1993):

$$G(\psi) = \frac{1}{\sqrt{\pi}} \left\{ \frac{1}{\sqrt{\pi}} + \eta e^{\eta^2} \left[1 + \text{erf}(\eta) \right] \right\} e^{-p_0^2/2},$$
 (5)

where $p_0=p/\sigma_{\rm p}$ is the measured PD_v in units of its error (which is just the error on q or u for a given point), $\eta=p_0\cos[2(\psi-\psi_0)]/\sqrt{2}$, ψ_0 is the measured value for the PA_v, and erf is the error function. The best fit can be obtained by minimizing the log-likelihood function

$$\log L = -2\sum_{i} \ln G(\chi_i),\tag{6}$$

with the sum taken over all phase bins i.

The model to be tested is a linear dependence of the PA with orbital phase:

$$\psi_{\rm L}(\varphi) = \psi_0 + \frac{1}{2}\varphi,\tag{7}$$

where 1/2 comes from the fact that a full loop of 360° in the (q, u)-plane corresponds to a 180° change in PA. If PA_v is distributed randomly, then the linear model is not expected to perform better than a constant model

$$\psi_c(\varphi) = \psi_0,$$
 (8)

The best-fit with the linear model gives $\log L = 32.7$, while the constant model gives $\log L = 37.5$. The difference $\Delta \log L = 4.8$ corresponds to the significance of $\exp(-\frac{1}{2}\Delta \log L) = 0.09$ that the linear model is preferred. As an additional test, we performed Monte-Carlo simulations distributing randomly 15 PAs in the interval $[-90^\circ, 90^\circ]$ and performing a fit with the linear model. In 5.2% cases we got the value of $\log L$ better than what we obtained with the real data for linear model.

The low significance of the linear trend is influenced by the outlier (Epoch 11), and may result from our assumption that the center of the loop in the (q, u)-plane remains constant over several years of observation. Hence, we performed the same analysis only for Epoch 1, which covers one whole orbital cycle. For Epoch 1, we get $\log L = 11.2$ for the linear model, while the constant model gives $\log L = 29.9$. The difference of $\Delta \log L = 18.7$ implies that the orbital variations in Epoch 1 are significant at the confidence level of 8.7×10^{-5} ($\approx 4\sigma$). Monte-Carlo simulations for 10 randomly distributed PAs give 0.2% chance of getting a value of $\log L$ lower than what we got for real data with the linear model, corresponding to $\approx 3\sigma$ significance. The best-fit to Epoch 1 data with the linear model is shown in Fig. 7 with the solid line. We note that the data are consistent with only one cycle per orbit, and that the PA rotates counterclockwise. This contrasts with the behavior of optical polarization in this source, which exhibits two loops per cycle in the (q, u)-plane and a clockwise rotation (Kravtsov et al. 2023).

3.3. Superorbital variability

Next, we tested presence of super-orbital variability in the X-ray polarization data. The period of these modulations was reported to vary over time: both ~300 d and ~150 d were found (e.g., Brocksopp et al. 1999b; Lachowicz et al. 2006; Ibragimov et al. 2007; Zdziarski et al. 2011). The nature of these variations remains uncertain, but the scenario with precession of the accretion disk or its inner parts is consistent with variations of several observables simultaneously (Bochkarev & Karitskaya 1983; Poutanen et al. 2008). If true, this model predicts coordinated variations of the X-ray polarimetric signatures. These variations, however, can be mixed with the orbital variability, hence polarization from different superorbital phases should be compared for the same orbital bins. Moreover, because of the change of the average PD between hard and soft states, polarization changes cannot be considered jointly for both states.

To test the precessing inner flow scenario, we folded the hard-state X-ray polarization measurements according to the phase of the superorbital period $P_{\rm so} = 294$ d with zero point JD 2440000 (Priedhorsky et al. 1983; Kemp et al. 1983)⁴. In Fig. 5 we show the resulting PD and PA color-coded according to the superorbital phase. Current data show no obvious dependence of the polarization properties on the superorbital phase: for the same orbital phase bins, both PD and PA are consistent with being constant for different superorbital phases. The only exception is the PA of Epoch 11 (orange cross centered at orbital

⁴ No significant variations of X-ray polarization were previously found over ~73 d (Krawczynski et al. 2022), which corresponds to the strongest long-term period observed in MAXI (Matsuoka et al. 2009) light curves, but had an instrumental origin.

phase 0.9), which, however, has similar super-orbital phase to the Epochs 9 and 10 (centered at orbital phases 0.9 and 0.4, respectively), which are well aligned with other points at different superorbital phases (blue crosses). This indicates that the PA of the outlier Epoch 11 is not directly related to the superorbital changes. Current data suggest that, if present, the superorbital changes of PA do not exceed $\pm 5^\circ$ with 3σ confidence. This value is substantially smaller than the previously suggested misalignment angle between the orbital and inner flow axes $\sim \! 15^\circ - \! 20^\circ$ needed to explain the observed variations of fluxes and polarization signatures.

3.4. Multiwavelength behavior

IXPE observations were supported by optical and radio polarimetric observations. In Fig. 2 we show the results of multiwavelength polarization evolution. The average PAs of intrinsic (corrected for interstellar contribution) optical and radio polarization are well aligned with the PA in X-rays (see Fig. 8. At the same time, the average PAs in radio (PA_R = $-28^{\circ} \pm 4^{\circ}$), optical (PA_O = $-25^{\circ} \pm 5^{\circ}$), and X-rays (PA_X = $-25^{\circ} \pm 5^{\circ}$) are all aligned with the jet direction ($\approx -25^{\circ}$; Stirling et al. 2001; Miller-Jones et al. 2021).

Optical PD and PA are known to show orbital variability, leading to the spread of points visible in Fig. 2b. Superorbital variability is known to affect the orbit-average PD and can also be expected to be seen through the shifts of orbit-average PA (Kemp et al. 1983; Kravtsov et al. 2023). Overall, optical polarization does not show any pronounced dependence on the spectral state.

Current radio polarization data are not sufficient to trace any signs of orbital or superorbital variability; however, the PAs of all individual datasets are well aligned with the optical and X-ray PAs. The radio PD, on the other hand, seems to be sensitive to the state transitions: nearly five-fold increase in PD is observed during the transition to the soft state (around Epoch 13). At the same time, the X-ray polarization shows a pronounced drop. Hence, if any connection exists, the radio polarization appears to be anti-correlated with the X-ray polarization.

4. Discussion

4.1. Source of orbital variability

Several processes may induce orbital variations of the observed X-ray polarization in BHXRBs: reflection of X-rays off the companion star (Ahlberg et al. 2024; Rankin et al. 2024) or from the bow shock (V. Ahlberg et al., in prep.), scattering in the stellar or accretion disk wind (Kallman et al. 2015; Nitindala et al. 2025), or changes in the accretion disk orientation (Bochkarev & Karitskaya 1983). Below we consider two major classes of models: (i) variations of orientation of the region where the X-ray polarization is produced and (ii) scattering of the incident emission at the intrabinary structure. The models are constrained by the observed criteria imposed by polarization properties: (a) one loop in the (q, u)-plane per orbital cycle and (b) counter-clockwise rotation (Sect. 3.2 and the increasing angle with the orbital phase in Fig. 7).

The variations of X-ray polarization can be produced by the changing orientation of the site of X-ray production, we can apply the formalism developed for the rotating vector model (Radhakrishnan & Cooke 1969; Meszaros et al. 1988) to constrain the tilt of the X-ray-emitting inner flow (disk) with respect to the orbital plane. Variations in the PA in this scenario are

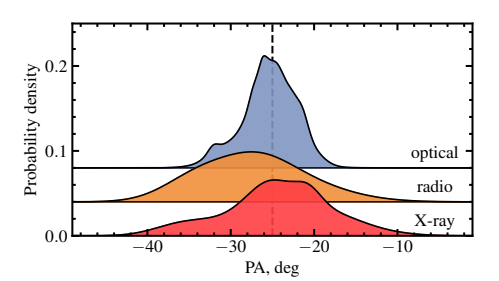


Fig. 8. Smoothed histogram of the observed PA of Cyg X-1 in X-rays (red), radio (orange), and optical (blue). Each observation here is represented as a Gaussian with the standard deviation equal to the error and the sum of those is divided by the number of observations. Graphs are shifted vertically for clarity. The vertical dashed line shows the radio jet direction

attributed to changes in the position angle of the projected inner flow axis on the sky. If the disk axis changes its orientation as a function of orbital phase, the PA will vary accordingly. The limited range of PA variations (Fig. 5) corresponds to a small tilt, $\beta \approx 2^\circ$, which can account for the observed changes. The observed PD variations are caused by the changing inclination. We consider a simplified model in which the PD depends on the cosine μ of the angle between the disk axis and the observer line of sight, given by PD = PD_{max}(1 – μ). While the actual angular dependence may be more complex, it can be approximated as a linear function of μ within a narrow angular range. The solid black lines in Fig. 5 (loop in the (q, u)-plane and sine waves in PD, PA representation) correspond to the best-fit predictions of this model with the tilt $\beta = 2^\circ$, PD_{max} = 0.37% and fixed orbital inclination $i = 153^\circ$.

Changes of the inner disk or flow orientation with respect to the average direction of the orbital axis can be related to tidal forces or precession. In the case of tidal locking, the orientation of the disk is expected to be fixed with respect to the line connecting the compact object and companion star (e.g., always facing the companion star). In this case, the movement of the disk axis on the sky follows the sense of rotation of the compact object around the supergiant (see Fig. 9). This, however, is not observed: the criterion (b) implies that rotation of polarization is counter-clockwise, while the binary system is undergoing clockwise rotation on the sky ($i > 90^\circ$; Miller-Jones et al. 2021).

Alternatively, the disk may experience precession in the direction opposite to the direction of orbital motion (retrograde precession). Furthermore, if the precession is synchronous with the orbital period, it should proceed in the binary system with companions of comparable masses, low eccentricity and no known third-body influence. If all these criteria are satisfied, the precession can explain the observed orbital changes of X-ray polarization; however, no known binary system currently fits all of the aforementioned criteria. Hence, we consider this scenario implausible.

In the second class of models (ii), the changing polarization is produced by the scattering (or reflection) on the intrabinary structure. The PD in this case depends on the cosine of the scattering angle, μ , as PD = $(1-\mu^2)/(1+\mu^2)$ (single-scattering case, Chandrasekhar 1960). This relation predicts two PD peaks per orbital period, as μ^2 is identical for all diametrically opposite points along the orbit. To produce only one peak per orbit and

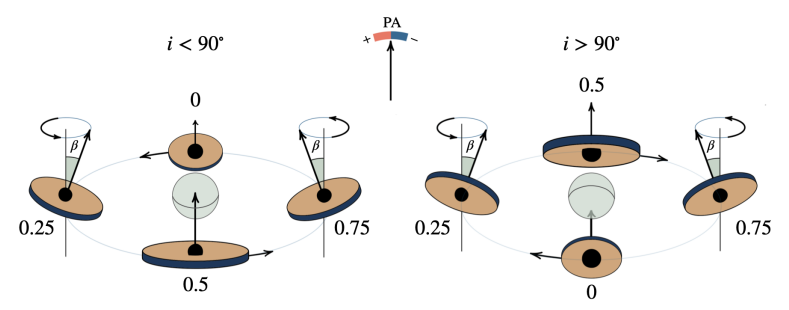


Fig. 9. Sketch of considered precessing disk geometry for two cases: $i < 90^{\circ}$ and $i > 90^{\circ}$.

comply with criterion (a), the scattering matter should either be asymmetrically distributed relative to the orbital plane, or the fraction of scattered radiation should vary significantly with the orbital phase. The latter case has been considered in the context of an asymmetric bow shock producing pronounced orbital variability of X-ray polarization in Cyg X-3 (Veledina et al. 2024, and Ahlberg et al., in prep.). Polarization in this case can be orthogonal to the orbital axis, hence, it is effectively subtracted from the average polarization of the source, leading to higher net PD at phases when the contribution of the scattering is low. This makes this scenario potentially compliant with criterion (b); however, further quantitative study is needed to draw conclusions on the applicability of this scenario.

4.2. Long-term trend in polarization

The long-term stability of the X-ray polarization in Cyg X-1 is remarkable and indicates the stability of geometry of the site of polarization production. The statistically significant increase in PD with energy found in both hard and soft spectral states, along with the constant PA across the IXPE energy band (Sect. 3.1) imposes strong constraints on the Faraday rotation effects within the medium responsible for the production of the observed light and any screen between this site and the observer. These constraints translate to upper limits on the large-scale magnetic fields, for instance, a large-scale vertical field $B_z=10^6\,\mathrm{G}$ can induce the rotation of PA by $\sim 5^\circ$ across the IXPE band (Barnier & Done 2024). Our updated estimates on the energy dependence of PA can further refine the constraints on the magnitude of B-fields in Cyg X-1.

The statistically significant increase in PD with energy detected in the hard state challenges current models of polarization production. The spectrum is shaped by multiple Compton up-scatterings, with the PD increasing with each successive scattering order (e.g., Poutanen & Svensson 1996). One way to account for the high observed PD (given a fixed system inclination) in this state is to assume that the IXPE band is dominated by high-order Compton scatterings. This is equivalent to assuming a low energy for the seed photons, such as those originating from synchrotron radiation (e.g., Poutanen & Vurm 2009; Malzac & Belmont 2009; Veledina et al. 2013). However, this scenario leads to a suppression of any energy dependence of polarization, since the PD is known to saturate at high (≥5th) scattering orders (Poutanen & Svensson 1996; Poutanen et al. 2023). An alternative solution is to retain seed photons from the underlying accretion disc (the slab corona geometry), thus keeping the scattering orders in the IXPE band low to preserve the energy dependence of polarization, and enhance the PD by invoking a bulk matter outflow (Beloborodov & Poutanen 1999; Poutanen et al. 2023). However, realistic outflow velocities have been found insufficient to reproduce the observed \sim 4% PD at an inclination $i \approx 150^\circ$ for this geometry (Poutanen et al. 2023).

The soft-state polarization data are likewise challenging to interpret. The soft-state PA remains aligned with the jet axis throughout years, in contrast to the early expectations for the polarization produced by the optically thick atmosphere of the disk (Chandrasekhar 1960; Sobolev 1963; Rees 1975; Sunyaev & Titarchuk 1985). Furthermore, the IXPE band detects the Wien part of the disk spectrum (emission beyond the peak of its emission), where the effects of strong gravity and fast matter motion are most prominent and lead to a rotation of PA with energy and depolarization effects that increase with energy (e.g., Connors & Stark 1977; Stark & Connors 1977; Dovčiak et al. 2008; Li et al. 2009; Loktev et al. 2022, 2024). We find no evidence for either PA rotation or depolarization; in contrast, the PD is found to increase with energy at a high significance.

Possible scenarios that can reproduce the observed spectra and polarization signatures include a dominant role of returning radiation in the IXPE band (Steiner et al. 2024). This scenario, however, had been considered in the approximation of the energy-independent reflection albedo of unity, indicating a fully ionized accretion disk near the black hole. However, the presence of atomic lines is not aligned with this assumption. Furthermore, the predicted polarization remains below the detected values for the orbital inclination $i \approx 153^\circ$.

In an alternative scenario, the soft spectrum seen in the IXPE band is composed of both disk emission and the low-temperature Compton scattering continuum. Such a spectral decomposition implies the presence of both low-energy Maxwellian electrons and high-energy power-law-like electrons (the so-called hybrid Comptonization), and had been previously shown to fit the observed broadband spectrum of Cyg X-1 up to MeV energies (Gierliński et al. 1999; Poutanen & Vurm 2009). In this case, the expected PD and its increase with energy can be made consistent with the data (Bocharova et al., in prep.).

Interestingly, the increasing PD with energy is expected in both scenarios. The disk emission generally has lower polarization as compared to the reflected (self-irradiated) part that becomes dominant at energies above the disk peak (Schnittman & Krolik 2009), leading to the natural increase in PD with energy. In the hybrid Comptonization scenario, the

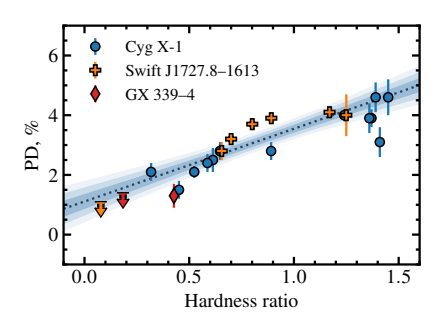


Fig. 10. Dependence of PD on spectral hardness for Cyg X-1, Swift J1727.8–1613 and GX 339–4. For consistency, the hardness ratio has been calculated the same way for all objects as a ratio of energy flux in 4–8 keV to that in 2–4 keV as measured by IXPE. The dotted line with 1, 2, and 3σ confidence intervals shows the linear fit to the data.

increase in PD is attributed to both the low disk intrinsic polarization and the presence of the first Compton scattering order that is polarized in the direction along the disk plane (Poutanen & Svensson 1996). The dominant role of the disk emission in the IXPE band during the soft state can likewise explain the observed increase of total PD with hardness (Fig. 4).

In Fig. 10 we compare the dependence of the X-ray PD on spectral hardness for sources that are believed to have low or intermediate inclinations: Cyg X-1, Swift J1727.8-1613 GX 339-4 (Svoboda et al. 2024; Podgorný et al. 2024; Mastroserio et al. 2025, see a similar comparison in Brigitte & Svoboda 2025). We note that in all these systems the X-ray PAs are found to be aligned with the jet direction (Krawczynski et al. 2022; Ingram et al. 2024; Mastroserio et al. 2025). To enable comparison between systems of various brightness, we computed the spectral hardness the same way for all considered objects as the ratio of the energy flux in 4-8 keV band to that in the 2-4 keV band, as measured by IXPE. The polarimetric data have been adopted from Podgorný et al. (2024) and Mastroserio et al. (2025). Note that this definition of spectral hardness differs from the hardness ratio used earlier in this work. The new data on Cyg X-1 reveal a PD-hardness dependence similar to that observed in the other BHXRBs, both in slope and in absolute values. This suggests a remarkable consistency in polarization behavior across different sources and luminosities, for state transitions occurring in both the upper and lower branches of the q-diagram (Belloni 2010).

4.3. Multiwavelength view

The optical polarization is believed to be produced by the scattering of primary star's radiation by the matter surrounding the black hole (i.e. the accretion disk). In that case, the average optical PA indicates the orientation of the symmetry axis of the large-scale disk in the sky. The observed variations of the optical PA with the amplitude of $\Delta PA \approx 5^{\circ}$ are caused by the orbital motion of the black hole in the binary (more details can be found in Kravtsov et al. 2023).

Radio polarization in X-ray binaries arises from synchrotron radiation, the dominant emission mechanism within their jets (Westfold 1959; Bjornsson & Blumenthal 1982; Han & Hjellming 1992; Corbel et al. 2000). In these systems –

where jets are typically optically thin or partially self-absorbed – the polarization angle is expected to be orthogonal to the magnetic field responsible for particle acceleration (see, e.g., Longair 1994, for a review). Although relativistic aberration and internal Faraday effects can complicate this picture (e.g., Lyutikov et al. 2005), the observed alignment of the radio polarization angle with the jet axis implies a magnetic field structure that is predominantly toroidal, with its projected component on the sky lying perpendicular to the jet. The temporal stability of this polarization angle further suggests a long-lived, ordered magnetic field configuration in the jet's emission region. A similar alignment in the hard state jets was observed in the BHXRBs GRS 1915+105 (Hannikainen et al. 2000) and MAXI J1836–194 (Russell et al. 2015), suggestive of a similar magnetic field geometry.

Following the source transition from hard to soft state (around 2024 December 12; MJD 60656), we observed a fivefold increase in radio polarization degree (PD), from <1% to ~5%. During such transitions, BHXRBs are known to disrupt their (steady) hard state jets and launch discrete plasma knots, which — when polarimetric data are available — often appear more highly polarized (e.g., Han & Hjellming 1992; Brocksopp et al. 2007; Curran et al. 2014. Whether this increase is driven by changes in absorption conditions or intrinsic jet structure remains unclear. A spatially resolved ejection in Cyg X-1 observed by Fender et al. (2006) supports the idea that the PD increase may correspond to such an event. A more detailed analysis of radio polarization of Cyg X-1 will be given in the follow-up paper (Hughes et al., in prep.).

Because X-ray polarization likely originates in the innermost regions of the accretion disk, reflecting the geometry of the inner disk and corona, the observed alignment of PAs across radio, optical, and X-ray bands places valuable constraints on the large-scale geometry of Cyg X-1.

5. Summary

We present the results of a comprehensive three-year observational campaign of Cyg X-1 using X-ray, optical, and radio polarimetry. Thirteen IXPE observations conducted between 2022 and 2024 reveal a clear dependence of the X-ray polarization on the spectral state. We find the PD to be approximately twice as high in the hard state ($\approx\!4.0\%$) as compared to the soft state ($\approx\!2.2\%$), and stable over time.

In both states, the PD increases with energy. The X-ray PA remains independent of the spectral state and shows no clear dependence on photon energy. Our improved constraints further limit the strength of Faraday effects, providing tight bounds on the magnetic field strength in the region where the X-rays are produced.

We investigate the presence of orbital variability in the X-ray polarization data and find it to be significant for the Epoch 1, which covers the entire orbital period. Interestingly, the X-ray polarization changes are cyclic with orbital period, corresponding to one loop in the (q,u)-plane, with PA rotating counterclockwise. This contrasts with the optical polarization behavior, which shows two loops per orbital period and clockwise rotation. We discuss the potential sources of the X-ray polarization variability and suggest that it may result from scattering of X-ray emission by the circumstellar or intrabinary medium. Future high-precision X-ray polarimetric observations are essential for further identification of this variability.

We find no evidence of superorbital variability in the X-ray polarization data at the previously reported period of $P_{\rm so}=294\,\rm d$. We place an upper limit of 5° on the tilt between the

orbital axis and the instantaneous axis of the accretion disk or inner flow. This constraint rules out the earlier hypothesis that the high PD observed in the hard state could be attributed to a favorable phase of superorbital precession, specifically one that would have increased the inclination of the hot inner flow by $15^{\circ}-20^{\circ}$ relative to the orbital axis during the 2022 observation.

We compare Cyg X-1 with other low- to intermediate-inclination BHXRBs in the PD-spectral hardness diagram and find a remarkable consistency in polarization behavior across different sources and luminosities, on both the upper and lower branches of the q-diagram. Our multiwavelength data suggest a possible anti-correlation between the X-ray and radio PDs, while no clear correlation is observed with optical polarization. We show that the average PAs are well aligned across all bands. These results have broad implications for theoretical models of multiwavelength polarization production in BHXRBs.

Acknowledgements. The Imaging X-ray Polarimetry Explorer (IXPE) is a joint US and Italian mission. The US contribution is supported by the National Aeronautics and Space Administration (NASA) and led and managed by its Marshall Space Flight Center (MSFC), with industry partner Ball Aerospace (contract NNM15AA18C). The Italian contribution is supported by the Italian Space Agency (Agenzia Spaziale Italiana, ASI) through contract ASI-OHBI-2022-13-1.0, agreements ASI-INAF-2022-19-HH.0 and ASI-INFN-2017.13-H0, and its Space Science Data Center (SSDC) with agreements ASI-INAF-2022-14-HH.0 and ASI-INFN 2021-43-HH.0, and by the Istituto Nazionale di Astrofisica (INAF) and the Istituto Nazionale di Fisica Nucleare (INFN) in Italy. This research used data products provided by the IXPE Team (MSFC, SSDC, INAF, and INFN) and distributed with additional software tools by the High-Energy Astrophysics Science Archive Research Center (HEASARC), at NASA God dard Space Flight Center (GSFC). This research has made use of data from the RoboPol programme, a collaboration between Caltech, the University of Crete, IA-FORTH, IUCAA, the MPIfR, and the Nicolaus Copernicus University, which was conducted at Skinakas Observatory in Crete, Greece. We thank the staff of Lord's Bridge, Cambridge, for their support in making the AMI observation This research has been supported by the Finnish Cultural Foundation (VK), the Academy of Finland grant 355672 (AV) and the Magnus Ehrnrooth foundation (APN). MD, JPod, and JS acknowledge the support from the Czech Science Foundation project GACR 21-06825X and the institutional support from the Astronomical Institute RVO:6798581. FM, ADM, and FLM are partially supported by MAECI with grant CN24GR08 "GRBAXP: Guangxi-Rome Bilateral Agreement for X-ray Polarimetry in Astrophysics". AI acknowledges support from the Royal Society. IL was funded by the European Union ERC-2022-STG-BOOTES-101076343. Views and opinions expressed are however those of the author(s) only and do not necessarily reflect those of the European Union or the European Research Council Executive Agency. Neither the European Union nor the granting authority can be held responsible for them. SAT is supported by the Ministry of Science and Higher Education of the Russian Federation grant 075-15-2022-262 (13.MNPMU.21.0003). MB acknowledges the support from GAUK project No. 102323. GM acknowledges financial support from the European Union's Horizon Europe research and innovation programme under the Marie Skłodowska-Curie grant agreement No. 101107057. POP acknowledges financial support from the Action Thématique PEM from CNRS and from the french spacial agency CNES. AAZ has been supported by the Polish National Science Center grants 2019/35/B/ST9/03944 and 2023/48/Q/ST9/00138.

References

```
Ahlberg, V., Kravtsov, V., & Poutanen, J. 2024, A&A, 688, A220
Baldini, L., Barbanera, M., Bellazzini, R., et al. 2021, Astropart. Phys., 133, 102628
Baldini, L., Bucciantini, N., Lalla, N. D., et al. 2022, SoftwareX, 19, 101194
Bardeen, J. M., Press, W. H., & Teukolsky, S. A. 1972, ApJ, 178, 347
Barnier, S., & Done, C. 2024, ApJ, 977, 201
Belloni, T. M. 2010, in The Jet Paradigm, (Berlin Heidelberg: Springer Verlag), Lecture Notes in Physics, 794, 53
Beloborodov, A. M., & Poutanen, J. 1999, ApJ, 517, L77
Bjornsson, C. I., & Blumenthal, G. R. 1982, ApJ, 259, 805
Blinov, D., Kiehlmann, S., Pavlidou, V., et al. 2021, MNRAS, 501, 3715
Bochkarev, N. G., & Karitskaya, E. A. 1983, Soviet. Astron. Lett., 9, 6
Bowyer, S., Byram, E. T., Chubb, T. A., & Freidman, H. 1965, Science, 147, 394
Brentjens, M. A., & de Bruyn, A. G. 2005, A&A, 441, 1217
```

```
Brigitte, M., & Svoboda, J. 2025, in WDS'24 Proc. Contrib. Papers, Physics, eds.
    J. Šafránkov, & J. Pavlå (Prague: Matfyzpress), 178
Brocksopp, C., Tarasov, A. E., Lyuty, V. M., & Roche, P. 1999a, A&A, 343, 861
Brocksopp, C., Fender, R. P., Larionov, V., et al. 1999b, MNRAS, 309, 1063
Brocksopp, C., Miller-Jones, J. C. A., Fender, R. P., & Stappers, B. W. 2007,
    MNRAS, 378, 1111
Brown, J. C., McLean, I. S., & Emslie, A. G. 1978, A&A, 68, 415
CASA Team, Bean, B., Bhatnagar, S., et al. 2022, PASP, 134, 114501
Chandrasekhar, S. 1960, Radiative transfer (New York: Dover Publications, Inc.)
Connors, P. A., & Stark, R. F. 1977, Nature, 269, 128
Corbel, S., Fender, R. P., Tzioumis, A. K., et al. 2000, A&A, 359, 251
Curran, P. A., Coriat, M., Miller-Jones, J. C. A., et al. 2014, MNRAS, 437, 3265
Di Gesu, L., Marshall, H. L., Ehlert, S. R., et al. 2023, Nat. Astron., 7, 1245
Di Marco, A., Fabiani, S., La Monaca, F., et al. 2022, AJ, 164, 103
Done, C., Gierliński, M., & Kubota, A. 2007, A&AR, 15, 1
Dovčiak, M., Karas, V., & Matt, G. 2004, MNRAS, 355, 1005
Dovčiak, M., Muleri, F., Goosmann, R. W., Karas, V., & Matt, G. 2008, MNRAS,
Fender, R. P., Stirling, A. M., Spencer, R. E., et al. 2006, MNRAS, 369, 603
Forsblom, S. V., Tsygankov, S. S., Suleimanov, V. F., Mushtukov, A. A., & Poutanen, J. 2025, A&A, 696, A224
Fragos, T., Tremmel, M., Rantsiou, E., & Belczynski, K. 2010, ApJ, 719, L79
Gierliński, M., Zdziarski, A. A., Done, C., et al. 1997, MNRAS, 288, 958
Gierliński, M., Zdziarski, A. A., Poutanen, J., et al. 1999, MNRAS, 309, 496
Gies, D. R., & Bolton, C. T. 1986, ApJ, 304, 371
Han, X., & Hjellming, R. M. 1992, ApJ, 400, 304
Hannikainen, D. C., Hunstead, R. W., Campbell-Wilson, D., et al. 2000, ApJ,
Hickish, J., Razavi-Ghods, N., Perrott, Y. C., et al. 2018, MNRAS, 475, 5677
Ibragimov, A., Zdziarski, A. A., & Poutanen, J. 2007, MNRAS, 381, 723
Ingram, A., Bollemeijer, N., Veledina, A., et al. 2024, ApJ, 968, 76
Kallman, T., Dorodnitsyn, A., & Blondin, J. 2015, ApJ, 815, 53
Karitskaya, E. A., Voloshina, I. B., Goranskii, V. P., et al. 2001, Astron. Rep., 45,
Kemp, J. C., Barbour, M. S., Henson, G. D., et al. 1983, ApJ, 271, L65
Kim, D. E., Di Gesu, L., Liodakis, I., et al. 2024, A&A, 681, A12
Kim, D. E., Di Gesti, L., Liodakis, I., et al. 2024, A&A, 861, A12
Kravtsov, V., Berdyugin, A. V., Piirola, V., et al. 2020, A&A, 643, A170
Kravtsov, V., Berdyugin, A. V., Kosenkov, I. A., et al. 2022, MNRAS, 514, 2479
Kravtsov, V., Veledina, A., Berdyugin, A. V., et al. 2023, A&A, 678, A58
Krawczynski, H., & Behsehipiour, B. 2022, ApJ, 934, 4&A, 678, A58
Krawczynski, H., & Waleri, F., Dovčiak, M., et al. 2022, Science, 378, 650
Lachowicz, P., Zdziarski, A. A., Schwarzenberg-Czerny, A., Pooley, G. G., &
Kitamoto, S. 2006, MNRAS, 368, 1025
Li, L.-X., Narayan, R., & McClintock, J. E. 2009, ApJ, 691, 847
Loktev, V., Veledina, A., & Poutanen, J. 2022, A&A, 660, A25
Loktev, V., Veledina, A., Poutanen, J., Nättilä, J., & Suleimanov, V. F. 2024,
    A&A, 685, A84
Longair, M. S. 1994, High energy astrophysics, 2 (Cambridge: Cambridge
    University Press)
Lyutikov, M., Pariev, V. I., & Gabuzda, D. C. 2005, MNRAS, 360, 869
Malzac, J., & Belmont, R. 2009, MNRAS, 392, 570
Mastroserio, G., De Marco, B., Baglio, M. C., et al. 2025, ApJ, 978, L19
Matsuoka, M., Kawasaki, K., Ueno, S., et al. 2009, PASJ, 61
Meszaros, P., Novick, R., Szentgyorgyi, A., Chanan, G. A., & Weisskopf, M. C.
    1988, ApJ, 324, 105
Miller-Jones, J. C. A., Bahramian, A., Orosz, J. A., et al. 2021, Science, 371,
Naghizadeh-Khouei, J., & Clarke, D. 1993, A&A, 274, 968
Nitindala, A. P., Veledina, A., & Poutanen, J. 2025, A&A, 694, A230
Novikov, I. D., & Thorne, K. S. 1973, in Black Holes (Les Astres Occlus), eds.
    C. DeWitt, & B. DeWitt (New York: Gordon and Breach), 343
Offringa, A. R., McKiconley, B., Hurley-Walker, N., et al. 2014, MNRAS, 444,
Orosz, J. A., McClintock, J. E., Aufdenberg, J. P., et al. 2011, ApJ, 742, 84
Ott, M., Witzel, A., Quirrenbach, A., et al. 1994, A&A, 284, 331
Pacciani, L., Kim, D. E., Middei, R., et al. 2025, ApJ, 983, 78
Panopoulou, G., Tassis, K., Blinov, D., et al. 2015, MNRAS, 452, 715
Piirola, V., Berdyugin, A., & Berdyugina, S. 2014, in Ground-based and
Airborne Instrumentation for Astronomy V, eds. S. K. Ramsay, I. S. McLean,
    & H. Takami, Proc. SPIE, 9147, 91478I
Piirola, V., Berdyugin, A., Frisch, P. C., et al. 2020, A&A, 635, A46
Piirola, V., Kosenkov, I. A., Berdyugin, A. V., Berdyugina, S. V., & Poutanen, J.
    2021, AJ, 161, 20
Podgorný, J., Svoboda, J., Dovčiak, M., et al. 2024, A&A, 686, L12
Poutanen, J., & Svensson, R. 1996, ApJ, 470, 249
Poutanen, J., & Vurm, I. 2009, ApJ, 690, L97
Poutanen, J., Zdziarski, A. A., & Ibragimov, A. 2008, MNRAS, 389, 1427
Poutanen, J., Veledina, A., & Zdziarski, A. A. 2018, A&A, 614, A79
```

```
Poutanen, J., Veledina, A., & Beloborodov, A. M. 2023, ApJ, 949, L10
Poutanen, J., Tsygankov, S. S., & Forsblom, S. V. 2024a, Galaxies, 12, 46
Poutanen, J., Tsygankov, S. S., Doroshenko, V., et al. 2024b, A&A, 691, A123
Priedhorsky, W. C., Terrell, J., & Holt, S. S. 1983, ApJ, 270, 233
Purcell, C. R., Van Eck, C. L., West, J., Sun, X. H., & Gaensler, B. M. 2020, Astrophysics Source Code Library [record ascl:2005.003]
Radhakrishnan, V., & Cooke, D. J. 1969, Astrophys. Lett., 3, 225
Ramachandran, V., Sander, A. A. C., Oskinova, L. M., et al. 2025, A&A, 698, A37
Ramparakash, A. N., Rajarshi, C. V., Das, H. K., et al. 2019, MNRAS, 485, 2355
Rankin, J., Kravtsov, V., Muleri, F., et al. 2024, ApJ, 962, 34
Rao, A., Gandhi, P., Knigge, C., et al. 2020, MNRAS, 495, 1491
Rees, M. J. 1975, MNRAS, 171, 457
Russell, T. D., Miller-Jones, J. C. A., Curran, P. A., et al. 2015, MNRAS, 450, 1745
Schaltman, J. D., & Krolik, J. H. 2009, ApJ, 701, 1175
Shakura, N. I., & Sunyaev, R. A. 1973, A&A, 500, 33
Sobolev, V. V. 1963, A Treatise on Radiative Transfer (Princeton: Van Nostrand)
Soffitta, P., Baldini, L., Bellazzini, R., et al. 2021, AJ, 162, 208
Stark, R. F., & Connors, P. A. 1977, Nature, 266, 429
Stierier, J. F., Nathan, E., Hu, K., et al. 2024, ApJ, 969, 130
Stirling, A. M., Spencer, R. E., de la Force, C. J., et al. 2001, MNRAS, 327, 1273
Suleimanov, V. F., Forsblom, S. V., Tsygankov, S. S., et al. 2023, A&A, 678, A119
```

Sunyaev, R. A., & Titarchuk, L. G. 1980, A&A, 86, 121
Sunyaev, R. A., & Titarchuk, L. G. 1985, A&A, 143, 374
Svoboda, J., Dovčiak, M., Steiner, J. F., et al. 2024, ApJ, 966, L35
Tananbaum, H., Gursky, H., Kellogg, E., Giacconi, R., & Jones, C. 1972, ApJ, 177, L5

Veledina, A., Poutanen, J., & Vurm, I. 2013, MNRAS, 430, 3196 Veledina, A., Muleri, F., Dovčiak, M., et al. 2023, ApJ, 958, L16 Veledina, A., Muleri, F., Poutanen, J., et al. 2024, Nat. Astron., 8, 1031 Weisskopf, M. C., Soffitta, P., Baldini, L., et al. 2022, J. Astron. Telesc. Instrum. Syst., 8, 026002

Westfold, K. C. 1959, ApJ, 130, 241

Zdziarski, A. A., & Gierliński, M. 2004, Prog. Theor. Phys. Suppl., 155, 99 Zdziarski, A. A., Gierliński, M., Mikołajewska, J., et al. 2004, MNRAS, 351, 791

Zdziarski, A. A., Pooley, G. G., & Skinner, G. K. 2011, MNRAS, 412, 1985 Zwart, J. T. L., Barker, R. W., Biddulph, P., et al. 2008, MNRAS, 391, 1545

- ³ Astrophysics, Department of Physics, University of Oxford, Denys Wilkinson Building, Keble Road, Oxford OX1 3RH, UK
- ⁴ Astronomical Institute of the Czech Academy of Sciences, Boční II 1401/1, 14100 Praha 4, Czech Republic
- ⁵ INAF Osservatorio Astronomico di Cagliari, Via della Scienza 5, 09047 Selargius (CA), Italy
- ⁶ INAF Istituto di Astrofisica e Planetologia Spaziali, Via del Fosso del Cavaliere 100, 00133 Roma, Italy
- Institute of Astrophysics, FORTH, N. Plastira 100, GR-70013 Heraklion, Greece
- Bepartment of Physics, University of Crete, GR-70013 Heraklion, Greece
- ⁹ INAF Osservatorio Astronomico di Roma, Via Frascati 33, 00078 Monte Porzio Catone (RM), Italy
- ¹⁰ Astrophysics Group, Cavendish Laboratory, 19 J. J. Thomson Avenue, Cambridge CB3 0HE, UK
- School of Mathematics, Statistics, and Physics, Newcastle University, Newcastle upon Tyne NE1 7RU, UK
- Special Astrophysical Observatory of the Russian Academy of Sciences, Nizhnij Arkhyz 369167, Karachayevo-Cherkessia, Russia
 Astronomical Institute, Faculty of Mathematics and Physics,
- Charles University, V Holešovičkách 2, Prague 8 18000, Čzech Republic

 ¹⁴ Agenzia Spaziale Italiana, via della Scienza 5, 09047 Selargius
- (CA), Italy

 15 Physics Department, McDonnell Center for the Space Sciences, and Center for Quantum Leaps, Washington University in St. Louis, St.
- Center for Quantum Leaps, wasnington University in St. Louis, St. Louis, MO 63130, USA

 16 Dipartimento di Fisica, Università degli Studi di Roma 'Tor Ver-
- gata', Via della Ricerca Scientifica 1, 00133 Rome, Italy

 17 Department of Physics, P.O. Box 64, FI-00014 University of Helsinki, Finland
- Dipartimento di Fisica, Università Degli Studi di Milano, Via Celoria 16, 20133 Milano, Italy
- ¹⁹ Université Grenoble Alpes, CNRS, IPAG, 38000 Grenoble,
- ²⁰ INAF Astronomical Observatory of Rome, Via Frascati 33, 00040 Monte Porzio Catone, Italy
- 21 INFN Sezione di Roma 'Tor Vergata', Via della Ricerca Scientifica 1, 00133 Rome, Italy
- Nicolaus Copernicus Astronomical Center, Polish Academy of Sciences, Bartycka 18, PL-00-716 Warszawa, Poland

Department of Physics and Astronomy, FI-20014 University of Turku, Finland

Nordita, KTH Royal Institute of Technology and Stockholm University, Hannes Alfvéns väg 12, SE-10691 Stockholm, Sweden

Kravtsov V., Veledina A., Berdyugin A.V., Zdziarski A.A., Henson G.D., Piirola V., Sakanoi T., Kagitani M., Berdyugina S.V., Poutanen J. Peering into the tilted heart of Cyg X-1 with high-precision optical polarimetry

Astronomy & Astrophysics, 2023; 678: A58



Peering into the tilted heart of Cyg X-1 with high-precision optical polarimetry

Vadim Kravtsov¹, Alexandra Veledina^{1,2}, Andrei V. Berdyugin¹, Andrzej A. Zdziarski³, Gary D. Henson⁴, Vilppu Piirola¹, Takeshi Sakanoi⁵, Masato Kagitani⁵, Svetlana V. Berdyugina^{6,7}, and Juri Poutanen¹

- Department of Physics and Astronomy, 20014 University of Turku, Finland e-mail: vakrau@utu.fi
- Nordita, KTH Royal Institute of Technology and Stockholm University, Hannes Alfvéns väg 12, 10691 Stockholm, Sweden
- Nicolaus Copernicus Astronomical Center, Polish Academy of Sciences, Bartycka 18, 00-716 Warszawa, Poland
- Department of Physics and Astronomy, East Tennessee State University, Johnson City, TN 37614, USA
- Graduate School of Sciences, Tohoku University, Aoba-ku, 980-8578 Sendai, Japan
- Leibniz-Institut für Sonnenphysik, Schöneckstr. 6, 79104 Freiburg, Germany
- Istituto Ricerche Solari Aldo e Cele Daccò (IRSOL), Faculty of Informatics, Università della Svizzera italiana, 6605 Locarno, Switzerland

Received 18 May 2023 / Accepted 3 August 2023

ABSTRACT

We present high-precision optical polarimetric observations of the black hole X-ray binary Cygnus X-1 that span several cycles of its 5.6-day orbital period. The week-long observations on two telescopes located in opposite hemispheres allowed us to track the evolution of the polarization within one orbital cycle with the highest temporal resolution to date. Using the field stars, we determined the interstellar polarization in the source direction and subsequently its intrinsic polarization $P_{int} = 0.82\% \pm 0.15\%$ with a polarization angle $\theta_{int} = 155^{\circ} \pm 5^{\circ}$. The optical polarization angle is aligned with that in the X-rays recently obtained with the Imaging X-ray Polarimetry Explorer. Furthermore, it is consistent within the uncertainties with the position angle of the radio ejections. We show that the intrinsic polarization degree is variable with the orbital period with an amplitude of ~0.2% and discuss various sites of its production. Assuming that the polarization arises from a single Thomson scattering of the primary star radiation by the matter that follows the black hole in its orbital motion, we constrained the inclination of the binary orbit $i > 120^{\circ}$ and its eccentricity e < 0.08. The asymmetric shape of the orbital profiles of the Stokes parameters also implies the asymmetry of the scattering matter distribution in the orbital plane, which may arise from the tilted accretion disk. We compared our data to the polarimetric observations made in 1975-1987 and find good agreemnt within 1° between the intrinsic polarization angles. On the other hand, the polarization degree decreased by 0.4% over half a century, suggesting secular changes in the geometry of the accreting matter.

Key words. accretion, accretion disks – black hole physics – polarization – stars: black holes – stars: individual: Cyg X-1 – X-rays: binaries

1. Introduction

The determination of the large-scale accretion geometry and orbital parameters of X-ray binaries is a fundametally important problem. Various techniques can be employed to examine the geometry of these systems, such as photometry, spectroscopy, imaging, and timing. A special place in this list belongs to polarimetry, which is known to be most sensitive to changes in geometry. The geometrical properties can be determined by tracking the changes in polarization degree (PD) and polarization angle (PA) as a function of the orbital phase. The stochastic variability on timescales comparable to the orbital period may significantly alter the average polarization profile. Dense coverage of an entire orbital cycle is needed to reliably determine the accretion geometry, shape, and orientation of the binary components.

The orbital parameters in binary systems are conventionally studied using optical and infrared polarimetry. For the low-mass X-ray binaries in outburst, emission in these wavelengths can be composed of several components: an (irradiated) accretion disk, a wind, a jet, and a hot accretion flow (Poutanen & Veledina 2014; Uttley & Casella 2014). Optical polarimetry has been used as a fine tool for distinguishing between them (Veledina et al. 2019; Kosenkov et al. 2020). In (near-)quiescence, optical polarimetry has helped constrain the role of the non-stellar components in total spectra (Kravtsov et al. 2022) and to determine the misalignment of the black hole (BH) and orbital spins (Poutanen et al. 2022). For high-mass X-ray binaries, emission in the infrared, optical, and ultraviolet bands is completely dominated by the donor star. The emission can be scattered by different large-scale components in the binary such as the accretion stream, disk, outflow or jet. The polarization signal in this case can reveal the location, orientation, and physical properties of the scattering component (Jones et al. 1994).

With the launch of the Imaging X-ray Polarimetry Explorer (IXPE; Weisskopf et al. 2022), the polarimetric field gained a second wind. It became possible to directly link the orientation of the large-scale binary components that are probed by the optical and infrared wavelengths to the innermost accretion geometry with the help of X-ray polarimetry. The prototypical BH X-ray binary Cygnus X-1 became the first target of these studies (Krawczynski et al. 2022). The week-long IXPE exposure has been accompanied by the global multiwavelength

campaigns, allowing it to cover a large fraction of its 5.6 d orbital Table 1. Log of the polarimetric observations of Cyg X-1. period.

Cyg X-1 is the first discovered BH X-ray binary and a wellstudied system (Bowyer et al. 1965). It is a persistent source and a high-mass binary hosting a supergiant \sim 40 M_{\odot} donor star of spectral type O in a nearly circular orbit (eccentricity $e \sim 0.02$) with the most massive Galactic BH $M_{\rm BH} = 21.2 \pm 2.1 \, M_{\odot}$ known to date (Miller-Jones et al. 2021). The donor is close to filling its Roche lobe, and the compact object accretes the matter through the focused stellar wind (Gies & Bolton 1986a). Accretion proceeds through the disk, whose emission is often seen in the X-rays (Gierliński et al. 1997, 1999; Zdziarski & Gierliński 2004), and a fraction of matter leaves the system in the form of the jet (Stirling et al. 2001; Fender et al. 2006; Miller-Jones et al. 2021).

Optical radiation is dominated by the light of the companion star and shows pronounced variations at an orbital period that is caused by the asymmetric shape of the donor (Kemp et al. 1983; Gies & Bolton 1986b; Brocksopp et al. 1999b; Orosz et al. 2011). Optical polarization measurements also show pronounced orbital variability (Nolt et al. 1975). The observed double-peak sinusoidal variations of the PD and PA are consistent with the scenario in which polarization arises from Thomson scattering of the donor star radiation by optically thin matter located within the binary (Brown et al. 1978; Milgrom 1978). This pattern is typical for binary systems and was observed in a variety of sources from classical (Piirola 1980; Berdyugin & Harries 1999) to gamma-ray binaries (Kraytsov et al. 2020). The synchronization with the orbital phase indicates that the source of the polarization is connected to the orbital motion of the BH around the companion star.

Polarization may originate from the accretion stream, its impact point on the accretion disk or the disk matter itself, or it might be related to the outflow/jet. Which component causes variations in the polarization in Cyg X-1 is unknown. The shapes of the PD and PA profiles have been used in several works to constrain orbital parameters such as inclination and eccentricity (Kemp et al. 1978, 1983; Karitskaya 1981; Dolan & Tapia 1989; Nagae et al. 2009).

The long orbital period of Cyg X-1 became an obstacle to tracking the polarimetric variations over a large fraction of a single cycle, and the average profile was obtained by including data from many cycles. This approach may lead to a substantial deviation of the obtained mean profile from the individual cycles, however, because the system is known to show substantial superorbital variability (Priedhorsky et al. 1983; Karitskaya et al. 2001; Poutanen et al. 2008; Zdziarski et al. 2011). This means that the scattering matter gradually rearranges within the binary over the superorbital period, leading to a systematic bias in the determination of the binary inclination from the mean orbital profile. On the other hand, the data obtained during a single orbital period at one telescope are unavoidably under-sampled (Dolan & Tapia 1989; Nagae et al. 2009). We performed multiobservatory polarimetric observations of Cyg X-1 that for the first time covered up to 30% of the orbit in one cycle. This was achieved by observing with nearly identical polarimeters from telescopes that were separated by $\sim 140^{\circ}$ in longitude.

In this paper, we present the results of joint analysis of the new high-precision optical polarimetric observations of Cyg X-1, historical polarimetric data obtained in 1975-1987, and optical flux measurements, which allowed us to make a new attempt to qualitatively and quantitatively constrain the geometry of Cyg X-1. The paper is organized as follows. In Sect. 2 we describe the observations of the source and of the field stars

Dates	MJD	$N_{\rm obs}$	Telescope
1975 Jun-1987 Oct	42572-47068	1511	PMO
2002 April-May	52381-52394	10	KVA
2002 April-May	52391-52394	4	NOT
2022 March-July	59652-59788	27	T60
2022 May 15-21	59714-59719	6	NOT

to determine the contribution of the interstellar polarization. In Sect. 3 we present the main results of the study: the variations in the polarization on different timescales. We present a model for the observed orbital and superorbital variability of the polarization in Sect. 4. Finally, we summarize our findings in Sect. 5.

2. Data acquisition and analysis

We performed high-precision optical polarimetric observations of Cyg X-1 with the broad-band BVR polarimeters DIPol-2 (Piirola et al. 2014) and DIPol-UF (Piirola et al. 2021). DIPol-2 is mounted on the remotely controlled 60 cm Tohoku telescope (T60) at Haleakala Observatory, Hawaii. DIPol-UF is a visitor instrument installed at the 2.56 m Nordic Optical Telescope (NOT) at the Observatorio del Roque de los Muchachos (ORM) on La Palma, Spain. DIPol-2 and DIPol-UF are high-precision double-image CCD polarimeters, capable of measuring polarization simultaneously in three optical (BVR) bands. The polarization of the sky (even if it changes during observations) is optically eliminated by the design of the instruments. The instrumental polarization of both instruments is low ($<10^{-4}$) and is well calibrated by observing 15-20 unpolarized standard stars. The zero-point of the PA was determined by observing the highly polarized standards HD 204827 and HD 161056. Each measurement of the Stokes parameters (q_{obs}, u_{obs}) took about 20 s, and more than 200 individual measurements were obtained during the average observing night. A more detailed description of the methods and calibrations can be found in Piirola et al. (2020) and Kravtsov et al. (2022).

Cyg X-1 was observed for 27 nights between 2022 March 28 and July 28 at the T60 and for 6 nights, 2022 May 15-21, at the NOT (see Table 1). Taking advantage of the ~140° difference in the longitude of the observatories, we covered 30% of the orbit of Cyg X-1 simultaneously with IXPE observations (red stripe in Fig. 1). We refer to this dataset as season 2 (or just S2) hereafter. The typical errors on the 30-min-averaged measurement of the Stokes parameters are $\sigma_{\rm p}\approx 0.004\%$ for the NOT and $\approx\!0.01\%$ for the T60 data.

We additionally used the historical observations carried out at the Pine Mountain Observatory (PMO), United States, in 1975-1987 (see Table 1 and Fig. 2). The reduced data were presented in parts in several papers (Kemp et al. 1978, 1979, 1983), but have never been published as a raw dataset. With the kind permission of the Pine Mountain Observatory staff, we are publishing these data (hereafter PMO data) in the public domain for the first time¹

The description of the observational techniques can be found in Kemp & Barbour (1981). Each PMO observation is a nightly average value with a typical integration time of several hours. We also used previously unpublished polarimetric observations of Cyg X-1, carried out in 2002 April-May with the TurPol

All the polarimetric data we used in the paper are available in VizieR.

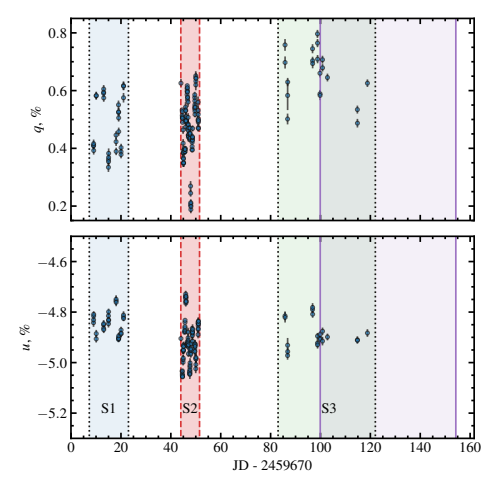


Fig. 1. Observed normalized Stokes parameters for Cyg X-1 in the *B* band. The vertical dotted black lines limit the observational seasons S1 and S3. The two vertical dashed red lines show the start and end of the IXPE campaign on 2022 May 15–21 (season 2). The vertical solid purple lines show the start and end of the TESS observations.

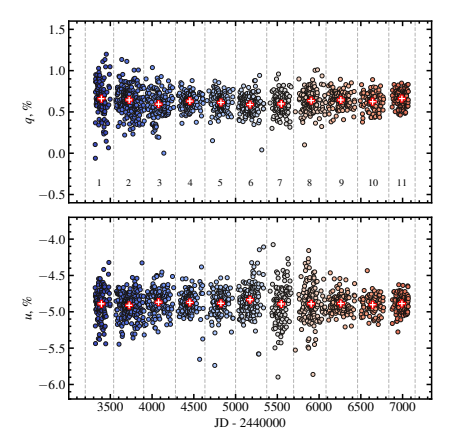


Fig. 2. Long-term variations in the normalized Stokes parameters q and u of Cyg X-1, measured in 1975–1987. The vertical dashed lines separate 11 observing seasons, which is roughly equal to one year of observations. The red crosses show season-averaged values.

polarimeter (Piirola 1973, 1988), installed on NOT, and with the 60 cm KVA telescope, ORM, La Palma.

In addition to the polarimetric data, we retrieved and analyzed the publicly available² Transiting Exoplanet Survey Satellite (TESS; Ricker et al. 2014) optical light curves of Cyg X-1. We used calibrated data with a 2-min cadence (PDCSAP_FLUX),

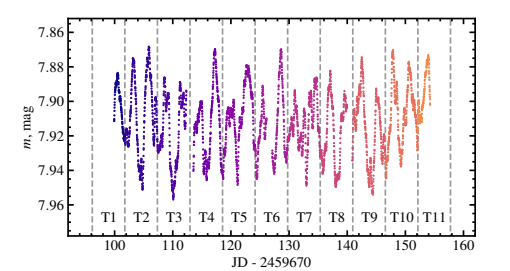


Fig. 3. TESS optical light curve of Cyg X-1. The vertical dashed lines separate the consecutive orbital periods T1–T11.

obtained in sectors 54 and 55 (2022 July – September; see Fig. 3).

3. Results

3.1. Average intrinsic polarization and its secular changes

The observed polarization of Cyg X-1 is the sum of the intrinsic polarization of the source and the interstellar (IS) polarization component that arises from the dichroism of the dust grains located between the observer and the target. The IS polarization was estimated and subtracted from the observed polarization. To find a reliable estimate of IS polarization in the source direction, we observed a sample of six field stars (see Fig. 4) that are close to Cyg X-1, as indicated by their *Gaia* parallaxes (see Fig. 5). We considered the wavelength dependence of the observed polarization (to exclude stars with intrinsic polarization) and took both the angular separation and proximity to the target into account. We conclude that the polarization of star Ref 2 from our sample can serve as the IS polarization estimate. Hereafter, we denote the normalized Stokes parameters of Ref 2 as $(q_{\rm IS}, u_{\rm IS})$ and subtract them from the observed values of the target (q_{obs}, u_{obs}) to obtain the Stokes parameters of the intrinsic polarization (q_{int} , u_{int}). These are translated into the intrinsic PD P and angle θ ,

$$P = \sqrt{q_{\text{int}}^2 + u_{\text{int}}^2}, \quad \theta = \frac{1}{2} \arctan 2(u_{\text{int}}, q_{\text{int}}). \tag{1}$$

The uncertainty on the PD is equal to the uncertainty of the individual Stokes parameters, and uncertainty on the PA in radians was estimated as $\sigma_\theta = \sigma_p/(2P)$ (Serkowski 1962; Kosenkov et al. 2017). The average observed and intrinsic polarization of Cyg X-1, as well as the interstellar polarization estimates, are listed in Table 2.

A large fraction of the observed polarization, about 4% out of a total 4.5–5%, has an IS origin (Kemp et al. 1979; Nagae et al. 2009). Subtracting the interstellar component from the observed polarization, we find an intrinsic PD of $0.8\% \pm 0.2\%$ with a PA of $155^{\circ} \pm 5^{\circ}$ (or equivalently, -25° ; see Table 2). This value is comparable to the characteristic optical PDs in other accreting BH X-ray binaries in outburst (Kosenkov et al. 2017; Veledina et al. 2019). The average intrinsic optical PA matches that measured in the X-rays within the errors $(\theta_X = -22.^{\circ}2 \pm 2.^{\circ}2, Krawczynski et al. 2022)$.

The uniquely long history of polarimetric studies of Cyg X-1 allowed us to track the long-term evolution of the average PD almost 50 years back. We split the PMO *V*-band observations into 11 bins (PMO1-PMO11; see Fig. 2), each about a year

https://archive.stsci.edu/missions-and-data/tess

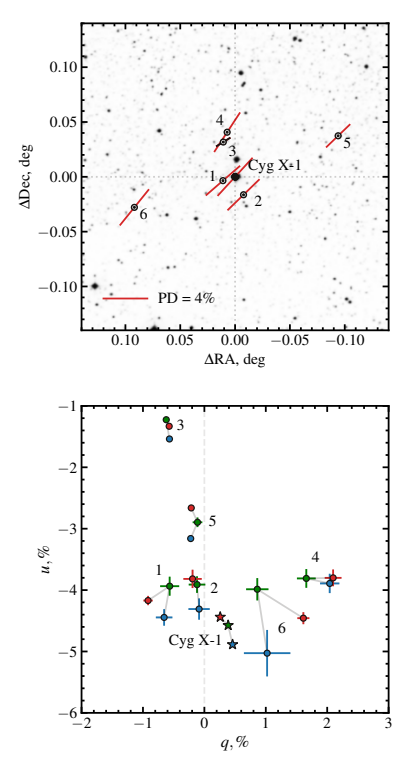


Fig. 4. Finding chart and polarization properties of Cyg X-1 and the field stars. *Top panel*: polarization map for Cyg X-1 and the field stars. The length of the bars corresponds to the PD, and the direction corresponds to the PA (measured from north to east). *Bottom panel*: observed normalized Stokes parameters q and u for Cyg X-1 (stars) and field stars (circles). The blue, green, and red points with 1σ error bars correspond to the B, V, and R filters, respectively.

long, and calculated the average values of the observed Stokes parameters within each bin. We plot them in the (q, u) diagram in Fig. 6 (colored crosses) along with our NOT+T60 2022 average polarization (red circle), KVA+NOT 2002 data (empty circle), and other published data (orange square and green diamond; Dolan & Tapia 1989; Nagae et al. 2009). We show the estimated value of the IS polarization with a blue square.

The blue and red lines connect the PMO and NOT+T60 2022 data with the IS estimate, respectively. The length and direction (from the IS estimate toward the data points) of these lines correspond to the vectors of the average intrinsic polarization for different epochs. The vector directions match with a high accuracy $(\Delta\theta_{\rm int} < 1^{\circ})$. This supports our choice of the reference star Ref 2 as an estimate of interstellar polarization because the alignment of the intrinsic polarization vectors is unlikely to be accidental. We note that the other historical values shown in Fig. 6 are substantially scattered in the q-u plane, despite their small error bars. This may be caused by the orbital variations: At least sev-

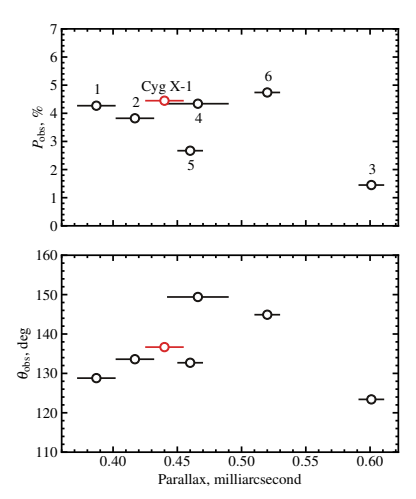


Fig. 5. Dependence of the PD ($top\ panel$) and PA ($bottom\ panel$) on the Gaia parallax for Cyg X-1 (red circle) and the field stars (black circles) in the R band. The horizontal error bars correspond to the errors on the Gaia parallaxes. The errors on the PD and PA are smaller than the symbol size.

eral different orbital periods must be averaged to obtain a robust estimate of the average polarization.

The average intrinsic polarization for our NOT+T60 2022 data differs significantly from the PMO data ($|\Delta P_{\rm int}| \approx 0.4\%$), indicating secular changes in the PD while preserving a constant PA. The decrease in the intrinsic PD may be caused by the decrease in the scattered flux, tailored to the secular changes of the wind density, changes in the accretion disk size, and/or its spatial orientation. Figure 2 shows that the one-year polarization averages change slightly from one season to the next. The different spread of all data points shows that the amplitude of the variability also varies on yearly timescales.

3.2. Short-term variability of the orbital profiles

The significant variability in the Stokes (q_{obs}, u_{obs}) parameters with an amplitude of about 0.1%-0.2% is clearly visible in our 2022 observations (see Fig. 1). We performed a timing analysis of our BVR polarimetric data that revealed that the main variation period of the Stokes parameters has not changed since the 1970s and is equal to half of the orbital period within the errors. To study the possible changes in the average orbital profiles of the polarization over decades, we folded our data and the PMO polarization data with the orbital phase, adopting the period $P_{\rm orb}$ from the photometric ephemeris (Brocksopp et al. 1999a). To suppress the stochastic and instrumental noise, we split the data into 18 orbital phase bins, in which we calculated weighted average values of the Stokes parameters that were subsequently used to obtain the PD P and PA θ . The comparison of our light curve and the PMO polarization light curves is shown in Fig. 7. Except for the systematic offset between our and PMO data, the nature of which is discussed above, the shapes of the average PD and PA orbital profiles agree exceptionally well with each other.

Table 2. Observed PD and PA, interstellar polarization, and intrinsic polarization of Cyg X-1, obtained by averaging S1–S3 data.

	Observed		Interstellar		Intrinsic	
Filter	P _{obs} (%)	$\theta_{\rm obs}$ (deg)	P _{is} (%)	θ _{is} (deg)	P _{int} (%)	$\theta_{\rm int}$ (deg)
В	4.91 ± 0.06	138 ± 1	4.31 ± 0.17	134 ± 1	0.83 ± 0.17	158 ± 6
V	4.59 ± 0.06	138 ± 1	3.91 ± 0.14	134 ± 1	0.86 ± 0.14	155 ± 5
R	4.44 ± 0.05	137 ± 1	3.82 ± 0.15	134 ± 1	0.79 ± 0.15	155 ± 5

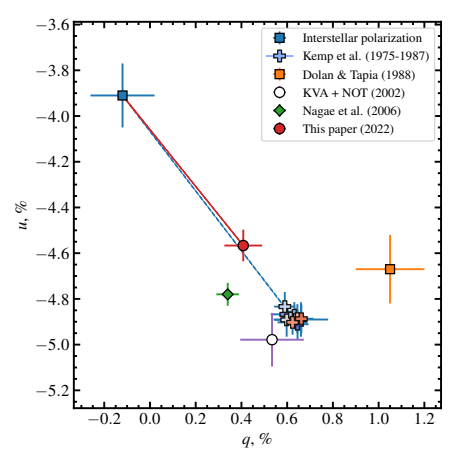


Fig. 6. Normalized Stokes parameters $(q_{\rm obs}, u_{\rm obs})$ of Cyg X-1 in the V band. The red circle with the error bar is the average polarization of Cyg X-1 in 2022. The crosses of different colors (from cool to warm) with error bars correspond to the average polarization in each of the 11 seasons of PMO observations in 1975–1987. The dashed blue and solid red lines show the directions of the average intrinsic polarization vector of Cyg X-1 for PMO and our observations, respectively. The other symbols correspond to the data obtained in other epochs, as described in the inset.

To determine how the shape of optical light curves changes from one period to another, we split TESS photometric data into 11 consecutive orbital periods T1–T11 (see Fig. 3). The shape of each individual profile is far from the double-sine wave that is expected in the case of ellipsoidal variations that are caused by the rotation of a tidally distorted star around the center of mass. A short-period variability is superimposed on the main double-sine curve, which leads to changes in the amplitudes and phases of the main maxima/minima. In Fig. 8 we show the orbital profiles of the intrinsic polarization in *R* band together with TESS photometric profiles. The optical polarization and optical flux both show double-sinusoidal orbital variations with minima in the conjunctions (phases 0 and 0.5) and maxima in the quadratures (phases 0.25 and 0.75).

Photometric variations arise from the nonspherical shape of the tidally distorted companion, whose visible area (and hence the flux) is largest around the quadratures. If the scattering of the donor star emission occurs in a region that is connected to the compact object, we expect the scattering angle to reach a maximum of 90° in the same phases, corresponding to the maximum PD in the case of Thomson scattering. In the conjunctions, the

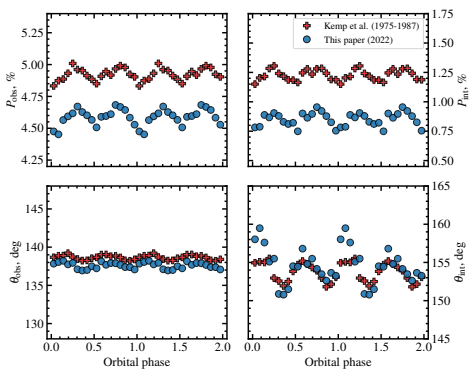


Fig. 7. Orbital profiles of the observed and intrinsic polarization of Cyg X-1. *Left panels*: observed PD, P, $(top\ panel)$ and PA, θ , $(bottom\ panel)$ of Cyg X-1 in the V band, folded with the orbital period. The blue circles correspond to the data obtained in 2022. The red crosses correspond to the PMO data obtained in 1975–1987. Each point corresponds to the average value, calculated within a phase bin of width $\Delta\phi=1/18$. The typical 1σ uncertainty is smaller than the symbol size. $Right\ panels$: same as the left panel, but showing the intrinsic polarization of Cyg X-1.

visible area of the supergiant approaches its minima, resulting in the lowest flux, while at the same time, the scattering angle reaches minimum or maximum, leading to a smaller PD. The short-term changes in both the flux and polarization, which are superimposed on the periodic variations, can originate from one or more mechanisms: the pulsations of the main star, spots on its surface, inhomogeneities of the wind, or eclipses of the bright parts of the disk by the infalling matter. We note that despite the correlation of flux and polarization, the polarization variability cannot be explained by variations in the unpolarized flux alone. For the intrinsic PD $P = F_{\rm pol}/F_{\rm tot} \sim 0.01$, the unpolarized flux variations of about $\Delta F_{\rm tot} \sim 5 \times 10^{-3} F_{\rm tot}$ give a negligibly small polarization variability:

$$\Delta P \approx P \frac{\Delta F_{\rm tot}}{F_{\rm tot}} \sim 5 \times 10^{-5},$$

while the observed one is at least factor 20 of larger.

With our exceptionally dense orbital coverage, we can compare the profiles of a single cycle with the average one, as given by the PMO data. In Fig. 9 we show the profile obtained from the 8-day-long monitoring of Cyg X-1 during season 2, overlaid on the average profile of the polarization variability in the V band. The figure shows that although the overall shapes of the polarization variability curves are roughly consistent with the patterns

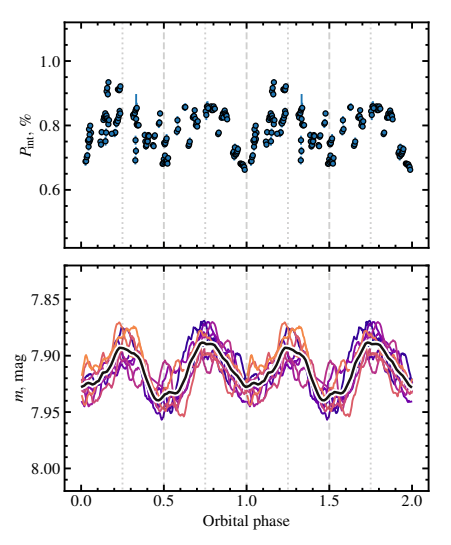


Fig. 8. Orbital profiles of the polarization and flux of Cyg X-1 in the optical band. *Top panel*: intrinsic polarization of Cyg X-1 in the *R* filter, folded with the orbital period (seasons 1–3 are plotted). Each circle with the 1σ error bar shows the average polarization, calculated within a 30-min bin. *Bottom panel*: TESS magnitude of Cyg X-1, folded with the orbital period. Different colors (from cold to warm) correspond to different orbital periods T1–T11. The solid black line shows the average orbital profile.

of 1975–1987, the amplitude of the variations is substantially higher in our season 2 data, where the harmonic content is also richer. These facts support the statement of Dolan & Tapia (1989) about the existence of nonorbital polarization variability and the importance to account for it when extracting orbital parameters. In the following sections, we describe the modeling of the polarization variability curves with different analytical models and discuss how the short-term variability affects the results.

3.3. Superorbital evolution of polarization profiles

In addition to the short-term variability, indications of long-term changes in the Cyg X-1 polarization profiles have been reported by several authors. Kemp et al. (1983) suggested long-term optical polarization variations at the superorbital period of 294 d, discovered in the X-rays (Priedhorsky et al. 1983). The authors discussed several models that could explain the variations, including the precession of the accretion disk and the obscuration of the scattering medium. Comparing the average optical polarization obtained between 1975 and 2006, Nagae et al. (2009) found secular variations in the average polarization component of Cyg X-1.

We find signatures of the long-term variability in our 2022 polarimetric data. Figure 10 shows the change in the polarization profiles with superorbital phase, separated roughly by a month (see Fig. 1). The changes in the average values of Stokes parameters along with the changes in the amplitude and profiles of the orbital variations are significant. In Fig. 11 we show the superor-

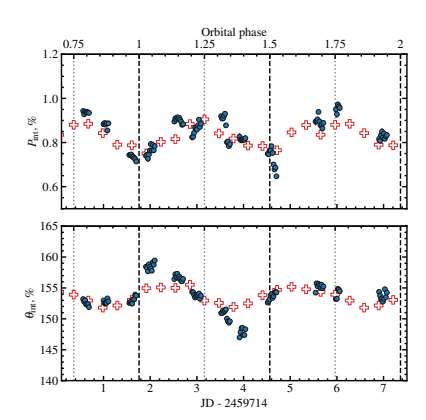


Fig. 9. Variability in the intrinsic PD (*upper panel*) and PA (*bottom panel*) of Cyg X-1 in V band, measured in May 2022 (blue circles). Each circle corresponds to the average value, calculated within a 30-min bin. The 1σ errors are smaller than the symbol size. The red crosses correspond to the average binned polarization, measured by Kemp with colleagues during 1975–1987, with a constant shift in PD by $\Delta P = -0.4\%$.

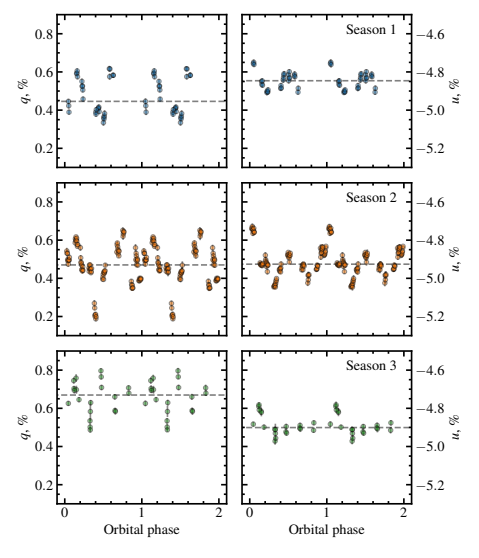


Fig. 10. Orbital variations in the observed normalized Stokes parameters q (left) and u (right) of Cyg X-1 in the B band for different seasons (seasons 1, 2, and 3 from top to bottom). The horizontal dashed lines show the weighted average values of the corresponding parameters.

bital profile of the V-band polarization of Cyg X-1. The average values of the PD for seasons S1 – S3 (empty red circles), folded with the superorbital period ($P_{\text{sup}}=294\,\text{d}$, JD $_0=2\,440\,000$), are consistent with the same part of the superorbital profile as observed in PMO data.

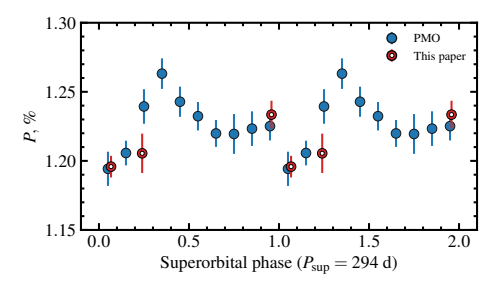


Fig. 11. Intrinsic PD of Cyg X-1 in the V band for PMO (blue circles) and S1–S3 (empty red circles) data, folded with the superorbital period. The red points are shifted by a constant $\Delta P = -0.4\%$ in the vertical direction to take secular changes in the PD into account.

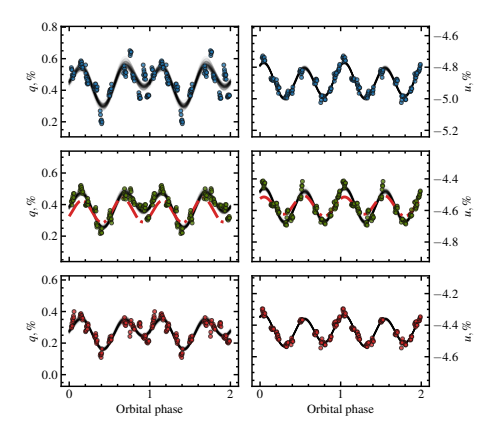


Fig. 12. Variability in the observed Stokes parameters of Cyg X-1, obtained during season 2 in B, V, and R bands (top, middle, and bottom panels, respectively). Each circle corresponds to the average value, calculated within a 30-min bin. The 1σ errors are smaller than the symbol size. The solid black lines correspond to the best fit with the Fourier series given by Eq. (2). The dashed red lines in the middle panels show the best fit of PMO historical V-band data with the same model, shifted vertically to overlap our data.

4. Modeling

To explain the behavior of the polarization at different timescales, we considered several possibilities for the geometry of scattering matter. We started with the generic model for polarization production in binary systems, in which polarization arises from the Thomson scattering of the companion star radiation by a cloud of an optically thin matter near the compact object (Brown et al. 1978). The key assumption of the model is the corotation of the scattering material with the secondary, in our case, with the compact object. The PD in this case peaks at orbital phases at which the scattering angle is 90°. For a circular orbit, the Stokes parameters of the linear polarization vary as a sine-like wave at twice the orbital frequency. In the case of eccentric orbit and/or asymmetry of the distribution of the light-scattering material about the orbital plane, the profiles become skewed and can be described by adding the first harmonic of the

orbital period. Alternatively, the appearance of the first harmonic can be related to the presence of an optically thick scattering material. Below, we study the harmonic content of the polarization profiles and consider different possibilities for the geometry of the scattering matter.

4.1. Fourier method

The polarization profiles corresponding to the case of the optically thin corotating scatterer in a circular orbit can be decomposed into Fourier series of the orbital longitude $\lambda=2\pi\phi$ (where ϕ is the orbital phase),

$$q_{\text{int}} = q_0 + q_1 \cos \lambda + q_2 \sin \lambda + q_3 \cos 2\lambda + q_4 \sin 2\lambda,$$

$$u_{\text{int}} = u_0 + u_1 \cos \lambda + u_2 \sin \lambda + u_3 \cos 2\lambda + u_4 \sin 2\lambda.$$
(2)

We employed Bayesian inference implemented as the Markov chain Monte Carlo (MCMC; Goodman & Weare 2010) ensemble sampler in the *emcee* package (Foreman-Mackey et al. 2013) in PYTHON to fit the orbital profiles of the Stokes parameters observed during season S2 with Eq. (2). The best-fit curves are shown in Fig. 12. Following the approach described in Drissen et al. (1986) and Kravtsov et al. (2020), we used the obtained Fourier coefficients to derive the inclination *i* of the binary.

$$\left(\frac{1-\cos i}{1+\cos i}\right)^4 = \frac{(u_3+q_4)^2 + (u_4-q_3)^2}{(u_4+q_3)^2 + (u_3-q_4)^2},$$
(3)

and the position angle Ω of the orbital axis on the sky,

$$\tan 2\Omega = \frac{A+B}{C+D},\tag{4}$$

wher

$$A = \frac{u_4 - q_3}{(1 - \cos i)^2}, \quad B = \frac{u_4 + q_3}{(1 + \cos i)^2},$$

$$C = \frac{q_4 - u_3}{(1 + \cos i)^2}, \quad D = \frac{u_3 + q_4}{(1 - \cos i)^2}.$$
(5)

By fitting the orbital polarization profiles obtained in S2 with Eq. (2), we obtained formal values of the inclination $i = 125^{\circ} \pm 5^{\circ}$ $(i > 90^{\circ})$ indicates the clockwise apparent motion of the compact object on the sky) and the position angle $\Omega = 129^{\circ} \pm 5^{\circ}$ of the orbital axis on the sky. However, the formal errors on the estimated orbital parameters obtained from the error propagation are underestimated and hence do not correspond to their actual confidence intervals, which are determined primarily by the internal properties of the model (2) and the amplitude of the stochastic variability in the data. The inclination estimates corresponding to the best-fit Fourier coefficients are always biased toward higher values (Aspin et al. 1981; Simmons et al. 1982; Wolinski & Dolan 1994). The confidence intervals on the orbital parameters for different signal-to-noise ratios can be obtained using Fig. 4 of Wolinski & Dolan (1994): 1σ and 2σ confidence intervals were calculated for four levels of data quality given by $\gamma = 0.5N(A/\sigma_p)^2$, where σ_p is the standard deviation of noise in the data, A is the amplitude of the polarimetric variability, and N is the number of observations. Our value of $\gamma_{\rm obs} = 0.5 \times 100 \times (6.7)^2 \approx 2200$ lies between their grid points $(\gamma = 120\,000)$ and $\gamma = 300)$. To calculate the confidence intervals on the inclination that we obtained for our S2 data, we therefore performed our own Monte Carlo simulations following the procedure described in Wolinski & Dolan (1994): We modeled the Stokes parameters for different values of i ranging from 90° to

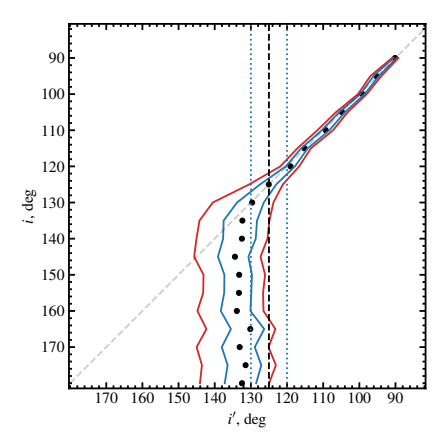


Fig. 13. Estimated 1σ and 2σ confidence intervals on the true inclination i for given estimate i' (solid blue and red lines). The vertical dashed black line corresponds to the best-fit inclination of Cyg X-1. The vertical dotted blue lines correspond to the 1σ error on the best-fit inclination

180° using the standard Brown et al. (1978) model (Eq. (6) in that paper). Then, we simulated the Gaussian noise in q and u by adding the fluctuations of the variance $\sigma_p^2 = 0.5NA^2/\gamma_{obs}$. The Fourier model (Eq. (2)) was then fit to the simulated data using the MCMC approach, and the inclination i' was calculated using Eq. (3). In Fig. 13 we show the inclination estimates i' (black points) with the 1σ and 2σ confidence intervals (solid blue and red lines) as a function of the true input inclination i.

The inclination $i \approx 125^{\circ}$ that we derived from the best-Fourier coefficients of Cyg X-1 in V and R bands (shown as the dashed vertical black line in Fig. 13) is close to the so-called critical angle $i'_{\rm crit}$. Above this angle, the 1σ confidence interval on the orbital inclination extends to $i = 180^{\circ}$ (Wolinski & Dolan 1994). This means that using high-precision polarimetry, we can only place a lower limit of $180^{\circ} > i > 120^{\circ}$ on the inclination value of the Cyg X-1 orbit. We note that previous polarimetrically derived inclination values (Kemp et al. 1978; Dolan & Tapia 1989; Nagae et al. 2009) are most likely overestimated because they were obtained by modeling the data with larger error bars, for which the critical angle is expected to be smaller than $i'_{\rm crit} \sim 130^\circ$. Our lower limit on the inclination $i > 120^{\circ}$ and the clockwise direction of the orbital motion on the sky are consistent with the value $i = 153^{\circ} \pm 1^{\circ}$ from Miller-Jones et al. (2021).

In contrast to the inclination, the value Ω obtained from Eq. (4) is an unbiased estimate of the true position angle of the projection of the orbital axis on the sky. We used the same MCMC approach as for the inclination to calculate the confidence interval on this angle. Our value $\Omega=129^{\circ}\pm10^{\circ}$ (or $\Omega=129^{\circ}-180^{\circ}=-51^{\circ}\pm10^{\circ}$ because of the $\pm180^{\circ}$ ambiguity) is consistent within 3σ with those that were determined by the direction of the intrinsic polarization $\theta_{\rm int}\approx-25^{\circ}$ and the position angle of the jet on the sky $\Omega_{\rm jet}\approx-26^{\circ}$ (Miller-Jones et al. 2021).

We emphasize that this low accuracy is not a result of the polarization measurement errors (which are smaller than 0.01% for the whole set of our data). Figure 12 shows a remarkable

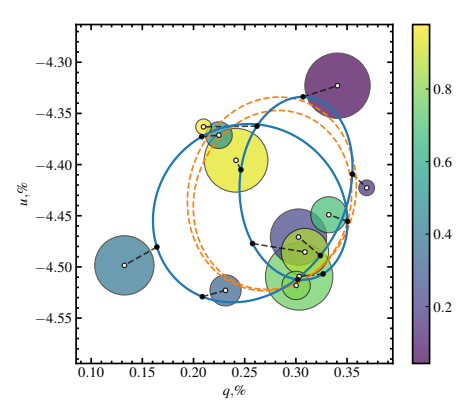


Fig. 14. Average Stokes parameters of Cyg X-1 obtained during season 2 in the R band. The color coding and size of the circle correspond to the orbital phase and 1σ uncertainty, respectively. The solid blue curve corresponds to the best fit with the Fourier series given by Eq. (2). The dashed orange line corresponds to the to the best-fit model of a scattering cloud on an eccentric orbit from the appendix of Kravtsov et al. (2020).

intrinsic scatter of the S2 data points around the fit curves that is especially noticeable for the Stokes q parameter. This aperiodic noise is explained by an additional suborbital variability component that appears on timescales shorter than one orbital cycle. Thus, the key assumption on corotation of the light-scattering material over (at least) a few consecutive orbital cycles does not hold for the Cyg X-1 binary system. Therefore, the traditional Fourier fit up to second harmonics made on polarization data cannot provide meaningful estimates of the orbital inclination, regardless of data quality, quantity, and sampling frequency.

4.2. Eccentric model

While for a circular orbit, theory predicts a smooth change in polarization with the dominant second harmonic of the orbital period, the eccentricity of the orbit shifts all the changes in the polarization toward the periastron. The polarization depends on the scattering angle, which changes according to the orbital motion of the scattering cloud. In the case of an eccentric orbit, this angle changes with different rates in different parts of the orbit, resulting in unequal distances between consecutive maxima/minima of the orbital Stokes parameters curves (this effect was observed for the binary with $e \approx 0.4$ in Berdyugin & Tarasov 1998). Therefore, the orbital curves of Stokes parameters can be used for an independent estimation of the orbital eccentricity. We adopted the Thomson scattering model from the appendix of Kravtsov et al. (2020) to describe the orbital changes in the polarization of Cyg X-1. By fitting this model to the V-band season 2 data, we were able to place 3σ upper limit on the eccentricity of Cyg X-1 orbit. The eccecntricity is e < 0.08.

Figure 14 shows the (q, u) plane of the average Stokes parameters of Cyg X-1 obtained during season 2, together with the best-fits with the Fourier series (Eq. (2)) and the model of the Thomson scattering by a cloud on an eccentric orbit (Kraytsov et al. 2020). The latter model (which is a special case

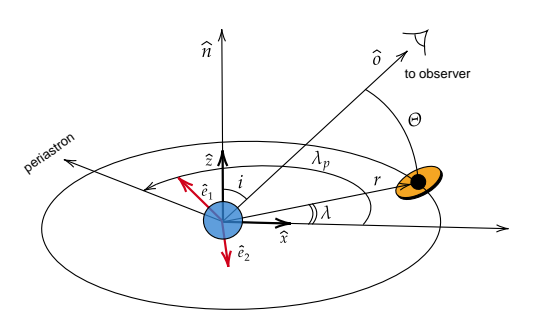


Fig. 15. Geometry of the system. Optical emission of the companion star (blue circle at the origin) is scattered by the tilted accretion disk (orange) and the optically thin material (indicated by the black circle in the center of the disk).

of the general BME model for symmetrically distributed matter in the orbital plane) cannot reproduce the pretzel-like shape of the trace left by orbital variations of Cyg X-1 on the (q, u)plane: The additional source of asymmetry is needed. To explain a similar pattern, Kemp et al. (1978) proposed a model in which the scattering region is eclipsed by the secondary body for half the orbit. This model requires a high $(90^{\circ} > i > 130^{\circ})$ orbital inclination, which contradicts the latest results (including this

4.3. Polarization by Thomson scattering off a precessing accretion disk

In this section, we present a model of polarization from Thomson scattering by a tilted precessing accretion disk, which can naturally explain the asymmetric pattern of the polarization variability observed in Cyg X-1 without requiring a highly inclined or eccentric orbit. We considered the following geometry: The orbit with an eccentricity e is inclined by an angle ito the line of sight \hat{o} (Fig. 15). The accretion disk, surrounded by a cloud of electrons, rotates around the optical companion together with the compact object. The disk axis \hat{n}_d is inclined by an angle β to the orbital axis \hat{n} (see Fig. 16). The axis of the disk can precess about the orbital axis with the period $T_{\rm sup}$

To describe the orbital motion, we introduced the coordinate system $(\hat{x}, \hat{y}, \hat{z})$, in which the \hat{z} -axis is directed along the orbital axis \hat{n} , the vector \hat{x} lies in the orbital plane and its projection on the sky is directed to the south, and the vector $\hat{\boldsymbol{y}}$ forms the righthanded basis. In this basis, $\hat{\boldsymbol{o}} = (\sin i, 0, \cos i), \hat{\boldsymbol{n}} = (0, 0, 1),$ and $\hat{\mathbf{n}}_{d} = (\sin \beta \cos \gamma, \sin \beta \sin \gamma, \cos \beta)$. The angle γ is the azimuth of the projection of the disk axis onto the orbital plane measured from \hat{x} to \hat{y} . To describe the polarization, we used the polarization basis (\hat{e}_1, \hat{e}_2) , in which the vector $\hat{e}_1 = (-\cos i, 0, \sin i)$ lies along the projection of the vector \hat{n} on the plane of the sky, and $\hat{e}_2 = (0, -1, 0)$ is perpendicular to \hat{e}_1 and lies in the plane of the

The distance between the compact object and the optical companion varies with the orbital longitude λ , measured from \hat{x} to \hat{y} . It can be expressed as

$$r(\lambda) = \frac{a(1 - e^2)}{1 + e\cos(\lambda - \lambda_p)},\tag{6}$$

where a is the semimajor axis of the orbit, and λ_p is the longitude of the periastron. The unit vector pointing toward the compact

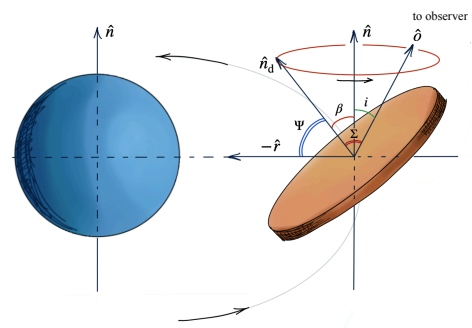


Fig. 16. Geometry of the precessing disk. The disk axis $\hat{n_d}$ is inclined by the angle β with respect to the orbital axis \hat{n} and rotates around it.

object is

$$\hat{\mathbf{r}} = (\cos \lambda, \sin \lambda, 0),\tag{7}$$

and the scattering angle Θ is given by

$$\mu = \cos \Theta = \hat{\mathbf{r}} \cdot \hat{\mathbf{o}} = \sin i \cos \lambda. \tag{8}$$

The observed flux $F_{\text{tot}} = F_* + F_{\text{sc}}$ is the sum of the flux produced by the optical companion F_* and the scattered flux F_{sc} . We assumed that the latter is produced by Thomson scattering (in an optically thin regime) of stellar radiation by the accretion disk and the surrounding cloud of electrons. In this case, the angular distribution of scattered luminosity can be represented as

$$L_{\rm sc}(\mu) = L_* f_{\rm sc} l(\mu) = \frac{3}{8} (1 + \mu^2) L_* (f_{\rm sc}^{\rm cloud} + f_{\rm sc}^{\rm disk}), \tag{9}$$

where $l(\mu)=3(1+\mu^2)/8$ is the Thomson scattering indicatrix, and $f_{\rm sc}^{\rm cloud}$ and $f_{\rm sc}^{\rm disk}$ are fractions of radiation scattered by the cloud and the disk, respectively. In both cases, this fraction is proportional to the total number of free electrons N_e in a cloud/disk and drops with the distance as $1/r^2(\lambda)$,

$$f_{sc}^{cloud} = \frac{N_e^{cloud} \sigma_T}{4\pi r^2(\lambda)},$$

$$f_{sc}^{disk} = \frac{N_e^{disk} \sigma_T}{4\pi r^2(\lambda)} \cos \Psi,$$
(10)

$$f_{\rm sc}^{\rm disk} = \frac{N_{\rm e}^{\rm disk} \sigma_{\rm T}}{4\pi r^2(1)} \cos \Psi, \tag{11}$$

where $\cos \Psi = -\hat{\mathbf{n}}_d \cdot \hat{\mathbf{r}} = -\sin\beta\cos\gamma\cos\lambda - \sin\beta\sin\gamma\sin\lambda =$ $-\sin\beta\cos(\gamma-\lambda)$. The $\cos\Psi$ term is proportional to the effective area of the disk intercepting the stellar radiation, which depends on the position of the disk in the orbit λ and the orientation of its axis $\hat{\mathbf{n}}_d$, defined by two angles: the inclination β of the disk, and its azimuth γ . The latter angle can change with time due to precession as $\gamma=\pm 2\pi\varphi_{sup}+\gamma_0$, where φ_{sup} is the precession phase, and γ_0 is the angle γ at zero phase. The sign determines

We scaled $f_{\rm sc}^{\rm cloud}$ and $f_{\rm sc}^{\rm disk}$ to the typical values $f_0^{\rm cloud}$ and $f_0^{\rm disk}$

$$f_{\rm sc}^{\rm cloud} = f_0^{\rm cloud} \left[\frac{a(1 - e^2)}{r(\lambda)} \right]^2 = f_0^{\rm cloud} \left[1 + e \cos(\lambda - \lambda_p) \right]^2, \tag{12}$$

$$f_{\rm sc}^{\rm disk} = f_0^{\rm disk} \left[\frac{a(1-e^2)}{r(\lambda)} \right]^2 \cos \Psi = f_0^{\rm disk} \left[1 + e \cos(\lambda - \lambda_{\rm p}) \right]^2 \cos \Psi. \tag{13}$$

The PD of scattered radiation in Thomson regime can be expressed in terms of the scattering angle Θ as

$$P_{\rm sc} = \frac{1 - \mu^2}{1 + \mu^2} = \frac{\sin^2 \Theta}{1 + \cos^2 \Theta}.$$
 (14)

The observer measures the PD $P = F_{sc}P_{sc}/F_{tot}$ of the total flux F_{tot} , most of which is unpolarized and produced by the optical companion star. The polarized flux of the scattered radiation is

$$F_{sc}P_{sc} = F_* f_{sc} l(\mu) \frac{1-\mu^2}{1+\mu^2} = F_* f_{sc} \frac{3}{8} (1-\mu^2).$$
 (15)

$$P = \frac{F_{sc}P_{sc}}{F_{tot}} \approx \frac{3}{8} \left[f_{sc}^{cloud} + f_{sc}^{disk} \right] (1 - \mu^2), \tag{16}$$

where we assumed that $F_{\rm sc} \ll F_*$ and substituted $f_{\rm sc} = f_{\rm sc}^{\rm cloud} + f_{\rm sc}^{\rm disk}$.

The normalized Stokes parameters of linear polarization are

defined as $q = P\cos(2\chi)$ and $u = P\sin(2\chi)$, where χ is the position angle of the polarization pseudo-vector \hat{p} in the polarization

$$\hat{\mathbf{p}} = \frac{\hat{\mathbf{o}} \times \hat{\mathbf{r}}}{|\hat{\mathbf{o}} \times \hat{\mathbf{r}}|} = \frac{1}{\sin \Theta} \left(-\cos i \sin \lambda, \cos i \cos \lambda, \sin i \sin \lambda \right), \quad (17)$$

where $\sin\Theta = \sqrt{1-\mu^2} = \sqrt{1-\sin^2 i \cos^2 \lambda}$. Thus, the expressions for the Stokes parameters can be written as

$$q = \frac{3}{8} \left[f_{sc}^{cloud} + f_{sc}^{disk} \right] (1 - \mu^2) \cos(2\chi),$$

$$u = \frac{3}{8} \left[f_{sc}^{cloud} + f_{sc}^{disk} \right] (1 - \mu^2) \sin(2\chi),$$
(18)

where the polarization angle χ is defined by the expressions

$$\cos \chi = \hat{\boldsymbol{e}}_1 \cdot \hat{\boldsymbol{p}} = \frac{\sin \lambda}{\sin \Theta}, \tag{19}$$

$$\sin \chi = \hat{\boldsymbol{e}}_2 \cdot \hat{\boldsymbol{p}} = -\frac{\cos i \cos \lambda}{\sin \Theta}. \tag{20}$$

$$\sin \chi = \hat{\boldsymbol{e}}_2 \cdot \hat{\boldsymbol{p}} = -\frac{\cos i \cos \lambda}{\sin \lambda}. \tag{20}$$

The explicit expressions for $cos(2\chi)$ and $sin(2\chi)$ are

$$\cos(2\chi) = \frac{\sin^2 i - (1 + \cos^2 i)\cos(2\lambda)}{2\sin^2 \Theta},$$

$$\sin(2\chi) = -\frac{\cos i\sin(2\lambda)}{\sin^2 \Theta}.$$
(21)

$$\sin(2\chi) = -\frac{\cos i \sin(2\lambda)}{\sin^2 \Theta}.$$
 (22)

Combining Eqs. (18) with (21) and (22), we obtain

$$q = \frac{3}{16} \left[\sin^2 i - \left(1 + \cos^2 i \right) \cos 2\lambda \right] \left[f_{\text{sc}}^{\text{cloud}} + f_{\text{sc}}^{\text{disk}} \right],$$

$$u = -\frac{3}{8} \cos i \sin 2\lambda \left[f_{\text{sc}}^{\text{cloud}} + f_{\text{sc}}^{\text{disk}} \right].$$
(23)

The $f_{\rm sc}^{\rm disk}$ term depends on $\cos\Psi$, reflecting the difference in the amount of scattered radiation for different orientations of the disk axis \hat{n}_d relative to the source of the light. In our model, the disk is not transparent: it has two sides (top and bottom), only one of which is illuminated at any given time. The top of the disk is illuminated when $\cos \Psi > 0$, the bottom of the disk is bright when $\cos \Psi < 0$. The top of the disk is visible for the observer when $\cos \Sigma = \hat{\mathbf{n}}_d \cdot \hat{\mathbf{o}} > 0$, and the bottom of the disk is visible when $\cos \Sigma < 0$. Therefore, the disk is illuminated and visible only when the product $\cos \Psi \cos \Sigma$ is positive, or $f_{sc}^{disk} = 0$ when $\cos \Psi \cos \Sigma \leq 0$.

To compare the calculations with the observed Stokes parameters (q_{obs}, u_{obs}) , the orientation of the orbit on the sky must be taken into account: The projection of the orbital axis on the sky makes an angle Ω with direction to the north (we note that Ω defined in this way differs by $\pi/2$ from the longitude of the ascending node that is commonly used instead). The observed Stokes parameters $(q_{\rm obs}, u_{\rm obs})$ can be obtained by rotating the vector (q, u) by an angle 2Ω ,

$$q_{\rm obs} = q\cos(2\Omega) - u\sin(2\Omega), \tag{24}$$

$$u_{\text{obs}} = q \sin(2\Omega) + u \cos(2\Omega). \tag{25}$$

The modeled Stokes parameters are functions of the orbital longitude λ and need to be computed as functions of the orbital phase ϕ . While for the circular (or nearly circular) orbit, λ can be calculated as $\lambda = 2\pi(\phi + \phi_p) + \lambda_p$, where ϕ_p is the phase of the periastron, for the eccentric orbit, we need to solve Kepler's equation: From the true anomaly of the orbit $\lambda - \lambda_p$, we can find the eccentric anomaly E,

$$\tan\left(\frac{E}{2}\right) = \sqrt{\frac{1-e}{1+e}} \tan\left(\frac{\lambda - \lambda_{p}}{2}\right),\tag{26}$$

and then the mean anomaly M.

$$M = E - e \sin E, (27)$$

which can be converted into the orbital phase as

$$\phi_{\text{orb}} = M/(2\pi) + \phi_{\text{p}}. \tag{28}$$

Thus, the free parameters of the model are the inclination i, the eccentricity e, the longitude of periastron λ_p , the position angle of the projection of the orbit axis on the sky Ω , the phase of periastron ϕ_p , the inclination of the disk β and its initial position angle γ_0 in the orbital plane, the period of precession T_{sup} (which can be set to be infinite for the nonprecessing case), and the scattering fractions f_0^{disk} and f_0^{cloud} . In order to fit the data, there is a need for additional constant Stokes parameters q_0 and u_0 , which describe the average polarization.

We fit the described model to S2 data by adopting the orbital parameters of Cyg X-1: eccentricity e = 0.02, inclination i =153° (Miller-Jones et al. 2021), and inclination of the disk β = 20° (Ibragimov et al. 2007). The position angle of the orbital axis was set to be $\Omega = -26^{\circ}$ to match the position angle of the jet. The contributions from the disk and the cloud were assumed to be $f_0^{\text{disk}} = 0.75$ and $f_0^{\text{cloud}} = 0.25$. Because the S2 data cover only one full orbital cycle, the precession period T_{sup} was set to be much longer than the orbital period so that possible precession of the disk was not taken into account.

The solid blue and dashed red lines in Figs. 17 and 18 show the fits of the model described above to S2 data with and without scattering off the tilted accretion disk, respectively. Although the reduced χ^2 of the fits does not differ dramatically $(\chi^2 [\text{disk} + \text{cloud}] = 1.01 \text{ versus } \chi^2 [\text{cloud}] = 1.23)$, the asymmetric pretzel-like trace of the polarization on the (q, u)-plane cannot be reproduced by the scattering cloud alone. Additionally, the model with the tilted accretion disk predicts the changes in the shape of the orbital polarization profiles with the precession phase: If the superorbital variability observed from the radio to the X-rays is related to the disk precession, the pretzel will make a complete turn around its center once per superorbital period T_{sup} . To detect this effect, a significant part of the superorbital period must be covered with continuous high-precision optical polarimetric observations.

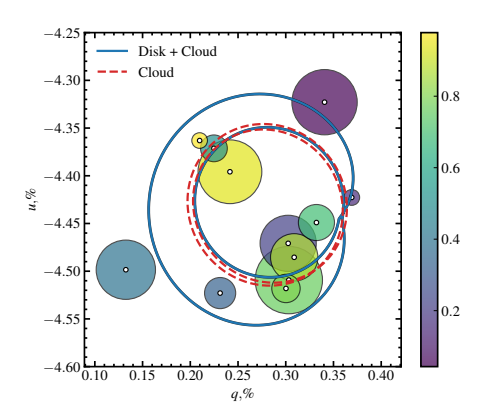


Fig. 17. Same as Fig. 14, but showing the model curves at the (q, u)-plane calculated with (solid blue line) and without (dashed red line) scattering by the accretion disk.

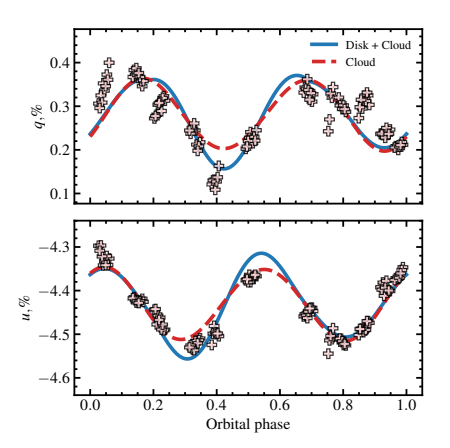


Fig. 18. Stokes parameters of Cyg X-1, obtained during season 2 (light crosses) together with the best-fit models with (solid blue line) and without (dashed red line) scattering by the tilted accretion disk.

5. Summary

We presented new high-precision polarimetric observations of the BH X-ray binary Cyg X-1. Combining them with the 12-year-long PMO observations performed in 1975–1987, we were able to study the polarization behavior at the timescales ranging from hours to decades. The interstellar polarization, which dominates the observed optical polarization $P_{\rm obs} \sim 4.5\%$, was accurately measured and subtracted from the data, allowing us to determine the intrinsic polarization of Cyg X-1 as $P_{\rm int} = 0.82\% \pm 0.15\%$ with a PA $\theta_{\rm int} = 155^{\circ} \pm 5^{\circ}$. The alignment of the X-ray and optical PA, as well as the stability of this angle during the secular PD change, indirectly support our estimate of intrinsic polarization of Cyg X-1. Around-the-clock monitoring of the polarization with two telescopes located in different hemispheres allowed us to track the evolution of the

polarization within one orbital cycle with a temporal resolution that is unrivalled so far. The intrinsic polarization of Cyg X-1 shows the orbital variations with two pronounced peaks in the quadratures and two minima in conjugations, most probably produced by Thomson scattering of the companion star radiation by matter that is gravitationally bound to the black hole. The amplitudes of the two consecutive polarization minima measured within one orbital cycle differ significantly, which implies asymmetry of the scattering matter in the orbital plane. We suggest that a tilted accretion disk could be the source of this asymmetry. We find that a misalignment of $\beta \gtrsim 15^{\circ}$ can reproduce the orbital polarization variations. This is in line with the recent finding of a significant misalignment between the orbital and jet axes (Zdziarski et al. 2023). Our modeling of orbital variations in the Stokes parameters allowed us to constrain the eccentricity < 0.08 and inclination of the orbit $i > 120^{\circ}$.

In addition to the orbital variations, we found a significant change ($\Delta P_{\rm int} \approx -0.4\%$) in the average intrinsic PD of Cyg X-1 on a timescales of several decades while preserving the constant intrinsic PA. The decrease in the PD indicates the change in the fraction of scattered radiation, which in turn depends on the amount of scattering material and its effective scattering cross section. This may reflect secular changes in the size/shape of the accretion disk and/or changes in its spatial orientation. We note that the asymmetry of the (q,u)-plane trace of the polarization can be purely artificial. It may result from a complex superposition of periodic and nonperiodic variations and the orbital phase sampling. A long-term high-precision monitoring program with good orbital and superorbital coverage is needed to exclude this.

Analyzing high-precision TESS photometric data, we found stochastic variations of the flux on timescales shorter than the orbital period. Together with the stochastic variability found in the optical polarization, this suggests that one or several additional components are at play: pulsations of the optical companion, spots on its surface, wind clumpiness, eclipses of the bright part of the accretion disk by the infalling matter, and precession of the accretion disk.

Acknowledgements. This paper is based on observations made with the Nordic Optical Telescope, owned in collaboration by the University of Turku and Aarhus University, and operated jointly by Aarhus University, the University of Turku, and the University of Color, representing Denmark, Finland, and Norway, the University of Iceland and Stockholm University at the Observatorio del Roque de los Muchachos, La Palma, Spain, of the Instituto de Astrofisica de Canarias. The DIPol-2 and DIPol-UF polarimeters were built in cooperation between the University of Turku, Finland, and the Leibniz-Institut für Sonnenphysik, Germany. We are grateful to the Institute for Astronomy, University of Hawaii, for the allocated observing time. VK acknowledges support from the Vilho, Yrjö and Kalle Väisälä Foundation and Suomen Kulttuurirahasto. AAZ has been supported by the Polish National Science Center under the grant 2019/35/B/ST9/03944.

References

Aspin, C., Simmons, J. F. L., & Brown, J. C. 1981, MNRAS, 194, 283
Berdyugin, A. V., & Harries, T. J. 1999, A&A, 352, 177
Berdyugin, A. V., & Tarsov, A. E. 1998, Astron. Lett., 24, 111
Bowyer, S., Byram, E. T., Chubb, T. A., & Friedman, H. 1965, Science, 147, 394
Brocksopp, C., Tarasov, A. E., Lyuty, V. M., & Roche, P. 1999a, A&A, 343, 861
Brocksopp, C., Fender, R. P., Larionov, V., et al. 1999b, MNRAS, 309, 1063
Brown, J. C., McLean, I. S., & Emslie, A. G. 1978, A&A, 68, 415
Dolan, J. F., & Tapia, S. 1989, PASP, 101, 1135
Drissen, L., Lamontagne, R., Moffat, A. F. J., Bastien, P., & Seguin, M. 1986,
ApJ, 304, 188

Fender, R. P., Stirling, A. M., Spencer, R. E., et al. 2006, MNRAS, 369, 603 Foreman-Mackey, D., Hogg, D. W., Lang, D., & Goodman, J. 2013, PASP, 125, 306

Gierliński, M., Zdziarski, A. A., Done, C., et al. 1997, MNRAS, 288, 958 Gierliński, M., Zdziarski, A. A., Poutanen, J., et al. 1999, MNRAS, 309, 496

```
Gies, D. R., & Bolton, C. T. 1986a, ApJ, 304, 389
Gies, D. R., & Bolton, C. T. 1986b, ApJ, 304, 371
Goodman, J., & Weare, J. 2010, Commun. Appl. Math. Comput. Sci., 5, 65
Ibragimov, A., Zdziarski, A. A., & Poutanen, J. 2007, MNRAS, 381, 723
Jones, T. J., Gehrz, R. D., Kobulnicky, H. A., Molnar, L. A., & Howard, E. M.
    1994. AJ, 108, 605
Karitskaya, E. A. 1981, Soviet Astron., 25, 80
Karitskaya, E. A., Voloshina, I. B., Goranskii, V. P., et al. 2001, Astron. Rep., 45,
Kemp, J. C., & Barbour, M. S. 1981, PASP, 93, 521
Kemp, J. C., & Barbour, M. S., Herman, L. C., & Rudy, R. J. 1978, ApJ, 220, L123
Kemp, J. C., Barbour, M. S., Parker, T. E., & Herman, L. C. 1979, ApJ, 228,
Kemp, J. C., Barbour, M. S., Henson, G. D., et al. 1983, ApJ, 271, L65
Kosenkov, I. A., Berdyugin, A. V., Piirola, V., et al. 2017, MNRAS, 468, 4362
Kosenkov, I. A., Veledina, A., Berdyugin, A. V., et al. 2020, MNRAS, 496, L96
Kravtsov, V., Berdyugin, A. V., Piirola, V., et al. 2020, A&A, 643, A170
Kravtsov, V., Berdyugin, A. V., Kosenkov, I. A., et al. 2022, MNRAS, 514, 2479
Krawczynski, H., Muleri, F., Dovčiak, M., et al. 2022, Science, 378, 650 Milgrom, M. 1978, A&A, 65, L1
Miller-Jones, J. C. A., Bahramian, A., Orosz, J. A., et al. 2021, Science, 371,
Nagae, O., Kawabata, K. S., Fukazawa, Y., et al. 2009, AJ, 137, 3509
Nolt, I. G., Kemp, J. C., Rudy, R. J., et al. 1975, ApJ, 199, L27
Orosz, J. A., McClintock, J. E., Aufdenberg, J. P., et al. 2011, ApJ, 742, 84
Piirola, V. 1973, A&A, 27, 383
```

```
Piirola, V. 1980, A&A, 90, 48
Piirola, V. 1988, in Polarized Radiation of Circumstellar Origin, eds. G. V. Coyne, A. M. Magalhaes, A. F. Moffat, R. E. Schulte-Ladbeck, & S. Tapia (Vatican City State/Tucson, AZ: Vatican Observatory/University of Arizona Press), 735
Piirola, V., Berdyugin, A., & Berdyugina, S. 2014, in Ground-based and Airborne Instrumentation for Astronomy V. Proc. SPIE, 9147, 914781
Piirola, V., Berdyugin, A., Frisch, P. C., et al. 2020, A&A, 635, A46
Piirola, V., Kosenkov, I. A., Berdyugin, A. V., Berdyugina, S. V., & Poutanen, J. 2021, AJ, 161, 20
Poutanen, J., & Veledina, A., Berdyugin, A. V., Berdyugina, S. V., & Poutanen, J., Zdziarski, A. A., & Ibragimov, A. 2008, MNRAS, 389, 1427
Poutanen, J., Vededina, A., Berdyugin, A. V., et al. 2022, Science, 375, 874
Priedhorsky, W. C., Terrell, J., & Holt, S. S. 1983, ApJ, 270, 233
Ricker, G. R., Winn, J. N., Vanderspek, R., et al. 2014, Proc. SPIE, 9143, 914320
Serkowski, K. 1962, Adv. Astron. Astrophys., 1, 289
Simmons, J. F. L., Aspin, C., & Brown, J. C. 1982, MNRAS, 198, 45
Stirling, A. M., Spencer, R. E., de la Force, C. J., et al. 2001, MNRAS, 327, 1273
Uttley, P., & Casella, P. 2014, Space Sci. Rev., 183, 453
Veledina, A., Berdyugin, A. V., Kosenkov, I. A., et al. 2019, A&A, 623, A75
Weisskopf, M. C., Soffitta, P., Baldini, L., et al. 2022, JATIS, 8, 026002
Wolinski, K. G., & Dolan, J. F. 1994, MNRAS, 267, 5
Zdziarski, A. A., & Gierliński, M. 2004, Prog. Theor. Phys. Suppl., 155, 99
Zdziarski, A. A., Pooley, G. G., & Skinner, G. K. 2011, MNRAS, 412, 1985
```

Zdziarski, A. A., Veledina, A., Szanecki, M., et al. 2023, ApJ, 951, L45

Krawczynski H., Muleri F., Dovčiak M., Veledina A., Rodriguez Cavero N., Svoboda J., Ingram A., Matt G., Garcia J.A., Loktev V., Negro M., Poutanen J., Kitaguchi T., Podgorný J., Rankin J., Zhang W., Berdyugin A.V., Berdyugina S.V., Bianchi S., Blinov D., Capitanio F., Di Lalla N., Draghis P., Fabiani S., Kagitani M., Kravtsov V., et al. Polarized X-rays constrain the disk-jet geometry in the black hole X-ray binary Cygnus X-1

Science, 2022; 378: 650

BLACK HOLES

Polarized x-rays constrain the disk-jet geometry in the black hole x-ray binary Cygnus X-1

Henric Krawczynski¹*, Fabio Muleri²*, Michal Dovčiak³*, Alexandra Veledina^{4,5,6}* Nicole Rodriguez Cavero¹, Jiri Svoboda³, Adam Ingram⁷, Giorgio Matt⁸, Javier A. Garcia⁹, Vladislav Loktev⁴, Michela Negro^{10,11,12}, Juri Poutanen^{4,6}, Takao Kitaguchi¹³, Jakub Podgorný^{3,14,15}, John Rankin², Wenda Zhang¹⁶, Andrei Berdyugin⁴, Svetlana V. Berdyugina^{17,18,19}, Stefano Bianchi⁸, Dmitry Blinov^{20,21}, Fiamma Capitanio², Niccolò Di Lalla²², Paul Draghis²³, Sergio Fabiani², Masato Kagitani²⁴, Vadim Kravtsov⁴, Sebastian Kiehlmann^{20,21}, Luca Latronico²⁵, Alexander A. Lutovinov⁶, Nikos Mandarakas^{20,21}, Frédéric Marin¹⁴, Andrea Marinucci²⁶, Jon M. Miller²³, Tsunefumi Mizuno²⁷, Sergey V. Molkov⁶, Nicola Omodei²², Pierre-Olivier Petrucci²⁸, Ajay Ratheesh², Takeshi Sakanoi²⁴, Andrei N. Semena⁶, Raphael Skalidis^{20,21}, Paolo Soffitta², Allyn F. Tennant²⁹, Phillipp Thalhammer³⁰, Francesco Tombesi^{31,32,33}, Martin C. Weisskopf²⁹, Joern Wilms³⁰, Sixuan Zhang²⁷, Iván Agudo³⁴, Lucio A. Antonelli^{35,36}, Matteo Bachetti³ Luca Baldini^{38,39}, Wayne H. Baumgartner²⁹, Ronaldo Bellazzini³⁸, Stephen D. Bongiorno²⁹ Raffaella Bonino^{25,40}, Alessandro Brez³⁸, Niccolò Bucciantini^{41,42,43}, Simone Castellano³⁸ Elisabetta Cavazzuti²⁶, Stefano Ciprini^{32,36}, Enrico Costa², Alessandra De Rosa², Ettore Del Monte², Laura Di Gesu²⁶, Alessandro Di Marco², Immacolata Donnarumma²⁶, Victor Doroshenko⁴⁴, Steven R. Ehlert²⁹, Teruaki Enoto¹³, Yuri Evangelista⁷, Riccardo Ferrazzoli², Shuichi Gunji⁴⁵, Kiyoshi Hayashida⁴⁶†, Jeremy Heyl⁴⁷, Wataru lwakiri⁴⁸, Svetlana G. Jorstad^{49,50}, Vladimir Karas³, Jeffery J. Kolodziejczak²⁹, Fabio La Monaca², Ioannis Liodakis⁵¹, Simone Maldera²⁵ Alberto Manfreda³³, Alan P. Marscher⁴⁹, Herman L. Marshali⁵², Ikuyuki Mitsuishi⁵³, Chi-Yung Ng⁵⁴, Stephen L. O'Dell²⁹, Chiara Oppedisano²⁵, Alessandro Papitto³⁵, George G. Pavlov⁵⁵, Abel L. Peirson²². Matteo Perri^{36,35}. Melissa Pesce-Rollins³⁸. Maura Pilia³⁷. Andrea Possenti³⁷ Simonetta Puccetti³⁶, Brian D. Ramsey²⁹, Roger W. Romani²², Carmelo Sgrò³⁸, Patrick Slane⁵⁶ Gloria Spandre³⁸, Toru Tamagawa¹⁵, Fabrizio Tavecchio⁵⁷, Roberto Taverna⁵⁸, Yuzuru Tawara⁵³, Nicholas E. Thomas²⁹, Alessio Trois³⁷, Sergey Tsygankov^{4,6}, Roberto Turolla^{58,59}, Jacco Vink⁶⁰, Kinwah Wu⁵⁹, Fei Xie^{2,61}, Silvia Zane⁵⁹

A black hole x-ray binary (XRB) system forms when gas is stripped from a normal star and accretes onto a black hole, which heats the gas sufficiently to emit x-rays. We report a polarimetric observation of the XRB cygnus X-1 using the Imaging X-ray Polarimetry Explorer. The electric field position angle aligns with the outflowing jet, indicating that the jet is launched from the inner x-ray-emitting region. The polarization degree is 4.01 ± 0.20% at 2 to 8 kiloelectronvolts, implying that the accretion disk is viewed closer to edge-on than the binary orbit. These observations reveal that hot x-ray-emitting plasma is spatially extended in a plane perpendicular to, not parallel to, the jet axis.

ygnus X-1 (Cyg X-1, also cataloged as HD 226868) is a bright and persistent x-ray source. It is a binary system containing a 21.2 ± 2.2 solar-mass black hole in a 5.6-day orbit with a $40.6^{+7.7}_{-7.1}$ solar-mass star and is located at a distance of $2.22_{-0.17}^{+0.18}$ kiloparsecs (kpc) (1). Gas is stripped from the companion star; as it falls in the strong gravitational field of the black hole, it forms an accretion disk that is heated to millions of kelvin. The hot incandescent gas emits x-rays. Previous analyses of the thermal x-ray flux, its energy spectrum, and the shape of the x-ray emission lines have indicated that the black hole in Cyg X-1 spins rapidly, with a dimensionless spin parameter a > 0.92 (close to the maximum possible value of 1) (2). Cyg X-1 also produces two pencil-shaped outflows of magnetized plasma, called jets, that have been imaged in the radio band (3). It is therefore classified as a microquasar, being analogous to much larger radio-loud quasars (supermassive black holes with iets).

Black hole x-ray binaries are observed in states of x-ray emission thought to correspond to different configurations of the accreting matter (4). In the soft state, the x-rays are dominated by thermal emission from the accretion disk. The thermal emission is expected to be polarized because x-rays scatter off electrons in the accretion disk (5-7). In the hard state, the x-ray emission is produced by (single or multiple) scattering of photons (emitted by the accretion disk or electrons in the magnetic field) off electrons in hot coronal gas. Observations constrain the corona to be much hotter $(k_{\rm B}T_{\rm e}\sim 100$ keV, where $k_{\rm B}$ is the Boltzmann constant and T_e is the electron temperature) than the accretion disk ($k_{\rm B}T_{\rm d}\sim 0.1$ keV, where $T_{\rm d}$ is the disk temperature). The shape of the corona and its location with respect to the accretion disk are both debated (4, 8) but could be constrained by x-ray polarimetry (9). Reflection of x-rays emitted by the corona off the accretion disk produces an emission component that includes the iron Kα fluorescence

line at \sim 6.4 keV, which can constrain the velocity of the accretion disk gas orbiting the black hole and the time dilation close to the black hole. This reflection component is also expected to be polarized (10,11).

We performed x-ray polarimetric observations of Cyg X-1 using the Imaging X-ray Polarimetry Explorer (IXPE) space telescope (12). Theoretical predictions of the Cyg X-1 polarization degree (in the 2-8 keV IXPE band) were ~1% or lower, depending on the emission state (6, 7, 9, 13). These predictions used an inclination angle (the angle between the black hole spin axis and the line of sight) of $i = 27.5 \pm 0.8$ inferred from optical observations of the binary system (1). Earlier polarization observations with the Eighth Orbiting Solar Observatory (OSO-8) space telescope gave a polarization degree of $2.44 \pm 1.07\%$ and a polarization angle (measured on the plane of the sky from north to east) of $-18^{\circ} \pm 13^{\circ}$ at 2.6 keV (14, 15) and a nondetection at higher energies (16). IXPE observed Cyg X-1 from 15 to 21 May 2022 with an exposure time of ~242 kiloseconds (ks) The IXPE 2-8 keV observations were coordinated with simultaneous x-ray and gamma-ray observations by other space telescopes covering the energy range 0.2-250 keV, including the Neutron Star Interior Composition Explorer (NICER, 0.2-12 keV), the Nuclear Spectroscopic Telescope Array (NuSTAR, 3-79 keV), the Swift X-ray Telescope (XRT, 0.2-10 keV), the Astronomical Roentgen Telescope-X-ray Concentrator (ART-XC, 4-30 keV) of the Spectrum-Röntgen-Gamma observatory (SRG), and the INTEGRAL Soft Gamma-Ray Imager (ISGRI, 30-80 keV) on the International Gamma-Ray Astrophysics Laboratory (INTEGRAL) (17). Simultaneous optical observations were performed with the Double Image Polarimeter 2 (DIPol-2) instrument mounted on the Tohoku 60-cm telescope at the Haleakala Observatory, Hawaii, and the Robotic Polarimeter (RoboPol) at the 1.3-m telescope of the Skinakas Observatory,

During the observation campaign, Cyg X-1 was highly variable over the entire 0.2-250 keV energy range (fig. S1). The source was in the hard x-ray state with a photon index of 1.6 (table S5) and a 0.2-250 keV luminosity of 1.1% of the Eddington luminosity (the luminosity at which the radiation pressure on electrons equals the gravitational pull on the ions of the accreted material). We detected linear polarization in the IXPE data with >200 statistical confidence (where σ is the standard deviation) (Fig. 1 and fig. S3), measuring a 2-8 keV polarization degree of 4.01 \pm 0.20% at an electric field position angle of -20°7 ± 1°4. The polarization degree and angle are consistent with the previous results of OSO-8 at 2.6 keV (15). Evidence for an increase in the polarization degree with energy (Fig. 1 and fig. S5) is significant at the 3.4σ level (17). We find a 2.4σ indication that the polarization degree increases with the source flux (fig. S6).

We find no evidence that the polarization depends on the orbital phase of the binary system (fig. S7). This excludes the possibility that the observed x-ray polarization originates from the scattering of x-ray photons off the companion star or its wind and shows that these effects do not measurably affect the polarization properties.

We calculated a suite of emission models and compared them with the observations (17). We estimate that >90% of the x-rays come from the inner ~2000-km-diameter region surrounding the ~60-km-diameter black hole. The x-ray polarization angle aligns with the billion-kilometer-scale radio jet to within ~5° (Fig. 2).

We decomposed the broadband energy spectra observed simultaneously with IXPE, NICER, NuSTAR, and INTEGRAL into a multi-temperature black-body component (thermal emission from the accretion disk), a power-law component (from multiple Compton scattering events in the corona), emission reflected off the accretion disk, and emission from more distant stationary plasma (fig. S8) (17). We find that the coronal emission strongly dominates in the IXPE energy band, contributing ~90% of the observed flux. The accretion disk and reflected emission components contribute <1% and ~10% of the emission, respectively. Therefore, our polarization measurements

are likely to be dominated by the coronal emission.

We analyzed the optical data at multiple wavelengths (17), finding an intrinsic optical polarization degree of ~1% and polarization angle of -24° . The uncertainties on these results are dominated by systematic effects related to the choice of polarization reference stars and are $\pm 0.1\%$ on the polarization degree and $\pm 13^\circ$ on the polarization direction (figs. S11 to S13 and table S4). The optical polarization direction is thought to indicate the orientation of the orbital axis projected onto the sky (18). We find that it aligns with the x-ray polarization direction and the radio jet.

The alignment of the x-ray polarization with the radio jet indicates that the inner x-ray-emitting region is directly related to the radio jet. If the x-ray polarization is perpendicular to the inner accretion disk plane, as favored in our models (17), this implies that the inner accretion disk is perpendicular to the radio jet, at least on the plane of the sky. This is consistent with the hypothesis that jets of microquasars (and, by extension, of quasars) are launched perpendicular to the inner accretion flow (19).

Figure 3 compares our observed polarization with theoretical predictions made using models of the corona (17). We find that the only models that are consistent with the observations are those in which the coronal plasma is extended perpendicular to the jet axis, and therefore probably parallel to the accretion disk. In these models, repeated scatterings in the plane of the corona polarize the x-rays perpendicular to that plane. Two models are consistent with our observations: (i) a hot corona sandwiching the accretion disk (20), as predicted by numerical accretion disk simulations (21); or (ii) a composite accretion flow with a truncated cold disk that is geometrically thin and optically thick and an inner laterally extended region (geometrically thick but optically thin) of hot plasma, possibly produced by evaporation of the cold disk (22). If the jet is launched from the inner, magnetized region of the disk, the jet carrying away disk angular momentum could leave behind a radially extended hot and optically thin

The polarization data rule out models in which the corona is a narrow plasma column or cone along the jet axis, or consists of two compact regions above and below the black hole. Our modeling of these scenarios accounts for the effect of the coronal emission reflecting off the accretion disk (17). These models predict polarization degree well below the observed values. Models that produce high polarization degree predict polarization directions close to perpendicular to the jet axis, a decreasing polarization degree with energy, or both, and therefore disagree with the observations.

In our favored corona models, the high polarization degree we observe requires that the x-ray bright region is seen at a higher inclination than the ~27° inclination of the binary orbit. Sandwich corona models involving the

Department of Physics and McDonnell Center for the Space Sciences, Washington University in St. Louis, St. Louis, Mo 63130, USA. ²Istituto di Astrofisica e Planetologia Spaziali, Istituto Nazionale di Astrofisica (INAF), 00133 Roma, Italy. ²Astronomical Institute of the Czech Academy of Sciences, 14100 Praha 4, Czech Republic. ⁵Department of Physics and Astronomy, 20014 University of Truku, Turku, Infland. ⁵Nordic Institute for Technology and Stockholm University, Sci. 1610 Stockholm, Sweden. ⁵Space Research Institute of the Russian Academy of Sciences, Moscow 117997, Russia. ⁵School of Mathematics, Statistics, and Physics, Newcastle University, Newcastle upon Tryne RLI 7810, U.K. ⁵Dipartimentor di Matematica e Fisica, Iniversità degli Studi Roma Tre, 00146 Roma, Italy, Swission of Physics, Mathematics and Astronomy, California Institute of Technology, Pasadena, CA 91125, USA. ¹⁰NexAS Goddard Space Flight Center Cestrology, Pasadena, CA 91125, USA. ¹⁰Center for Space Sciences and Technology, Hallong, NASA-GSFC, Greenbelt, MD 20771, USA. ¹⁰Rikagaku Kenkyūjoy (RIKEN) Cluster for Ploneering Research, 2-1 Hirosawa, Wako, Satama 331-0198, Japan. ¹⁰Centre rational de la recherche scientifique, Observatoire Astronomique de Strasbourg, Université de Strasbourg, Vinité Mixte de Recherche 7550, 67000 Strasbourg, France. ¹⁵Astronomical Institute, Caradis Pasadema, 1610 Pasadema,

*Corresponding author. Email: krawcz@wustl.edu (H.K.); fabio.muleri@inaf.it (F.Mu.); dovciak@astro.cas.cz (M.D.); alexandra.veledina@utu.fi (A.V.) †Deceased.

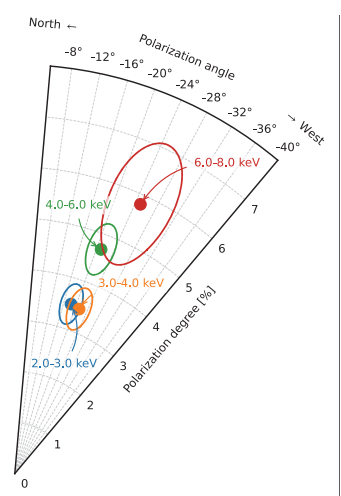


Fig. 1. Energy-dependent x-ray polarization of Cyg X-1. The polarization degree and polarization angle, derived from the IXPE observations, are shown for four energy bands (labeled and in different colors). The ellipses denote the 68.3% confidence regions.

Compton scattering of disk photons with initial energies of -0.1 keV require inclinations exceeding 65°. Truncated disk models invoking Compton scattering of the disk or internally generated lower-energy (-1-10 eV) synchrotron photons (24) can reproduce the observed polarization degree for inclinations of -45°. In comparison to the models with disk photons, the larger number of scatterings required to energize lower-energy synchrotron photons to kiloelectronvolt energies results in higher polarization degree in the IXPE energy band (fig. S9) (77).

Although the x-ray polarization, optical polarization, and radio jet approximately align in the plane of the sky, the inclination of the x-ray bright region exceeds that of the binary orbit, implying that the inner accretion flow is seen more edge-on than the binary orbit. Because the bodies of a stellar system typically orbit and spin around the same axis (as do most planets in the Solar System), we consider potential explanations for the mismatch between the inner accretion disk inclination and the orbital inclination.

Stellar-mass black holes are formed during supernovae. The supernova that occurred in Cyg X-1 might have left the black hole with a misaligned spin. Gravitational effects could align the inner accretion flow angular momentum vector with the black hole spin vector (25). In this scenario, aligning the inner accretion

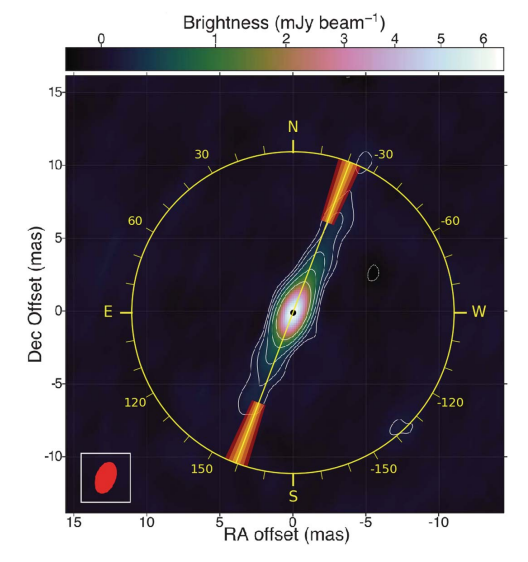
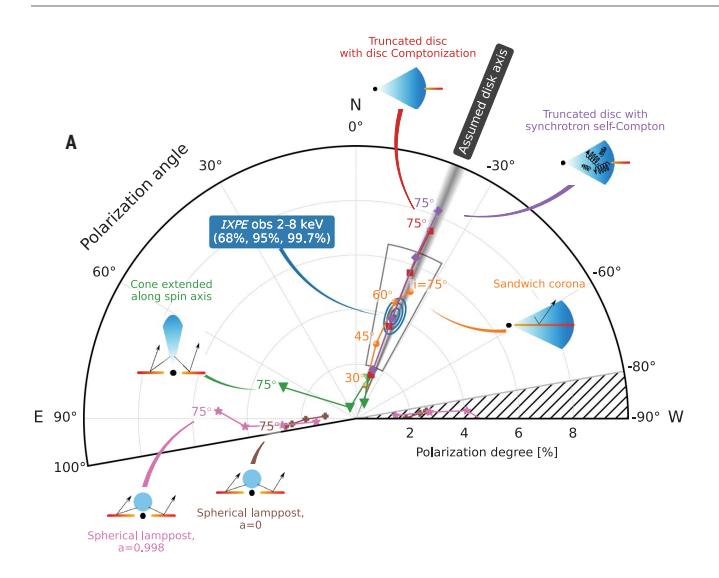


Fig. 2. Comparison of the x-ray polarization direction with the radio jet. The 2–8 keV electric vector position angle is shown with the yellow line, and the 1σ , 2σ , and 3σ confidence regions are given by the orange-to-red shading. The background image is a radio observation of the jet (1). We infer (see text) that most x-rays are emitted by a ~2000-km-diameter region surrounding the ~60-km-diameter black hole, far smaller than the resolution of the radio image (which is indicated by the red ellipse). The coordinate offsets in right ascension (RA) and declination (Dec) (J2000 equinox) are in units of milliarcseconds (mas). The color scale shows the radio flux in milli-Jansky, with 1 Jansky being 10^{-26} W m^{-2} Hz $^{-1}$.

disk angular momentum vector with the black hole spin vector would also align the radio jet produced by the inner accretion disk with the black hole spin vector. Several, but not all, analyses of Cyg X-1 reflected emission spectra give inclinations consistent with our $i > 45^\circ$ constraint (26, 27).

An alternative explanation for the large inclination of the x-ray-emitting region invokes the precession of the inner accretion flow with a period much longer than the orbital period (28). From our analysis of a 2-4 keV long-term x-ray light curve, we infer that the IXPE observations were performed close to the maximum inner disk inclination (fig. S2) (17). We tested the hypothesis that the inner flow precesses with an amplitude of >17.05 by performing an additional 86-ks IXPE target of opportunity observation of Cyg X-1 from 18 to 20 June 2022, 33 days after the May observations, which corresponds to half of the current superorbital period (17). If this hypothesis is correct, we expect the polarization degree to drop from 4.01 ± 0.20% to ≪1% owing to the inclination changing from $i > 45^{\circ}$ in May to $i \lesssim 10^{\circ}$ in June. The observations showed the source in the same hard state with a 2-8 keV polarization degree and angle of $3.84\pm0.31\%$ and $-25^\circ.7\pm2^\circ.3$, respectively (fig. 84) (17). The polarization degree remained constant (within the statistical uncertainties) between the May and June observations. We therefore disfavor the hypothesis that precession of the inner accretion flow leads to the high polarization degree of the May observation. The combined May and June polarization degree and angle are $3.95\pm0.17\%$ and $-22.^\circ2\pm1^\circ2$, respectively (fig. 84) (17).

In previous work, others have argued that optically thin synchrotron emission from the base of the jet could contribute up to 5% to the Cyg X-1 x-ray emission in the hard state (29, 30). Synchrotron emission from electrons gyrating around magnetic field lines is polarized perpendicular to those field lines. Our observation of the x-rays being polarized parallel to the jet axis would require synchrotron emission from a toroidal magnetic field, wound around the jet axis. For this magnetic field geometry, seen at an inclination of 27%, the theoretical upper limit on the polarization degree of the synchrotron emission is 8% (31). The jet thus contributes < 0.4% of the observed polarization degree. If the almost-constant jet



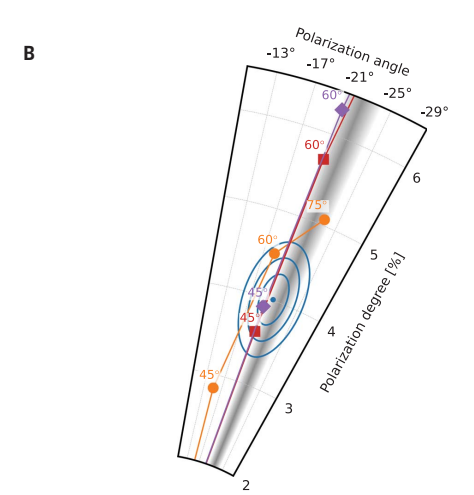


Fig. 3. Comparison of the observed 2-8 keV polarization degree and angle with model predictions. (A) The blue dot shows the polarization degree and angle, with the blue ellipses indicating the 68, 95, and 99.7% confidence levels (equivalent to 1_o, 2_o, and 3_o, respectively). Model predictions assume that the inner disk spin axis has position angle of -22° (consistent with the radio jet), and that the inner disk angular momentum vector points away from the observer (as does the orbital angular momentum vector) (1). The gray band shows the uncertainty of the radio jet orientation; we adopt this as the uncertainty of the disk spin axis in all models. Each colored line shows the model results for each chosen corona geometry, with symbols indicating different values as a function of the inner disk inclination i. Inset diagrams schematically depict the assumed black hole (black), corona (blue), and accretion disk (orange-red) configurations. Black arrows indicate photon paths. Models with coronae extending parallel to the inner accretion disk can match the IXPE observations, but coronae located or extending along the spin axis of the inner accretion disk cannot. The position angles are shown from -80° to +100° (instead of -90° to +90°) to clarify the models that straddle the ±90° borders. (B) A zoom into the region around the measured value, marked with the gray box in (A).

emission was the main source of the observed polarization, we would expect that a rise in the x-ray flux from the inner accretion flow would lead to an overall smaller polarization degreecontrary to the observed trend (fig. S6).

The polarized x-rays from the immediate surroundings of the black hole carry the imprint of the geometry of the emitting gas. We conclude that the x-ray bright plasma is extended perpendicular to the radio jet. The high observed polarization degree either implies a more edge-on viewing geometry than given by the optical data, or it suggests that unidentified physical effects are responsible for production of the x-rays in accreting black hole systems.

REFERENCES AND NOTES

- J. C. A. Miller-Jones et al., Science 371, 1046–1049 (2021).
 L. Gou et al., Astrophys. J. 790, 29 (2014).
- 3. A. M. Stirling et al., Mon. Not. R. Astron. Soc. 327, 1273-1278
- (2001). C. Done, M. Gierliński, A. Kubota, Astron. Astrophys. Rev. 15,
- 1–66 (2007).
 P. A. Connors, T. Piran, R. F. Stark, Astrophys. J. 235, 224
- (1980). L.-X. Li, R. Narayan, J. E. McClintock, Astrophys. J. 691,
- 847-865 (2009). J. D. Schnittman, J. H. Krolik, Astrophys. J. **701**, 1175–1187
- (2009).
- (2009). C. Bambi *et al.*, Space Sci. Rev. **217**, 65 (2021). J. D. Schnittman, J. H. Krolik, Astrophys. J. **712**, 908–924

- G. Matt. Mon. Not. R. Astron. Soc. 260, 663-674 (1993).
- 11. J. Poutanen, K. N. Nagendra, R. Svensson, Mon. Not. R. Astron. Soc. 283, 892-904 (1996).
- 12. M. C. Weisskopf et al., J. Astron. Telesc. Instrum. Syst. 8 026002 (2022).
- H. Krawczynski, B. Beheshtipour, Astrophys. J. 934, 4 (2022).
- M. C. Weisskopf et al., Astrophys. J. 215, L65 (1977).
 K. S. Long, G. A. Chanan, R. Novick, Astrophys. J. 238, 710 (1980)
- M. Chauvin et al., Nat. Astron. 2, 652-655 (2018).
- Materials and methods are available as supplementary materials. J. C. Kemp, M. S. Barbour, T. E. Parker, L. C. Herman, Astrophys. J. 228, L23–L27 (1979).
- M. C. Begelman, R. D. Blandford, M. J. Rees, Rev. Mod. Phys 56, 255–351 (1984).
- F. Haardt, L. Maraschi, Astrophys. J. 380, L51 (1991).
 B. E. Kinch, J. D. Schnittman, S. C. Noble, T. R. Kallman, J. H. Krolik, Astrophys. J. 922, 270 (2021).
- F. Meyer, E. Meyer-Hofmeister, Astron. Astrophys. 288, 175-182 (1994)
- P. O. Petrucci, J. Ferreira, G. Henri, J. Malzac, C. Foellmi, Astron. Astrophys. 522, A38 (2010).
 A. Veledina, J. Poutanen, I. Vurm, Mon. Not. R. Astron. Soc.
- **430**, 3196-3212 (2013).
- 25. J. M. Bardeen, J. A. Petterson, Astrophys. J. 195, L65 (1975).
- J. A. Tomsick et al., Astrophys. J. 780, 78 (2014).
 M. L. Parker et al., Astrophys. J. 808, 9 (2015).
 P. Lachowicz, A. A. Zdziarski, A. Schwarzenberg-Czerny
- G. G. Pooley, S. Kitamoto, Mon. Not. R. Astron. Soc. 368 1025-1039 (2006). 29 D. M. Russell, T. Shahhaz, Mon. Not. R. Astron. Soc. 438.
- M. Rdssch, H. Shahbaz, Moh. Noc. N. Ashon. Soc. 433, 2083–2096 (2014).
 A. A. Zdziarski, P. Pjanka, M. Sikora, Ł. Stawarz, Mon. Not. R.
- Astron. Soc. **442**, 3243–3255 (2014).

 31. M. Lyutikov, V. I. Pariev, D. C. Gabuzda, *Mon. Not. R. Astro.*Soc. **360**, 869–891 (2005).
- P. Thalhammer, J. Wilms, N. Rodriguez Cavero, X-ray observations of black hole binary Cyg X-1 with INTEGRAL, version 1, Zenodo
- (2022); https://doi.org/10.5281/zenodo.7140274.

 33. V. Kravtsov et al., Optical polarimetric observations of black hole binary Cyg X-1 with DIPol-2, version 1, Zenodo (2022);
- https://doi.org/10.5281/zenodo.7108247.

 34. D. Blinov, S. Kiehlmann, N. Mandarakas, R. Skalidis, Optical polarimetric observations of the black hole binary star Cyg X-1 with RoboPol, version 1, Zenodo (2022):
- https://doi.org/10.5281/zenodo.7127802. 35. W. Zhang, M. Dovčiak, M. Bursa, Astrophys. J. **875**, 148 (2019)
- 36. A. Veledina, J. Poutanen, Polarization of Com emission in slab geometry, version 1, Zenodo (2022); https://doi.org/10.5281/zenodo.7116125.

ACKNOWLEDGMENTS

We thank I. Miller-lones I. Orosz, and A. Zdziarski for very helpful discussions of the optical constraints on the orbital inclination of Cvg X-1 and optical position angles. We are grateful to three anonymous referees, whose excellent comments contributed to strengthening the paper. We thank T. Maccarone for emphasizing that stellar wind absorption may modify the jet orientation measurement results. This work is based on observations made with the IXPE mission, a joint US and Italian mission. The US contribution to the IXPE mission is supported by NASA and led and

rospace (contract NNM15AA18C). The Italian contribu the IXPE mission is supported by the Italian Space Agency (ASI) through contract ASI-0HBI-2017-12-I.0, agreements ASI-INAF-2017-12-H0 and ASI-INFN-2017.13-H0, and its Space Science Data Center (SSDC) with agreements ASI-INAF-2022-14-HH.0 and ASI-INFN 2021-43-HH.0; and by INAF and the Istituto Nazionale di Fisica Nucleare (INFN) in Italy. This research used data and software products or online services provided by the IXPE Team (Marshall Space Flight Center, the SSDC of the Italian Space Agency, the INAF, and INFN), as well as the High-Energy Astrophysics Science Archive Research Center (HEASAR NASA Goddard Space Flight Center. We thank the NICER. NuSTAR INTEGRAL, Swift, and SRG/ART-XC teams and Science Opera Centers for their support of this observation campaign, DIPol-2 is a joint effort between University of Turku (Finland) and Leibniz Institut für Sonnenphysik (Germany). We are grateful to the Institute for Astronomy, University of Hawaii, for allocating observing time for the DIPol-2 polarimeter, and to the Skinakas Observatory for performing the observations with the RoboPol polarimeter at their 1.3-m telescope. **Funding:** H.K. acknowledg NASA support under grants 80NSSC18K0264, 80NSSC22K1291. 80NSSC2IK1817, and NNX16AC42G. F.Mu., J.R., S.B., S.F., A.R., P.So., E.D.M., E.Co., A.D.M., G.M., Y.E., R.F., F.L.M., M.Pe., and A.T were funded through contract ASI-INAF-2017-12-HO, L.B., R.Bo., R.Be., A.Br., L.L., S.Ca., S.M., A.Man., C.O., M.P.-R., C.S., and G.S. were funded by the ASI through contracts ASI-INFN-2017.13-HO and ASI-INFN 2021-43-HH.O. M.Pi. was funded through contr ASI-INAF-2022-14-HH.O. I.A. acknowledges support from MICINN (Ministerio de Ciencia e Innovación) Severo Ochoa award for the IAA-CSIC (SEV-2017-0709) and through grants AYA2016-80889-P and PID2019-107847RB-C44. M.D., J.S., and V.Ka. acknowledge support from GACR (Grantová agentura České republiky) project 21-06825X and institutional support from the Astronomica Institute of the Czech Academy of Sciences (RVO:67985815).

J.A.G. acknowledges support from NASA grant 80NSSC20K0540 J.Pod. acknowledges support from Charles University project GA UK No. 174121 and from the Barrande Fellowship Program of the Czech and French governments. A.V., J.Pou., and S.S.T owledge support from Russian Science Foundation gran 20-12-00364 and the Academy of Finland grants 333112, 347003, 349144, and 349906, M.N. acknowledges support from NASA under award number 80GSFC2IM0002. T.K. is supported by JSPS KAKENHI Grant Number JPI9K03902. P.-O.P. acknowledges support from the High Energy National Programme (PNHE) of Centre national de la recherche scientifique (CNRS) and from the French space agency (CNES) as well as from the Barrande Fellowship Programme of the Czech and French governments D.B., S.K., N.M., and R.S. acknowledge support from the European Research Council (ERC) under the European Union's Horizon 2020 research and innovation program under grant agreement no 771282. V.Kr. thanks Vilho, Yrjö and Kalle Väisälä Foundation P.T. and J.W. acknowledge funding from Bundesministerium Wirtschaft and Klimaschutz under Deutsches Zentrum für Luft- und Raumfahrt grant 50 OR 1909. A.I. acknowledges support from the Royal Society, J.H. acknowledges the support of the Natural Sciences and Engineering Research Council of Canada (NSERC), funding reference number 5007110, and the Canadian Space Agency, S.G. Land A.P.M. are supported in part by National Science Foundation grant AST-2108622, by NASA Fermi Guest Investigator grant 80NSSC21K1917, and by NASA Swift Guest Investigator grant 80NSSC22K0537. C.-Y.N. is supported by a

managed by its Marshall Space Flight Center, with industry partne

General Research Fund of the Hong Kong Government under grant number HKU 17305419. P.Sl. acknowledges support from NASA Contract NAS8-03060. **Author contributions:** H.K., F.Mu., M.D., A.V., N.R.C., J.S., A.I., G.M., J.A.G., V.L., and J.Pou. participated in the planning of the observation campaign and the analysis and modeling of the data. M.N., T.K., J.Pod., J.R., and W.Z. contributed to the analysis or modeling of the data. A.V.B., V.Kr., S.V.B., M.K., T.S., D.B., S.K., N.M., and R.S. contributed to the optical polarimetric data. J.M.M. and P.D. contributed the Swift results; J.W. and P.T. the INTEGRAL results; and A.A.L., S.V.M., and A.N.S. the SRG/ART-XC results. S.B., F.C., N.D.L., L.L., A.Mar., T.M., N.O., A.R., P.-O.P, P.So., A.F.T., F.To., M.C.W., and S.Zh. contributed to the discussion of the results. F.Ma. and S.F. served as internal referees. All other authors contributed to the design and science case of the IXPE mission and to planning the observations used in this paper. All authors provided input and comments on the manuscript. **Competing interests:** The authors declare no competing interests. Data and materials availability: The May and June IXPE observations are available at https://heasarc.gsfc.nasa.gov/FTP/ixpe/data/obs/01/01002901/ and https://heasarc. gsfc.nasa.gov/FTP/ixpe/data/obs/01/01250101/, respectively.
The NICER data are available at https://heasarc.gsfc.nasa.gov/ docs/nicer/nicer archive.html under ObsIDs 5100320101. 5100320102, 5100320103, 5100320104, 5100320105, 5100320106, and 5100320107. The NuSTAR data are available at https://heasarc.gsfc.nasa.gov/db-perl/W3Browse/w3table.pl? tablehead=name%3Dnumaster&Action=More+Options under ObsIDs 30702017002, 30702017004, and 30702017006. The SWIFT XRT data are available at https://heasarc.gsfc.nasa.gov/ cgi-bin/W3Browse/swift.pl under ObsIDs 00034310009. 00034310010, 00034310011, 00034310012, 00034310013, and 00034310014. The extracted INTEGRAL ISGRI data are archived at Zenodo (32). The SRG ART-XC data are available at ftp://hea.iki rssi.ru/public/SRG/ART-XC/data/Cygnus_X-1/. The MAXI light curves are available at http://maxi.riken.ip/star_data/J1958+352/ J1958+352.html. The raw DIPol-2 and RoboPol data are archived at Zenodo (33, 34). The KERRC code (13) is available at https://gitlab. com/krawcz/kerrc-x-ray-fitting-code.git. The MONK code (35) is available at https://projects.asu.cas.cz/zhang/monk. The ixpeobssim software is available at https://github.com/ lucabaldini/ixpeobssim and documented at https://ixpeobssim readthedocs.io. Our derived x-ray polarization measurements are listed in tables S1 and S2, and the optical polarization measurements are listed in table S4. The numerical results of our model fitting are listed in table S5. Our models of polarized emission in the truncated disk geometry are archived at Zenodo (36). License information: Copyright © 2022 the authors, some rights reserved; exclusive licensee American Association for the Advancement of Science. No claim to original US government works. https://www.science.org/about/science-licenses-journal

SUPPLEMENTARY MATERIALS

science.org/doi/10.1126/science.add5399 Materials and Methods Figs. S1 to S12 Fables S1 to S5 References (37-79)

Submitted 18 June 2022; accepted 17 October 2022 Published online 3 November 2022 10.1126/science.add5399



Supplementary Materials for

Polarized x-rays constrain the disk-jet geometry in the black hole x-ray binary Cygnus X-1

Henric Krawczynski et al.

Corresponding authors: Henric Krawczynski, krawcz@wustl.edu; Fabio Muleri, fabio.muleri@inaf.it; Michal Dovčiak, dovciak@astro.cas.cz; Alexandra Veledina, alexandra.veledina@utu.fi

DOI: 10.1126/science.add5399

The PDF file includes:

Materials and Methods Figs. S1 to S12 Tables S1 to S5 References

Materials and Methods

Data Sets and Analysis Methods

IXPE observed Cyg X-1 from 2022 May 15 to 21 for 242 ksec. Following the results from the May IXPE observation campaign, we performed an additional 86 ksec target of opportunity observation of Cyg X-1 from 2022 June 18 to 20.

The spectral fitting of the IXPE data uses the level 2 IXPE data and the software tools XSPEC (37) and Sherpa (38-41). The model-independent Stokes parameter analysis (42) of the IXPE polarization data was performed with the ixpeobssim software (43). The ixpeobssim\xpbin command (42, 43) is used to extract Stokes parameters and the polarization degree and angle from the Level 2 data. The confidence regions for the polarization measurements were calculated using standard methods (44, 45). The results were cross-checked by fitting the Stokes I, Q and U data with XSPEC using the response matrices from the High Energy Astrophysics Science Archive Research Center (HEASARC) data archive (46). Source and background data were selected based on the reconstructed arrival direction in celestial coordinates. The source events were selected with a circular region of ~80 arcsec radius; background events were selected with a concentric annulus of inner and outer radii of \sim 150 and \sim 310 arcsec, respectively. We use the additive property of the Stokes parameters to subtract the background. The signal exceeds the background by >70 times over the entire energy range of the polarization measurements.

The NuSTAR spacecraft (47) acquired a total of 42 ksec of data between 2022 May 18 and May 21. The NuSTAR data were processed with the NuSTARDAS software (version 1.9.7) of the HEAsoft package (version 6.30.1) (48).

NICER (49) acquired a total of 87 ksec of data between May 15 and May 21, 2022. The NICER data were processed with the NICERDAS software (version 9.0) of the HEASoft package.).

Swift observed Cyg X-1 daily between May 15 and May 20, 2022 for a total of ~54 ksec, with the XRT instrument operating in Windowed Timing (WT) mode. The observations were processed using the tools in HEASOFt. The initial event cleaning was performed using XRTPIPELINE, the spectra and light curves were extracted using XSELECT, and ancillary response files (ARF) were generated using XRTMKARF.

The Mikhail Pavlinsky ART-XC telescope (50) on board the SRG observatory (51) carried out two observations of Cyg X-1 on 2022 May 15 to 16 and 18 to 19, simultaneous with IXPE, with 86 and 85 ks exposures, respectively. ART-XC data were processed with the analysis software ART-PRODUCTS v0.9 with the CALDB (calibration data base) version 20200401.

INTEGRAL observed Cyg X-1 between 2022 May 15 and May 20 with a total exposure time of ~196 ksec. INTE-GRAL/ISGRI light curves and energy spectra were extracted using version 11.2 of the OFF-LINE SCIENTIFIC ANALYSIS (OSA) software (52).

We used the Cyg X-1 observations with the Monitor of All-sky X-ray Image (MAXI) (53) to extract a long-term 2–4 keV light curve (Figure S2). Figure S1 shows the IXPE, NICER, NuSTAR, Swift/XRT, SRG/ART-XC, and INTEGRAL light curves.

As mentioned in the main article, we used IXPE to test the

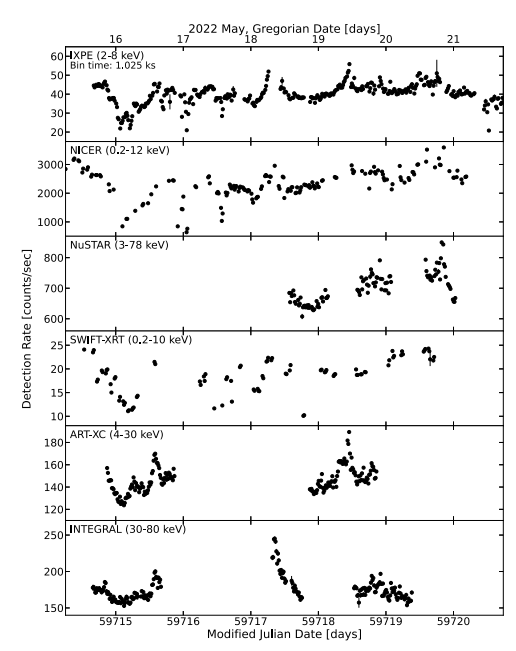


Figure S1: X-ray light curves of Cyg X-1 from the 2022 May 15 to 21 observation campaign. From top to bottom: the IXPE, NICER, NuSTAR, Swift/XRT, SRG/ART-XC, and INTEGRAL light curves.

hypothesis that the high polarization fraction of the May 15-21 IXPE observations was caused by the superorbital (i.e. with a period exceeding the orbital period) precession of the inner accretion flow (54,55). Cyg X-1 exhibits superorbital flux modulations that are stable over periods of years (28,56).

Figure S2 shows the Cyg X-1 2–4 keV flux between December 17, 2020 and August 9, 2022. The blue dashed lines show the dates of the fitted superorbital flux minima. The green solid lines indicate the time of the first (May 15–21) and second (June 18–20) IXPE observation campaigns, close to the time of a superorbital flux minimum (first observation) and maximum (second observation). If the inner accretion flow indeed precesses, the superorbital flux minimum should correspond to inclination and polarization degree maxima, and the superorbital flux maximum should correspond to inclination and polarization degree minima. As described in the main text, the IXPE observations did not show the drastic change of the polarization degree predicted by the precession hypothesis.

IXPE Polarization Results

Figure S3 shows the IXPE polarization signal from the May 15 to May 21, 2022 observations in terms of the normalized Stokes parameters Q/I and U/I, giving the polarized beam intensity along the north-south (Q/I>0) and east-west (Q/I<0) directions as well as along the northeast–southwest (U/I>0) and

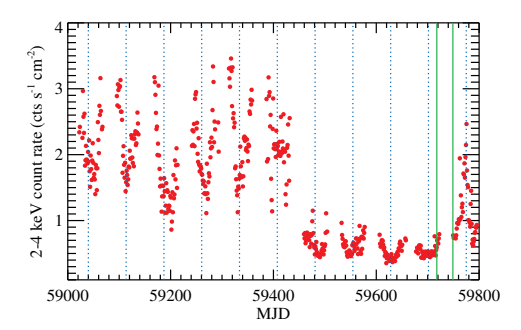


Figure S2: Long-term Cyg X-1 x-ray light curve. The figure shows the daily 2–4 keV count rate obtained from the MAXI monitor from May 31, 2020 (MJD 59000) to August 9, 2022 (MJD 59800). Phases of high 2–4 keV fluxes during the soft state and low 2–4 keV fluxes during the hard state can be recognized. The vertical dotted lines (blue) show the dates of the superorbital flux minima, appearing at MJD = 59040.0 + 73.5n, with n being an integer number. The two vertical solid lines (green) show the mid-times of two IXPE campaigns, 2022 May 15 to 21 and June 18 to 20, respectively. The first observation was close to the superorbital flux minimum, and the second was shifted by about half-period. The second observation was taken right before the short incursion into the soft state.

northwest–southeast (U/I<0) directions. Tables ${\bf S1}$ and ${\bf S2}$ give the results of both analyses in terms of the Stokes parameters, and polarization degree and angle, respectively. The consistency of the radio-jet – x-ray polarization alignment is limited by the precision of the radio results. Different studies have found -26° (I), or -21° to -24° in 3 epochs, but -17° for the inner jet in another epoch (3). The variability of the results could be explained by the phase dependent absorption of the radio emission by the stellar wind (I).

The target of opportunity observations of Cyg X-1 from June 18 to 20, 2022 showed the source still in the hard state. We measure a polarization degree and angle of $3.84\pm0.31\%$ and $-25^{\circ}7\pm2^{\circ}3$, respectively, for this data set. We present the results from the May and June observations as well as the results from the cumulative data set in Figure S4. The results are consistent with time independent polarization degree and polarization angle. The polarization degree and direction of the cumulative data set are $3.95\pm0.17\%$ and $-22^{\circ}2\pm1^{\circ}2$, respectively.

In the following we limit the analysis to the data acquired in May to avoid merging data taken a month apart. The polarization degree increases with energy from 3.5 \pm 0.2% in the energy band 2–5 keV to 5.3 \pm 0.5% in the energy band 5–8 keV (17). Fitting a model of constant polarization is rejected at the 99.93% confidence level. The polarization degree (PD) increase with energy is better matched by a linear model $PD=A+B\times(E/\text{keV}-1)$ with $A=(2.9\pm0.4)\%$ and $B=(0.58\pm0.15)\%$ (Figure S5 A). On theoretical grounds, we expect that the x-ray emission around the Fe $K\alpha$ line energy of 6.4 keV exhibits a reduced polarization

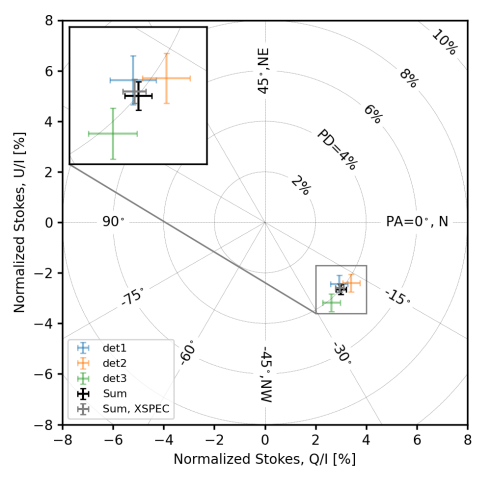


Figure S3: X-ray linear polarization of Cyg X-1 from the 2022 May 15 to 21 observations. The linear polarization of the x-rays from Cyg X-1 is shown in the plane of the normalized Stokes Q/I and U/I parameters measured with each of the three IXPE x-ray telescopes (coloured data points), and for the combined signal from all three telescopes (black). The grey data point shows the results from the analysis of the data using the XSPEC tool, instead of IXPEOBSSIM . The two approaches give a result which is compatible within the statistical uncertainties. The circles give the contours of constant polarization degree (PD) while the radial lines correspond to constant polarization angle (PA). The error bars are 1σ .

degree. We find however, that the dips of the polarization degree at 4.5–5 and 6–6.5 keV are not statistically significant. The fit of a linear function has a χ^2 of 4.04 for 9 degrees of freedom and a chance probability of larger χ^2 -values of 90.9%. Moreover, based on the constraints on the equivalent width of the fluorescent Fe $K\alpha$ -line from the spectral analysis of the NICER and NuSTAR data, we find that the maximum possible Fe $K\alpha$ depolarization is much smaller than the observed dips. A fit of the polarization angle as a function of energy with a constant function gives a statistically acceptable fit with a chance probability for larger χ^2 -values of 57.5% (Figure S5 B).

The light curves in Figure S1 show that the Cyg X-1 IXPE count rates varied between 20 and 60 count s $^{-1}$. We investigated the flux dependence of the polarization properties by analyzing three count-rate selected data sets. The average fluxes of those data sets are 3.5, 3.9, and 4.5 times $10^{-9}~\rm erg~cm^{-2}~s^{-1}$. The polarization degree increase with the flux from $3.63\pm0.30\%$ to $3.87\pm0.34\%$ to $5.03\pm0.41\%$ (Figure S6). The overall trend is statistically significant at the 98.3% confidence level.

Figure S7 shows that the polarization properties (Stokes Q/I and U/I) do not depend on the orbital phase of the binary. Fitting

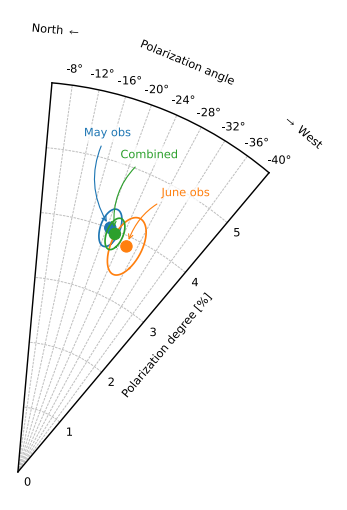
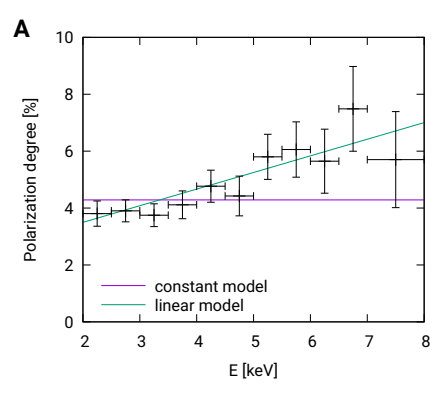


Figure S4: Linear x-ray polarization of Cyg X-1 measured in two occasions, as well as the combined result. The figure shows the polarization degree and angle of the 2022 May 15 to 21 observations (blue), the 2022 June 18 to 20 observations (orange), and for the combined data set (green). For each result the most likely values (circles) and 68.3% confidence regions (ellipses) are shown.

the polarization along the orbit with a constant provides an acceptable null hypothesis probability. Data are summed between 2 and 8 keV. The assumed period is 5.599829 days, with T_0 at MJD 52872.288 (57).

IXPE, NICER, NuSTAR, and INTEGRAL energy spectra

We used the XSPEC package for fitting a simple model to the broadband Stokes I spectrum provided by NICER, IXPE, NuS-TAR, and INTEGRAL and the Stokes Q and U spectra provided only by IXPE. We use the data from the first NuSTAR observation and the simultaneously acquired NICER data, to eliminate differences due to spectral variability. We use the entire IXPE and INTEGRAL observations to maximize the signal-to-noise ratio. We fit the two NuSTAR Focal Plane Modules (FPMs) and the three IXPE detector inits separately in the fit. For the Stokes I spectrum, we employ the XSPEC fitting models MBPO* TBABS * (DISKBB + XILLVERCP + RELXILLCP + NTHCOMP).Here DISKBB represents thermal disk emission and NTHCOMP represents Compton scattered emission observed directly from the corona. The RELXILLCP component represents coronal xrays that are reflected from the inner accretion disk and distorted by relativistic effects. We assume that the flux irradiating the disk decreases with increasing radial distance proportional to r^{-3} . The XILLVERCP component represents coronal x-rays that are reflected from the outer disk and the companion star and not subject to strong relativistic effects. TBABS accounts for line-of-



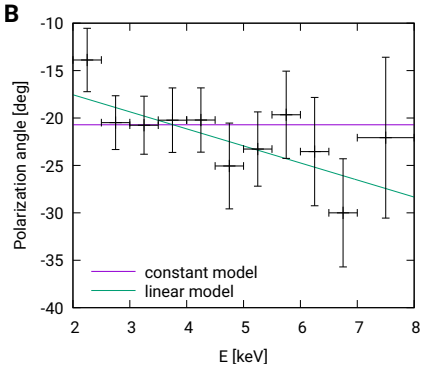


Figure S5: Energy dependence of the observed polarization degree (A) and polarization angle (B). The data (black crosses with 1σ error bars) are produced using the PCUBE algorithm of the xpbin tool and summed over all detector units. The constant (violet) and linear (green) models fitted to the data are also depicted (see the text for details).

sight absorption by the interstellar medium.

The model MBPO is included to account for cross-calibration discrepancies we encountered between the four observatories. It multiplies the model spectrum by a broken power law, MBPO(E) = $N(E/E_{\rm br})^{\Delta\Gamma}$, where E is the energy of the photon and N is a normalization constant giving the ratio of the detection areas of the satellites at the energy $E_{\rm br}$ at which the power law index of the model changes from the value $\Delta\Gamma_1$ to $\Delta\Gamma_2$. For NICER, we fix the power-law indices to zero and the normalization to unity. For each NuSTAR FPM and INTEGRAL, we tie $\Delta\Gamma_2 = \Delta\Gamma_1$ (i.e. employing only a single power law) but leave $\Delta\Gamma_1$ and N as free parameters of the fit. For the IXPE detector units, we leave all MBPO parameters free. We also include a 0.5% systematic uncertainty to further account for cross-calibration discrepancies. Finally, the NuSTAR FPM A disagrees with the FPM B and NICER in the 3–4 keV band, and IXPE de-

tector unit #3 disagrees with all other instruments (even with the use of MBPO) in the $> 5~{\rm keV}$ energy range, and so we ignore these ranges in our model fitting.

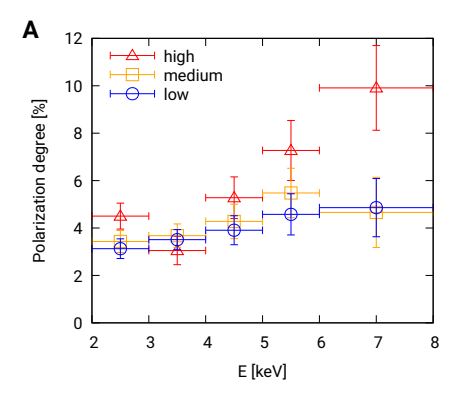
We first jointly fit the model to the NICER, NuSTAR and IN-TEGRAL data, then add IXPE Stokes I to fit the model before finally adding IXPE Stokes Q and U. At each stage, the best-fit parameters change by less than their uncertainties. We tie the seed photon temperature of the NTHCOMP component (parameter $kT_{\rm bb}$) to the temperature of the inner edge of the accretion disk (parameter $k\,T_{\rm d}$ of the DISKBB model). We tie the RELX-ILLCP photon index to that of the NTHCOMP component, but are unable to do this for the seed photon temperature as this hardwired to 0.05 keV in the RELXILLCP grid. We initially forced the RELXILLCP and NTHCOMP components to have the same coronal electron temperature $kT_{\rm e}$, but found that the fit improved dramatically ($\gg 5 \sigma$ according to an F-test) after relaxing this assumption. The discrepancy between the corona temperature seen by the observer (NTHCOMP temperature of 94 keV) and by the disc (RELXILLCP temperature of 140 keV) may be due to general relativistic effects (redshifting the emission seen by the observer), and due to the different viewing angles of the corona. We calculate 90% confidence level uncertainties on the fitting results with a Markov Chain Monte Carlo simulation that uses the Goodman-Were algorithm with a total length of 307,200 steps spread over 256 walkers following an initial burn-in period of 19,968 steps. The best-fit spectral parameters are listed in Table

Figure S8a shows the best-fit Stokes I model and the data unfolded around that model, as well as the contributions from the different model components. The DISKBB, XILLVERCP and RELXILLCP components contribute respectively 0.6%, 0.5% and 10.0% of the flux. The fractional contribution of each model component is consistent whether we consider only NICER, NuSTAR and INTEGRAL or also include IXPE. Because the direct coronal flux dominates the 2–8 keV flux, it must also dominate the polarization. For instance, the relativistic reflection component would need to be $\sim 40\%$ polarized to achieve the observed overall polarization of $\sim 4\%$. However, the reflected emission exhibits most likely much smaller polarization degree (10, 11, 58, 59) (see also Figures S9 and S10).

As a simple toy model, we therefore assign a constant (independent of energy) polarization degree and angle to the NTH-COMP component (the model POLCONST) and assume that the other components are unpolarized. Fig. S8c shows the resulting fit to IXPE Stokes Q and U. We find a reduced χ^2 of $\chi^2/({\rm degrees~of~freedom}) = 2575.72/2466$. Panel Fig S8d shows the contributions from each energy channel to χ , we find that there are no structured residuals. The best-fit polarization degree and angle of the corona from this simple model are respectively $3.63 \pm 0.26\%$ and $-20^\circ 5 \pm 2^\circ 1$ (90% confidence).

Model constraints on the inclination of the inner accretion disk

We studied the energy spectra and polarization properties of different corona shapes and properties with the raytracing codes KERRC (13), MONK (35), and with an iterative radiation transport solver (36,60). We present simulation results that match the



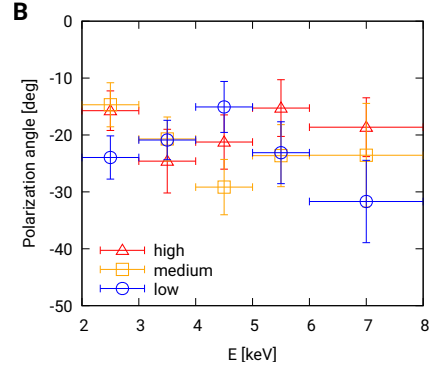


Figure S6: Polarization of Cyg X-1 at different flux levels. Comparison of the polarization degree (A) and polarization angle (B) for three different flux selected data sets.

IXPE, NICER, and NuSTAR energy spectra qualitatively, and the predicted polarization properties.

The Cyg X-1 binary system spins clockwise (1); we therefore plot position angles assuming that the inner disk and the black hole also spin clockwise. This assumption impacts the sign of the predicted polarization angles. We assume furthermore that the inner disk and black hole spin axes are aligned and are at 0° position angle. The position angles shown in Figure 3 were obtained by subtracting 22° from the position angles in the models.

We used the general relativistic ray tracing codes KERRC to evaluate the polarization that cone-shaped coronae centered on the black hole spin axes and wedge-shaped coronae sandwiching the accretion disk can produce. The code assumes a standard geometrically thin, optically thick accretion disk extending from the innermost stable circular orbit to 100 gravitational radii $r_{\rm g}=G\,M/c^2$ with G being the gravitational constant, M the black hole mass, and c the speed of light. The code uses Monte Carlo methods to simulate the polarized emission of the accretion disk photons assuming Novikov-Thorne temperature profiles, the geodesic propagation of the x-rays including the gen

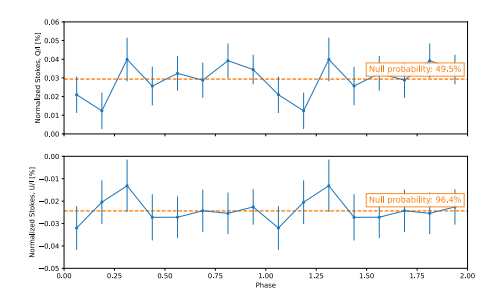


Figure S7: Orbital phase dependence of the Cyg X-1 x-ray polarization properties. The observed x-ray normalized Stokes parameters Q/I and U/I (summed from 2 to 8 keV) are statistically consistent with being constant as a function of the orbital phase. Note that the results are shown for two orbital periods. The orbital phase of 0 corresponds to the superior conjunction maximizing the stellar wind absorption of the x-rays.

eral relativistic polarization direction evolution, the polarizationchanging Compton scattering of the photons in the corona, and the reflection of the photons off the accretion disk adopting the XILLVER reflection model for the reflected intensity (61-63), and an analytical solution for the reflected polarization (64). In both cases, we chose corona parameters which maximize the predicted polarization degree, i.e., cone-shaped coronae close to the accretion disk, and thin wedge-shaped coronae with a half opening angle of 10°. The model parameters are given in Table S3. For all models, we assume that the black hole spin vector and the inner disk spin vector are aligned. The sandwich and cone corona models (as well as the extended lamppost corona model discussed below) are phenomenological - the coronal temperatures are not derived self-consistently. Coronae could cool radiatively, to the point that the predicted energy spectra are softer than the observed ones (65, 66). Processes that heat and cool the coronal plasma are debated, as are their relative contributions (21, 67, 68).

We also used the ray tracing code MONK, which is similar to KERRC but implements the simulation of an extended lamppost corona. The lamppost corona is centered on the spin axis of the accretion disk at a radial coordinate of $r=10\,r_{\rm g}$ and has a radius of 8 $r_{\rm g}$, an electron temperature of 100 keV, and Thomson optical depth of 1 (defined as $n_e \sigma_T R_c$, where n_e is the electron density of the corona, $\sigma_{\rm T}$ is the Thomson cross section, and R_c is the radius of the corona). Simulations were performed for both Schwarzschild (a = 0) and Kerr (a = 0.998) black holes, with mass accretion rate of 4.71×10^{17} and 2.64×10^{18} g s⁻¹, respectively. For the MONK simulations, we first calculated the Stokes parameters generated by the direct emission and then added those of the reflected emission. The reflected emission was normalized to reproduce the reflected emission fraction from the analysis of the NICER, IXPE, NuSTAR, and INTEGRAL energy spectra. We compared the MONK results before and after accounting for the reflected emission. The reflected emission lowers the total

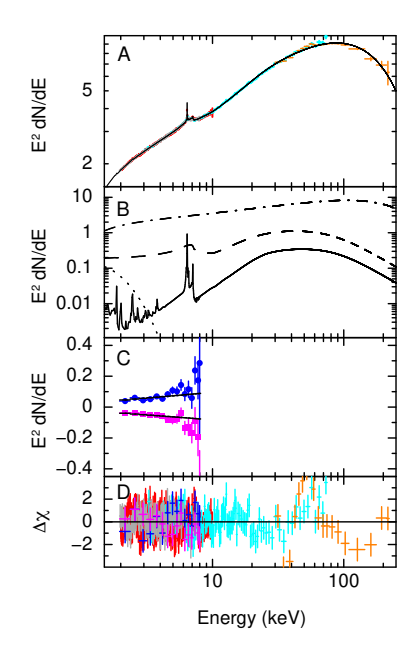
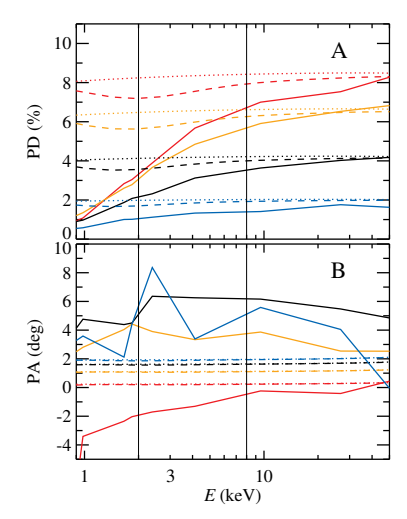


Figure S8: Results of spectropolarimetric fitting. (A) NICER (red), NuSTAR (cyan), IXPE (grey) and INTEGRAL/ISGRI (orange) Stokes I spectrum unfolded around the best-fit model (black solid line). For each bin of the energy spectrum, the unfolded data point is the number of observed counts times the bestfit model value divided by the counts expected in the bin for the best-fit model. For plotting purposes only, data and model are both divided by the relevant MBPO model to remove calibration discrepancies. The specific photon flux dN/dE has units of photons cm⁻² s⁻¹ keV⁻¹. (**B**) Individual components of the best-fit model: thermal disk emission (dotted line), Compton scattered emission from the corona (dashed dotted line), relativistic reflection (dashed line), non-relativistic reflection (solid line). (C) Stokes Q (blue circles) and U (magenta squares), also unfolded around the best-fit model. (**D**) Residuals (contributions to χ). For plotting purposes only, data from different detectors of the same observatory have been grouped together, and a maximum of 10 energy channels have been grouped together to achieve a signal-to-noise ratio of 150.

polarization degree by $\sim\!20\%$ (e.g. a polarization degree of 3% before accounting for reflection becomes 2.5% after accounting for the impact of reflection) as the different polarization directions of the direct and reflected emission components lead to the partial cancellation of the different polarizations.

We studied the polarization of the truncated disk/inner hot flow scenario with the iterative radiation transport solver mentioned above. The code treats Compton scattering of polarized radiation



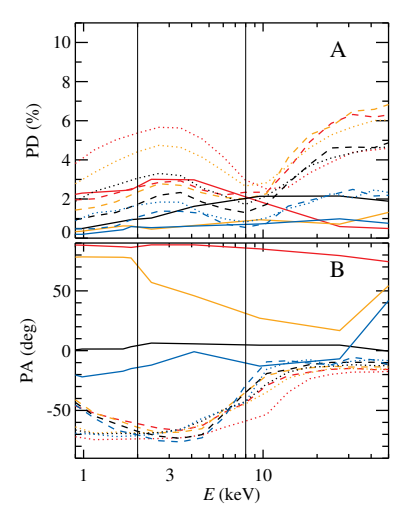


Figure S9: Polarization degree (A) and polarization angle (B) for models with coronae extending parallel to the accretion disk. The solid lines show the predictions of the sandwich corona, the dashed and dotted lines show the predictions of the hot inner flow inside a truncated disk, with accretion disk photons (dashed lines) and synchrotron photons (dotted lines) acting as seed photons for the inverse Compton scattering. The colors encode the inclination angle at which the coronae are observed: red (75°), orange (60°), black (45°) and blue (30°). The vertical lines delineate the IXPE band from 2–8 keV. For very low polarization degrees the polarization angle in the sandwich corona model fluctuates by a few degrees owing to the finite number of simulated events. Positive polarization angles correspond to counterclockwise rotations of the polarization vector relative to the projected disk spin axis on the plane of the sky in Figure 3.

Figure S10: Same as Figure S9, but for models with coronae located on the spin axis of the accretion disk. The solid lines show the predictions for a cone-shaped corona extended along the disk spin axis, the dashed and dotted lines shows the results for an extended lamppost corona for a non-spinning black hole (a=0, 4)0, dashed line) and a spinning black hole (a=0.998, 4)0 dotted line).

degree for $i \gtrsim 60^{\circ}$. The polarization direction aligns within a

few degrees with the inner disk spin axis. The hot inner flow in-

side a truncated disk exhibits higher polarization degree at lower

energies than the sandwich corona. We interpret this difference

as follows: for the sandwich corona, the first scatterings of pho-

tons coming from the accretion disk and scattering towards the observer create a net polarization parallel to the accretion disk that competes with the perpendicular polarization of the emission scattering multiple times in the plane of the corona. In con-

trast, the first scatterings of truncated disk photons entering the

hot inner flow from the sides create a net perpendicular polar-

ization similar to the perpendicular polarization of the photons

scattering multiple times in the plane of the hot flow. In prin-

ciple, high-precision polarization measurements can distinguish

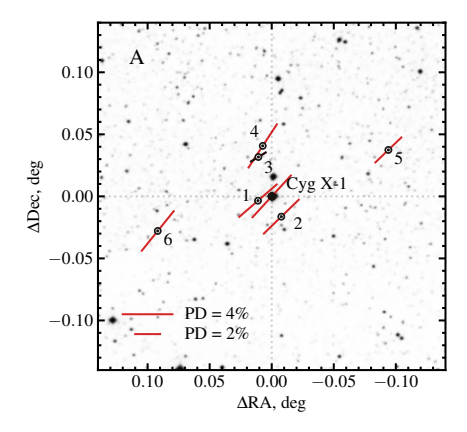
between the two models. However, the uncertainties about the

in a plane-parallel geometry in flat space. It uses exact Compton scattering redistribution matrices for isotropic electrons (69) and solves the polarized radiation transfer equations using an expansion of the intensities in scattering orders. We do not include reflection off the cold disk (11) to avoid uncertainties related to the properties of the reflecting plasma. The code simulates a plane parallel slab, using a prescription to inject seed photons that mimics the truncated disk scenario with the hot flow height-to-radius ratio of 1. The electron temperature is assumed to be $kT_{\rm e}=100\,{\rm keV}$, the seed blackbody temperature $kT_{\rm bb}=0.1\,{\rm keV}$ and the Thomson optical depth $\tau_{\rm T}=1.0\,(70,71)$. Analytical prescriptions are used to account for the impact of special and general relativistic effects on the observed polarization degree and angle (72) in the Schwarzschild metrics.

shape and properties of the corona and the disk preclude us from drawing firm conclusions. The polarization degree of the observed keV photons are higher if the corona Compton scatters synchrotron photons (rather than accretion disk photons). In this case, $\sim\!\!4\%$ polarization degrees can already be observed for $i \geq 45^\circ$ (Figure S9). As the synchrotron photons initially have lower energies ($\sim\!\!1-10$ eV) than the accretion disk photons ($\sim\!\!0.1$ keV), more scatterings are required to scatter them into the keV energy range, leading to high but rather constant 2-8 keV polarization degrees.

Figures S9 and S10 summarize the polarization predictions. Figure S9 shows the simulation results for models with coronae extending parallel to the accretion disk. The sandwich corona simulated with KERRC generates sufficiently large polarization

Figure S10 shows the simulation results for models with coro-



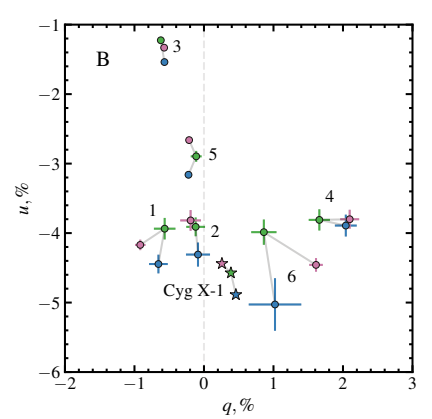


Figure S11: Polarization of nearby field stars around Cyg X-1. (A) Polarization vectors of the field stars (open circles) and Cyg X-1 (filled circle) in the B-filter, with field stars image as a background. The length of the solid lines is proportional to the polarization degree. The deviations in declination $(\Delta \mathrm{Dec})$ and right ascension $(\Delta \mathrm{RA})$ are relative to the Cyg X-1 position (grey dotted lines). (B) The observed normalized Stokes parameters q and u for the field stars (circles) and Cyg X-1 (stars). Blue, green and magenta colors correspond to B, V, and R filters, respectively. For clarity, the grey solid lines connect the B, V, and R results for each source. Uncertainties are 1σ . The vertical grey dashed line indicates the q=0 axis. Stars Ref 1 and Ref 2 are chosen as the IS polarization standards.

nae located on the spin axis of the accretion disk. The cone shaped corona simulated with KERRC includes the effects of the reflected emission and exhibits small (< 2%) 2–8 keV polarization degree for $i=30^\circ$ and $i=45^\circ$ inclinations. For $i=60^\circ,$

the polarization of the emission from the corona reaching the observer directly, and the emission from the corona reflecting off the disk cancel to give $\lesssim 1\%$ polarization degree at all energies. For $i=75^\circ$, the polarization parallel to the disk is higher, giving a net polarization was calculated reaching $\sim\!\!3\%$. Although even larger inclination can produce polarization degree meeting or exceeding the observed 4% polarization degree, the direction stays parallel to the disk, contradicting the observed alignment of the polarization direction and the radio jet. The polarization of the Monk extended lamppost model (including the effect of the reflected emission) was calculated for a=0 and a=0.998, respectively. The high-spin models exhibit polarization degree meeting or exceeding the observed 4% polarization degree but again, the polarization direction is parallel to the accretion disk.

Optical polarimetry

The optical polarimetric observations were performed using DIPol-2 polarimeter, installed on the remotely operated Tohoku 60 cm (T60) telescope at the Haleakala Observatory, Hawaii. DIPol-2 is a double-image CCD polarimeter, capable of measuring linear and circular polarization in three (B, V, and R) optical filters simultaneously (73, 74). The design of this instrument optically eliminates the sky polarization (even if it is variable) to a polarization level of $<10^{-5}$. The instrumental polarization is $<10^{-4}$ and measured by observing twenty unpolarized nearby stars. The zero point of the polarization angle was determined by observing two highly polarized standard stars (HD 20 4827 and HD 25 443).

We observed Cyg X-1 for five nights during the week 2022 May 15 to 21, for about 4 hours each night. Each measurement of Stokes parameters took about 20 s and we obtained 2298 simultaneous measurements of the normalized Stokes parameters $q_{\rm obs} = Q_{\rm obs}/I_{\rm obs}$ and $u_{\rm obs} = U_{\rm obs}/I_{\rm obs}$ in the three filters (B, V, and R). These individual measurements were used to compute average intranight values of Stokes parameters using the 2σ weighting algorithm (74, 75). The uncertainty of the final average corresponds to the standard deviation of individual measurements resulting from the orbital variability of the source. The polarization produced by the interstellar (IS) medium was estimated by observing a sample of field stars (Figure S11), which are close in distance to the target as indicated by their Gaia parallaxes (Figure S12) (76, 77). Taking into account angular separation on the image, closeness in distance, and the wavelength dependence of the polarization, we choose two stars (designating them Ref 1 and Ref 2) from our sample as the IS polarization standards (see Figure S11). We considered two cases: the Stokes parameters of the IS polarization were set to be equal to those of Ref 2, and, alternatively, to the weighted average of those of Ref 1 and Ref 2. For both cases, the normalized Stokes parameters (q_{is}, u_{is}) were subtracted from the measured values of Stokes parameters of the target $(q_{\rm obs}, u_{\rm obs})$ to obtain the intrinsic polarization $(q_{\rm int},$ u_{int}) estimates. From this we determine the intrinsic polarization degree (PD) and polarization angle (PA) as

$$PD = \sqrt{q_{\rm int}^2 + u_{\rm int}^2}, \quad PA = \frac{1}{2} atan2(u_{\rm int}, q_{\rm int}).$$
 (S1)

The uncertainty on the polarization degree $\Delta(PD)$ was estimated as the uncertainty of the individual Stokes parameters, and in-

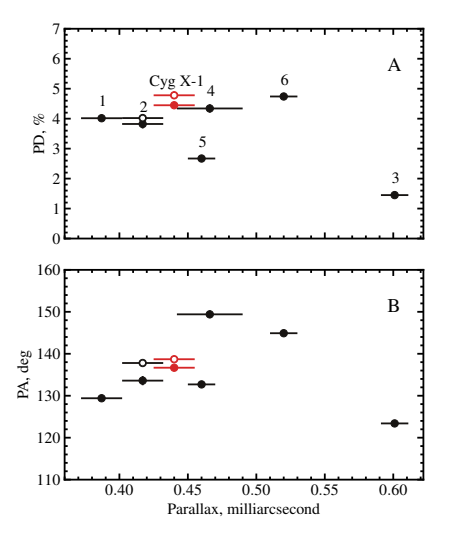


Figure S12: Polarization of nearby field stars around Cyg X-1 as a function of parallax. (A) Polarization degree (PD) and (B) polarization angle (PA) for a set of field stars (black) and Cyg X-1 (red) as measured with DIPol-2 (filled circles) and RoboPol (open circles) in the R-band. Error bars show uncertainties at the 1σ confidence level.

cludes both the source and IS polarization uncertainties. The uncertainty on the polarization angle (in radians) was estimated as $\Delta(\text{PA}) = \Delta(\text{PD})/(2\,\text{PD})$ (78). The observed normalized Stokes parameters, the IS polarization and the intrinsic Stokes parameters as well as the polarization degree and polarization angle are reported in Table **S4**.

We used the RoboPol polarimeter in the focal plane of the 1.3 m telescope of the Skinakas observatory (Greece) to obtain additional R-band polarimetry. The observations were performed between 2022 May 13 and June 2 with multiple pointings in 10 nights. In total, 21 exposures series were acquired, each series consisting of 10 to 20 exposures, each of 1 to 2 seconds duration. The instrumental polarization was found with a set of unpolarized standards stars (BD+284211, BD+332642, BD +32 3739, BD +40 2704, HD 154 892). The zero polarization angle was determined based on three highly polarized standard stars (VI Cyg 12, Hiltner 960 and CygOB2 14). The Cyg X-1 measurements do not reveal any polarization variability exceeding that of the standard stars (for which the standard deviation from the mean values, $\sigma_a = 0.12\%, \sigma_u = 0.08\%$, were obtained). We determined the average polarization parameters of Cyg X-1 from calculating the sigma-clipped median of the relative Stokes parameters. The uncertainties were determined by error propagation adding the instrumental polarization uncertainties in quadrature. We determined the intrinsic source polarization by subtracting the IS polarization using the same Ref 2 star as used in the DIPol-2 analysis (Table S4).

We find optical polarization angles of Cyg X-1 between -37° to -11° , close to the position angle of the jet from radio interferometry (from -26° to -9°) (3, 79). The blue supergiant companion star dominates the optical emission from Cyg X-1 (30). The optical polarization is likely produced by the scattering of the stellar radiation off the bulge formed by the accretion stream interacting with the accretion disk (18).

References and Notes

- J. C. A. Miller-Jones, et al., Science 371, 1046 (2021). doi:10.1126/science.abb3363
- L. Gou, et al., Astrophys. J. 790, 29 (2014). doi:10.1088/0004-637X/790/1/29
- 3. A. M. Stirling, et al., Mon. Not. R. Astron. Soc. 327, 1273 (2001). doi:10.1046/j.1365-8711.2001.04821.x
- C. Done, M. Gierliński, A. Kubota, Astron. Astrophys. Rev. 15, 1 (2007). doi:10.1007/s00159-007-0006-1
- P. A. Connors, T. Piran, R. F. Stark, Astrophys. J. 235, 224 (1980). doi:10.1086/157627
- L.-X. Li, R. Narayan, J. E. McClintock, Astrophys. J. 691, 847 (2009). doi:10.1088/0004-637X/691/1/847
- J. D. Schnittman, J. H. Krolik, Astrophys. J. 701, 1175 (2009). doi:10.1088/0004-637X/701/2/1175
- C. Bambi, et al., Space Sci. Rev. 217, 65 (2021). doi:10.1007/s11214-021-00841-8
- J. D. Schnittman, J. H. Krolik, Astrophys. J. 712, 908 (2010). doi:10.1088/0004-637X/712/2/908
- G. Matt, Mon. Not. R. Astron. Soc. 260, 663 (1993). doi:10.1093/mnras/260.3.663
- J. Poutanen, K. N. Nagendra, R. Svensson, Mon. Not. R. Astron. Soc. 283, 892 (1996). doi:10.1093/mnras/283.3.892
- M. C. Weisskopf, et al., J. Astron. Telesc. Instrum. Syst. 8, 026002 (2022). doi:10.1117/1.JATIS.8.2.026002
- H. Krawczynski, B. Beheshtipour, Astrophys. J. 934, 4 (2022). doi:10.3847/1538-4357/ac7725
- M. C. Weisskopf, et al., Astrophys. J. Lett. 215, L65 (1977). doi:10.1086/182479
- K. S. Long, G. A. Chanan, R. Novick, Astrophys. J. 238, 710 (1980). doi:10.1086/158027
- M. Chauvin, et al., Nature Astronomy 2, 652 (2018). doi:10.1038/s41550-018-0489-x
- 17. Materials and methods are available as supplementary materials
- J. C. Kemp, M. S. Barbour, T. E. Parker, L. C. Herman, Astrophys. J. Lett. 228, L23 (1979). doi:10.1086/182895

- 19. M. C. Begelman, R. D. Blandford, M. J. Rees, 38. P. Freeman, S. Doe, A. Siemiginowska, "Sherpa: a mission-Reviews of Modern Physics 56, 255 (1984). doi:10.1103/RevModPhys.56.255
- 20. F. Haardt, L. Maraschi, Astrophys. J. Lett. 380, L51 (1991). doi:10.1086/186171
- 21. B. E. Kinch, J. D. Schnittman, S. C. Noble, T. R. Kallman, J. H. Krolik, Astrophys. J. 922, 270 (2021). doi:10.3847/1538-4357/ac2b9a
- 22. F. Meyer, E. Meyer-Hofmeister, Astron. & Astrophys. 288, 175 (1994).
- 23. P. O. Petrucci, J. Ferreira, G. Henri, J. Malzac, C. Foellmi, Astron. & Astrophys. 522, A38 (2010). doi:10.1051/0004-6361/201014753
- 24. A. Veledina, J. Poutanen, I. Vurm, Mon. Not. R. Astron. Soc. 430, 3196 (2013). doi:10.1093/mnras/stt124
- 25. J. M. Bardeen, J. A. Petterson, Astrophys. J. Lett. 195, L65 (1975). doi:10.1086/181711
- 26. J. A. Tomsick, et al., Astrophys. J. 780, 78 (2014). doi:10.1088/0004-637X/780/1/78
- 27. M. L. Parker, et al., Astrophys. J. 808, 9 (2015). doi:10.1088/0004-637X/808/1/9
- 28. P. Lachowicz, A. A. Zdziarski, A. Schwarzenberg-Czerny, G. G. Pooley, S. Kitamoto, Mon. Not. R. Astron. Soc. 368, 1025 (2006). doi:10.1111/j.1365-2966.2006.10219.x
- 29. D. M. Russell, T. Shahbaz, Mon. Not. R. Astron. Soc. 438, 2083 (2014). doi:10.1093/mnras/stt2330
- 30. A. A. Zdziarski, P. Pjanka, M. Sikora, Ł. Stawarz, Mon. Not. R. Astron. Soc. 442, 3243 (2014). doi:10.1093/mnras/stu1009
- 31. M. Lyutikov, V. I. Pariev, D. C. Gabuzda, Mon. Not. R. Astron. Soc. 360, 869 (2005). doi:10.1111/j.1365-2966.2005.08954.x
- 32. P. Thalhammer, J. Wilms, N. Rodriguez Cavero, Zenodo, DOI: 10.5281/zenodo.7140274 (2022).
- 33. V. Kravtsov, et al., Zenodo, DOI: 10.5281/zenodo.7108247 (2022).
- 34. D. Blinov, S. Kiehlmann, N. Mandarakas, R. Skalidis, Zenodo, DOI: 10.5281/zenodo.7127802 (2022).
- 35. W. Zhang, M. Dovčiak, M. Bursa, Astrophys. J. 875, 148
- 36. A. Veledina, J. Poutanen, Zenodo, DOI: 10.5281/zenodo.7116125 (2022).
- 37. K. A. Arnaud, "XSPEC: The First Ten Years". in Astronomical Data Analysis Software and Systems V, G. H. Jacoby, J. Barnes, Eds. (vol. 101 of Astronomical Society Pacific Conference Series, 1996), pp. 17-20.

- independent data analysis application", in Proc. SPIE 4477, Astronomical Data Analysis, J.-L. Starck, F. D. Murtagh, Eds. (Society of Photo-Optical Instrumentation Engineers, 2001), pp. 76-87.
- 39. S. Doe, et al., "Developing Sherpa with Python", in Astronomical Data Analysis Software and Systems XVI, R. A. Shaw, F. Hill, D. J. Bell, eds. (vol. 376 of Astronomical Society of the Pacific Conference Series, 2007), pp. 543-546.
- 40. B. L. Refsdal, et al., "Sherpa: 1D/2D modeling and fitting in Python", in Proc. 8th Python in Science Conference, G. Varoquaux, S. van der Walt, J. Millman, eds. (Pasadena, CA USA, 2009), pp. 51-57.
- 41. B. Refsdal, S. Doe, D. Nguyen, A. Siemiginowska, "Fitting and Estimating Parameter Confidence Limits with Sherpa", in Proc. 10th Python in Science Conference, S. van der Walt, J. Millman, eds. (2011), pp. 10-16.
- 42. F. Kislat, B. Clark, M. Beilicke, H. Krawczynski, Astroparticle Physics 68, 45 (2015).
- 43. L. Baldini, et al., SoftwareX 19, 101194 (2022), https://ixpeobssim.readthedocs.io/en/ latest/?badge=latest, https://github.com/ lucabaldini/ixpeobssim. Accessed: 2012-10-05.
- 44. M. C. Weisskopf, R. F. Elsner, S. L. O'Dell, "On understanding the figures of merit for detection and measurement of xray polarization", in Proc. SPIE 7732, Space Telescopes and Instrumentation 2010: Ultraviolet to Gamma Ray, M. Arnaud, S. S. Murray, T. Takahashi, Eds. (Society of Photo-Optical Instrumentation Engineers, 2010), p. 77320E.
- 45. F. Muleri, "Analysis of the data from photoelectric gas polarimeters", in Handbook of X-ray and Gamma-ray Astrophysics, C. Bambi, A. Santangelo, Eds. (Springer, Singapore, in press).
- 46. T. E. Strohmayer, Astrophys. J. 838, 72 (2017).
- 47. F. A. Harrison, et al., Astrophys. J. 770, 103 (2013).
- 48. Heasoft, "a unified release of the ftools and xanadu software packages", https://heasarc.gsfc.nasa. gov/docs/software/heasoft/. Accessed: 2012-09-22.
- 49. K. C. Gendreau, Z. Arzoumanian, T. Okajima, "The Neutron star Interior Composition ExploreR (NICER): an Explorer mission of opportunity for soft x-ray timing spectroscopy", in Proc. SPIE 8443, Space Telescopes and Instrumentation 2012: Ultraviolet to Gamma Ray, T. Takahashi, S. S. Murray, J.-W. A. den Herder, Eds. (Society of Photo-Optical Instrumentation Engineers, 2012), p. 844313
- 50. M. Pavlinsky, et al., Astron. & Astrophys. 650, A42 (2021).
- 51. R. Sunyaev, et al., Astron. & Astrophys. 656, A132 (2021).

- 52. Integral off-line scientific analysis software (osa), 74. V. Piirola, I. A. Kosenkov, A. V. Berdyugin, S. V. Berdyughttps://heasarc.gsfc.nasa.gov/docs/ integral/inthp_analysis.html. Accessed: 2012-09-22.
- 53. M. Matsuoka, et al., Publ. Astron. Soc. Japan 61, 999
- 54. R. Whitehurst, A. King, Mon. Not. R. Astron. Soc. 249, 25 (1991).
- 55. M. M. Kotze, P. A. Charles, Mon. Not. R. Astron. Soc. 420, 1575 (2012).
- 56. J. Poutanen, A. A. Zdziarski, A. Ibragimov, Mon. Not. R. Astron. Soc. 389, 1427 (2008).
- 57. D. R. Gies, et al., Astrophys. J. 678, 1237 (2008).
- 58. M. Dovčiak, F. Muleri, R. W. Goosmann, V. Karas, G. Matt, Astrophys. J. 731, 75 (2011).
- 59. J. Podgorný, M. Dovčiak, F. Marin, R. Goosmann, A. Różańska, Mon. Not. R. Astron. Soc. 510, 4723 (2022).
- 60. J. Poutanen, R. Svensson, Astrophys. J. 470, 249 (1996).
- 61. J. García, T. R. Kallman, R. F. Mushotzky, Astrophys. J. 731, 131 (2011).
- 62. J. García, et al., Astrophys. J. 768, 146 (2013).
- 63. J. García, et al., Astrophys. J. 782, 76 (2014).
- 64. S. Chandrasekhar, Radiative transfer (Dover Publications, 1960).
- 65. J. Malzac, A. M. Dumont, M. Mouchet, Astron. & Astrophys. 430, 761 (2005).
- 66. J. Poutanen, A. Veledina, A. A. Zdziarski, Astron. & Astrophys. 614, A79 (2018).
- 67. K. Nishikawa, I. Duţan, C. Köhn, Y. Mizuno, Living Reviews in Computational Astrophysics 7, 1 (2021).
- 68. N. Sridhar, L. Sironi, A. M. Beloborodov, MNRAS, in press arXiv:2203.02856 (2022).
- 69. D. I. Nagirner, J. Poutanen, Astron. & Astrophys. 275, 325 (1993).
- 70. M. Gierlinski, et al., Mon. Not. R. Astron. Soc. 288, 958 (1997).
- 71. A. A. Zdziarski, J. Poutanen, W. S. Paciesas, L. Wen, Astrophys. J. 578, 357 (2002).
- 72. V. Loktev, A. Veledina, J. Poutanen, Astron. & Astrophys. 660, A25 (2022).
- 73. V. Piirola, A. Berdyugin, S. Berdyugina, "DIPOL-2: a double image high precision polarimeter", in Proc. SPIE 9147, Ground-based and Airborne Instrumentation for Astronomy V, S. K. Ramsay, I. S. McLean, H. Takami, Eds. (Society of Photo-Optical Instrumentation Engineers, 2014), p. 91478I.

- ina, J. Poutanen, Astron. J. 161, 20 (2021).
- 75. I. A. Kosenkov, et al., Mon. Not. R. Astron. Soc. 468, 4362
- 76. Gaia Collaboration, et al., Astron. & Astrophys. 649, A1 (2021).
- 77. L. Lindegren, et al., Astron. & Astrophys. 649, A4 (2021).
- 78. K. Serkowski, Advances in Astronomy and Astrophysics 1,
- 79. M. J. Reid, et al., Astrophys. J. 742, 83 (2011).

Kravtsov V., Berdyugin A.V., Piirola V., Kosenkov I.A., Tsygankov S.S., Chernyakova M., Malyshev D., Sakanoi T., Kagitani M., Berdyugina S.V., Poutanen J Orbital variability of the optical linear polarization of the γ -ray binary LS I +61 303 and new constraints on the orbital parameters

Astronomy & Astrophysics, 2020; 643: A170

Orbital variability of the optical linear polarization of the γ -ray binary LS I +61° 303 and new constraints on the orbital parameters

Vadim Kravtsov^{1,2}, Andrei V. Berdyugin¹, Vilppu Piirola¹, Ilia A. Kosenkov^{1,3}, Sergey S. Tsygankov^{1,2}, Maria Chernyakova^{4,5}, Denys Malyshev⁶, Takeshi Sakanoi⁷, Masato Kagitani⁷, Svetlana V. Berdyugina^{8,9}, and Juri Poutanen^{1,2,10}

- Department of Physics and Astronomy, University of Turku, 20014 Turku, Finland e-mail: vakrau@utu.fi
- ² Space Research Institute of the Russian Academy of Sciences, Profsoyuznaya Str. 84/32, Moscow 117997, Russia
- ³ Department of Astrophysics, St. Petersburg State University, Universitetskiy Pr. 28, Peterhof, 198504 St. Petersburg, Russia
- ⁴ School of Physical Sciences and CfAR, Dublin City University, Dublin 9, Ireland
- ⁵ Dublin Institute for Advanced Studies, 31 Fitzwilliam Place, Dublin 2, Ireland
- ⁶ Institut für Astronomie und Astrophysik Tübingen, Universität Tübingen, Sand 1, 72076 Tübingen, Germany
- Graduate School of Sciences, Tohoku University, Aoba-ku, 980-8578 Sendai, Japan
- ⁸ Leibniz-Institut für Sonnenphysik, Schöneckstr. 6, 79104 Freiburg, Germany
- ⁹ Institute for Astronomy, University of Hawaii, 2680 Woodlawn Drive, Honolulu, HI 96822-1897, USA
- Nordita, KTH Royal Institute of Technology and Stockholm University, Roslagstullsbacken 23, 10691 Stockholm, Sweden

Received 25 June 2020 / Accepted 14 September 2020

ABSTRACT

We studied the variability of the linear polarization and brightness of the γ -ray binary LSI+61° 303. High-precision BVR photopolarimetric observations were carried out with the Dipol-2 polarimeter on the 2.2 m remotely controlled UH88 telescope at Mauna Kea Observatory and the 60 cm Tohoku telescope at Haleakala bservatory (Hawaii) over 140 nights in 2016–2019. We also determined the degree and angle of the interstellar polarization toward LSI+61° 303 using two out of four nearby field stars that have *Gaia*'s parallaxes. After subtracting the interstellar polarization, we determined the position angle of the intrinsic polarization $\theta \simeq 11^{\circ}$, which can either be associated with the projection of the Be star's decretion disk axis on the plane of sky, or can differ from it by 90°. Using the Lomb-Scargle method, we performed timing analyses and period searches of our polarimetric and photometric data. We found statistically significant periodic variability of the normalized Stokes parameters q and u in all passbands. The most significant period of variability, $P_{\text{Pol}} = 13.244 \pm 0.012 \,\text{d}$, is equal to one half of the orbital period $P_{\text{orb}} = 26.496 \,\text{d}$. The fits of the polarization variability curves with Fourier series show a dominant contribution from the second harmonic which is typical for binary systems with circular orbits and nearly symmetric distribution of light scattering material with respect to the orbital plane. The continuous change of polarization with the orbital phase implies co-planarity of the orbit of the compact object and the Be star's decretion disk. Using a model of Thomson scattering by a cloud that orbits the Be star, we obtained constraints on the orbital parameters, including a small eccentricity e < 0.2 and periastron phase of $\phi_p \approx 0.6$, which coincides with the peaks in the radio, X-ray, and TeV emission. These constraints are independent of the assumption about the orientation of the decretion disk plane on the sky. We also extensively discuss the apparent inconsistency with the previous measurements of the orbital parameters from radial velocities. By folding the photometry data acquired during a three-year time span with the orbital period, we found a linear phase shift of the moments of the brightness maximum, confirming the possible existence of superorbital variability.

Key words. binaries: general – gamma rays: stars – polarization – stars: emission-line, Be – stars: individual: LS I +61 303

1. Introduction

Gamma-ray binaries constitute a subclass of high-mass binary systems with the emission peaking in the GeV band (see recent review by Chernyakova & Malyshev 2020). In fact, LS I +61° 303 is one of the best-studied y-ray binaries and was observed in the last few decades over the whole range of the electromagnetic spectrum, from the radio to the very high-energy γ -rays (Taylor & Gregory 1982; Paredes et al. 1994; Zamanov et al. 1999; Harrison et al. 2000; Abdo et al. 2009; Albert et al. 2006). This binary system consists of a B0 Ve star with a circumstellar disk (Casares et al. 2005) and a compact companion star orbiting the primary star on an apparently eccentric ($e \geq 0.5$) orbit. The nature of the compact object, a black hole, or a neutron star is still unknown.

Using a Bayesian analysis of 20 years of radio data, Gregory (2002) determined the orbital period $P_1=26.4960\pm0.0028$ d. The compact object moving around the Be star and interacting with circumstellar matter produces the orbital variability seen in all parts of the spectrum (Taylor et al. 1992; Mendelson & Mazeh 1989; Leahy 2001; Grundstrom et al. 2007). A Lomb-Scargle timing analysis of 37 years of radio data resulted in the detection of the second period, $P_2=26.935\pm0.013$ d (Massi & Torricelli-Ciamponi 2016), which is consistent with a previously determined period of morphological changes in the radio structure, mapped in the VLBI images (Massi et al. 2012). Recently, the VLBA astrometry increased the accuracy of the period to $P_2=26.926\pm0.005$ d (Wu et al. 2018). The beat of these two periods $P_{\rm beat}=(P_1^{-1}-P_2^{-1})^{-1}\approx 1660$ d is very close to the period of the long-term superorbital variability

Table 1. Log of polarimetric observations of LSI+61° 303.

Dates	MJD	$N_{\rm obs}$	Telescope
2016 Sep-2016 Oct	57646-57784	15	UH88
2016 Oct-2017 Jan	57646-57784	20	T60
2017 Sep-2018 Feb	58026-58158	50	T60
2018 Aug-2019 Jan	58337-58474	32	T60
2019 July-2019 Sep	58684-58727	23	T60

 $P_{\text{sup}} \approx 1700 \,\text{d}$ observed in the radio (Massi & Jaron 2013), $H\alpha$ emission (Zamanov et al. 2013), X-rays (Chernyakova et al. 2012; Li et al. 2014), and γ -rays (Ackermann et al. 2013).

From the analysis of the optical spectropolarimetric data, Nagae et al. (2006, 2009) showed that the polarization position angle (PA) was stable over the two-year period at $\theta \simeq 25^\circ$. According to these studies, the linear polarization in LS I +61° 303 arises as a result of Thomson scattering in the Be star's decretion disk, and this disk is most likely co-aligned with the orbit of the compact companion (Nagae et al. 2009).

In this paper, we present the results of our *BVR* high-precision photopolarimetric observational campaign of LSI+61° 303, which allowed us to determine the orbital period directly from the variability of the Stokes parameters of linear polarization for the first time and provide new constarints on the orbital parameters. In addition, we discuss our photometry data obtained for this object in terms of both orbital and superorbital variability.

2. Photopolarimetric observations

2.1. Observed polarization

The observations of LSI+61° 303 were performed with the broad-band BVR polarimeter Dipol-2 (Piirola et al. 2014) mounted on the remotely controlled 2.2 m UH88 telescope at Mauna Kea Observatory and the 60 cm Tohoku telescope (T60) at Haleakala Observatory, Hawaii. The object was observed during 140 nights from 2016 September 15 to 2019 September 1 (MJD 57646-58728). Every night, 24 to 48 measurements of the normalized Stokes parameters q and u were made simultaneously in the B, V, and R-passbands. The total integration time with a typical ten-second exposure was 25-50 min. A summary of our observations is given in Table 1. The observational errors of q and u were computed as the standard errors of the weighted mean values and are in the range of 0.01-0.03%. In each of our five observing runs, the value of instrumental polarization was determined from observations of 15-20 nearby bright, unpolarized stars. The value of instrumental polarization is $\leq 5 \times 10^{-5}$ for all passbands and is measured with the accuracy of a few parts per million (10⁻⁶). To determine the PA zero point, the highly polarized standard stars HD 204827 and HD 25443 were observed. Detailed descriptions of the calibration and observation procedures can be found in Kosenkov et al. (2017) and Piirola et al. (2020). Table 2 shows the observed average values of the polarization degree (PD) $P_{\rm obs}$ and the PA $\theta_{\rm obs}$.

We also extracted the fluxes of LS I+61° 303 and the closest field star (star 4, see Fig. 1) in the B, V, and R passbands from our polarimetry images acquired with the T60 telescope, and we used them for the measurements of relative brightness variations of LS I+61° 303.

2.2. Interstellar and intrinsic polarization

In order to obtain the degree and direction of the intrinsic linear polarization, P_{int} and θ_{int} , it is necessary to estimate the parameters of the interstellar (IS) polarization. For this purpose, we observed the polarization of four of the nearest field stars, located at the angular distance of <7' from LS I +61° 303 (Fig. 1) and with known parallaxes. Figure 2 shows the dependence of the observed PD P and PA θ on parallax for LSI+61° 303 and the field stars (parallaxes are taken from the Gaia Data Release 2; Prusti et al. 2016; Brown et al. 2018). The directions of the IS polarization for the field stars lie in the 110°-125° interval. Assuming that the field stars are intrinsically unpolarized, we see that the degree of IS polarization decreases with distance (i.e., it grows with parallax) from $\approx 4\%$ to $\approx 2\%$ in the closest vicinity of the LS I +61° 303. This unusual behavior may result from the depolarization effect in several dust clouds with nearly orthogonal orientations of the Galactic magnetic field, located along the line of sight toward LSI+61° 303.

For a more detailed study of IS polarization, we analyzed the data from Heiles' stellar polarization catalog (Heiles 2000) in a $10^{\circ} \times 10^{\circ}$ region around LS I + 61° 303. The dependence of PD on distance for 232 stars in this area of the sky is shown in Fig. 3. We see that there is a significant scatter of the IS PD for distant stars. Moreover, the PD of LS I + 61° 303 is smaller than that of all field stars at similar distances. It means that LS I + 61° 303 has a significant intrinsic polarization of which the direction does not match that of the IS polarization. The large scatter in the degree of IS polarization at the distances d > 2 kpc may be linked to the complex structure of the IS medium inside the Heart Nebula (IC 1805) that is located in close proximity to LS I + 61° 303. Thus, a careful approach, taking into account both proximity to the line of sight and proximity in distance, must be used for estimating the IS polarization for this object.

We chose the average polarization of two nearby field stars (#1 and #2), which are close in distance to LS 1+61° 303, as the best estimate for the IS polarization in the direction of the binary. Table 2 shows the estimated values $P_{\rm is}$ and $\theta_{\rm is}$ of the IS polarization in all passbands and the average values $P_{\rm int}$ and $\theta_{\rm int}$ of the intrinsic polarization for LS I+61° 303, obtained after subtracting IS polarization. The values of IS polarization derived by us are in good agreement with those obtained by Nagae et al. (2006) from the polarization in H α emission line: $P_{\rm is} = 2.20 \pm 0.18\%$, $\theta_{\rm is} = 126^\circ 5 \pm 3^\circ 7$.

The values of the average intrinsic polarization of LSI+61° 303 in the B, V, and R-bands are the same within the errors. This suggests that Thomson scattering on free electrons in the disk around the Be star is likely the polarization mechanism responsible for the constant component of polarization in LSI+61° 303. This conclusion is in agreement with the results obtained by Nagae et al. (2006, 2009). It is interesting to note that the direction of the average intrinsic polarization in all passbands differs from the value of 25° derived by Nagae et al. (2006). The PA of the intrinsic optical polarization of LSI+61° 303, obtained by us as the average for the BVR bands, is ~11°. This difference, however, is most likely a result of uncertainty in the determination of the IS polarization and does not imply physical changes of the disk orientation with time. As we mentioned above, we used the average polarization of two (close in distance) field stars as an estimate of the IS polarization, whereas Nagae et al. (2009) used polarization in $H\alpha$ and the empirical Serkowski law (Serkowski 1973), which is not applicable when the structure of the IS medium is complex (i.e., consisting of multiple clouds of different properties), as is

Table 2. Observed PD and PA of LS I +61° 303, interstellar polarization and average intrinsic polarization.

	Observed		Interstellar		Intrinsic	
Filter	P _{obs} (%)	$\theta_{ m obs}$ (deg)	P _{is} (%)	$\theta_{\rm is}$ (deg)	$P_{ m int}$ $(\%)$	$\theta_{\rm int}$ (deg)
В	1.14 ± 0.05	139.5 ± 1.5	2.31 ± 0.03	117.3 ± 0.5	1.66 ± 0.07	13.5 ± 0.9
V	1.21 ± 0.05	136.4 ± 1.2	2.40 ± 0.03	115.0 ± 0.5	1.72 ± 0.05	10.8 ± 0.7
R	1.25 ± 0.04	135.4 ± 1.0	2.34 ± 0.03	113.9 ± 0.5	1.66 ± 0.05	8.4 ± 0.7

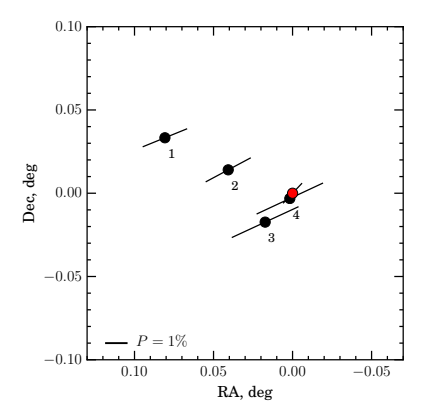


Fig. 1. Polarization map of LS I+61° 303 (red circle at the origin) and field stars (black circles) in the R band. The length of the bars corresponds to the degree of linear polarization P, and the direction corresponds to the PA θ (measured from the north to the east).

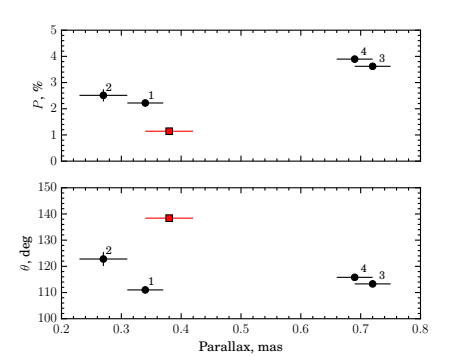


Fig. 2. Dependence of observed PD P and PA θ on parallax (Gaia DR2) for LS1+61° 303 (red) and field stars (black) in the B band. The numbering of the field stars is the same as in Fig. 1. The error bars correspond to the 1σ errors.

demonstrated by a peculiar distance dependence of the PD for the nearby field stars shown in Fig. 3.

The intrinsic polarization PA allows us to put constraints on the orientation of the Be circumstellar disk on the sky. As was shown by Quirrenbach et al. (1997) for four Be stars, the polarization vector is parallel to the projection of the rotation

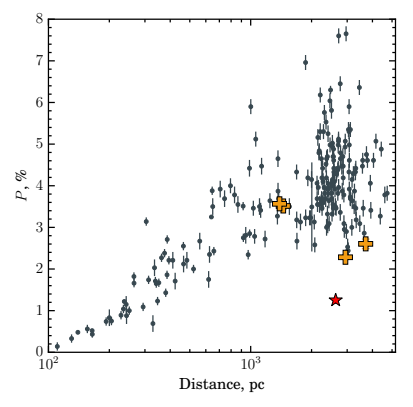


Fig. 3. Dependence of linear PD P (Heiles 2000) on distance (evaluated from the inverse of the Gaia DR2 parallaxes) for the stars in the $10^{\circ} \times 10^{\circ}$ area around LS1+61° 303 in the R band. The red star indicates our value of the observed polarization of LS1+61° 303, the orange crosses correspond to the four nearby field stars shown in Fig. 1. The vertical bar corresponds to the 1σ error in polarization.

axis of the circumstellar disk. However, all their stars showed wavelength-dependent PD, which is an indication of the important role of bound-free hydrogen absorption in the envelope of a Be star. On the other hand, our intrinsic PD does not depend on the wavelength, implying that the electron scattering dominates. In this case, if the disk is optically thick, the polarization vector of radiation escaping from the disk may be perpendicular to the PA of the rotational axis (Chandrasekhar & Breen 1947; Sobolev 1949; Wood et al. 1996). In the following, we consider both possibilities.

3. Orbital variability

3.1. Polarization variability

The variability curves for the Stokes parameters q and u in the V band, obtained over three years of observations of LS I +61° 303, are shown in Fig. 4. Our observations have revealed a small but significant variability with the amplitude of 0.2–0.3% in all passbands. To study this variability, we performed a timing analysis of our BVR polarimetric data. For this purpose, we applied the Lomb-Scargle method 1 of spectral analysis (Lomb 1976; Scargle 1982), using the ASTROPY package (Astropy Collaboration 2018).

https://docs.astropy.org/en/stable/timeseries/
lombscargle.html

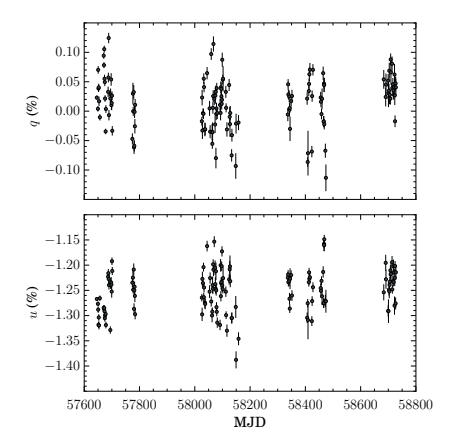


Fig. 4. Observed Stokes parameters q (top panel) and u (bottom panel) with 1σ errors for LS1+61° 303 in the V band, measured from 2016 September 15 to 2019 September 1 (MJD 57646–58728).

The Lomb-Scargle periodograms for the normalized Stokes parameter u in the BVR passbands are shown in Fig. 5. We see that the period of the highest peak in each band is close to one half of the orbital period $P_{\text{orb}} = 26.4960 \pm 0.0028 \,\text{d}$, as is expected in binary systems. Despite significant nonperiodic scatter, this peak is clearly present in all passbands and both Stokes q and u. For example, the period in the V band in Stokes u is $P_V =$ $13.25 \pm 0.06 \, d$ with a false alarm probability $\sim 10^{-5}$, which was independently estimated using an analytical approximation of Baluev (2008) and a bootstrap method from the ASTROPY package. The error on the found period was estimated in two different ways. In the first case, we simulated 10⁴ light curves, varying the observed data points around the mean values in accordance with the observational errors. In the second case, we also simulated 10⁴ light curves assuming sinusoidal variations with the fixed period $P = 13.25 \,\mathrm{d}$ and the amplitude, time stamps, and errors as in the observed data. For both cases, we computed the periodograms of the light curves and estimated an error on the found period as the half width of the distribution of the highest peak positions. The value of the error in the first case was from three to ten times larger than in the second case, depending on the passband, due to the presence of the superorbital variability and other possible periodicities in the data. For the final error estimate, we chose the largest of the two. The mean for the three passband periods in Stokes u is $P_{\rm pol} = 13.244 \pm 0.012$ d, which differs by less than 1σ from $P_{\rm orb}/2$. Thus, for the very first time, the orbital period of LSI+61° 303 was obtained directly from the polarimetric measurements.

Folding the data with the orbital period using the ephemeris given in Aragona et al. (2009), we obtained the phase curves for the PD $P_{\rm int}$ and the PA $\theta_{\rm int}$ of the intrinsic polarization (Fig. 6) and for the normalized Stokes parameters $q_{\rm int}$ and $u_{\rm int}$ (Fig. 7). The synchronization of the variable component of linear polarization in LSI+61° 303 with the phase of the orbital period clearly indicates that it arises due to the orbital motion of the compact component. In the binary system with the compact companion and Be star, the extended hot region with enhanced electron density can be formed around or near a neutron star or a black hole in a process of their interaction with the disk material.

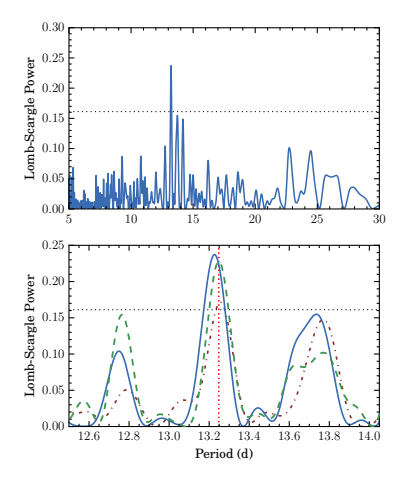


Fig. 5. Top panel: Lomb-Scargle periodogram for normalized Stokes parameter u in the B band. Bottom panel: Lomb-Scargle periodogram zoom for the normalized Stokes parameter u in the B, V, and R bands (solid blue, dashed green, and dotted red curves, respectively). The horizontal dashed line corresponds to false alarm probability (FAP) = 1%. The vertical red line corresponds to one half of the orbital period $P_{\text{orb}} = 26.496 \text{ d.}$

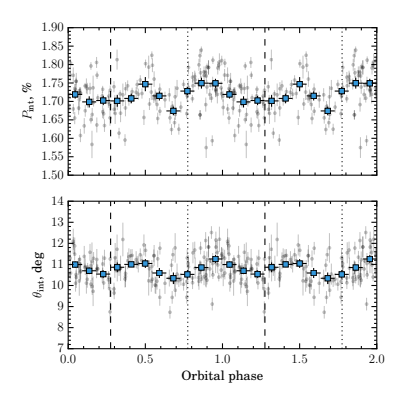


Fig. 6. Orbital variability of intrinsic PD $P_{\rm int}$ and PA $\theta_{\rm int}$ of LS1+61° 303 in V band. The filled blue squares with 1σ errors correspond to the average values of the individual observations (represented by gray circles with error bars) and the standard errors of the mean calculated within the phase bins of width $\Delta \phi = 0.091$. The vertical dashed lines correspond to the phases of periastron ($\phi = 0.275$) and apastron ($\phi = 0.775$) as derived by Aragona et al. (2009).

Thomson scattering of stellar photons on such a structure orbiting Be star can explain the regular small-amplitude variations in the observed polarization of LS I+61° 303. Moreover, a continuous change of polarization implies co-planar orientation of the orbit and the Be star decretion disk. This conclusion directly follows on from the observed polarization variability and does not require any assumptions on the nature of compact companion (see Nagae et al. 2009). There is also a strong nonperiodic

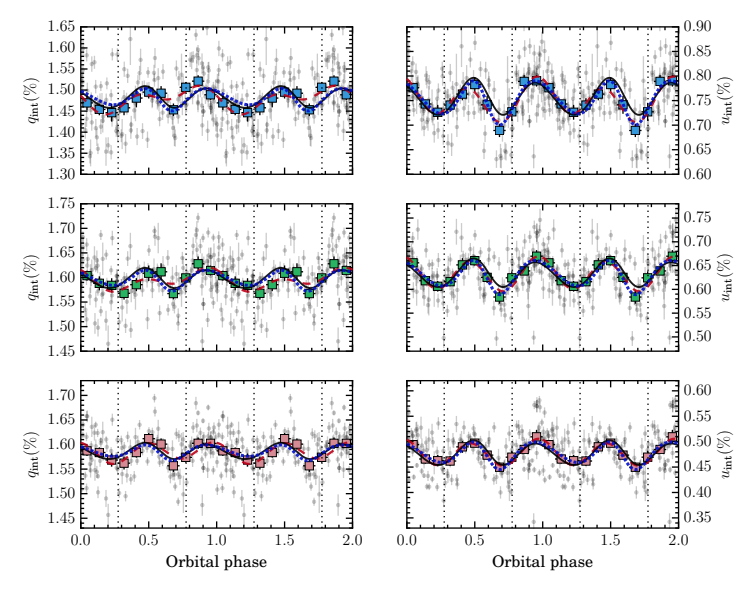


Fig. 7. Variability of intrinsic Stokes parameters q_{int} (left column) and u_{int} (right column), in B, V, and R bands (top, middle and bottom panels, respectively) with the orbital phase folded with the period $P_{orb} = 26.496 \,\mathrm{d}$. The filled squares with 1σ errors correspond to the average values of the individual observations (gray circles with error bars) and the standard errors of the mean calculated within phase bins of width $\Delta \phi = 0.091$. The vertical dashed lines correspond to the phases of periastron ($\phi = 0.275$) and apastron ($\phi = 0.775$) as derived by Aragona et al. (2009). The red dashed lines show the best fit with Fourier series given by Eq. (1). The black solid and blue dotted lines correspond to the best fit model of a scattering cloud on an eccentric orbit from Sect. 3.3, for an Ω constrained close to θ_{int} and with a free Ω , respectively.

component, which arises due to the long- and short-term changes in the distribution and density of the light scattering material in the Be decretion disk.

The dominant second harmonic in the variability of the Stokes parameters is typical for a binary system with symmetric density distribution of the scattering matter about the orbital plane and a circular orbit (Brown et al. 1978). The polarization arising from light scattering on gaseous structures like clouds, streams, and so on, peaks at orbital phases where the scattering angle is close to 90°. For a co-rotating envelope and a circular binary orbit, this gives two prominent symmetric peaks in polarization separated by the phase interval ~0.5. In the case of a (weak) asymmetry of the distribution of the light scattering material about the orbital plane, the first harmonic appears. This is apparently observed in LSI+61° 303. As we see in Figs. 6 and 7, there are two nearly symmetric peaks near the phases 0.5 and 1.0. They are most pronounced in the variations of the Stokes u and the PA θ .

3.2. Modeling polarization with circular orbit

According to the common approach (Brown et al. 1978), the phase curves of the Stokes parameters in binary systems with a circular orbit and co-rotating light scattering envelope can be represented through a Fourier series of the orbital longitude $\lambda = 2\pi\phi$ (where ϕ is a phase of the orbital period):

$$q_{\text{int}} = q_0 + q_1 \cos \lambda + q_2 \sin \lambda + q_3 \cos 2\lambda + q_4 \sin 2\lambda, u_{\text{int}} = u_0 + u_1 \cos \lambda + u_2 \sin \lambda + u_3 \cos 2\lambda + u_4 \sin 2\lambda.$$
 (1)

We fit the intrinsic Stokes parameters q_{int} and u_{int} with these functions, using q_0 – q_4 and u_0 – u_4 as free parameters. The best fit parameters together with the χ^2 values and the degrees of freedom (d.o.f.) are given in Table 3. The best fit curves are shown in Fig. 7 (red dashed lines). We see that variabilities of Stokes parameters q and u are dominated by the second harmonic of the orbital period. This is expected, because of the position of the highest peak in the Lomb-Scargle periodogram close to the frequency corresponding to one half of the orbital period. The parameters

$$A_q = \sqrt{\frac{q_4^2 + q_3^2}{q_2^2 + q_1^2}}, \quad A_u = \sqrt{\frac{u_4^2 + u_3^2}{u_2^2 + u_1^2}}, \tag{2}$$

giving the ratio of the amplitudes of the second to the first harmonic, attain the values $A_q = 0.9, 1.0, 3.3$ and $A_u = 2.5, 5.5, 5.4$ for the B, V, and R bands, respectively.

It is possible to derive the inclination i of the binary orbit and the position angle Ω of the projection of the orbital axis (see Eqs. (A.17) and (A.18)) from the best fit Fourier coefficients in Eq. (1) to the observed (or intrinsic) Stokes parameters q and u(Drissen et al. 1986):

$$\left(\frac{1-\cos i}{1+\cos i}\right)^4 = \frac{(u_3+q_4)^2 + (u_4-q_3)^2}{(u_4+q_3)^2 + (u_3-q_4)^2}$$

$$\tan 2\Omega = \frac{A+B}{C+D},$$
(4)

$$\tan 2\Omega = \frac{A+B}{C+D},\tag{4}$$

Table 3. Fourier coefficients and their errors of the best fits to the data in BVR bands with Eq. (1).

Filter	q_0	u_0	q_1	u_1	q_2	u_2	q_3	u_3	q_4	u_4	$\chi^2(q)^{(a)}$	$\chi^2(u)^{(b)}$
В	1.479	0.751	-0.0005	0.014	-0.021	0.005	0.008	0.029	-0.017	-0.021	7.1	6.3
	± 0.005	± 0.004	± 0.007	± 0.005	± 0.007	± 0.006	± 0.007	± 0.006	± 0.007	± 0.005		
V	1.594	0.631	0.009	0.006	-0.011	0.001	0.012	0.030	-0.007	-0.013	7.9	3.7
	± 0.004	± 0.003	± 0.006	± 0.005	± 0.006	± 0.004						
R	1.585	0.477	0.0006	0.005	-0.006	-0.0002	0.019	0.022	-0.002	-0.009	7.6	2.2
	± 0.003	± 0.003	± 0.004	± 0.004	± 0.005	± 0.004	± 0.005	± 0.004	± 0.005	± 0.004		

Notes. (a) χ^2 values for Stokes q fit with 6 d.o.f. (b) χ^2 values for Stokes u fit with 6 d.o.f.

wher

$$A = \frac{u_4 - q_3}{(1 - \cos i)^2}, \quad B = \frac{u_4 + q_3}{(1 + \cos i)^2},$$

$$C = \frac{q_4 - u_3}{(1 + \cos i)^2}, \quad D = \frac{u_3 + q_4}{(1 - \cos i)^2}.$$

However, there is a bias in the polarimetrically derived orbit inclination because of the unavoidable noise (finite accuracy) in the polarization data (Aspin et al. 1981; Simmons et al. 1982; Wolinski & Dolan 1994). The inclination of orbit i derived from the best fit Fourier coefficients is always biased toward a higher value. For noisy data, the inclination approaches 90° with wide confidence intervals extending to very low values (see Wolinski & Dolan 1994). Similar bias can also be induced by stochastic noise, arising from an intrinsic nonperiodic component of the polarization variability (Manset & Bastien 2000). As the errors on q and u increase, a straight line becomes an acceptable fit to the (q, u) light curves. Because a straight-line fit to the (q, u) data yields a 90° inclination for the system (Brown et al. 1978), the derived value of i is biased toward 90° when a high noise level is present in the data.

Due to the strong nonperiodic component in the polarization variability of LS 1+61° 303, the inclination of the orbit derived from the Fourier coefficients for all passbands is close to 90° , with 2σ confidence intervals extending down to values of $i \leq 20^\circ$. Thus, assuming a (nearly) circular orbit in LS 1+61° 303, we can only say that our polarization data are consistent with orbit inclination i in the range $\approx\!20^\circ\!-\!90^\circ$. The position angle Q, derived from Eq. (4), is about 30° for all passbands. As was shown by Wolinski & Dolan (1994), there is no bias in the value of Ω derived from polarimetry. This is due to the fact that the value of Ω is determined by the positions of the polarization maxima and minima, which are not affected by the noise in the same way as the amplitude and shape of the polarization variability curve.

3.3. Modeling polarization with an eccentric orbit

The latest value of eccentricity *e* derived for LS I +61° 303 from the radial velocity variations in the optical spectral lines is 0.54 ± 0.03 (Aragona et al. 2009). For such an eccentric orbit, one should expect fast changes in polarization occurring near the periastron passage (Brown et al. 1982; Simmons & Boyle 1984). According to the orbital geometry shown in Fig. 3 of Aragona et al. (2009), we should expect one sharp peak just before, and another one soon after, the periastron passage, which occurs at phase 0.275. These two peaks must be followed by a gradual change of polarization during the remaining part of the orbital motion toward apastron. Such a behavior of intrinsic polarization has been detected in the interacting binary HD 187399, which has an orbit eccentricity of

 $e \simeq 0.4$ (Berdyugin & Tarasov 1998), but this is not observed in LS I +61° 303.

Using the approach proposed by Simmons & Boyle (1984), we tried to model the observed shape of the polarization variability curve in LSI+61° 303. We considered a simple scenario of a small cloud of free electrons orbiting the central illuminating source and scattering its radiation (see Appendix A for the model). Under this assumption, the modeled Stokes parameters depend on the eccentricity e, the orbit inclination i, as well as on the longitude of the periastron λ_p , and typical scattering fraction f_0 (see Eq. (A.16)). Polarization, produced by such a system, depends on time through the orbital longitude λ , which can be connected to the observed orbital phase ϕ through an eccentric anomaly (Eq. (A.19)) and a Kepler equation (Eq. (A.20)). The orbital phase is then corrected for the phase of the periastron ϕ_p (corresponding to $\lambda = \lambda_p$) using Eq. (A.21). The model Stokes pseudo-vector should also be rotated to account for the position angle Ω of the projection of the orbital axis (see Eqs. (A.17) and (A.18)) relative to the north. The constant levels of intrinsic polarization corresponding to the emission from the decretion disk is represented by the pseudo-vectors (q_0, u_0) .

We employed Bayesian inference to fit this model to the intrinsic polarization light curves of LSI+61° 303 in three filters simultaneously, allowing different levels of constant polarization (q_0, u_0) and a typical scattering fraction f_0 in each band. We applied a Hamiltonian Monte Carlo algorithm (Duane et al.) 1987) implemented in the GRETA package (Golding 2019) for R (R Core Team 2019), which utilizes the TENSORFLOW backend (see Abadi et al. 2015). First, we took the eccentricity e = 0.54and the argument of the periastron $\omega = \lambda_p \pm 90^\circ = 40^\circ$ from Aragona et al. (2009), but other parameters were allowed to vary in the broadest possible intervals. We were not able to fit the observed variability of the Stokes parameters q and u for the whole range of reasonable inclinations (i.e., $i = 20^{\circ} - 90^{\circ}$) resulting in $\chi^2/\text{d.o.f.} > 180/54$. Then, we fixed only eccentricity $e \simeq 0.5$ and tried to fit the curves by varying other orbital parameters. We could only fit variations of one Stokes parameter reasonably well, with the resulting $\chi^2/\text{d.o.f.} = 177/53$. Thus, we were not able to find a set of orbital parameters providing a sufficiently good fit for both Stokes q and u for $e \ge 0.5$. This can be simply explained by the influence of eccentricity on the shape of the polarization curve. We can see that in our data (Fig. 7) the distance between the neighboring maxima is $\Delta \phi \approx 0.4$, while in the case of the eccentricity $e \approx 0.5$, it should be $\Delta \phi \approx 0.15$.

Finally, we allowed all parameters, including eccentricity e, to vary. At the first step, we assumed that the projection of the decretion disk axis on the sky coincides with the PA of the average intrinsic polarization. If the orbit of the compact object and the decretion disk are nearly co-planar (see Sect. 3.1), we expect that $\Omega \approx \theta_{\rm int}$. We thus limited the prior distribution of Ω to follow a Gaussian with the peak at 11° ($\theta_{\rm int}$ from Table 2) with

Table 4. Best fit parameter estimates for the model described in Sect. 3.3 and Appendix A.

Filter	e (a)	i (a)	Ω (a)	$\lambda_{\rm p}$ (a)	$\phi_{\rm p}^{~(a)}$	q_0	<i>u</i> ₀	f_0	χ^2 /d.o.f.
		(deg)	(deg)	(deg)		(%)	(%)	(%)	
					$\Omega = \theta_{int} \pm 1$	0°			
B						1.458 ± 0.007	0.721 ± 0.007	0.23 ± 0.03	
V	0.06 ± 0.02	86 ± 3	28 ± 3	146 ± 22	0.62 ± 0.07	1.579 ± 0.005	0.605 ± 0.006	0.18 ± 0.03	67/52
R						1.571 ± 0.005	0.454 ± 0.005	0.15 ± 0.02	
					Free Ω				
B						1.503 ± 0.006	0.790 ± 0.006	0.24 ± 0.03	
V	0.11 ± 0.03	87 ± 3	120 ± 2	225 ± 13	0.59 ± 0.04	1.614 ± 0.005	0.661 ± 0.005	0.19 ± 0.03	50/52
R						1.599 ± 0.004	0.499 ± 0.004	0.14 ± 0.02	

Notes. Errors are 1σ . (a) Parameter is the same for all three filters.

an arbitrarily chosen standard deviation of 10° and truncation interval of [-10° ; 40°]. The best fit parameters together with the values of χ^2 and the d.o.f. are given in the upper part of Table 4, and a comparison of the model with the data is shown in Fig. 7. The posterior distributions are shown in Fig. 8. A corresponding orbital geometry is demonstrated in the left panel of Fig. 9.

We see that our eccentric orbit fit gives an upper limit on e of 0.15, with the best fit value $e \simeq 0.06$. The high value of inclination i obtained from the eccentric orbit fit is most likely a result of a similar bias as for the circular orbit model. The best fit value of $\Omega \approx 28^\circ$ coincides with the value of 30° obtained from the fits with the circular orbit model in Sect. 3.2. The best fit phase of the periastron $\phi_p \approx 0.62$ differs significantly from the usually assumed value of 0.275. We note that some of the parameters are degenerate: for example, λ_p and Ω can be substituted by $\lambda_p \pm 180^\circ$ and $\Omega \pm 180^\circ$ without affecting the Stokes parameters. Furthermore, at low eccentricities (such as the best fit values that we obtained), λ_p and ϕ_p are correlated (see Eqs. (A.19)–(A.21)). This effect can be observed in the joint posterior distribution of λ_p and ϕ_p shown in Fig. 8.

As it follows from the formulae given in the appendix of the paper by Simmons & Boyle (1984)² a large orbit eccentricity should lead to the appearance of a noticeable third harmonic of the orbital period in the variations of q and u. However, in the observed polarization variability of LS I +61° 303, the contribution from this harmonic is insignificant. A good fit can only be obtained if we assume a nearly circular orbit (producing a strong second harmonic). Thus, the behavior of the variable component of linear polarization in LS I +61° 303 is in an apparent contradiction with a high ($e \ge 0.5$) value of the eccentricity of the binary orbit.

We note that the χ^2 value of the fit with constrained Ω seems too large (67 for 52 d.o.f.). Therefore, at the next step, we relaxed the constraints on Ω , choosing a very wide prior interval. The best fit parameters together with the values of χ^2 and the d.o.f. are shown in Fig. 10. The comparison of the model to the data is shown in Fig. 7 with the blue dotted line. A sketch of the possible orbit is pictured in the right panel of Fig. 9. We note that the χ^2 value of the fit is much smaller than in the case of constrained Ω (50 versus 67) and the best-fit $\Omega \approx 120^\circ$, which differs by 90° from the value obtained in the first case. Such a value for Ω can be interpreted in two different ways. This might indicate that the orbit of the compact object is nearly perpendicular to the disk

plane, which is not likely (see Sect. 3.1). A more probable interpretation is that the projection of the decretion disk axis makes a 90° angle to the average intrinsic PA, and the orbit of the compact object is nearly co-planar to the disk (i.e., $\Omega \approx \theta_{int} + 90^{\circ}$). In this geometry, the polarization vector of radiation scattered in a cloud is predominantly perpendicular to the PA of the average polarization associated with the disk. This explains why, at the phases where the scattering angle is about 90° and maximum polarization of the scattered radiation is expected (i.e., at $\phi \approx 0.2$ and 0.7), the minima are observed in both q and u. Despite a very different geometry, the best fit eccentricity is identical to the case of $\Omega \approx \theta_{int}$. Also the best fit phase of the periastron ϕ_p is still very close to 0.6. Thus, we conclude that the obtained values for the eccentricity and the periastron phase are robust and do not depend on our assumptions on the disk and compact object orbit orientations. We discuss the implications of the obtained orbital parameters in Sect. 5.

4. Optical photometry

In addition to the optical polarimetry, we also studied the brightness variations of LS I+61° 303 in the B, V, and R passbands by measuring the ratio of the fluxes from the binary and the nearest field star #4. For the images taken with the UH88 telescope, the small size of the field of view places star #4 too close to the edge of the image field, preventing us from using these images for reliable relative photometry. Thus, only the images taken with the T60 telescope have been used. An example of the light curve in the V band, obtained from three years of observations, is shown in Fig. 11.

As in the case of the Stokes parameters, we used a Lomb-Scargle timing analysis to find the period of the variability of the brightness in LS I +61° 303. The frequency of the highest peak on the Lomb-Scargle periodograms (Fig. 12) is close, but not exactly equal to the orbital period $P_{\rm orb} = 26.4960 \pm 0.0028$ d. For the BVR bands, the determined periods are $P_B = 26.56 \pm 0.05$, $P_V = 26.58 \pm 0.04$, and $P_R = 26.60 \pm 0.03$ d, with the false alarm probabilities $\sim 10^{-5}$, 10^{-10} , and 10^{-14} , respectively. The errors of the periods were estimated via the randomization of the data within 6σ interval and recalculation of the periodogram (number of recalculations N = 10000).

The light curves of LSI+61° 303, folded with the orbital period $P_{\rm orb}$ are shown in Fig. 13. The shape of these curves (sinusoidal-like wave with an amplitude of about 0.03 mag, minimum near the periastron and maximum in the apastron) is in a good agreement with the previous results obtained by Mendelson & Mazeh (1989), Zaitseva & Borisov (2003), and

² The paper by Simmons & Boyle (1984) contains an error in Eq. (A.2): inside the last square brackets, the "+" sign is missing between the terms $2e\cos(\lambda-\lambda_p)$ and $(e^2/2)\cos[2(\lambda-\lambda_p)]$.

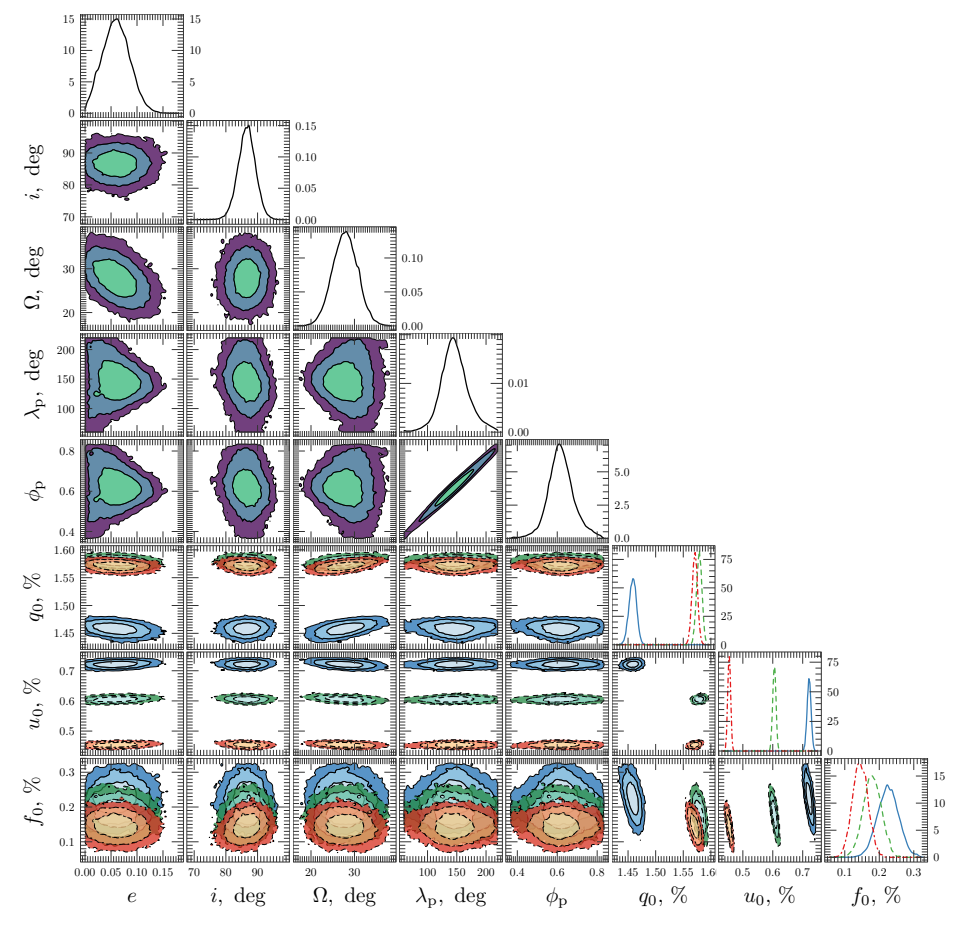


Fig. 8. Posterior distributions for parameters of model described in Sect. 3.3 and Appendix A for $\Omega = \theta_{int} \pm 10^\circ$. Diagonal panels: distributions of model parameters. The blue solid, green dashed, and red dot-dashed lines correspond to per-passband B, V, and R distributions, respectively. Lower-triangle panels: joint posterior distributions of two parameters. The green, blue, and violet contours correspond to 0.68, 0.95, and 0.997 probability levels of parameters i, Ω , λ_p , and ϕ_p . The shades of blue, green, and red correspond to the same probability levels for B, V, and R filters, respectively.

Paredes-Fortuny et al. (2015). Like in the case of polarization variability, there is a noticeable scatter around the light curves in all passbands, which indicates the presence of a nonperiodic component.

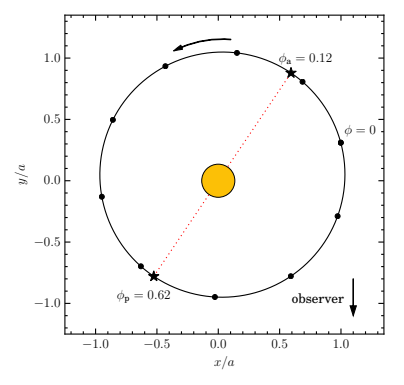
In order to find a possible superorbital phase shift of the maximum of brightness, which is discussed for example in Paredes-Fortuny et al. (2015), we divided our data into eleven subsets (see Table 5 and Fig. 11). We then folded them with the orbital period P_{orb} and fit with the function

$$m(\phi) = -A\cos[2\pi(\phi - \phi_0)] + m_0,$$
 (6)

where ϕ_0 (phase of the peak), A (amplitude), and m_0 (vertical offset) are free parameters. The data and the best fit curves are

shown in Fig. 14. The values of the best fit parameters are given in Table 5. The errors on the parameters were calculated as a square root of the diagonal elements of the covariance matrix of the fit. The measurement errors are smaller than the intrinsic scatter in the photometric data. For a more accurate estimation of errors of the fit parameters, we used the standard deviation of the data instead of the measurement errors for the fitting (in that case, the reduced $\chi^2 \approx 1$).

We see from Fig. 14 that there is a significant phase shift by $\Delta\phi_0\approx 0.3$ seen between observing seasons S1 and S11. The quality of fits for the first two seasons, S1 and S2, are quite low, but the linear shift of the phase of the maximum of brightness is apparent even without them. Thus, our new photometry data are in agreement with the results obtained by



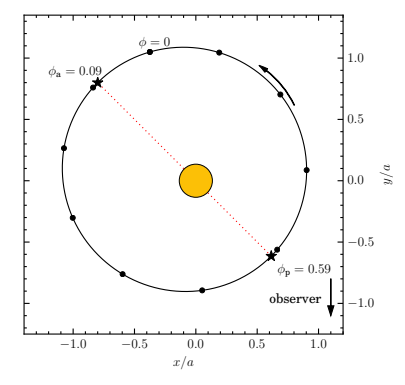


Fig. 9. Relative orbit of a compact object in LS I+61° 303 around Be star (yellow circle at the origin), which lies at the ellipse focus. The orbital parameters are taken from Table 4. The red dashed line is the major axis of the orbit. The black dots on the ellipse are spaced by the $\Delta \phi = 0.1$. Because of a 180° degeneracy in λ_p , the orbit can be also rotated by 180°. *Left panel*: orbit for constrained orientation relative to the decretion disk plane with $\Omega = \theta_{int} \pm 10^\circ$. *Right panel*: orbit assuming free Ω .

Paredes-Fortuny et al. (2015). The relatively short time baseline (three years) does not allow us to conclude whether this shift is periodic (superorbital) or linear. We have also studied a dependence of the amplitude of brightness variability over time (see bottom panel of Fig. 15). As is seen, there is no apparent trend here, unlike the one seen in the phase of the maximum. We must emphasize that, due to the presence of the nonperiodic brightness fluctuations, studying possible periodic (superorbital) events is complicated. These fluctuations introduce significant noise, which may completely diminish small-amplitude gradual changes occurring over long time scales.

It is worth pointing out that the observed light curve does not necessarily imply a high eccentricity of the binary orbit. On the contrary, if the brightness variations result from disruption of the disk by the compact object at the periastron passage (see Paredes-Fortuny et al. 2015), one would expect light curve asymmetry, that is, a fast dip near the previously assumed periastron phase $\phi_{\rm p} \simeq 0.275$ with more gradual growth toward apastron at $\phi_a \simeq 0.775$. The observed light curves in all passbands, apart from being noisy, do not show such asymmetry. The small and nearly equal amplitude in all passbands and the shape of light curve variability, can be similarly (if not better) explained by the occultation of the Be star or a bright emission area, by a dense gaseous cloud. The brightness variability can be interpreted in terms of viewing geometry, and this explanation does not require an eccentric orbit and periodic disk disruption. We note that the phase of the maximum brightness, $\phi_0 = 0.78 \pm 0.15$, differs significantly from the previously assumed periastron phase $\phi_{\rm p} = 0.275$, it is, however, much closer to our estimate of the periastron phase of ≈ 0.6 . We discuss this fact in Sect. 5.2.

5. Orbital parameters of LSI+61° 303

5.1. Eccentricity

The estimates of the orbit eccentricity *e* derived for LS I +61° 303 by different methods, vary across a wide range from 0.3 to 0.8 (see Grundstrom et al. 2007, and references therein). The most reliable and direct way to reconstruct the binary orbit is to measure radial velocity (RV) variations of the stellar atmospheric spectral lines. Several efforts have been

made to find orbital parameters for LS I +61° 303 from the RV variations (Hutchings & Crampton 1981; Casares et al. 2005; Grundstrom et al. 2007; Aragona et al. 2009). The latest solutions obtained from the RV curves for the He I and He II lines give the value of eccentricity from \approx 0.54 (Aragona et al. 2009) to \approx 0.72 (Casares et al. 2005).

The common feature seen in all RV curves for the LSI+61° 303 is a high degree of scatter of individual measurements around the fitting curve, which is particularly pronounced in the orbital phases after the previously assumed periastron phase around 0.3 and the 0.8–0.9 phase range. Another feature is the apparent presence of a "secondary bump" near the phase 0.7–0.8 (Grundstrom et al. 2007; Aragona et al. 2009).

We want to emphasize that such a shape of the RV curve is not exceptional, but rather typical for many Be components in X-ray and non-X-ray binary stars. The formal solution of such a curve often results in substantial eccentricity for the Be star orbit. An explanation of this phenomenon was proposed by Harmanec (1985, see his Figs. 1 and 3)³. The optical component in most of such systems is embedded in a dense disk. The spectral lines, seen in the optical and UV spectra and usually associated with this star, show complex profiles, often with emission wings. From that point of view, LSI+61° 303 is a typical Betype binary with spectral lines closely resembling so-called shell lines, which are identified in spectra of many interacting binary stars (see binary spectra published in Casares et al. 2005; Grundstrom et al. 2007; Aragona et al. 2009). Even the lines that do not show prominent emission are not purely atmospheric, but may be formed in the different parts of the optically thick disk or gaseous shell around the star. The RVs, measured for these lines (apart from the orbital motion) are affected by the complex kinematics of the gas motion in the different parts of the disk. Thus, they may not adequately reproduce the orbital motion of the Be star, and the solution of RV curves may result in spurious

³ The alternative model of massive X-ray binaries suggested by Harmanec (1985), which assumes that X-ray components in massive systems are not neutron stars or black holes, is outdated. However, his interpretation of the RV curves of spectral lines formed in the vicinity of the visible component in Be binary systems is correct at least in some

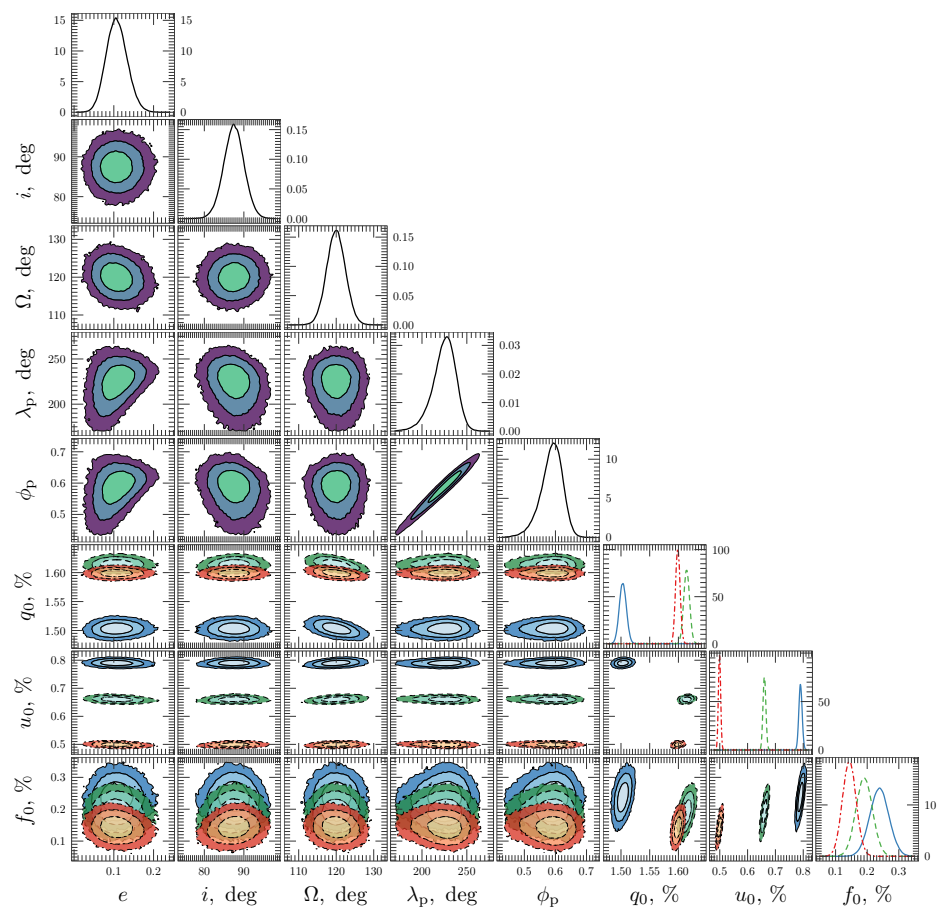


Fig. 10. Same as Fig. 8, but for free Ω .

(and different for the different lines) values of the eccentricity of the orbit (Harmanec 1985; see also more recent papers by Harmanec et al. 2015; Koubský et al. 2019).

The complications with RV curves are well illustrated by the behavior of the shell lines in the Be binary star KX And (Stefl et al. 1990). The formal solutions of the RV curves obtained for the six different groups of lines formed in the vicinity of the primary give an orbit eccentricity value ranging from 0.22 to 0.64 (see Table 5 in Stefl et al. 1990). In contrast, the RV variations of the spectral lines of the late-type secondary, which were detected and studied with high-resolution spectroscopy by Tarasov et al. (1998), revealed zero eccentricity and proved circular orbit in KX And.

We believe that the high value of eccentricity ($e \ge 0.5$) obtained from the RV curves for the LS 1+61° 303 (and perhaps for the LS 5039, see Aragona et al. 2009) is spurious. Of course, there is a morphological difference between the Be

systems with normal (nondegenerate) secondary components and high-mass X/y-ray binary systems with black hole/neutron star companions. However, the remarkable resemblance of the RV curves of the Be component in systems like KX And and many massive X/y-ray binaries, including LSI+61° 303 (see Fig. 3 in Harmanec 1985), cannot be ignored. Thus, the real orbit in LSI+61° 303 might be only slightly eccentric and close to circular. This is also suggested by the behavior of the periodic (orbitally phase-locked) variable polarization that we observed in the system.

5.2. Phase of the periastron

In addition to the high eccentricity, the RV measurements resulted in the value for the orbital phase of the periastron $\phi_{\rm p}=0.22-0.23$ (Casares et al. 2005), $\phi_{\rm p}=0.3$ (Grundstrom et al. 2007) and $\phi_{\rm p}=0.275$ (Aragona et al. 2009). However, the peak

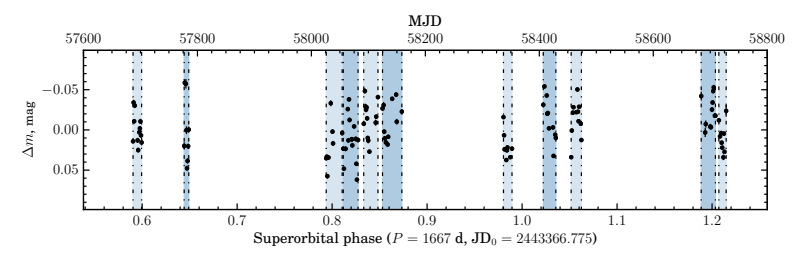


Fig. 11. Variation of relative amplitude of LS I $+61^{\circ}$ 303 around the mean in the V passband as a function of superorbital phase. The shaded blue bands correspond to the eleven observing seasons (S1–S11).

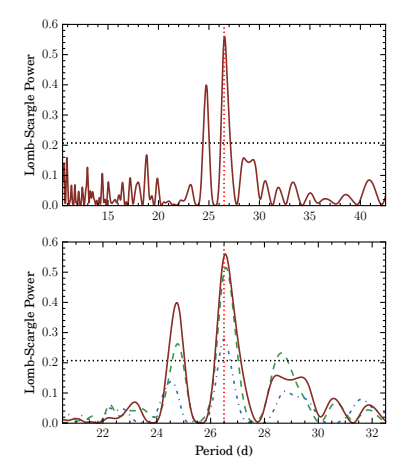


Fig. 12. Top panel: Lomb-Scargle periodogram for brightness variability of LS $1+61^\circ$ 303 in the R band. Bottom panel: Lomb-Scargle periodogram zoom for brightness variability in the BVR bands (dotted blue, dashed green, and solid red lines, respectively). The horizontal dotted line corresponds to the FAP = 1%. The vertical red dotted line marks the orbital period $P_{\rm orb} = 26.496$ d.

on the light curves does not occur on this orbital phase at most wavelengths. For example, the peaks in the radio, X-ray, and TeV light curves occur around the phase $\phi \approx 0.6$ (Massi et al. 2015; Archambault et al. 2016; Chernyakova et al. 2017). The peak of the optical brightness occurs with some delay relative to the peak in the high-energy emission (see Sect. 4, as well as Zamanov et al. 2014; Paredes-Fortuny et al. 2015). It is difficult to understand the nature of the phase delay between the passage of the periastron by a compact object and the maximum of radiation, especially in the case of high eccentricity. Our value for the orbital phase of periastron $\phi_{\rm p} \approx 0.6$ (see Table 4 and Fig. 9 for orbital parameters and a possible geometry), obtained from the modeling of the optical polarization, may explain all observational facts mentioned above as an interaction of the compact object, moving around the Be star, with the densest part of the circumstellar disk, near the periastron. A new set of orbital parameters should now be considered when modeling light curves in different energy bands.

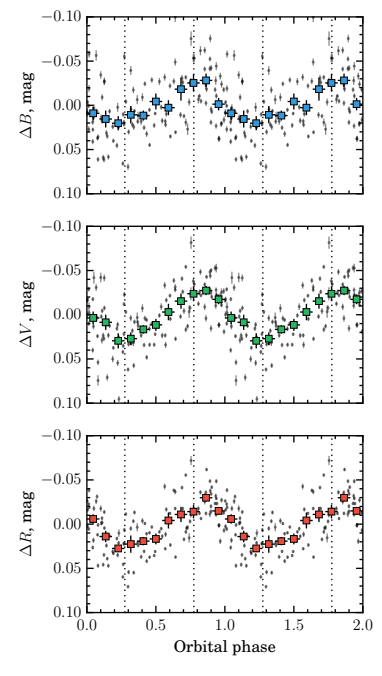


Fig. 13. Variability of LS I +61° 303 brightness in *BVR* bands (*top, middle*, and *bottom panels*, respectively) with the orbital period. The filled squares with 1σ errors correspond to the average values of the individual observations (gray crosses) and the standard errors of the mean calculated within the phase bin of width $\Delta\phi = 0.091$.

6. Summary

Our new high-precision BVR measurements of the linear polarization of the γ -ray binary LS I+61° 303 revealed periodic orbital variability in all passbands. The timing analysis of the Stokes parameters yielded the first ever detection of a polarimetric period $P_{\rm Pol}=13.244\,\rm d$, which is close to half of the orbital period $P_{\rm orb}=26.496\,\rm d$. The continuous change of polarization with the orbital phase implies that the variations arise from the orbital motion of the compact star whose orbit is co-planar with

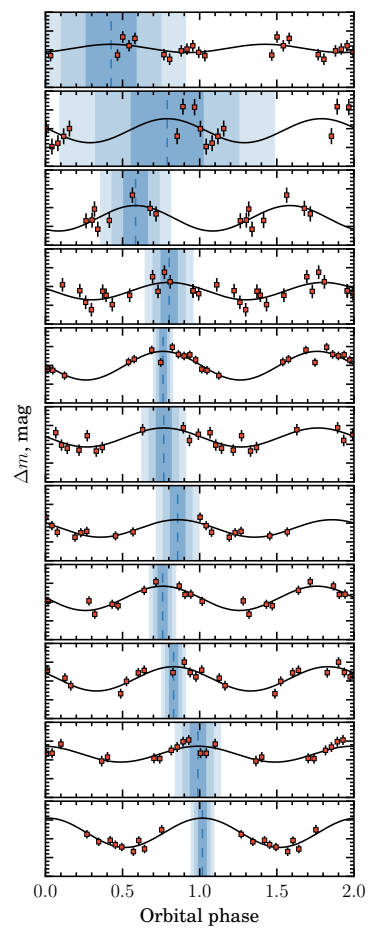


Fig. 14. Variability of LS1+61° 303 optical brightness in V-band for different parts of the data (seasons S1-S11 from top to bottom). The black solid lines correspond to the best fit of the data with function (6). The vertical dashed lines give the phases of the best fit maxima ϕ_0 , and the corresponding $\pm 1\sigma$, $\pm 2\sigma$, and $\pm 3\sigma$ confidence intervals are shown with varying shades of blue. The vertical scale [0.1, -0.1] is the same in all panels.

the Be star's decretion disk. The mechanism producing orbital variation of the polarization is most likely Thomson scattering of the stellar light in the high-temperature region around the compact object. The orbital variability curve is dominated by the second harmonic, which is typical for binaries with close to circular orbit and nearly symmetric distribution of the light scattering material with respect to the orbital plane. This implies that the high eccentricity of the binary orbit in LS I +61° 303 derived from the solution of the RV curves may not be real and that the true orbit is close to circular.

Table 5. Parameters of the best fit to the optical photometry of LS I+61 $^{\circ}$ 303 in the V band with function (6) for eleven observing seasons.

Seasons	MJD	A (mmag)	ϕ_0	m ₀ (mmag)
S1	57687-57702	11 ± 6	0.42 ± 0.16	-4 ± 6
S2	57777-57785	32 ± 17	0.78 ± 0.23	5 ± 40
S3	58026-58054	34 ± 22	0.58 ± 0.08	28 ± 15
S4	58056-58082	23 ± 6	0.80 ± 0.05	12 ± 5
S5	58092-58117	38 ± 7	0.76 ± 0.02	1 ± 5
S6	58125-58159	25 ± 7	0.76 ± 0.05	-18 ± 6
S7	58337-58352	23 ± 9	0.85 ± 0.05	14 ± 6
S8	58407-58429	32 ± 6	0.75 ± 0.03	-10 ± 4
S9	58456-58474	32 ± 7	0.83 ± 0.03	-6 ± 4
S10	58684-58709	21 ± 6	0.98 ± 0.05	-15 ± 4
S11	58715-58728	39 ± 11	1.01 ± 0.03	-16 ± 8

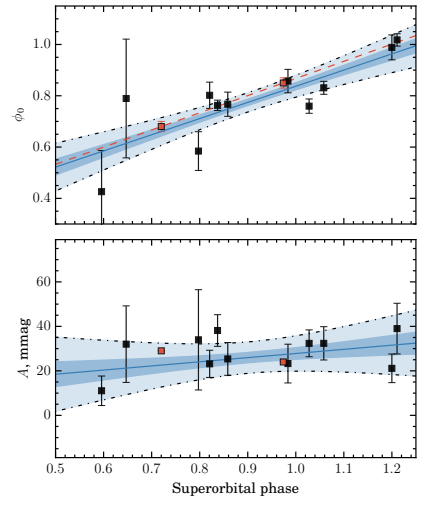


Fig. 15. Dependence of brightness maximum orbital phase ϕ_0 (*top panel*) and the amplitude *A* (*bottom panel*) of the sinusoidal fits on the superorbital phase. The solid blue lines correspond to the linear fit of the data, while the $\pm 1\sigma$ and $\pm 3\sigma$ confidence intervals are shown in dark and light blue. The red squares show the parameters from Table 3 of Paredes-Fortuny et al. (2015).

After the determination and subtraction of the interstellar polarization component, we obtained the PA of the constant component of polarization associated with the Be decretion disk at $\theta_{\rm int} \simeq 11^\circ$. Although this value differs from the previously determined $\simeq 25^\circ$ (Nagae et al. 2006, 2009), we believe that the difference is most likely due to the uncertainties in the determinations of the interstellar polarization component.

We considered two cases: when the position angle of the disk normal nearly coincides with $\theta_{\rm int}$, and when it differs by 90° from it. Using a model of a scattering cloud at an elliptical orbit nearly co-planar with the disk, we modeled orbital variations of Stokes parameters and constrained the eccentricity at e < 0.15 and the

phase of the periastron at $\phi_p \approx 0.6$. Both constraints are independent of the assumption on the disk orientation. The longitude of the periastron was found to be $\lambda_p \approx 146^\circ$ or 225° for the two cases. The obtained value for the periastron phase differs significantly from the previously assumed phase, which is based on the RV measurements, but is very close to the peaks of the radio, X-ray, and TeV light curves. Our results thus open a new avenue to model the broad-band emission from the enigmatic γ -ray binary LS I +61° 303.

We also found photometric orbital variability of LSI+61° 303 in B, V, and R filters with amplitudes $\Delta m \approx 0.1$ mag. The phase shift of the brightness maximum between the data sets acquired over the period of three years can be approximated with a simple linear model.

Acknowledgements. We acknowledge support from the Magnus Ehrnrooth foundation, the Finnish National Agency for Education (EDUFI) Fellowship (VK), the Russian Science Foundation grant 20-12-00364 (VK, SST and JP), the Academy of Finland grant 333112, and the ERC Advanced Grant HotMol ERC-2011-AGG-291659 (SVB, AVB). We thank the Academy of Finland (projects 317552, 331951) and the German Academic Exchange Service (DAAD, projects 57405000 and 57525212) for travel grants. DM acknowledges support from the DFG grant MA 7807/2-1 and from the bwHPC project of the state of Baden-Württemberg. The Dipol-2 polarimeter was built in cooperation by the University of Turku, Finland, and the Leibniz Institut für Sonnenphysik, Germany, with support from the Leibniz Association grant SAW-2011-KIS-7. We are grafted to the Institute for Astronomy, University of Hawaii, for the allocated observing

References

```
Abadi, M., Agarwal, A., Barham, P., et al. 2015, TensorFlow: Large-Scale Machine Learning on Heterogeneous Systems, Software available from
    tensorflow.org
Abdo, A. A., Ackermann, M., Aiello, M., et al. 2009, ApJ, 701, L123
Ackermann, M., Ajello, M., Ballet, J., et al. 2013, ApJ, 773, L35
Albert, J., Aliu, E., Anderhub, H., et al. 2006, Science, 312, 1771
Aragona, C., McSwain, M. V., Grundstrom, E. D., et al. 2009, ApJ, 698, 514
Archambault, S., Archer, A., Aune, T., et al. 2016, ApJ, 817, L7
Aspin, C., Simmons, J. F. L., & Brown, J. C. 1981, MNRAS, 194, 283
Astropy Collaboration (Price-Whelan, A. M., et al.) 2018, AJ, 156, 123
Baluev, R. V. 2008, MNRAS, 385, 1279
Berdyugin, A. V., & Tarasov, A. E. 1998, Astron. Lett., 24, 111
Brown, J. C., McLean, I. S., & Emslie, A. G. 1978, A&A, 68, 415
Brown, J. C., Aspin, C., Simmons, J. F. L., & McLean, I. S. 1982, MNRAS, 198,
Brown, A. G. A., Vallenari, A., Prusti, T., et al. 2018, A&A, 616, A1
Casares, J., Ribas, I., Paredes, J. M., Martí, J., & Allende Prieto, C. 2005,
MNRAS, 360, 1105
Chandrasekhar, S., & Breen, F. H. 1947, ApJ, 105, 435
Chernyakova, M., & Malyshev, D. 2020, Conf. Proc. Multifrequency Behaviour
of High Energy Cosmic Sources - XIII, submitted [arXiv:2006.03615]
Chernyakova, M., Neronov, A., Molkov, S., et al. 2012, ApJ, 747, L29
```

```
Drissen, L., Lamontagne, R., Moffat, A. F. J., Bastien, P., & Seguin, M. 1986,
    ApJ, 304, 188
Duane, S., Kennedy, A., Pendleton, B. J., & Roweth, D. 1987, Phys. Lett. B, 195,
Golding, N. 2019, J. Open Sour. Softw., 4, 1601
Gregory, P. C. 2002, ApJ, 575, 427
Grundstrom, E. D., Caballero-Nieves, S. M., Gies, D. R., et al. 2007, ApJ, 656,
Harmanec, P. 1985, Bull. Astron. Inst. Czechoslov., 36, 327
Harmanec, P., Koubský, P., Nemravová, J. A., et al. 2015, A&A, 573, A107
Harrison, F. A., Ray, P. S., Leahy, D. A., Waltman, E. B., & Pooley, G. G. 2000,
    ApJ, 528, 454
Heiles, C. 2000, AJ, 119, 923
Hutchings, J. B., & Crampton, D. 1981, PASP, 93, 486
Kosenkov, I. A., Berdyugin, A. V., Piirola, V., et al. 2017, MNRAS, 468, 4362
Koubský, P., Harmanec, P., Brož, M., et al. 2019, A&A, 629, A105
Leahy, D. A. 2001, Int. Cosm. Ray Conf., 6, 2524
Li, J., Torres, D. F., & Zhang, S. 2014, ApJ, 785, L19
Lomb, N. R. 1976, Ap&SS, 39, 447
Manset, N., & Bastien, P. 2000, AJ, 120, 413
Massi, M., & Jaron, F. 2013, A&A, 554, A105
Massi, M., & Torricelli-Ciamponi, G. 2016, A&A, 585, A123
Massi, M., Ros, E., & Zimmermann, L. 2012, A&A, 540, A142
Massi, M., Jaron, F., & Hovatta, T. 2015, A&A, 575, L9
Mendelson, H., & Mazeh, T. 1989, MNRAS, 239, 733
Nagae, O., Kawabata, K. S., Fukazawa, Y., et al. 2006, PASJ, 58, 1015
Nagae, O., Kawabata, K. S., Fukazawa, Y., et al. 2009, AJ, 137, 3509
Paredes, J. M., Marziani, P., Marti, J., et al. 1994, A&A, 288, 519
Paredes-Fortuny, X., Ribó, M., Bosch-Ramon, V., et al. 2015, A&A, 575, L6
Piirola, V., Berdyugin, A., & Berdyugina, S. 2014, in Ground-based and Airborne Instrumentation for Astronomy V, Proc. SPIE, 9147, 914781
Piirola, V., Berdyugin, A., Frisch, P. C., et al. 2020, A&A, 635, A46
Prusti, T., de Bruijne, J. H. J., Brown, A. G. A., et al. 2016, A&A, 595, A1 Quirrenbach, A., Bjorkman, K. S., Bjorkman, J. E., et al. 1997, ApJ, 479, 477
R Core Team 2019, R: A Language and Environment for Statistical Computing,
R Foundation for Statistical Computing, Vienna, Austria
Scargle, J. D. 1982, ApJ, 263, 835
Skatgic, J. D. 1962, Apr. 203, 637
Serkowski, K. 1973, in Interstellar Dust and Related Topics, eds. J. M. Greenberg, & H. C. van de Hulst, IAU Symp., 52, 145
Simmons, J. F. L., & Boyle, C. B. 1984, A&A, 134, 368
Simmons, J. F. L., Aspin, C., & Brown, J. C. 1982, MNRAS, 198, 45
Sobolev, V. V. 1949, Uch. Zap. Leningrad Univ., 16
Stefl, S., Harmanec, P., Horn, J., et al. 1990, Bull. Astron. Inst. Czechoslov., 41,
Tarasov, A. E., Berdyugina, S. V., & Berdyugin, A. V. 1998, Astron. Lett., 24,
Taylor, A. R., & Gregory, P. C. 1982, ApJ, 255, 210
Taylor, A. R., Kenny, H. T., Spencer, R. E., & Tzioumis, A. 1992, ApJ, 395, 268
Wolinski, K. G., & Dolan, J. F. 1994, MNRAS, 267, 5
Wood, K., Bjorkman, J. E., Whitney, B., & Code, A. 1996, ApJ, 461, 847
Wu, Y. W., Torricelli-Ciamponi, G., Massi, M., et al. 2018, MNRAS, 474,
    4245
Zaitseva, G. V., & Borisov, G. V. 2003, Astron. Lett., 29, 188
Zamanov, R. K., Martí, J., Paredes, J. M., et al. 1999, A&A, 351, 543
Zamanov, R., Stoyanov, K., Martí, J., et al. 2013, A&A, 559, A8
Zamanov, R., Martí, J., Stoyanov, K., Borissova, A., & Tomov, N. A. 2014, A&A,
    561, L2
```

Chernyakova, M., Babyk, I., Malyshev, D., et al. 2017, MNRAS, 470, 1718

Appendix A: Polarization from Thomson scattering by an orbiting cloud

We consider an orbital plane with the rotation axis \hat{n} inclined by angle i to the line of sight. Let us choose the polarization basis (\hat{e}_1, \hat{e}_2) such that vector \hat{e}_1 is along the projection of the vector \hat{n} on the plane of the sky, \hat{e}_2 lies at the interception of the plane of the sky, and the orbital plane is perpendicular to \hat{e}_1 . This basis can be supplemented by \hat{e}_3 , which coincides with the direction to the observer \hat{o} to form a right-handed coordinate system. In this system, $\hat{n} = (\sin i, 0, \cos i)$. The center of the coordinates is on the source of light (i.e., the Be star).

Let us introduce longitude λ in the orbital plane measured from the southern part of the line formed by the intersection of the orbital plane with the plane containing (\hat{n}, \hat{o}) , as in Simmons & Boyle (1984; see our Fig. A.1 and their Fig. 1). The orbital distance to the scattering cloud varies with longitude as

$$r(\lambda) = \frac{a(1 - e^2)}{1 + e\cos(\lambda - \lambda_p)},\tag{A.1}$$

where a is the orbit semi-major axis and λ_p is the longitude of the periastron. The unit vector towards the cloud is

$$\hat{\mathbf{r}} = (-\cos i \cos \lambda, -\sin \lambda, \sin i \cos \lambda), \tag{A.2}$$

and the scattering angle Θ is given by

$$\mu = \cos \Theta = \hat{\mathbf{r}} \cdot \hat{\mathbf{o}} = \sin i \cos \lambda. \tag{A.3}$$

The total flux observed at Earth from the system F_{tot} consists of the direct radiation from the Be star $F_* = L_*/(4\pi D^2)$ and the scattered flux $F_{\rm sc} = L_{\rm sc}(\mu)/(4\pi D^2)$, where L_* and $L_{\rm sc}$ are corresponding luminosities and D is the distance. Assuming that Thomson scattering (in an optically thin regime) is responsible for scattered flux, the angular distribution of scattered luminosity can be represented as

$$L_{\rm sc}(\mu) = L_* f_{\rm sc} l(\mu), \tag{A.4}$$

where

$$l(\mu) = \frac{3}{9}(1 + \mu^2) \tag{A.5}$$

is the Thomson scattering indicatrix,

$$f_{\rm sc} = \frac{N_{\rm e}\sigma_{\rm T}}{4\pi r^2(\lambda)} \tag{A.6}$$

is the fraction of scattered photons that is related to the total number of free electrons N_e in a cloud and the distance between the Be star and the scattering cloud, and $\sigma_{\rm T}$ is the Thomson cross-section. We can scale $f_{\rm sc}$ to some typical value f_0 as

$$f_{\rm sc} = f_0 \left[\frac{a(1 - e^2)}{r(\lambda)} \right]^2 = f_0 \left[1 + e \cos(\lambda - \lambda_{\rm p}) \right]^2.$$
 (A.7)

The polarization degree of scattered light is

$$P_{\rm sc} = \frac{1 - \mu^2}{1 + \mu^2} = \frac{\sin^2 \Theta}{1 + \cos^2 \Theta},\tag{A.8}$$

but the observed one is diluted by the star. The polarized flux for

$$F_{\text{sc}}P_{\text{sc}} = F_* f_{\text{sc}} l(\mu) \frac{1-\mu^2}{1+\mu^2} = F_* f_{\text{sc}} \frac{3}{8} (1-\mu^2).$$
 (A.9) $\tan\left(\frac{E}{2}\right) = \sqrt{\frac{1-e}{1+e}} \tan\left(\frac{\lambda - \lambda_p}{2}\right)$

A170, page 14 of 15

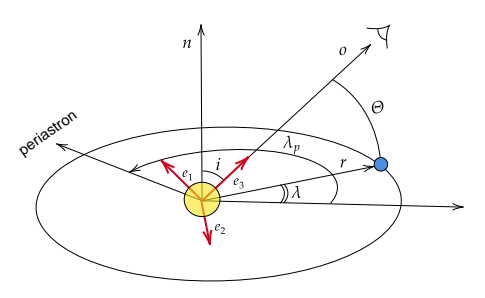


Fig. A.1. Geometry of orbit.

The polarization degree of the total flux is $P = F_{sc}P_{sc}/F_{tot}$, but if we assume that scattered radiation contributed very little to the total flux $F_{\rm sc} \ll F_*$, we get

$$P = \frac{3}{8} f_{sc} (1 - \mu^2) = \frac{3}{8} f_0 \sin^2 \Theta \left[1 + e \cos(\lambda - \lambda_p) \right]^2.$$
 (A.10)

The polarization (pseudo-)vector \hat{p} , defined by the direction of dominant oscillations of electromagnetic waves, is perpendicular to the scattering plane, so

$$\hat{\mathbf{p}} = \frac{\hat{\mathbf{o}} \times \hat{\mathbf{r}}}{|\hat{\mathbf{o}} \times \hat{\mathbf{r}}|} = \frac{1}{\sin \Theta} (\sin \lambda, -\cos i \cos \lambda, 0), \tag{A.11}$$

and $\sin \Theta = \sqrt{1 - \mu^2} = \sqrt{1 - \sin^2 i \cos^2 \lambda}$. The position angle χ of \hat{p} is given by the following formulae:

$$\cos \chi = \hat{\boldsymbol{e}}_1 \cdot \hat{\boldsymbol{p}} = \frac{\sin \lambda}{\sin \Theta},\tag{A.12}$$

$$\sin \chi = \hat{\boldsymbol{e}}_2 \cdot \hat{\boldsymbol{p}} = -\frac{\cos i \cos \lambda}{\sin \Theta}.$$
 (A.13)

Because the normalized Stokes parameters are defined as q = $P\cos(2\chi)$ and $u = P\sin(2\chi)$, we need

$$\cos(2\chi) = \frac{\sin^2 i - (1 + \cos^2 i)\cos(2\lambda)}{2(1 + \cos^2 i)\cos(2\lambda)},$$
(A.14)

$$\cos(2\chi) = \frac{\sin^2 i - (1 + \cos^2 i)\cos(2\lambda)}{2\sin^2 \Theta},$$

$$\sin(2\chi) = -\frac{\cos i\sin(2\lambda)}{\sin^2 \Theta}.$$
(A.14)

Combining that with expression (A.10) for polarization degree

$$q = \frac{3f_0}{16} \left[\sin^2 i - \left(1 + \cos^2 i \right) \cos 2\lambda \right] \left[1 + e \cos \left(\lambda - \lambda_p \right) \right]^2,$$

$$u = \frac{3f_0}{8} \left[-\cos i \sin 2\lambda \right] \left[1 + e \cos \left(\lambda - \lambda_p \right) \right]^2.$$
(A.16)

The observed Stokes parameters also depend on the position angle Ω of the projection of the orbital axis, which are obtained by rotating vector (q, u) by angle 2Ω :

$$q_{\text{obs}} = q\cos(2\Omega) - u\sin(2\Omega), \tag{A.17}$$

$$u_{\text{obs}} = q \sin(2\Omega) + u \cos(2\Omega). \tag{A.18}$$

The obtained Stokes parameters are functions of the longitude λ and need to be computed as functions of the orbital phase. From the true anomaly of the orbit $\lambda - \lambda_p$, we find the eccentric

$$\tan\left(\frac{E}{2}\right) = \sqrt{\frac{1-e}{1+e}} \tan\left(\frac{\lambda - \lambda_{\rm p}}{2}\right) \tag{A.19}$$

and the mean anomaly

$$M = E - e \sin E, \tag{A.20}$$

which can be converted to the orbital phase measured in the interval [0,1] using an additional free parameter, the phase of the periastron ϕ_p :

$$\phi_{\text{orb}} = M/(2\pi) + \phi_{\text{p}}. \tag{A.21}$$

Thus, the model free parameters are the inclination i, eccentricity e, latitude of the periastron $\lambda_{\rm p}$, the PA of the projection of the orbit axis on the sky Ω , the phase of the periastron $\phi_{\rm p}$, and the scattering fraction f_0 . We note that Ω defined this way differs by $\pi/2$ from the PA of the ascending node usually used to describe binary star orbits. In order to fit the data, there is a need for additional constant Stokes parameters q_0 and u_0 , which describe permanent polarization and are not related to the orbital motion of the scattering cloud.

Kravtsov V., Veledina A., Berdyugin A.V., Poutanen J., Tsygankov S.S., Shahbaz T., Torres M.A.P., Jermak H.E., McCall C., Steele I.A., Kajava J.J.E., Piirola V., Sakanoi T., Kagitani M., Berdyugina S.V Optical and near-infrared polarization of the black hole X-ray binary A0620–00 in quiescence

Astronomy & Astrophysics, 2025; 703: A14

Optical and near-infrared polarization of the black hole X-ray binary A0620-00 in quiescence

Vadim Kravtsov^{1, ★}, Alexandra Veledina^{1,2}, Andrei V. Berdyugin¹, Juri Poutanen¹, Sergey S. Tsygankov¹ Tariq Shahbaz^{3,4}, Manuel A. P. Torres^{3,4}, Helen E. Jermak⁵, Callum McCall⁵, Iain A. Steele⁵ Jari J. É. Kajava^{1,6}, Vilppu Piirola ¹0, Takeshi Sakanoi⁷, Masato Kagitani⁷, and Svetlana V. Berdyugina^{8,9}

- Department of Physics and Astronomy, FI-20014 University of Turku, Finland
- Nordita, KTH Royal Institute of Technology and Stockholm University, Hannes Alfvéns väg 12, SE-10691 Stockholm, Sweden
- Instituto de Astrofísica de Canarias, E-38205 La Laguna, Tenerife, Spain
- Departamento de Astrofísica, Universidad de La Laguna, E-38206 La Laguna, Tenerife, Spain
- Astrophysics Research Institute, Liverpool John Moores University, 146 Brownlow Hill, Liverpool L3 5RF, United Kingdom
- Serco for the European Space Agency (ESA), European Space Astronomy Centre, Camino Bajo del Castillo s/n, E-28692 Villanueva de la Cañada, Madrid, Spain
- Graduate School of Sciences, Tohoku University, Aoba-ku, 980-8578 Sendai, Japan
- Istituto Ricerche Solari Aldo e Cele Daccó (IRSOL), Faculty of Informatics, Universitá della Svizzera italiana, 6605 Locarno, Switzerland
- Institut für Sonnenphysik (KIS), Georges-Köhler-Allee 401a, 79110 Freiburg, Germany

Received 10 July 2024 / Accepted 25 August 2025

ABSTRACT

We present simultaneous high-precision optical polarimetric and near-infrared (NIR) to ultraviolet (UV) photometric observations of the low-mass black hole X-ray binary A0620-00 in a quiescent state. Subtracting interstellar polarization, estimated from a sample of field stars, we derived the intrinsic polarization of A0620-00. We show that the intrinsic polarization degree (PD) varies with the orbital period with an amplitude of \sim 0.3%, at least in the R band, where the signal-to-noise ratio of our observations is the best. This implies that some fraction of the optical polarization is produced by a scattering of stellar radiation off the matter that follows the black hole in its orbital motion. In addition, we see a rotation of the orbit-average intrinsic polarization angle (PA) with the wavelength from 163° in the R to 177° in the B band. All of the above, combined with the historical NIR-to-optical polarimetric observations, demonstrates the complex behavior of the average intrinsic polarization of A0620-00: the PA continuously rotates from the infrared to the blue band by ~53° in total, while the PD of ~1% remains nearly constant over the entire spectral range. The spectral dependence of the PA can be described by Faraday rotation with a rotation measure of -0.2 rad µm⁻², implying a magnetic field of a few gauss in the plasma surrounding the black hole accretion disk. However, our preferred interpretation of the peculiar wavelength dependence is an interplay between two polarized components with different PAs. Polarimetric measurements in the UV range can help in distinguishing between these scenarios.

Key words. accretion, accretion disks – polarization – stars: black holes – stars: individual: A0620–00 – X-rays: binaries

1. Introduction

A0620-00 is the prototypical black hole (BH) low-mass Xray binary (LMXB). It was discovered during its 1975 outburst (Elvis et al. 1975), when its luminosity increased by more than a million times compared to the quiescent levels, reaching the Eddington luminosity. Since then, the object has been in a quiescent state, with its spectrum dominated by the emission of a $0.4\,M_\odot$ K-type star orbiting a ${\sim}6\,M_\odot$ BH (McClintock & Remillard 1986; van Grunsven et al. 2017) with an orbital period (P_{orb}) of 7.75 h. Nevertheless, additional sources of nonstellar origin (such as jet, accretion disk, inner hot accretion flow, and hot spot) were considered in the literature to explain the excess of radio, infrared (IR), and ultraviolet (UV) emission of A0620-00 near quiescence (McClintock et al. 1995; Muno & Mauerhan 2006; Froning et al. 2011; Gallo et al. 2019; Cherepashchuk et al. 2019). Their contributions to the broadband spectrum are difficult to distinguish, especially in light of the alteration between accretion modes (passive, loop, and active modes; Cantrell et al. 2008). An additional source of information is needed to distinguish between different spectral models. Polarization of the optical radiation may provide such

Optical and near-infrared (NIR) radiation produced in various physical processes, including the electron scattering of stellar radiation off the accretion disk or flow and synchrotron emission in the presence of an ordered magnetic field, can be polarized. The polarization degree (PD), polarization angle (PA), and their spectral properties are different for different processes, which makes polarimetry a powerful technique for studies of the physical mechanisms responsible for the optical and NIR emission production in BH X-ray binaries. A recent systematic study has shown, however, that in many quiescent BHs, the intrinsic optical polarization (corrected for interstellar contribution) is very small – in most cases $P_{\rm int} \lesssim 0.5\%$ (Kravtsov et al. 2022). On the other hand, several BH LMXBs show significant polarization during (or near) quiescence: MAXI J1820+070 had a high PD (up to 5%), with the blue spectrum and PA different from the jet direction, suggesting a BH spin-orbit

^{*} Corresponding author: vakrau@utu.fi

misalignment (Poutanen et al. 2022); A0620–00 had ~1% optical and NIR polarization in the quiescent state (Dubus et al. 2008; Russell et al. 2016).

In X-ray quiescence, A0620–00 shows optical state changes: according to the (Cantrell et al. 2008) classification, there are two different states of optical activity – passive and active. In the passive state, variations in the optical flux are consistent with ellipsoidal variations produced by the rotation of the tidally distorted optical companion. In the active state, the source is 20% brighter and shows an aperiodic high-frequency variation usually called "flickering."

In this paper we present the results of quasi-simultaneous high-precision optical polarimetric and multiwavelength (NIR to UV) photometric observations of A0620–00 during its passive quiescent state. The paper is organized as follows. In Sect. 2 we describe the observational data. In Sect. 3 we present the main results of our study: determination of the intrinsic optical polarization of A0620–00, its significant orbital variability, and the rotation of the average intrinsic PA with wavelength. In Sect. 4 we discuss possible physical mechanisms that can reproduce the observed behavior. Finally, in Sect. 5 we summarize our findings.

2. Data acquisition and analysis

2.1. Optical polarimetric observations

High-precision optical polarimetric observations of A0620-00 were performed using broadband BVR polarimeter DIPol-UF (Piirola et al. 2021), a visitor instrument installed at the 2.56 m Nordic Optical Telescope (NOT), Observatorio del Roque de los Muchachos, La Palma, Spain. Field stars used for the interstellar (IS) polarization estimation were observed with DIPol-2 (Piirola et al. 2014), mounted on the remotely controlled 60 cm Tohoku telescope (T60) at Haleakala Observatory, Hawaii. Both polarimeters utilize a "double-image" design that effectively eliminates the polarization of the sky, even if it varies throughout the observations. The instrumental polarization of both instruments is small $(<10^{-4})$ and was well calibrated by observing of 10-15 unpolarized standard stars. The zero points of the PAs were determined by observing highly polarized standards HD 236928 and HD 25443. A more detailed description of the methods and calibrations can be found in Piirola et al. (2020) and Kravtsov et al. (2022), and references therein.

A0620-00 was observed on two nights between 2022 December 24 and 26, and 140 and 52 individual measurements of the Stokes parameters were made on the two nights, respectively. The first observation was continuous, 8 h long, and hence covered the whole orbital period of the binary, while the second observation covered only 40% of the period. Hereafter we refer to the average polarization measured during the first observation as the orbit-averaged polarization. Each individual linear polarization measurement was obtained from four consecutive images with 50-s exposures taken at different half-wave plate positions, resulting in one polarization measurement per ~3.3 min. To increase the signal-to-noise ratio, we split the data into bins such that each bin contains ten individual measurements of the Stokes parameters. The errors of the normalized Stokes parameters q and u were computed as the standard errors of the weighted mean values within the bin. The Stokes parameters (q, u) then were translated into the PD (P) and PA (θ) ,

$$P = \sqrt{q^2 + u^2}, \qquad \theta = \frac{1}{2} \operatorname{atan2}(u, q).$$
 (1)

Table 1. Polarimetric and photometric observations of A0620-00 in December 2022.

Telescope	UT Date 2022	Filters	$N_{ m obs}$
NOT	Dec 24-26	B, V, R	2
GTC	Dec 25	$K_{\rm s}, H, J$	1
LT	Dec 20-24	u, g, r, i, z, B, V	3
UVOT	Dec 23-26	B, V, u, w1, m2, w2	4

The uncertainty on the PD is equal to the uncertainty of the individual Stokes parameters, and uncertainty on the PA in radians was estimated as $\sigma_\theta = \sigma_P/(2P)$ (Serkowski 1962; Kosenkov et al. 2017). The phase-resolved PD was corrected for the bias caused by the low signal-to-noise ratio using the relation $P_0 = (P^2 - 2\sigma_P^2)^{1/2}$ (Simmons & Stewart 1985).

2.2. Multiwavelength photometry

Quasi-simultaneous multiwavelength photometric observational campaign was organized on several telescopes (see Table 1). Near-infrared JHK photometry was made using EMIR widefield imager (Garzón et al. 2022), installed on the 10.4 m Gran Telescopio Canarias (GTC), La Palma, Spain. Observations in the broadband SDSS-ugriz, Bessel V, and Bessel B filters were performed using IO:O instrument of the 2-m Liverpool Telescope (LT; Steele et al. 2004), La Palma, Spain. For all the instruments, basic data reductions such as bias and dark subtraction and flat fielding are done via the internal common pipelines. As the photometric standards, we used two stars with known Sloan Digital Sky Survey (SDSS) magnitudes. To obtain fluxes of the object from its magnitudes we used standard zero-points for SDSS and Johnson-Cousins systems (Fukugita et al. 1996; Bessell 1979).

2.3. Swift/UVOT

The Neil Gehrels Swift Observatory (Gehrels et al. 2004) observed A0620–00 four times from 2022 December 23 to 26 (see Table 1) with total exposure of about 7 ks. The image analysis has been done following the procedure provided by the UK Swift Science Data Centre¹. Photometry in all available filters (V, B, U, UVW1, UVW2, and UVM2) was performed using the tool UVOTSOURCE from the HEASOFT package version 6.32 and the latest calibration files. The source and background photons were extracted from the apertures with radii of 5" and 10", respectively. The background was chosen with the center about 18" away from the source for all filters.

For the spectral fitting, all available data were converted to the spectral files. For the *Swift/UVOT* data the UVOT2PHA tool was applied using the corresponding response files in the CALDB. All other data were converted to the spectral files using tool FTFLX2XSP from the FTOOLS package. The following spectral fitting was performed using XSPEC version 12.13.1 (Arnaud 1996).

3. Results

3.1. Average intrinsic polarization

The observed optical polarization of a distant star is a combination of the intrinsic polarization of the object and IS polarization.

⁽¹⁾ https://www.swift.ac.uk/analysis/uvot/

Table 2. Polarization of field stars and A0620-00.

		В			V		R		
Field star	Parallax (mas)	q (%)	и (%)	q (%)	и (%)	q (%)	и (%)		
Ref 1	0.72 ± 0.04	0.71 ± 0.03	-1.45 ± 0.03	0.56 ± 0.03	-1.45 ± 0.03	0.64 ± 0.02	-1.40 ± 0.02		
Ref 2	0.87 ± 0.02	0.64 ± 0.07	-1.32 ± 0.07	0.45 ± 0.04	-1.29 ± 0.04	0.45 ± 0.03	-1.20 ± 0.03		
Ref 3	0.56 ± 0.02	0.50 ± 0.08	-1.33 ± 0.08	0.49 ± 0.08	-1.06 ± 0.08	0.38 ± 0.06	-1.26 ± 0.06		
Ref 4	0.55 ± 0.02	0.84 ± 0.20	-1.32 ± 0.20	0.36 ± 0.12	-0.68 ± 0.12	0.56 ± 0.07	-0.92 ± 0.07		
A0620-00	0.69 ± 0.12	1.33 ± 0.11	-1.44 ± 0.11	1.52 ± 0.07	-1.78 ± 0.07	1.33 ± 0.04	-1.85 ± 0.04		

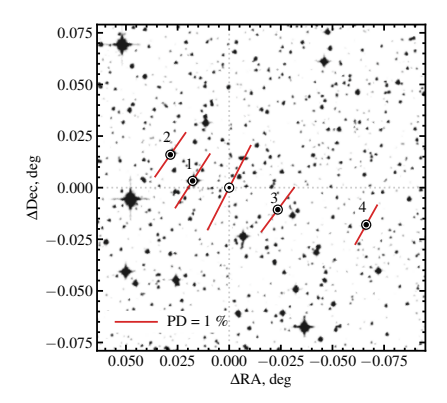
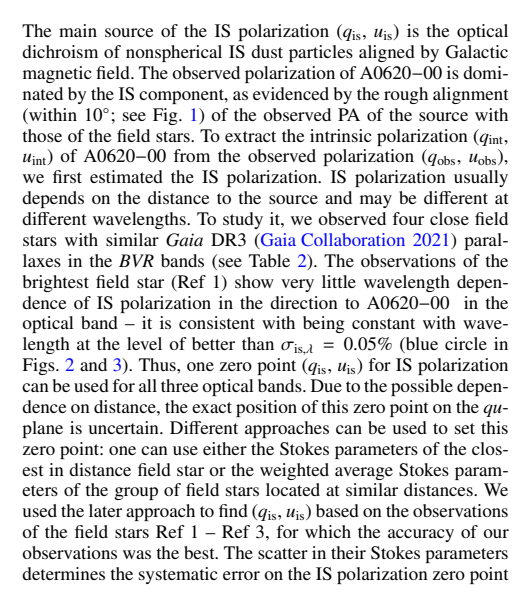


Fig. 1. Polarization map of A0620–00 (at the origin) and field stars in the R band. The lines correspond to the observed polarization, with the length of the bars showing the PD, and the direction indicating the PA (measured from north to east).



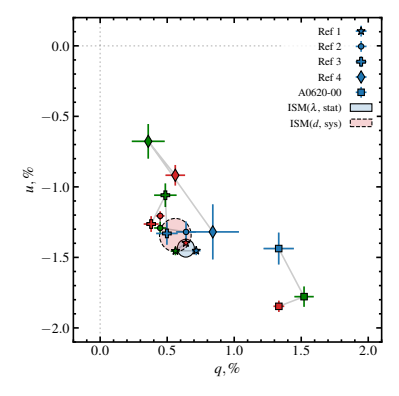


Fig. 2. Observed orbit-average Stokes parameters of A0620–00 (squares) and field stars in the B, V, and R bands (blue, green, and red markers, respectively). The light blue circle shows the uncertainty of the IS polarization with wavelength $\sigma_{\rm is,l}$; the light red circle shows the systematic error on the IS polarization zero point, $\sigma_{\rm is,NS}$.

 $\sigma_{\rm is}^{\rm sys}=0.12\%$ (shown as red circle in Figs. 2 and 3). To find the intrinsic polarization of A0620–00, we subtracted the IS Stokes parameters $(q_{\rm is}, u_{\rm is})$ from the observed Stokes parameters $(q_{\rm obs}, u_{\rm obs})$ of the source. The statistical errors on the intrinsic Stokes parameters of A0620–00 were calculated as $\sigma_{\rm int}^2=\sigma_{\rm obs}^2+\sigma_{\rm is,4}^2$; the $\sigma_{\rm is,4}^2$ term includes possible dependence of the IS polarization on wavelength. Then, Eq. (1) is used to calculate the PD and PA together with their statistical errors. The systematic error $\sigma_{\rm is,sys}$ on the IS zero point translates to the systematic errors of the intrinsic PD and PA $\sigma_{\rm pys}^{\rm sys}=0.12\%$ and $\sigma_{\rm pys}^{\rm sys}\approx 4^\circ$.

Subtracting the IS component from the observed polarization, we find the average intrinsic polarization of A0620–00 to be P=0.8-1.0% with θ changing from 163° in the R filter to 177° in B (see Table 3). The fit with a constant to the intrinsic PA gives unacceptable fit with $\chi^2/\text{d.o.f.}=10/2$. Combining NIR polarization with our optical measurements, we see the continuous rotation of the intrinsic polarization vector with the wavelength from NIR to B (see Fig. 3). The fit with a constant to all intrinsic PAs from NIR to B gives unacceptable fit with $\chi^2/\text{d.o.f.}=32/6$. The amplitude of the polarization vector rotation on the sky is $\Delta\theta=\theta(B)-\theta(K_s)\approx53^\circ$ (see Fig. 4). In contrast to the PA, PD barely changes with wavelength remaining at $\sim1\%$ level from K_s to B band (constant fit gives $\chi^2/\text{d.o.f.}=5/6$).

We note that although the determination of the intrinsic PA strongly depends on the accuracy of the IS polarization estimate,

Table 3. One-orbit-average observed and intrinsic PD and PA of A0620-00 together with the IS polarization estimate.

Observed		rved	Interstell	ar	Intrinsic		
F	P _{obs} (%)	$\theta_{\rm obs}$ (deg)	P _{is} (%)	θ_{is} (deg)	<i>P</i> _{int} (%)	$\theta_{\rm int}$ (deg)	
B	1.96 ± 0.11	156 ± 2			$0.78 \pm 0.12^{stat} \pm 0.12^{sys}$	$177 \pm 5^{stat} \pm 5^{sys}$	
V	2.34 ± 0.07	155 ± 1	$1.45 \pm 0.05^{\text{stat}} \pm 0.12^{\text{sys}}$	$146 \pm 1^{\text{stat}} \pm 2^{\text{sys}}$	$1.05 \pm 0.09^{\text{stat}} \pm 0.12^{\text{sys}}$	$168 \pm 2^{\text{stat}} \pm 3^{\text{sys}}$	
R	2.27 ± 0.04	153 ± 1			$0.92 \pm 0.06^{stat} \pm 0.12^{sys}$	$163 \pm 2^{stat} \pm 4^{sys}$	

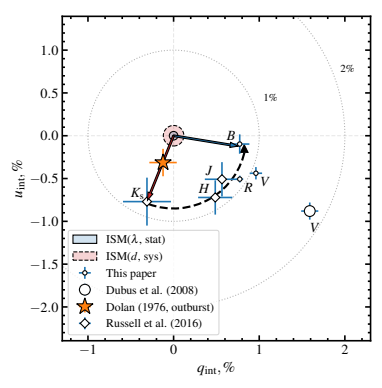


Fig. 3. Intrinsic Stokes parameters of the polarization of A0620–00 in quiescence measured in different filters from the K_s to B, as indicated by letters near each data point. The light blue circle at the origin illustrates the possible uncertainty of the IS polarization with wavelength, $\sigma_{\rm is,4}$, the light red circle shows the systematic error on the IS polarization zero point, $\sigma_{\rm is,59}$. The red and blue arrows indicate the intrinsic polarization vector directions in the K_s and B bands, respectively. The dashed curved arrow shows the track left by the intrinsic polarization vector during its rotation from the IR to the blue part of the spectrum. An orange star shows the polarization of A0620–00 in V measured during the 1975 outburst by Dolan (1976).

there is an additional reason to believe that the intrinsic polarization estimate is close to its true value. Although the observed PD of A0620–00 in Dubus et al. (2008) V-band observations was significantly higher than in this paper, subtracting our estimate of the IS polarization from their observed Stokes parameters, we get the PA of intrinsic polarization matching our value within a few degrees – this can be seen in Fig. 3, if one connects the origin to the corresponding observational points and compare the directions of the resulting vectors. This alignment of the intrinsic polarization vectors is unlikely to be coincidental and may appear naturally if the intrinsic PD of the source changes while the PA is stable.

3.2. Orbital variability of the polarization

We folded the photometric and polarimetric observations of A0620–00 in the R band (for which the S/N is the best) with the orbital period using the recent ephemeris of Cherepashchuk et al. (2019). We find significant variability of intrinsic polarization of the source in the R filter (Fig. 5b,c). We plotted the orbital profile of the observed polarization together with the optical light curve of A0620–00, obtained simultaneously (Fig. 5a). We see the pronounced peak in PD at the orbital

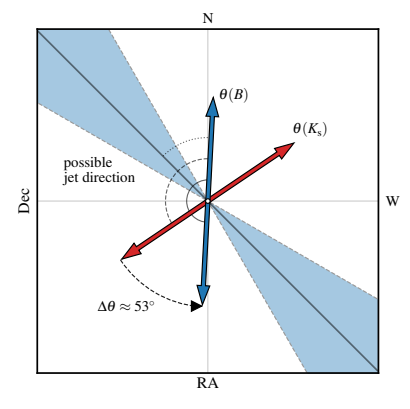


Fig. 4. Rotation of the polarization on the sky. Red and blue arrows correspond to the direction of the polarization in the B and K_c filters, respectively. The blue region shows the direction of the radio ejections as measured in Kuulkers et al. (1999).

phase of 0.75 and two minima at phases around 0.5 and 1.0. Similar peak in PD around phase 0.7 has been observed by Dolan & Tapia (1989). Such polarization behavior with minima in conjunctions and maxima in quadratures is expected and has been observed in other binary systems (discussed in detail in Sect. 4.3), and although our observations covered only 1.5 orbits, and the S/N for individual bins is at the threshold of significance, we can still cautiously state that the nature of observed polarization variability is more likely to be orbital rather than stochastic. The absence of flickering in the photometric observations together with the visual magnitude $V = 18.3 \pm 0.1$ of A0620-00 suggests that the source was in the passive quiescent state during our campaign (Cantrell et al. 2008).

3.3. Broadband spectrum

The observed NIR-to-UV spectral energy distribution (SED) of A0620–00 in passive quiescent state, corrected for reddening assuming E(B-V)=0.35 (Wu et al. 1983) is shown in Fig. 6. The key feature of the SED is the excess of UV photons, previously observed in the quiescent state (Froning et al. 2011; McClintock et al. 1995) – an extra source of UV radiation in addition to the optical companion is needed to reproduce the observed shape of the spectrum. The spectrum alone, however, does not allow an unambiguous separation of the second component: even the simplest model with one additional blackbody is degenerate due to the uncertainty in the stellar spectrum normalization. Various different methods were used to estimate the

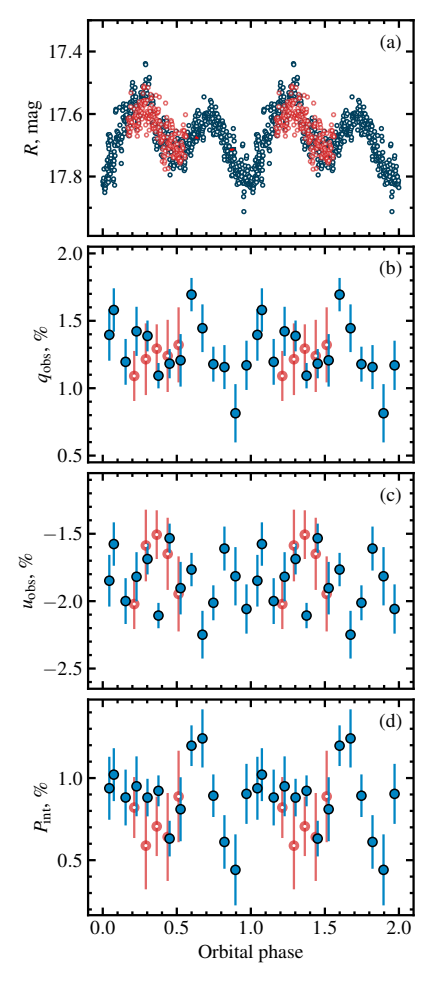


Fig. 5. Orbital profiles of the flux and of the normalized Stokes parameters of A0620–00. Solid blue and empty red circles correspond to the data from two different orbits. Panel (a): Photometric R magnitudes of A0620–00 folded with the orbital period. Panel (b) and Panel (c): Observed normalized Stokes parameters. Panel (d): Intrinsic PD of A0620–00 in the R filter folded with the orbital period. Each circle with a 1σ error bar shows the 35-minute average polarization.

contribution of nonstellar emission to the quiescent spectrum of A0620–00 (Marsh et al. 1994; Gelino et al. 2001; Harrison et al. 2007; Froning et al. 2011; Dinçer et al. 2018). Despite the fact that there is no complete consensus, it can be cautiously noted that most authors agree that the companion star dominates the entire NIR-to-optical range in the passive quiescent state, with the contribution of additional component increasing toward the blue part of the spectrum. The additional component becomes comparable with the stellar flux only near the *B* band, where its contribution

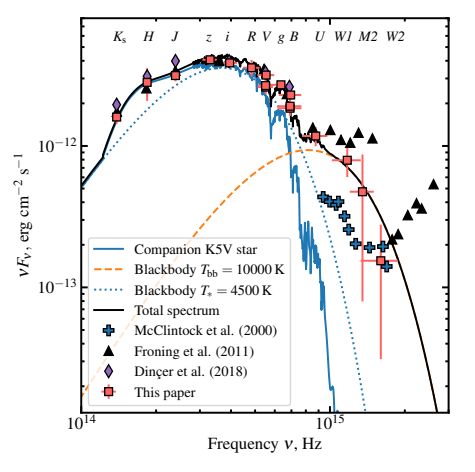


Fig. 6. SED of A0620–00, corrected for reddening assuming E(B-V)=0.35. Red squares with error bars correspond to the data from this paper. Blue crosses, black triangles, and purple diamonds show data from McClintock & Remillard (2000), Froning et al. (2011), and Dinçer et al. (2018), respectively. Solid blue, dotted blue, and dashed orange lines show the spectra of the K5V star (Pickles 1998), the blackbody of $T_*=4500$ K, and an additional blackbody of $T_{\rm bb}=10\,000$ K, respectively.

reaches 20–50%. Nonstellar emission spectrum can be described with the blackbody of temperature $T_{\rm bb}=9000-11\,000$ K depending on the state of activity. The nature of the additional component is still under discussion, but most likely it corresponds to the brightest part of the accretion disk (either the hot inner disk regions or the bright spot formed at the impact point of the accretion stream). The bright spot is clearly present in the Doppler tomograms (Marsh et al. 1994; Shahbaz et al. 1994, 2004; Neilsen et al. 2008) and it is needed to explain the asymmetric light curves (Froning & Robinson 2001; Cantrell et al. 2010; van Grunsven et al. 2017; Cherepashchuk et al. 2019). The contribution of the nonstellar radiation is variable on short (Haswell et al. 1993) and long (Cantrell et al. 2008) timescales. Our new observations are consistent with both interpretations (see Fig. 6 and Sect. 4).

4. Discussion

4.1. The source of the polarization

The first optical polarimetric observations of A0620–00 were performed during its 1975 outburst (Dolan 1976, see the orange star in Fig. 3). The observed PD, PA, and their spectral properties were found to be consistent with the IS origin. Our IS polarization estimate is very close to the outburst polarization level of A0620–00, which confirms the above statement. Subpercent intrinsic optical polarization of A0620–00 is in line with that of the other BH X-ray binaries – most known sources observed during the outburst show low intrinsic polarization levels (XTE J1118+480, Schultz et al. 2004; MAXI J0637–430, Kravtsov et al. 2019; MAXI J1820+070, Veledina et al. 2019; Kosenkov et al. 2020; Swift J1727.8–1613, Kravtsov et al. 2023a; V404 Cyg, Tanaka et al. 2016; Kosenkov et al. 2017;

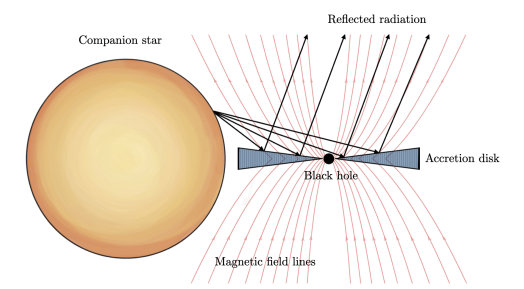


Fig. 7. Schematic illustration of the scattering geometry (not to scale).

GX 339–4, Mastroserio et al. 2025; LMC X-3, Boyd et al. 2001). However, the intrinsic PD of some BH LMXBs increases significantly as they approach quiescence (e.g., MAXI J1820+070, Poutanen et al. 2022, and A0620–00, Dubus et al. 2008). Intrinsic optical polarization is also detected in some NS X-ray binaries (Aql X-1, Charles et al. 1980; Cyg X-2, Koch Miramond & Naylor 1995; Sco X-1, Schultz et al. 2004; 4U 0614+091, Baglio et al. 2014; XTE J1709–267, Higgins et al. 2019).

The orbit-averaged intrinsic polarization of A0620–00 in the quiescent state has nearly the same PD $\sim 1\%$ at all wavelengths from the K_s to B band, yet PA shows a significant rotation over those wavelengths (Fig. 3). This makes A0620–00 the only source known to date for which such a strong PA dependence on the wavelength is observed. Such polarization behavior cannot be explained in terms of simple mechanisms of polarization production. Indeed, if the polarization is produced mostly by scattering, its PA should not depend on the wavelength.

We first studied the case in which the observed dependence of PA on wavelength is caused by Faraday rotation. We considered the scenario illustrated in Fig. 7. The unpolarized radiation of the companion star gets scattered by the accretion disk and the polarized scattered radiation has initial PA independent of the wavelength. After the scattering, the linearly polarized radiation propagates toward the observer through the magnetized plasma surrounding the accretion disk. The PA of the light propagating along the magnetic field lines experiences the Faraday rotation, resulting in the observed PA dependence on wavelength.

The PA of linearly polarized radiation propagating through the magnetized plasma rotates with the wavelength λ as

$$\theta(\lambda) = \theta_0 + RM \lambda^2, \tag{2}$$

where the rotation measure (RM) is defined through the integral along the line of sight:

$$RM = \frac{e^3}{2\pi m_c^2 c^4} \int n_c(l) B_{\parallel}(l) dl,$$
 (3)

where $n_{\rm e}$ is the electron number density, B_{\parallel} (in G) is the line of sight magnetic field strength, e is the electric charge, $m_{\rm e}$ is the electron mass and c is the speed of light. If B_{\parallel} is constant, the RM can be expressed through the Thomson optical depth $\tau_{\rm T} = \int n_{\rm e} \sigma_{\rm T} dl$. In this case, RM $\approx 0.4 \tau_{\rm T} B_{\parallel} \, {\rm rad \, \mu m^{-2}}$.

We used Eq. (2) with parameters θ_0 and RM to find the best-fit solution for the Faraday rotation of PA in our optical points and NIR points reported in Russell et al. (2016). We find the best-fit parameters $\theta_0 = 175^{\circ} \pm 4^{\circ}$ and RM =

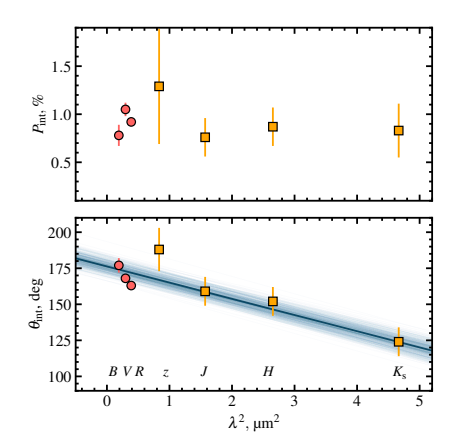


Fig. 8. Dependence of the intrinsic PD and PA of A0620–00 on λ^2 . The circles and squares correspond to optical observations from this paper and NIR polarimetric observations from Russell et al. (2016), respectively. The blue line shows the best-fit Faraday rotation model given by Eq. (2).

 $-0.20\pm0.01~{\rm rad}\,\mu{\rm m}^{-2}$ (see Fig. 8). The latter value gives the relation between the line-of-sight optical depth and magnetic field (in gauss) $\tau_T B_{\parallel} \approx 0.5$. For the realistic values of matter density in quiescence $\tau_T \lesssim 0.1$, we find $B \gtrsim 5~{\rm G}$. This value is roughly consistent with the magnetic fields expected in the quiescent-state optically thin accretion flows (Wallace & Pe'er 2021), which may be similar to those of optically thin plasma surrounding the disk (Fig. 7).

We note, however, that the NIR data were taken almost ten years prior to our optical observations, and hence potential magnetic field variations may lead to the inconsistency of trends between the optical and NIR PA points. We indeed observe that our recent measurements (leftmost three points in Fig. 8) lie on a straight line with the slope differing from the general trend. If we apply Eq. (2) only to our data, we obtain $\theta_0=186^\circ\pm6^\circ$ and RM $=-1.3\pm0.3\,\mathrm{rad\,um^{-2}}$ (see Fig. 8). This translates to $\tau_T B_\parallel \approx 3.2$, requiring almost seven times higher magnetic field strength for the Faraday rotation to occur in the optically thin plasma $(\tau_T \lesssim 1)$.

Next, we considered the scenario in which the observed polarization arises from two components: one coming from the scattering of the stellar light and the other from the polarized contribution of the additional UV component. The scattering component is assumed to have constant PD and PA, which implies a constant fraction of the scattered radiation, and spectrum as that of the optical companion (solid blue line in Fig. 9a). The additional UV component (dashed orange line), which was used to describe the UV part of the observed SED, is set to have constant PD and PA, whose values were free to vary. The blue lines in Fig. 9b and c show the dependence of PD and PA for this two-component scenario. To reproduce the rotation of the PA from the NIR to the B band, the components must have different PAs: $PA_{sc} \approx 150^{\circ}$ and $PA_{UV} \approx 190^{\circ}$. Because the components have comparable contribution to the optical flux, the PD of the UV component (PD_{UV} $\approx 1.8\%$) should be significantly higher than that of the scattering component (PD_{sc} $\approx 0.8\%$) to dominate the PA in B. The polarization of the UV component can

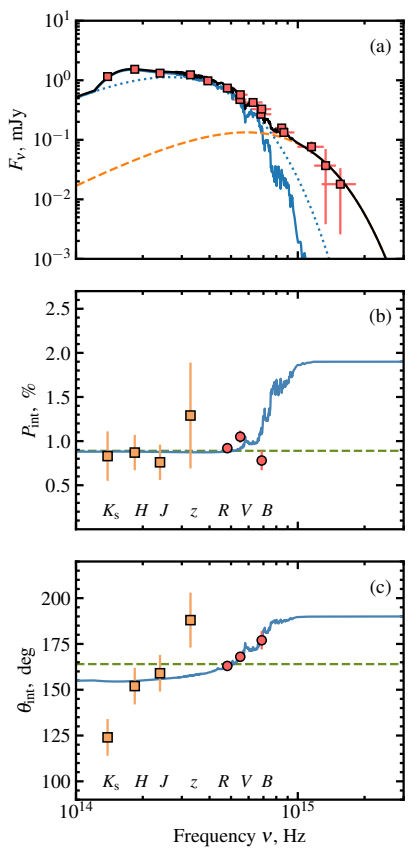


Fig. 9. Polarimetric properties of A0620–00. Panel (a): Energy dependence of flux (F_y) , as in Fig. 6 but only the data from this paper are shown. Panels (b) and (c): Energy dependence of the intrinsic PD and PA of A0620–00. Circles and squares correspond to optical observations from this paper and NIR polarimetric observations from Russell et al. (2016), respectively. The blue line corresponds to the model with two polarized components described in Sect. 4.1. Dashed green lines correspond to the constant polarization model.

arise from the first (single) Compton up-scattering of the disk or synchrotron photons by electrons in the hot accretion flow, similar to the case of MAXI J1820+070 (Poutanen et al. 2022). The difference of PA in the scattered and UV components can then indicate misalignment by $\sim\!50^\circ$ (or $\sim\!40^\circ$) between the axes of these components. This scenario predicts rise of PD and further rotation of PA toward the UV band (see Fig. 9).

While this model fairly well describes the rotation of the optical PA, it cannot reproduce the dataset in full detail. First of all, the intrinsic PAs in K_s and z differ from the model predictions. This difference may arise due to the fact that the observations in NIR were preformed a decade prior to the optical campaign while the source may have been in a different

state (loop or active, Cantrell et al. 2008). There is evidence that in active quiescent state, the additional component contributes to the NIR part of the spectrum (Froning et al. 2007; Dincer et al. 2018; Cherepashchuk et al. 2019), which could be a jet, an accretion stream-disk impact point, or a dusty circumbinary disk (Muno & Mauerhan 2006; Gallo et al. 2007; Cherepashchuk et al. 2019). This additional NIR component, not present in our passive state observations, could however be responsible for an additional polarization in the K_s band in the epoch of the Russell et al. (2016) observations; that would explain the observed difference in the PA. Some deviations in NIR may also arise from the Faraday rotation. Additionally, although the model describes the flat PD spectrum from NIR to R reasonably well and replicates the PD rise due to the absorption line in V well, the PD in B is about 0.3% lower than the level predicted by the model. The reason for the apparent drop of the PD in B is unknown, but we argue that the actual broadband spectrum of an object obtained simultaneously with polarization measurements should be used instead of the model spectrum of the companion star to analyze such subtle effects. Polarimetric observation in the UV band, in which we expect significant increase in the PD, can unambiguously infer the nature of PA rotation in A0620-00 and, subsequently, shed light on the nature of the UV excess in the binary.

4.2. On the synchrotron origin of the polarization

Synchrotron emission has been suggested to contribute to the polarization of A0620–00 in NIR in addition to scattering (Russell et al. 2016). By assuming the scattering component to have polarization with PA $\sim 173^\circ$ and PD $\sim 1\%$ and by subtracting it from the observed K_s polarization, authors got the PD of synchrotron emission to be $\sim 1.3\%$. Then, by assuming the jet contribution in K_s to be 8–37%, authors found the jet to be polarized at the level of PD_{jet} =3–18%. However, we argue that such a separation of polarized components cannot be done unambiguously with the existing data for several reasons.

First, the PA changes significantly within the optical range, meaning that polarization cannot be produced by scattering alone. Therefore, the PA of the scattered component cannot be determined explicitly with the optical data only. In previous section, we estimated the PA of scattered component to be closer to $\sim 150^{\circ}$, which, if subtracted from observed K_s polarization, would result in much smaller PD of synchrotron emission ~0.8% with the PA of ~180°. We note also that although the observed PA in K_s seems to be perpendicular to the possible direction of the radio jet (see Fig. 4), after subtracting the scattering contribution, the PA of remaining synchrotron component differs from the jet axis by about 45°, which cannot be easily explained with the jet model. Second, there is no direct evidence of the presence of NIR excess in the photometric data in passive quiescence. The apparent increase in the flux in NIR relative to blackbody is well described by the stellar spectrum alone – the "bump" at K_s and H is well pronounced in the K5V companion spectrum in Fig. 6. Therefore, it is rather difficult to determine the contribution of jet emission to the observed spectrum, especially given the strong variability of the object both within and between states. Adding the jet as a third component in addition to the scattering and UV components to the modeling is hardly justified given the quality and the number of polarimetric observations. Taking all of the above into account, although we do not rule out the possibility that jet contributes to the NIR polarization, we argue that its accurate determination is a challenging task that requires more

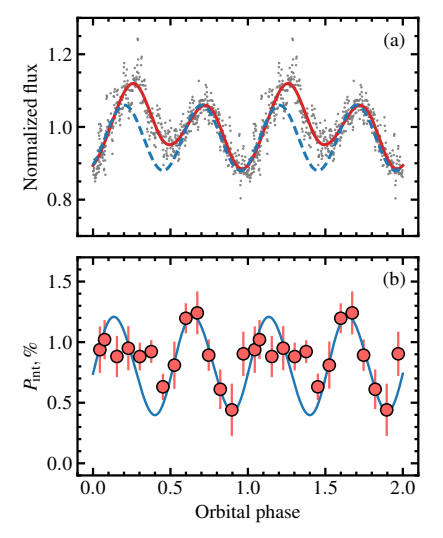


Fig. 10. Flux and PD variations of A0620–00. Panel (a): Normalized flux, folded with the orbital phase (gray circles). The solid red line corresponds to the best fit of the data with the Fourier series, while the dashed blue line corresponds to the sinusoidal variations, assumed to be produced by the tidally distorted optical companion. Panel (b): Intrinsic PD of A0620–00 (red circles) folded with the orbital period together with the model of a scattering cloud on a circular orbit from the appendix of Kravtsov et al. 2020 (blue line).

precise simultaneous multiwavelength polarimetric observations than we have to date.

4.3. The source of the polarization variations

In addition to the changes in the polarization between different spectral states, we also see intra-day variability of the polarization. Although the 2% orbital modulation of the polarization observed by Dolan & Tapia (1989) has not been confirmed (Dubus et al. 2008), we see the variations at a level of 0.3% on timescales of hours (see Fig. 5). To confidently claim that the polarization of A0620-00 is variable with the orbital phase, one would need to cover at least two consecutive orbital periods with high-precision polarimetric observations (which is a rather difficult task given the brightness of the object in quiescence and its short orbital period). That said, we can cautiously state that the observed polarization variability is related to the orbital phase rather than having a stochastic nature. Indeed, the polarization of A0620-00, folded with the orbital phase, shows the pattern typical for binary stars - double-sinusoidal variations with the PD reaching minima in the conjunctions (phases 0 and 0.5) and maxima in the quadratures (phases 0.25 and 0.75). This is due to Thomson scattering of the stellar radiation on the matter, which follows the compact object in its orbital motion (Brown et al. 1978; Kraytsov et al. 2020), and is similar to what is observed in other BH (Kemp et al. 1979; Gliozzi et al. 1998; Kravtsov et al. 2023b) and neutron star (Egonsson & Hakala 1991; Combi et al. 2004; Baglio et al. 2016) X-ray binaries. In Fig. 10 we see a fairly good agreement of the PD variations with the expected behavior (the blue line shows the model of a scattering cloud on a circular orbit; see the appendix of Kravtsov et al. 2020). In addition, our first and second observations, performed during two different orbits are consistent with each other (see Fig. 5). We note also that Stokes parameters of A0620–00, folded with the orbital period, show scatter, similar to one observed in Dubus et al. (2008) — while Stokes q shows more pronounced orbital variability, Stokes u seems to behave more erratically. The amplitude of this scatter, however, is comparable to the measurement errors, which complicates its interpretation, but one explanation could be the presence of inhomogeneities (clumps) in the scattering matter.

The optical light curve shown in Fig. 10 has an asymmetric profile - the peak and the dip at the first half of the orbit are brighter than the other peak and dip. The so-called ellipsoidal variations of the flux, produced by the tidally distorted optical star (shown by the dashed blue line at Fig. 10), cannot produce such asymmetry; therefore, an additional source of flux variations is needed. There are two alternatives: either there is an additional bright component visible only at the first part of the orbit and generating additional flux (e.g., noncircular accretion disk or bright spot in the accretion stream; see, e.g., Haswell et al. 1993), or some object blocks the light of the optical companion, reducing the total flux at phases from 0.5 to 1.0 (e.g., dark spots at the surface of the star; e.g., Cherepashchuk et al. 2019). We see similar asymmetry in the orbital polarization profile of A0620-00 - while around orbital phases from 0.5 to 1.0 the PD shows good agreement with the Thomson scattering model, at the first part of the orbit the PD is consistent with being constant. The additional bright unpolarized component, visible only at phases from 0.0 to 0.5, could reduce the polarization at these phases and explain both the asymmetric PD and flux variations; therefore, we argue that the bright spot or phase-dependent disk models are more likely than the dark star spot model. Another alternative is that the asymmetric PD profile is produced by scattering of stellar radiation off slightly tilted accretion disk. In this scenario, the illuminated part of the accretion disk is visible to the observer only for half of the orbit (see Kravtsov et al. 2023b). However, scattering alone is not enough to reproduce the ~ 10% increase in flux observed at the first half of the orbit, and the quality of our polarimetric data is not sufficient to discriminate between the complex

5. Conclusions

We have presented new high-precision phase-resolved optical polarimetric and quasi-simultaneous NIR-to-UV photometric observations of BH X-ray binary A0620-00 in a passive quiescent state. We determined and subtracted the IS polarization, which allowed us to derive the intrinsic polarization of A0620-00. Using that combined with the NIR polarimetric observations from Russell et al. (2016), we found that the orbitaverage intrinsic PA rotates with the wavelength, changing from 124° in the K_s filter to 177° in B, while the PD remains at the ~1% level throughout this spectral range. Folding our polarimetric observations with the orbital period, we found the significant orbital variability of polarization properties in the R band. The shape of the variations, with two minima and two maxima per period, suggests that the polarization is most probably produced by Thomson scattering of the companion star emission off the matter, which follows the BH in its orbital motion (e.g., scattering off the accretion disk or stream). The lack of variations during the first part of the orbit suggests either that we see a

depolarization effect caused by the bright spot visible only at these phases or (less probably) that the scattering material producing the polarization is obscured or tilted relative to the orbital axis. However, more high-precision polarimetric observations from at least several consecutive orbital periods are needed to draw unambiguous conclusions about the geometry of the scattering medium.

The flat spectrum of the polarization and the presence of the orbital variations suggest that NIR-to-optical polarization has a scattering origin. However, in that case, the PA is not expected to change with the wavelength as observed. We first considered the possibility that stellar radiation scattered off the accretion disk experiences Faraday rotation while traveling toward the observer through the magnetized plasma surrounding the accretion disk. The estimated values of the magnetic field and optical depth can be considered consistent with realistic estimates if we take into account our optical points in combination with the NIR points taken almost ten years ago. On the other hand, the steep trend of our optical points favors a higher Faraday rotation rate, resulting in higher values for the line-of-sight magnetic field.

We considered the scenario of two polarized components that have different PDs and PAs. One component is coming from the stellar scattered light and the other is associated with the additional UV component seen in the spectrum. The second component may potentially arise from Compton up-scattering of the disk or synchrotron photons in the hot inner flow, similar to what is seen in the quiescent-state low-mass BH X-ray binary MAXI J1820+070. The PAs of these components differ by ~40°, which translates to either a 50° or 40° misalignment between their axes of symmetry. Future simultaneous polarimetric observations covering the NIR-to-UV range would be extremely helpful in unambiguously determining which of the two models best represents A0620–00.

Acknowledgements. Based on observations made with the Nordic Optical Telescope, owned in collaboration by the University of Turku and Aarhus University and operated jointly by Aarhus University, the University of Turku, and the University of Oslo, representing Denmark, Finland, and Norway, the University of Iceland and Stockholm University at the Observatorio del Roque de los Muchachos, La Palma, Spain, of the Instituto de Astrofisica de Canarias. The DIPol-2 and DIPol-UF polarimeters were built in cooperation between the University of Turku, Finland, and the Leibniz-Institut für Sonnenphysik, Germany. The Liverpool Telescope is operated on the island of La Palma by Liverpool John Moores University in the Spanish Observatorio del Roque de los Muchachos of the Instituto de Astrofisica de Canarias with financial support from the UK Science and Technology Facilities Council. MAPT acknowledge support from the Agencia Estatal de Investigación (MCIN/AEI) and the European Regional Development Fund under grant PID2021-124879NB-100. This research has been supported by the Finnish Cultural Foundation (VK) and by the Academy of Finland grants 355672 (AV). Nordita is supported in part by Nordforsk.

References

```
Arnaud, K. A. 1996, ASP Conf. Ser., 101, 17
Baglio, M. C., Mainetti, D., D'Avanzo, P., et al. 2014, A&A, 572, A99
Baglio, M. C., D'Avanzo, P., Campana, S., et al. 2016, A&A, 587, A102
Bessell, M. S. 1979, PASP, 91, 589
Boyd, P. T., Smale, A. P., & Dolan, J. F. 2001, ApJ, 555, 822
Brown, J. C., McLean, I. S., & Emslie, A. G. 1978, A&A, 68, 415
```

```
Cherepashchuk, A. M., Katysheva, N. A., Khruzina, T. S., et al. 2019, MNRAS,
Combi, J. A., Cellone, S. A., Martí, J., et al. 2004, A&A, 427, 959
Dinçer, T., Bailyn, C. D., Miller-Jones, J. C. A., Buxton, M., & MacDonald, R.
    K. D. 2018, ApJ, 852, 4
Dolan, J. F. 1976, ApJ, 210, 721
Dolan, J. F., & Tapia, S. 1989, PASP, 101, 1135
Dubus, G., Kern, B. D., Chaty, S., & Foellmi, C. 2008, Proc. Sci., 62, 115
Egonsson, J., & Hakala, P. 1991, A&A, 244, L41
Elvis, M., Page, C. G., Pounds, K. A., Ricketts, M. J., & Turner, M. J. L. 1975,
Froning, C. S., & Robinson, E. L. 2001, AJ, 121, 2212
Froning, C. S., Robinson, E. L., & Bitner, M. A. 2007, ApJ, 663, 1215
Froning, C. S., Cantrell, A. G., Maccarone, T. J., et al. 2011, ApJ, 743, 26
Fukugita, M., Ichikawa, T., Gunn, J. E., et al. 1996, AJ, 111, 1748
Gaia Collaboration (Brown, A. G. A., et al.) 2021, A&A, 649, A1
Gallo, E., Migliari, S., Markoff, S., et al. 2007, ApJ, 670, 600
Gallo, E., Teague, R., Plotkin, R. M., et al. 2019, MNRAS, 488, 191
Garzón, F., Balcells, M., Gallego, J., et al. 2022, A&A, 667, A107
Gehrels, N., Chincarini, G., Giommi, P., et al. 2004, ApJ, 611, 1005
Gelino, D. M., Harrison, T. E., & Orosz, J. A. 2001, AJ, 122, 266
Gliozzi, M., Bodo, G., Ghisellini, G., Scaltriti, F., & Trussoni, E. 1998, A&A,
    337, L39
Harrison, T. E., Howell, S. B., Szkody, P., & Cordova, F. A. 2007, AJ, 133, 162
Haswell, C. A., Robinson, E. L., Horne, K., Stiening, R. F., & Abbott, T. M. C.
    1993 ApJ 411 802
Higgins, A. B., Wiersema, K., Covino, S., et al. 2019, MNRAS, 482, 5023
Kemp, J. C., Barbour, M. S., Parker, T. E., & Herman, L. C. 1979, ApJ, 228, L23
Koch Miramond, L., & Naylor, T. 1995, A&A, 296, 390
Kosenkov, I. A., Berdyugin, A. V., Piirola, V., et al. 2017, MNRAS, 468, 4362
Kosenkov, I. A., Veledina, A., Berdyugin, A. V., et al. 2020, MNRAS, 496, L96
Kravtsov, V., Berdyugin, A., Veledina, A., et al. 2019, ATel., 13291, 1
Kravtsov, V., Berdyugin, A. V., Piirola, V., et al. 2020, A&A, 643, A170
Kravtsov, V., Berdyugin, A. V., Kosenkov, I. A., et al. 2022, MNRAS, 514, 2479
Kravtsov, V., Nitindala, A. P., Veledina, A., et al. 2023a, ATel., 16245, 1
Kravtsov, V., Veledina, A., Berdyugin, A. V., et al. 2023b, A&A, 678, A58
Kuulkers, E., Fender, R. P., Spencer, R. E., Davis, R. J., & Morison, I. 1999,
Marsh, T. R., Robinson, E. L., & Wood, J. H. 1994, MNRAS, 266, 137
Mastroserio, G., De Marco, B., Baglio, M. C., et al. 2025, ApJ, 978, L19 McClintock, J. E., & Remillard, R. A. 1986, ApJ, 308, 110
McClintock, J. E., & Remillard, R. A. 2000, ApJ, 531, 956
McClintock, J. E., Horne, K., & Remillard, R. A. 1995, ApJ, 442, 358
Muno, M. P., & Mauerhan, J. 2006, ApJ, 648, L135
Neilsen, J., Steeghs, D., & Vrtilek, S. D. 2008, MNRAS, 384, 849
Pickles, A. J. 1998, PASP, 110, 863
Piirola, V., Berdyugin, A., & Berdyugina, S. 2014, Proc. SPIE, 9147, 91478I
Piirola, V., Berdyugin, A., Frisch, P. C., et al. 2020, A&A, 635, A46
Piirola, V., Kosenkov, I. A., Berdyugin, A. V., Berdyugina, S. V., & Poutanen, J.
2021, AJ, 161, 20
Poutanen, J., Veledina, A., Berdyugin, A. V., et al. 2022, Science, 375, 874
Russell, D. M., Shahbaz, T., Lewis, F., & Gallo, E. 2016, MNRAS, 463, 2680
Schultz, J., Hakala, P., & Huovelin, J. 2004, Baltic Astron., 13, 581
Serkowski, K. 1962, Adv. Astron. Astrophys., 1, 289
Shahbaz, T., Ringwald, F. A., Bunn, J. C., et al. 1994, MNRAS, 271, L10
Shahbaz, T., Hynes, R. I., Charles, P. A., et al. 2004, MNRAS, 354, 31
Simmons, J. F. L., & Stewart, B. G. 1985, A&A, 142, 100
Steele, I. A., Smith, R. J., Rees, P. C., et al. 2004, Proc. SPIE, 5489, 679
Tanaka, Y. T., Itoh, R., Uemura, M., et al. 2016, ApJ, 823, 35
van Grunsven, T. F. J., Jonker, P. G., Verbunt, F. W. M., & Robinson, E. L. 2017,
    MNRAS, 472, 1907
Veledina, A., Berdyugin, A. V., Kosenkov, I. A., et al. 2019, A&A, 623, A75
Wallace, J., & Pe'er, A. 2021, ApJ, 916, 63
Wu, C. C., Panek, R. J., Holm, A. V., Schmitz, M., & Swank, J. H. 1983, PASP,
```

Cantrell, A. G., Bailyn, C. D., McClintock, J. E., & Orosz, J. A. 2008, ApJ, 673,

Cantrell, A. G., Bailyn, C. D., Orosz, J. A., et al. 2010, ApJ, 710, 1127

Charles, P. A., Thorstensen, J. R., Bowyer, S., et al. 1980, ApJ, 237, 154

Kravtsov V., Berdyugin A.V., Kosenkov I.A., Veledina A., Piirola V., Abdul Qadir Y., Berdyugina S.V., Sakanoi T., Kagitani M., Poutanen J. Optical polarization signatures of black hole X-ray binaries

Monthly Notices of the Royal Astronomical Society, 2022; 514: 2479



Monthly Notices

ROYAL ASTRONOMICAL SOCIETY

MNRAS **514,** 2479–2487 (2022) Advance Access publication 2022 May 31



Optical polarization signatures of black hole X-ray binaries

Vadim Kravtsov , ¹* Andrei V. Berdyugin, ¹ Ilia A. Kosenkov , ¹ Alexandra Veledina , ¹, ², ² Vilppu Piirola, ¹ Yasir Abdul Qadir, ¹ Svetlana V. Berdyugina, ⁴ Takeshi Sakanoi, ⁵ Masato Kagitani and Juri Poutanen , ¹, ³

Accepted 2022 May 23. Received 2022 April 22; in original form 2022 April 22

ABSTRACT

Polarimetry provides an avenue for probing the geometry and physical mechanisms producing optical radiation in many astrophysical objects, including stellar binary systems. We present the results of multiwavelength (BVR) polarimetric studies of a sample of historical black hole X-ray binaries, observed during their outbursts or in the quiescent (or near-quiescent) state. We surveyed both long- and short-period systems, located at different Galactic latitudes. We performed careful analysis of the interstellar polarization in the direction on the sources to reliably estimate the intrinsic source polarization. Intrinsic polarization was found to be small (<0.2 percent) in sources observed in bright soft states (MAXI J0637–430 and 4U 1957+115). It was found to be significant in the rising hard state of MAXI J1820+070 at the level of ~0.5 per cent and negligible in the decaying hard state and during its failed outbursts, while Swift J1357.2–0933 showed its absence in the rising hard state. Three (XTE J1118+480, V4641 Sgr, V404 Cyg) sources observed during quiescence show no evidence of significant intrinsic polarization, while MAXI J1820+070 is the only black hole X-ray binary which showed substantial (>5 per cent) intrinsic quiescent-state polarization with a blue spectrum. The absence of intrinsic polarization at the optical wavelengths puts constraints on the potential contribution of non-stellar (jet, hot flow, accretion disc) components to the total spectra of black hole X-ray binaries.

Key words: polarization – X-rays: binaries.

1 INTRODUCTION

Accreting stellar-mass black holes in X-ray binaries (BHXRBs) are natural laboratories for studying the interaction between matter and radiation under extreme physical conditions. During periods of violent activity – the outbursts – such systems efficiently convert the gravitational energy into radiation that is observed over a broad range of electromagnetic wavelengths, from radio to X/γ -rays. The outburst radio emission is coming from the jet, while the X-rays are produced by the hot accretion flow or corona. Optical and infrared emission, as evidenced by spectral and timing properties, is a product of a complex interplay between the jet, wind, irradiated disc, and hot accretion flow components (Poutanen & Veledina 2014; Uttley & Casella 2014)

An outburst typically continues for several weeks to months, eventually decaying into a quiescent state, a long period of inactivity. The main components of the system – the companion star, the accretion disc, the inner accretion flow – all may contribute to the optical and infrared emission in the quiescence. The hotspot/line (the point of intersection of the stream of matter from the companion

star and the outer parts of the disc, see e.g. McClintock, Horne & Remillard 1995; Froning et al. 2011) and jet (Shahbaz et al. 2013) were also proposed as potential sources of quiescent emission.

Identifying different spectral components and studying their radiative properties are essential for understanding the mechanisms that trigger the outbursts. The contribution of different components to the total spectrum has been studied utilizing a variety of methods, with polarimetry often overlooked and undervalued. Polarization carries information about the geometrical properties of the emitting/scattering media, which may otherwise be inaccessible to an observer.

Polarized radiation can be produced by several physical processes, including synchrotron radiation in the presence of an ordered magnetic field of the jet or hot accretion flow, electron scattering in the accretion disc atmosphere or scattering of the accretion disc radiation in the outflow (jet/wind) by electrons or, in quiescence, by dust. Each component has different polarization characteristics (or no polarization at all), which makes polarimetry an excellent tool for probing the geometry of the source and physical mechanisms responsible for optical radiation in black hole X-ray binaries.

A number of recent studies of polarized optical emission of black hole X-ray binaries were focused on BHXRBs in the outbursts (e.g. Shahbaz et al. 2016; Tanaka et al. 2016; Itoh et al. 2017;

¹Department of Physics and Astronomy, University of Turku, FI-20014 Turku, Finland

²Nordita, KTH Royal Institute of Technology and Stockholm University, Hannes Alfvéns vég 12, SE-10691 Stockholm, Sweden

³Space Research Institute of the Russian Academy of Sciences, Profsoyuznaya Str. 84/32, Moscow 117997, Russia

⁴Leibniz-Institut für Sonnenphysik, Schöneckstr. 6, D-79104 Freiburg, Germany

⁵Graduate School of Sciences, Tohoku University, Aoba-ku, 980-8578 Sendai, Japan

^{*} E-mail: vakrau@utu.fi

2480 V. Kravtsov et al.

Table 1. List of observed BHXRBs.

Object	Companion	m_V mag	α	δ	π mas	i deg	P _{orb} h	References
XTE J1118+480	K7 V – M1 V	19.6 ± 0.2^a	11 ^h 18 ^m 10.79	+48° 02′ 12″32	0.30 ± 0.40	68 ± 2	4.07841(5)	[1, 2, 9]
Swift J1357.2-0933	M5 V	17.27 ± 0.02^a	13 ^h 57 ^m 16 ^s 84	$-09^{\circ} 32' 38''.79$	-	>70	2.8 ± 0.3	[1, 3]
4U 1957+115	-	$\approx 19.0^{b}$	19h 59m 24s01	+11° 42′ 29″.86	0.07 ± 0.15	20 - 70	9.33(1)	[1, 4, 5, 10]
V404 Cyg	K3 III	$\approx 18.7^{c}$	20h 24m 03s82	+33° 52′ 01″.90	0.42 ± 0.02	67 ± 3	155.35(2)	[1, 6, 7, 11]
V4641 Sgr	B9 III	$\approx 13.5^{c}$	18h 19m 21s63	$-25^{\circ} 24' 25''.85$	0.17 ± 0.03	72 ± 4	67.61(2)	[1, 8, 12]
XTE J2012+381	-	21.3 ± 0.1^d	20 ^h 12 ^m 37 ^s .76	+38° 11′ 00″.77	-	_		[1]
MAXI J1820+070	K6 IV	_	18h 20m 21s94	+07° 11′ 07″29	0.37 ± 0.08	73 ± 6	16.4518(2)	[1, 13, 14, 15]
MAXI J0637-430	-	$\approx 16.5^{c}$	06h 36m 23s59	$-42^{\circ}52'04''.10$	-	_	-	[1]

Notes. References: (1) Gaia Collaboration (2021), (2) Gelino et al. (2006), (3) Corral-Santana et al. (2013), (4) Hakala, Muhli & Dubus (1999), (5) Bayless et al. (2011), (6) Miller-Jones et al. (2009), (7) Khargharia, Froning & Robinson (2010), (8) MacDonald et al. (2014), (9) Torres et al. (2004), (10) Thorstensen (1987), (11) Casares, Charles & Naylor (1992), (12) Orosz et al. (2011), (13) Torres et al. (2020), (14) Poutanen et al. (2022), (15) Mikolajewska et al. (2022). "StanCam photometry, b Hakala, Muhli & Charles (2014), "AAVSO magnitudes, "Hynes et al. (1999).

Kosenkov et al. 2017; Veledina et al. 2019; Kosenkov et al. 2020). However, only a few attempts to study quiescent polarization have been made to date. Dolan & Tapia (1989) found variable optical polarization of BHXRB 1A 0620-00 and constrained its inclination by modelling the dependence of Stokes parameters on orbital phase. Significant quiescent optical polarization of 1A 0620-00 at the level of $P \approx 3$ per cent was later confirmed (Dubus et al. 2008). Russell et al. (2016) claimed detection of near-infrared quiescent intrinsic polarization of 1A 0620-00 and Swift J1357.2-0933. MAXI J1820+070, observed in near-quiescence after its 2018 outburst, demonstrated a large intrinsic polarization degree exceeding 5 per cent in B-band and blue polarization spectra, likely caused by scattering either in the hot accretion flow or by the dusty equatorial wedge (Poutanen et al. 2022). A difference by 45° between polarization angle and the position angle of the jet was interpreted as a signature of a high, more than 40°, misalignment between the orbital angular momentum and the black hole spin (Poutanen et al. 2022). Similar polarization signatures, if found in other sources, could be used to study the statistical distribution of orbital-BH spin misalignment angle, constraining binary evolution and black hole

In this paper, we present a study of optical (BVR) polarization of a sample of BHXRBs during the outbursts and in the quiescent or near-quiescent states. We surveyed both long- and short-period systems with different spectral classes of the companion star, located at different Galactic latitudes. We put tight constraints on the magnitude of intrinsic polarization for most of the sources with the help of polarimetric observations of the field stars. The properties of intrinsic polarization allowed us to estimate the potential contribution of non-stellar components (jet/hot flow) to the total spectra.

2 DATA ACQUISITION AND REDUCTION

The observations of BHXRBs were carried out with two copies of DIPol-2 polarimeter (Piirola, Berdyugin & Berdyugina 2014) and a single unit of DIPol-UF polarimeter (Piirola et al. 2021). One copy of DIPol-2 is installed at the 60 cm Tohoku T60 telescope, Haleakala Observatory, Hawaii, USA; another was mounted on the 60 cm KVA telescope, Observatorio del Roque de los Muchachos (ORM), La Palma, Spain, and was also used as a visitor instrument at 4.2 m William Herschel Telescope (WHT, ORM) and 2.2 m Univesity of Hawaii telescope (UH88, Mauna Kea, Hawaii, USA). DIPol-UF is a visitor instrument installed at the 2.56 m Nordic Optical Telescope (NOT ORM)

We have collected the polarimetric data on eight BHXRBs with declination $\delta > -30^\circ$ (constrained by the geography of the telescopes used) and visual magnitude $m_V < 21$ mag, limited by the capabilities of the NOT (see Table 1). These include both short- and long-period systems ($P_{\rm orb}$ from ~ 2.8 h to 6.5 d), systems with different spectral classes of companion stars (from B9 III to M5 V), located at broad range of Galactic latitudes (Fig. 1 and Table 1).

XTE J1118+480, Swift J1357.2–0933, 4U 1957+115, and XTE J2012+381 were observed for one night each (DIPol-UF at NOT). MAXI J0637–430 was observed for three nights during its soft state in 2019 November (DIPol-2 at T60). V4641 Sgr was observed for a total of 11 nights: eight nights during its quiescent state (three nights with DIPol-2 at T60 in 2018 and five nights with DIPol-UF at NOT in 2019–2020) and for another three nights during its 2021 failed outburst (DIPol-2 at T60). V404 Cyg was observed for two nights during its quiescent state in 2019 July and 2021 July (DIPol-UF at NOT). MAXI J1820+070 was observed for a total of 10 nights during its failed outbursts in 2019 August and 2020 March (DIPol-2 at T60).

We complement the new measurements with the previously published DIPol-2 and DIPol-UF data. These data include the results of polarimetric observations of V404 Cyg and MAXI J1820+070 during a total of 12 and 65 nights respectively. V404 Cyg was monitored for five nights during its 2015 outburst (DIPol-2 at T60), for another five nights, after the outburst has ended (DIPol-2 at WHTT) and for two nights during the quiescent state with DIPol-2 mounted at the UH88 (Kosenkov et al. 2017). MAXI J1820+070 was monitored for 12 nights during the rising hard state (DIPol-2 at T60; Veledina et al. 2019), for 26 and 9 nights during the soft and decaying hard states, respectively (DIPol-2 at T60; Kosenkov et al. 2020), and for 18 nights during the quiescent state (DIPol-UF at NOT; Poutanen et al. 2022).

The only relatively bright source in the sample, V4641 Sgr, was observed using a conventional amplifier, while for fainter targets we used electron-multiplication regime of DIPol-UF, which provides better signal-to-noise ratio under such conditions (for a detailed description of instrument modes, see Piirola et al. 2021; Kosenkov 2021c). In addition to the polarimetry, we were able to perform photometric measurements of XTE J1118+480 and Swift J1357.2-0933 with the StanCam CCD photometer, mounted at the NOT. The photometric observations were made within the same night as the polarimetric measurements (MJD 59326). We also used the public AAVSO light curves to estimate V-band magnitudes of V404 Cyg, V4641 Sgr, and MAXI J0637-430. Stellar magnitudes for all targets are given in Table 1.

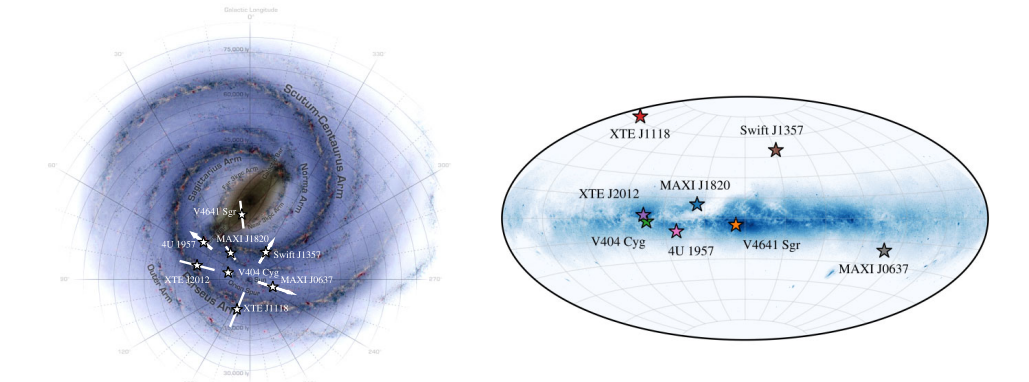


Figure 1. Galactic distribution of the observed X-ray binaries: pole-on view (left-hand panel) and edge-on view (right-hand panel). Background image credit: NASA/JPL-Caltech/R.Hurt (SSC/Caltech), inverted.

Both instruments used for polarimetric observations are remotely operated (Kosenkov 2021a) 'double-image' CCD polarimeters capable of obtaining polarization images in three (BVR) filters simultaneously. The optical beam from a star is split into two orthogonally polarized rays (ordinary 'o' and extraordinary 'e'), resulting in two separate and orthogonally polarized images of a star recorded in different parts of the CCD sensor. The orthogonally polarized images of the sky overlap on each stellar image, effectively eliminating the sky polarization at the instrumental level. The accuracy of polarization measurements can reach 10⁻⁵, limited in practice by the photon noise (Piirola 1973; Berdyugin et al. 2018; Piirola et al. 2020).

Each obtained image undergoes standard calibration procedures, including bias and dark subtraction and flat fielding (Berdyugin, Piirola & Poutanen 2019). The difference in brightness between 'o' and 'e' images is measured using differential aperture photometry, and Stokes parameters are computed from their intensity ratios. The individual Stokes parameters are then averaged using ' 2σ ' averaging procedure (Piirola 1975; Kosenkov 2021b, c), obtaining average Stokes parameters and their statistical errors, which are then used to calculate average polarization degree and polarization angle (Simmons & Stewart 1985).

The presence of an interstellar (IS) medium between the observer and the object affects the observed polarization. The IS polarization has to be estimated and subtracted from the observed polarization. One of the most reliable methods for estimating the IS polarization component is to observe a sample of field stars located at distances similar to that of the source. For each source at low galactic latitudes, we observed at least two field stars with close parallaxes, while for the high-latitude objects we used the data from the catalogue of Berdyugin et al. (2014).

3 RESULTS

Results of optical polarization measurements obtained for our sample of BHXRBs are given in Table 2. The results of the determination of their IS polarization are shown in Table 3. The intrinsic polarization estimates are given in Table 4.

3.1 XTE J1118+480

XTE J1118+480 was discovered during its outburst in 2000 by the Rossi X-ray Timing Explorer All-Sky Monitor (RXTE/ASM; Remillard et al. 2000). The high galactic latitude ($b \approx 62^\circ$) and large distance from the Galactic plane (≈ 1.7 kpc) result in a very small absorption in the direction of the source, making it one of the most popular laboratories for studying outbursts and quiescent states in BHXRBs. The mass of the black hole is estimated to be 6–9 M_\odot (Wagner et al. 2001; Gelino et al. 2006; Chatterjee et al. 2019, while the mass of the companion star is 0.3 ± 0.2 M_\odot (Mirabel et al. 2001). The orbital period of this system is $P_{orb} \approx 4$ h (Torres et al. 2004). The second outburst in 2005 was extensively monitored in different wavelengths from the radio and optical to the X-rays (Pooley 2005; Remillard et al. 2005; Rupen, Dhawan & Mioduszewski 2005; Turia et al. 2006)

Because of the high galactic latitude, the stellar number density in the direction of XTE J1118+480 is relatively small. As a result, there are no stars located within the instrument field of view (~1 arcmin in the B-band and \sim 45 arcsec in the V and R-bands). Fortunately, the IS medium density decreases dramatically at high galactic latitudes, making the contribution of the IS polarization component negligible. IS polarization survey of the high galactic latitudes (Berdyugin et al. 2014), puts an upper limit on the IS polarization in the direction of XTE J1118+480 of $P_{1S} < 0.2$ per cent (Table 3 and Fig. 2). To check if the polarization of XTE J1118+480 differs significantly from this value, we first need to correct its observed polarization degree for the bias, which arises due to the small signal-to-noise ratio (P/σ) < 5), shifting the polarization degree towards higher values. The unbiased maximum-likelihood estimator $P_0 = (P^2 - 2\sigma^2)^{1/2}$ from Simmons & Stewart (1985) gives us the following estimations of the true values of the polarization degree: $P_{B,0} = 1.2 \pm 0.8$, $P_{V,0} =$ 1.4 ± 0.8 , and $P_{R,0} = 1.3 \pm 0.5$ per cent. Based on these data we can only confirm the absence of substantial (e.g. ≥4 per cent) optical intrinsic polarization in the quiescence for this transient. The previous polarimetric measurement of $P_{\rm obs} = 0.21 \pm 0.16$ per cent in the V-band during the outburst in 2000 is consistent with the IS polarization level (Schultz, Hakala & Huovelin 2004).

2482 V. Kravtsov et al.

Table 2. Observed polarization of BHXRBs. Errors are 1σ .

			i	В		V	R	!
Instrument	State	Date	P	θ	P	θ	P	θ
		MJD	per cent	deg	per cent	deg	per cent	deg
			XTE J	1118+480				
DIPol-UF	Quiescence	59326.03	1.65 ± 0.80	22.7 ± 13.0	1.76 ± 0.77	79.4 ± 11.8	1.49 ± 0.53	51.2 ± 9.5
			Swift J	357.2-0933				
DIPol-UF	Failed outburst	59326.10	0.34 ± 0.07	34.5 ± 6.1	0.18 ± 0.08	4.2 ± 12.4	0.25 ± 0.06	$69.8 \pm 8.$
				957+115				
DIPol-UF	Soft	59401.14	0.65 ± 0.07	59.4 ± 3.1	0.61 ± 0.09	54.8 ± 4.0	0.62 ± 0.08	$60.2 \pm 3.$
			V4	641 Sgr				
		58347.40	0.46 ± 0.05	34.6 ± 2.9	0.52 ± 0.07	34.8 ± 4.0	0.54 ± 0.07	40.6 ± 3
DIPol-2	Quiescence	58348.40	0.41 ± 0.04	44.7 ± 2.8	0.38 ± 0.05	38.7 ± 3.9	0.39 ± 0.04	44.3 ± 2
		58351.39	0.42 ± 0.08	33.0 ± 5.0	0.47 ± 0.08	29.8 ± 5.0	0.50 ± 0.09	$28.4 \pm 5.$
		58686.98	0.53 ± 0.03	43.6 ± 1.6	0.40 ± 0.04	46.0 ± 2.7	0.45 ± 0.02	$50.7 \pm 0.$
		58961.19	0.46 ± 0.02	36.8 ± 1.4	0.49 ± 0.06	45.7 ± 3.6	0.42 ± 0.06	48.7 ± 4
DIPol-UF	Quiescence	58964.21	0.49 ± 0.01	40.2 ± 0.8	0.43 ± 0.03	44.7 ± 1.8	0.44 ± 0.02	50.7 ± 1
		58966.22	0.50 ± 0.03	40.1 ± 1.4	0.44 ± 0.04	46.0 ± 2.3	0.48 ± 0.04	50.0 ± 2
		58967.20	0.51 ± 0.05	44.4 ± 2.9	0.50 ± 0.10	43.2 ± 5.7	0.45 ± 0.10	51.2 ± 6
		59519.71	0.56 ± 0.08	38.5 ± 4.0	0.36 ± 0.15	31.9 ± 10.9	0.29 ± 0.12	46.9 ± 11
DIPol-2	Failed outburst	59521.71	0.54 ± 0.08	41.8 ± 4.2	0.37 ± 0.20	45.7 ± 13.9	0.58 ± 0.09	49.5 ± 4
		59522.71	0.47 ± 0.08	42.1 ± 4.8	0.48 ± 0.48	38.6 ± 4.4	0.50 ± 0.10	44.4 ± 5
			V4	04 Cyg				
DIPol-2	Rising harda	57195-57200	8.55 ± 0.20	6.7 ± 0.7	7.47 ± 0.06	8.6 ± 0.2	7.51 ± 0.03	$6.8 \pm 0.$
DIPol-2	Quiescence ^a	57206-57210	7.84 ± 0.16	7.9 ± 0.6	6.58 ± 0.05	11.1 ± 0.2	7.13 ± 0.03	$7.7 \pm 0.$
DIPol-2	Quiescence ^a	57651-57652	-	-	7.32 ± 0.38	9.7 ± 1.5	7.37 ± 0.21	7.2 ± 0.3
DIPol-UF	Quiescence	58688.02	-	-	8.07 ± 0.41	3.1 ± 1.5	7.30 ± 0.14	5.3 ± 0.3
		59402.16	7.15 ± 0.47	3.6 ± 1.9	7.78 ± 0.21	5.5 ± 0.8	7.85 ± 0.07	6.9 ± 0.2
			MAXI	J1820+070				
DIPol-2	Rising hard ^b	58195-58222	0.76 ± 0.01	53.9 ± 0.3	0.79 ± 0.01	54.7 ± 0.4	0.76 ± 0.01	53.3 ± 0
		58222-58234	0.76 ± 0.02	51.4 ± 0.6	0.87 ± 0.02	50.5 ± 0.8	0.86 ± 0.02	45.8 ± 0
DIPol-2	Soft ^c	58312-58344	0.66 ± 0.01	61.5 ± 0.4	0.67 ± 0.01	62.2 ± 0.5	0.62 ± 0.01	63.5 ± 0
DIPol-2	Decaying hard ^c	58406-58428	0.76 ± 0.04	62.2 ± 1.4	0.63 ± 0.06	64.1 ± 2.6	0.67 ± 0.04	62.0 ± 1
DIPol-2	Failed outburst	58721-58726	0.67 ± 0.13	65.9 ± 5.6	0.78 ± 0.15	65.0 ± 5.5	0.62 ± 0.10	64.3 ± 4
		58911-58932	0.60 ± 0.11	64.5 ± 5.3	0.79 ± 0.20	65.4 ± 7.5	0.71 ± 0.12	68.4 ± 5
DIPol-UF	Quiescence ^d	58961-59401	2.88 ± 0.26	-16.8 ± 3.1	1.67 ± 0.25	-13.6 ± 5.5	0.63 ± 0.17	1.5 ± 7.
			MAXI	J0637-430				
DIPol-2	Soft	58792-58796	0.28 ± 0.26	38.8 ± 26.5	-	-	-	-

Notes. Source of the data: aKosenkov et al. (2017), bVeledina et al. (2019), Kosenkov et al. (2020), Poutanen et al. (2022).

3.2 Swift J1357.2-0933

The black hole transient Swift J1357.2–0933 was discovered in 2011 using Neil Gehrels Swift Observatory Burst Alert Telescope (Swift/BAT; Krimm et al. 2011). Similar to XTE J1118+480, the binary separation of Swift J1357.2–0933 is very small (the orbital period $P_{\rm orb}\approx 2.8$ h) and the black hole in the system has a mass $M_{\rm BH}>9$ M $_{\odot}$ (Mata Sánchez et al. 2015; Casares 2016). The analysis of optical spectra revealed remarkable broad double-peaked H α emission line, which is a strong indication of a high ($i>70^{\circ}$) binary inclination (Corral-Santana et al. 2013).

During our observations of the source, the beginning of its optical and X-ray re-brightening event was reported (Baglio et al. 2021; Bellm 2021; Beri et al. 2021; Caruso et al. 2021). There are no nearby stars in the field of view of Swift J1357.2–0933, but its location at the high galactic latitude (\approx 50°) allows us to put the upper limit of 0.2 per cent on the expected level of IS polarization from the survey of Berdyugin et al. (2014), see Table 3 and

Fig. 2. The small value of the observed polarization of the source is consistent with the IS polarization level and hence the optical polarization of Swift J1357.2–0933 observed during its transition from the quiescence to the faint outburst (with X-ray luminosity of about $L_{\rm X} \sim 10^{34}$ erg s⁻¹; Beri et al. 2021), most likely has an IS origin.

Śhahbaz et al. (2003) argued that the quiescent optical to midinfrared emission is dominated by the synchrotron jet emission. This emission is expected to be strongly (up to 70 per cent) polarized, which allows us to estimate its contribution to the total optical spectrum. Our non-detection of intrinsic polarization at the level of $P_{\rm int} < 0.2$ per cent suggests this contribution to be less than a few per cent of the total optical emission during the initial rise to the outburst. Additional polarization measurements during the true quiescent state are needed to estimate the role of the synchrotron emission to the quiescent optical spectrum of Swift J1357.2—0933.

Table 3. Polarization of field stars

				В		V		R	
Field star	Identifier	Parallax	Angular	P	θ	P	θ	P	θ
	HD/BD/Gaia DR3	mas	separation	per cent	deg	per cent	deg	per cent	deg
			XT	E J1118+480					
Ref A ^a	$BD + 48\ 1955$	4.18 ± 0.02	~100 arcmin	-	-	0.06 ± 0.03	89 ± 12	-	-
			Swif	t J1357.2-0933					
Ref A ^a	HD 122835	4.15 ± 0.30	\sim 100 arcmin	-	_	0.12 ± 0.05	101 ± 13	-	_
			41	U 1957+115					
Ref A	4303869526257087360	0.36 ± 0.13	<1 arcmin	0.59 ± 0.15	53 ± 7	0.72 ± 0.12	53 ± 5	0.48 ± 0.08	62 ± :
Ref B	4303869599285320832	0.17 ± 0.08	<1 arcmin	0.65 ± 0.07	55 ± 3	-	-	0.52 ± 0.05	$54 \pm$
				V4641 Sgr					
Ref A	4053096384526868736	0.24 ± 0.03	<10 arcmin	0.56 ± 0.08	55 ± 4	0.40 ± 0.03	50 ± 2	0.39 ± 0.02	$56 \pm$
Ref B	4053096491998429952	0.40 ± 0.03	<10 arcmin	0.54 ± 0.05	52 ± 3	0.62 ± 0.08	51 ± 4	0.59 ± 0.06	62 ±
Ref C	4053096315807371008	0.51 ± 0.03	<10 arcmin	0.26 ± 0.05	59 ± 5	0.29 ± 0.04	62 ± 4	0.33 ± 0.02	63 ±
Ref D	4053096320199414528	0.65 ± 0.03	<10 arcmin	0.57 ± 0.08	67 ± 4	0.45 ± 0.09	65 ± 6	0.45 ± 0.06	74 ±
Ref E	4053096595077613568	0.42 ± 0.03	<10 arcmin	0.70 ± 0.11	56 ± 4	0.47 ± 0.07	56 ± 4	0.40 ± 0.02	$51 \pm$
Ref F	4053096487606085632	0.53 ± 0.03	<10 arcmin	0.29 ± 0.08	67 ± 8	0.38 ± 0.08	77 ± 6	0.35 ± 0.06	69 ±
				V404 Cyg					
Ref 4040 ^b	2056188620566335360	0.14 ± 0.11	1.4 arcsec	-	_	6.64 ± 0.22	12 ± 1	7.28 ± 0.09	9 ± 1
Ref 4042 ^b	2056188865390747136	0.35 ± 0.04	<10 arcmin	-	-	7.09 ± 0.42	11 ± 2	8.47 ± 0.17	9 ± 1
Ref 4043 ^b	2056190136700843264	0.34 ± 0.03	<10 arcmin	6.92 ± 0.29	3 ± 1	5.20 ± 0.15	11 ± 1	6.47 ± 0.07	$11 \pm$
			XT	E J2012+381					
Ref A	2061667766205170048	0.23 ± 0.05	<1 arcmin	3.36 ± 0.60	88 ± 5	3.90 ± 0.19	84 ± 1	3.69 ± 0.07	$83 \pm$
Ref B	2061673435561995008	0.19 ± 0.05	<1 arcmin	2.58 ± 0.42	83 ± 5	3.78 ± 0.16	90 ± 1	3.71 ± 0.07	$88 \pm$
			MA	XI J1820+070					
Ref 1-5	2,3,6,7,9 ^c	0.15 - 0.44	<10 arcmin	0.80 ± 0.03	64 ± 1	0.70 ± 0.03	69 ± 1	0.60 ± 0.02	$64 \pm$
				XI J0637.430					
Ref A	5569292377717900288	0.67 ± 0.01	<10 arcmin	0.57 ± 0.08	39 ± 4	-	-	-	-
Ref B	5569291931041304960	0.78 ± 0.02	<10 arcmin	0.42 ± 0.08	38 ± 6	-	-	-	-
Ref C	5569291999760781312	1.09 ± 0.26	<10 arcmin	0.14 ± 0.07	67 ± 14	-	-	-	_

Notes. ^aNearest stars from the catalogue of Berdyugin, Piirola & Teerikorpi (2014).

Table 4. Intrinsic polarization measurements of the observed sample. Both detected values and the upper limits are given. Intrinsic polarization estimate for XTE J2012+381 is not reliable, because of the confusion with the foreground star, and is not given in the table.

Source	State	P_B per cent	P_V per cent	P_R per cent
XTE J1118+480	Q	1.2 ± 0.8	1.4 ± 0.8	1.3 ± 0.5
Swift J1357.2-0933	RH^a	≤0.5	≤0.4	≤0.4
4U 1957+115	S	≤0.2	≤0.3	≤0.3
V4641 Sgr	RH^a	≤0.1	≤0.1	≤ 0.1
	Q	≤0.1	≤0.1	≤ 0.1
V404 Cyg	RH	0.8 ± 0.3	1.1 ± 0.1	0.5 ± 0.1
	Q	≤0.5	≤0.5	≤0.5
MAXI J1820+070	RH1	0.28 ± 0.01	0.36 ± 0.01	0.30 ± 0.01
	RH2	0.34 ± 0.02	0.51 ± 0.02	0.53 ± 0.02
	S	0.16 ± 0.01	0.15 ± 0.01	0.02 ± 0.01
	DH	0.06 ± 0.04	0.13 ± 0.06	0.09 ± 0.04
	RH^a	≤0.3	≤0.4	≤0.3
	Q	3.2 ± 0.2	1.9 ± 0.2	0.9 ± 0.1
MAXI 10637-430	S	< 0.2	_	_

Notes. ^aFailed outburst. States: Q – quiescence, RH – rising hard, S – soft, DH – decaying hard (see Table 2).

3.3 4U 1957+115

4U 1957+115 was detected by *Uhuru* satellite in 1973 (Giacconi et al. 1974) and since then remains in the soft state. Its emission is dominated by the accretion disc (Wijnands, Miller & van der Klis

2002) and modulated with the orbital period $P_{\rm orb} \approx 9.3$ h in optical light (Thorstensen 1987; Hakala et al. 1999; Bayless et al. 2011; Hakala et al. 2014), while the X-rays show no orbital modulation (Nowak & Wilms 1999). Optical light-curve modelling (Bayless et al. 2011) constrained inclination to be in range of $20^{\circ} < i < 70^{\circ}$.

To estimate the IS polarization in the direction of 4U 1957+115, we measured the polarization of two nearby field stars (Table 3 and Fig. 2). The observed degree $P_{\rm obs}=0.60\pm0.08$ per cent and the position angle $\theta_{\rm obs}=58^{\circ}\pm5^{\circ}$ of linear polarization of 4U 1957+115 coincides with the IS values within the measurement errors.

3.4 V4641 Sgr

Intermediate mass X-ray binary and a microquasar V4641 Sgr shows highly atypical behaviour for an X-ray transient. After the decay of the first outburst (in 't Zand et al. 1999), it underwent a series of over ten failed outbursts (full list can be found in Salvesen & Pokawanvit 2020). The compact object was dynamically identified as a black hole with the mass $M_{\rm bh}=6.4\pm0.6~\rm M_{\odot}$, and mass of the companion was found to be $M_{\rm c}\approx 3~\rm M_{\odot}$ (MacDonald et al. 2014). The relatively high mass of the companion makes V4641 Sgr one of the largest known Roche lobe-filling X-ray binaries. Orbital period of the binary is $P_{\rm orb}\approx 2.817~\rm d~(Orosz~et~al.~2001)$ and the inclination of the orbit $i=72^{\circ}\pm4^{\circ}$ (MacDonald et al. 2014).

We observed the source in 2018 August and 2021 November with DIPol-2, when an increased optical activity of V4641 Sgr with 0.3–0.5 mag enhancement was detected (Kong 2018; Zhirkov et al. 2021). DIPol-UF observations were performed during its quiescent

^bReference stars from table 3 of Kosenkov et al. (2017).

^cPolarization is given as the weighted average of the polarization of five field stars from table 2 of Veledina et al. (2019).

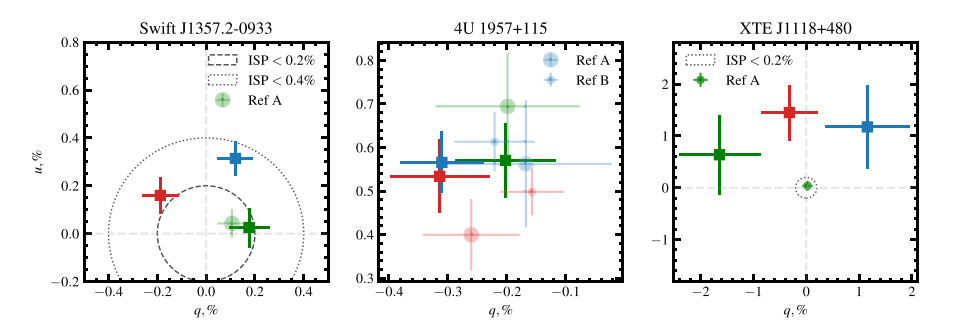


Figure 2. Normalized observed Stokes parameters (q, u) for Swift J1357.2-0933, 4U 1957+115, and XTE J1118+480 (from left to the right). The blue, green, and red squares with 1σ errors correspond to the B, V, and R optical polarimetric measurements of the targets and the circles correspond to nearby stars.

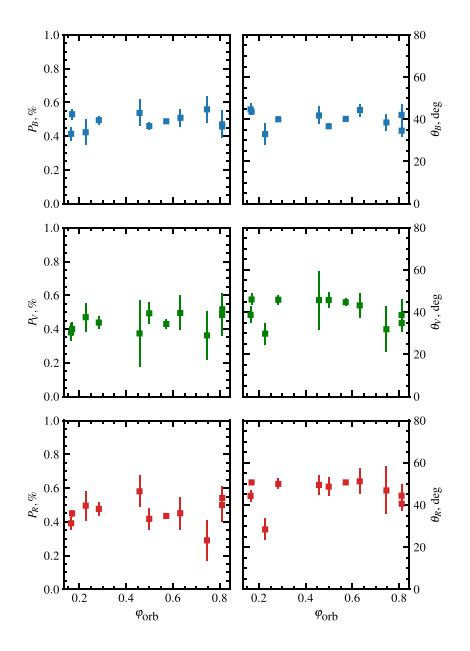
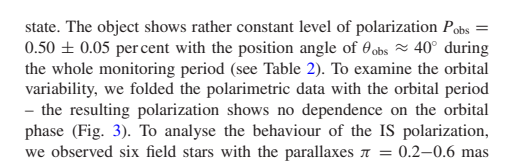


Figure 3. Dependence of the observed polarization degree (left-hand column) and polarization angle (right-hand column) of V4641 Sgr on the orbital phase in the BVR bands (from top to bottom). The errors are 1σ . The orbital period $P_{\rm orb} = 2.8173 \pm 0.00001$ d is taken from Orosz et al. (2001).



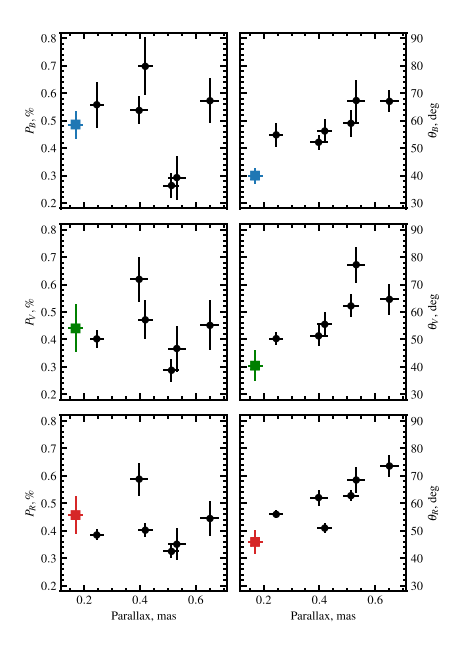


Figure 4. Dependence of the observed polarization degree (left-hand column) and polarization angle (right-hand column) on parallax for V4641 Sgr (coloured squares) and field stars (black circles) in the *BVR* bands (from top to bottom).

(Fig. 4). The degree of observed polarization falls in the range of 0.3–0.7 per cent for all observed stars, while the polarization angle increases with the parallax almost linearly. We conclude that the values of average polarization and polarization angle of V4641 Sgr in all passbands are consistent with the IS polarization. This fact, along with the absence of orbital variability of observed polarization,

suggests that V4641 Sgr has no intrinsic optical polarization in either the quiescence or failed outbursts.

3.5 V404 Cvg

Initially discovered as Nova Cyg 1938, V404 Cyg underwent outbursts in 1956 and 1989 (Richter 1989), and two outbursts in 2015 (Barthelmy et al. 2015; Lipunov et al. 2015). Since its first X-ray detection in 1989 by the Ginga satellite (Makino et al. 1989), V404 Cyg has been extensively monitored in wide energy ranges, including radio, optical, X-ray and gamma-rays (Casares & Charles 1994; Życki, Done & Smith 1999; Corbel, Koerding & Kaaret 2008; Loh et al. 2016). During the 2015 outburst, V404 Cyg reached 40 Crab in the hard X-rays (Rodriguez et al. 2015) and brightened in the optical from $m_V \approx 18$ up to $m_V \approx 11$ mag (Kimura et al. 2016).

V404 Cyg is one of a few low-mass X-ray binaries (LMXB) with orbital parameters and distance known with great accuracy. The K-type companion with the mass of $\sim 1 M_{\odot}$ orbits a $\sim 9 M_{\odot}$ black hole primary with the orbital period of ~ 6.5 d on the orbit, inclined to the observer on $i \approx 67^{\circ}$ (Khargharia et al. 2010). An accurate parallax $\pi = 0.42 \pm 0.02$ mas has been measured in Miller-Jones et al. (2009).

The 2015 outburst triggered several polarimetric campaigns (e.g. Shahbaz et al. 2016; Tanaka et al. 2016; Itoh et al. 2017; Kosenkov et al. 2017). Optical and near-infrared (ONIR) polarimetric measurements revealed high value of IS polarization (~7 per cent, see Table 3 and Tanaka et al. 2016) with atypical wavelength dependence – a potential signature of multiple dust clouds between the source and the observer (Kosenkov et al. 2017). V404 Cyg showed statistically significant intrinsic ONIR polarization during its re-brightening (IS polarization was estimated by observing a sample of field stars, see Table 3 and Kosenkov et al. 2017). Observed shortly after the outburst, however, V404 Cyg demonstrated no intrinsic polarization its observed polarization was identical to the observed polarization of a visually close (~1"4; Udalski & Kaluzny 1991) star, which was reliably resolved as soon as the brightness of the LMXB dropped to the quiescent level.

Several conditions affect the accuracy of polarimetric measurements of V404 Cyg and surrounding field stars. First, the presence of the visually close companion complicates target separation, especially under poor weather conditions (with seeing ≥ 1 ."0). Secondly, relatively high IS extinction ($A_V \approx 3.5$; Shahbaz et al. 2003), caused by the proximity to the galactic plane, increases the total integration time needed for reliable measurements, especially in the B filter. Both new polarimetric measurements of V404 Cyg made with the DIPol-UF suffer from these conditions: the first measurement (made during the technical night allocated for commissioning of DIPol-UF) was too short to reach sufficiently high accuracy in B and V filters, while the second measurement was carried out when the seeing was poor. Despite these obstacles, the quiescent polarization degree and angle in the R filter (where accuracy is adequate) are in agreement with the polarization obtained for the nearest field stars and are consistent with the previous observations (Kosenkov et al. 2017). We therefore see no signs of intrinsic polarization in V404 Cyg during the quiescence.

3.6 MAXI J1820+070

The LMXB MAXI J1820+070 was discovered in March of 2018 with the Monitor of All-sky X-ray Image (MAXI) nova alert system as a bright X-ray source (Kawamuro et al. 2018), which later was associated with the ASASN-18ey optical transient (Denisenko 2018). Over the following \sim 9 months MAXI J1820+070 underwent a violent outburst, reaching $m_V \approx 11.5$ mag (Littlefield 2018) and

 \sim 3 Crabs in X-rays (Bozzo et al. 2018). The initial hard state lasted for \sim 4 months and was followed by a soft state, in which the source resided for the same amount of time. MAXI J1820+070 had never reached the true quiescence after the 2018 outburst has ended; instead, it underwent three (Stiele & Kong 2020) nearly identical in profile and duration 'failed' outbursts, each time increasing its optical brightness from $m_V \approx 18.5$ to $m_V \approx 13.5$ mag.

Since the onset of the 2018 outburst, MAXI J1820+070 was extensively monitored both photometrically and polarimetrically. Similar to V404 Cyg, MAXI J1820+070 demonstrated small but statistically significant variable intrinsic optical polarization during rising hard and soft states (Veledina et al. 2019; Kosenkov et al. 2020). The position angle of intrinsic polarization in the rising hard state (~24°; Kosenkov et al. 2020) was found to be in good agreement with the position angles of radio (Bright et al. 2018) and X-ray (Espinasse et al. 2020) jets, providing evidence for a connection between the scattering medium and the jet axis.

MAXI J1820+070 showed no significant intrinsic polarization near the peaks of two failed outbursts (Table 2). Its observed polarization remained in good agreement with the IS polarization measured from a sample of field stars. Surprisingly, a dramatically different polarization picture was observed in the (near-)quiescent state: MAXI J1820+070 showed substantially higher (up to 5 per cent in B) intrinsic polarization with polarization angles offset from the jet axis (Poutanen et al. 2022). The misalignment and large polarization remained surprisingly stable between failed outbursts, suggesting a strong connection to geometrical properties of the source, which can be probed only during inactive phases, otherwise remaining completely obscured by the accretion–ejection processes happening during outbursts.

3.7 MAXI J0637-430

MAXI J0637–430 was discovered on 2019 November 2 by MAXI X-ray monitor (Negoro et al. 2019). A few hours after the discovery, the optical counterpart with the brightness of $m_a \approx 15$ mag was found in the direction on the X-ray transient with Swift/UVOT (Kennea et al. 2019). Follow-up optical spectroscopic (Strader et al. 2019) and X-ray (Tomsick et al. 2019) observations suggested that the source is an LMXB hosting a black hole. The mass of the compact object has not been reliably measured yet (using, e.g. quiescent state spectroscopy), but it was estimated $M_{\rm BH}=5-12~{\rm M}_{\odot}$ from the X-ray flux and the distance constraint of $d<10~{\rm kpc}$ (Jana et al. 2021).

The absence of a reliable estimate of the distance to the object complicates the estimation of IS polarization. To constrain it, we observed three field stars near MAXI J0637–430 with distances in the range of 0.9–1.5 kpc (Table 3). The polarization is higher for more distant sources reaching in the *B*-band about 0.6 per cent. The observed polarization of MAXI J0637–430 (Table 2) is consistent with zero with the 3σ upper limit of 1.1 per cent (obtained with Monte Carlo simulations) and is consistent with the IS values.

3.8 XTE J2012+381

An X-ray transient XTE J2012+381 was discovered in 1998 by RXTE (Remillard et al. 1998) reaching 150 mCrab in the 3–20 keV X-ray band. The Karl G. Jansky Very Large Array (VLA; Thompson et al. 1980) observations obtained in the same year revealed a radio source in the direction of the transient (Hjellming, Rupen & Mioduszewski 1998). Optical observations were able to identify a faint ($m_R \approx 20$ mag) optical counterpart at the coordinates, consistent with the radio and X-ray counterparts (Hynes et al. 1999).

2486 V. Kravtsov et al.

The faint optical counterpart of XTE J2012+381 is heavily blended with the visually close (~171; Hynes et al. 1999) and much brighter foreground star. We measured the polarization of the binary ($P_B = 0.06 \pm 0.14$, $P_V = 0.12 \pm 0.09$, $P_R = 0.17 \pm 0.07$ per cent), but our observational capacities did not allow us to separate the contribution of XTE J2012+381 from the contribution of the foreground star to the resulting value of linear polarization. Nevertheless, we obtained the polarization of two nearby field stars and estimated the value of IS polarization in the direction to the binary (Table 3), which can be used in the future polarization studies.

4 SUMMARY AND DISCUSSION

We performed optical polarimetric observations of a set of Galactic BHXRBs in various spectral states. Our survey consists of both longand short-period systems located at low and high Galactic latitudes and residing in quiescent, hard, and soft states. We used observations of the nearby field stars to estimate the IS polarization in the direction of the selected BHXRBs. This allowed us to constrain the intrinsic polarization in these sources. For virtually all systems in our sample, we were able to only put upper limits on the intrinsic polarization – see summary in Table 4.

Optical and infrared emission of BHXRBs consists of the contributions of several components – the companion star, accretion disc, inner accretion flow, hot spot/line, and jet. Their relative role in the total spectrum changes with state. All of them can be polarized, but the polarization degree and its spectral dependence are expected to be different and can be used to discriminate between them.

In the soft state, the optical emission is likely dominated by the disc emission, and the polarization may arise from the scattering processes in its atmosphere. In the case of pure electron scattering (Chandrasekhar 1960; Sobolev 1963), the polarization is expected to increase with the inclination of the disc, reaching a maximum of P=11.7 per cent for the edge-on disc. The observed soft-state sources, 4U 1957+115, MAXI J0637-430, and MAXI J1820+070, on the other hand, show polarization below ~ 1 per cent, albeit the latter having high inclination. This may indicate either the complex structure of the accretion disc, such as warp, or the interplay of the scattering and absorption effects in the atmosphere, both of these effects tend to decrease the total polarization.

Likewise, hard-state sources during both regular and failed outbursts show low levels of intrinsic polarization (<1 per cent). Only MAXI J1820+070 - and only during the rising hard state - has a reliable estimate of intrinsic polarization (P ~ 0.5 per cent). Its polarization angle coincides with the position angle of discrete ejections detected in the source and the epochs of polarization detection coincide with the detection of winds in the source (Kosenkov et al. 2020). This, combined with the red polarization spectrum, may indicate that the polarization is produced by scattering in the wind of the seed photons with the red spectrum. Such synchrotron emission is produced either in the hot accretion flow or jet. The absence of significant intrinsic polarization in all hard-state sources in our sample advocates against significant contribution of the jet synchrotron emission itself, as it is expected to be polarized at the level of tens of per cent (Rybicki & Lightman 1979; Veledina et al. 2019).

The detection of a significant, $P_B \sim 5$ per cent, quiescent-state polarization with blue spectrum in MAXI J1820+070 put tight constraints on its origin (Poutanen et al. 2022). Such polarization can be produced by the single Compton scattering in a hot medium, with seed photons coming from the surrounding disc (ring) of a cool matter. At the same time, scattering in the disc itself is excluded

based on the high value of the polarization, while polarization of jet synchrotron emission is disfavoured based on its spectrum. In contrast to MAXI J1820+070, the other two quiescent-state binaries in our sample show low levels of polarization, $P \lesssim 1$ per cent. This may indicate the absence of the hot medium in these sources and may indicate that they have entered the true quiescent state (while MAXI J1820+070 is still accreting at a very low level). Future high-precision polarimetric observations of sources in quiescent (and near-quiescent) states are required to confirm the proposed scenario. Confirmation of the presence of the hot accretion flow in sources undergoing frequent outbursts may indicate its connection to the outburst triggers.

ACKNOWLEDGEMENTS

DIPol-2 and DIPol-UF polarimeters is a joint effort between University of Turku and Leibniz Institut für Sonnenphysik. Polarimetric observations with DIPol-UF were performed at the Nordic Optical Telescope, owned in collaboration by the University of Turku and Aarhus University, and operated jointly by Aarhus University, the University of Turku, and the University of Oslo, representing Denmark, Finland, and Norway, the University of Iceland and Stockholm University at the Observatorio del Roque de los Muchachos, La Palma, Spain, of the Instituto de Astrofisica de Canarias. We are grateful to the Institute for Astronomy, University of Hawaii for the observing time allocated for us on the T60 telescope. AV acknowledges support from the Academy of Finland grant 309308. VK thanks Vilho, Yrjö and Kalle Väisälä Foundation, AV and JP received funding from the Russian Science Foundation grant 20-12-00364. Nordita is partially supported by Nordforsk.

DATA AVAILABILITY

The data underlying this article will be shared on reasonable request to the corresponding author.

REFERENCES

Baglio M. C., Caruso E., Russell D. M., Saikia P., Bramich D. M., Lewis F., 2021, Astron. Telegram, 14729, 1

Barthelmy S. D., D'Ai A., D'Avanzo P., Krimm H. A., Lien A. Y., Marshall F. E., Maselli A., Siegel M. H., 2015, GCN Circ., 17929, 1

Bayless A. J., Robinson E. L., Mason P. A., Robertson P., 2011, ApJ, 730, 43 Bellm E. C., 2021, Astron. Telegram, 14539, 1

Berdyugin A., Piirola V., Teerikorpi P., 2014, A&A, 561, A24

Berdyugin A., Veledina A., Kosenkov I., Poutanen J., Tsygankov S., Kajava J. J. E., Kagitani M., Sakanoi T., 2018, Astron. Telegram, 11445, 1

Berdyugin A., Piirola V., Poutanen J., 2019, in Mignani R., Shearer A., Słowikowska A., Zane S., eds, Astrophysics and Space Science Library Vol. 460, Astronomical Polarisation from the Infrared to Gamma Rays. Springer Nature, Cambridge, UK, p. 33

Beri A. et al., 2021, Astron. Telegram, 14573, 1

Bozzo E., Savchenko V., Ferrigno C., Ducci L., Kuulkers E., Ubertini P., Laurent P., 2018, Astron. Telegram, 11478, 1

Bright J., Motta S., Fender R., Perrott Y., Titterington D., 2018, Astron. Telegram, 11827, 1

Caruso E., Russell D. M., Baglio M. C., Saikia P., Bramich D. M., Lewis F., 2021, Astron. Telegram, 14623, 1

Casares J., 2016, ApJ, 822, 99

Casares J., Charles P. A., 1994, MNRAS, 271, L5

Casares J., Charles P. A., Naylor T., 1992, Nature, 355, 614

Chandrasekhar S., 1960, Radiative transfer. Dover Publications, Inc., New York, USA

```
Chatterjee D., Debnath D., Jana A., Chakrabarti S. K., 2019, Ap&SS, 364, 14
```

Corbel S., Koerding E., Kaaret P., 2008, MNRAS, 389, 1697

Corral-Santana J. M., Casares J., Muñoz-Darias T., Rodríguez-Gil P., Shahbaz T., Torres M. A. P., Zurita C., Tyndall A. A., 2013, Science, 339, 1048 Denisenko D., 2018, Astron. Telegram, 11400, 1

Dolan J. F., Tapia S., 1989, PASP, 101, 1135

Dubus G., Kem B. D., Chaty S., Foellmi C., 2008, in VII Microquasar Workshop: Microquasars and Beyond. Foca, Izmir, Turkey, p. 115

Espinasse M. et al., 2020, ApJ, 895, L31

Froning C. S. et al., 2011, ApJ, 743, 26

Gaia Collaboration 2021, A&A, 649, A1

Gelino D. M., Balman Ş., Kızıloğlu Ü., Yılmaz A., Kalemci E., Tomsick J. A., 2006, ApJ, 642, 438

Giacconi R., Murray S., Gursky H., Kellogg E., Schreier E., Matilsky T., Koch D., Tananbaum H., 1974, ApJS, 27, 37

Hakala P. J., Muhli P., Dubus G., 1999, MNRAS, 306, 701

Hakala P., Muhli P., Charles P., 2014, MNRAS, 444, 3802

Hjellming R. M., Rupen M. P., Mioduszewski A. J., 1998, IAU Circ., 6924,

Hynes R. I., Roche P., Charles P. A., Coe M. J., 1999, MNRAS, 305, L49

in 't Zand J., Heise J., Bazzano A., Cocchi M., di Ciolo L., Muller J. M., 1999, IAU Circ., 7119, 1

Itoh R. et al., 2017, PASJ, 69, 25

Jana A., Jaisawal G. K., Naik S., Kumari N., Chhotaray B., Altamirano D., Remillard R. A., Gendreau K. C., 2021, MNRAS, 504, 4793

Kawamuro T. et al., 2018, Astron. Telegram, 11399

Kennea J. A. et al., 2019, Astron. Telegram, 13257

Khargharia J., Froning C. S., Robinson E. L., 2010, ApJ, 716, 1105

Kimura M. et al., 2016, Nature, 529, 54

Kong A. K. H., 2018, Astron. Telegram, 11949

Kosenkov I. A., 2021a, DIPol-UF: Remote Control Software for DIPol-UF Polarimeter, Zenodo, https://doi.org/10.5281/zenodo.6338401

Kosenkov I. A., 2021b, Dipol2Red: Linear Polarization Data Reduction Pipeline for DIPol-2 and DIPol-UF Polarimeters, Zenodo, https://doi. org/10.5281/zenodo.5763989

Kosenkov I. A., 2021c, PhD thesis, University of Turku, Finland

Kosenkov I. A., Berdyugin A. V., Piirola V., Tsygankov S. S., Pallé E., Miles-Páez P. A., Poutanen J., 2017, MNRAS, 468, 4362

Kosenkov I. A. et al., 2020, MNRAS, 496, L96

Krimm H. A. et al., 2011, Astron. Telegram, 3138

Lipunov V. et al., 2015, Astron. Telegram, 8453

Littlefield C., 2018, Astron. Telegram, 11421 Loh A. et al., 2016, MNRAS, 462, L111

MacDonald R. K. D. et al., 2014, ApJ, 784, 2

Makino F., Wagner R. M., Starrfield S., Buie M. W., Bond H. E., Johnson J., Harrison T., Gehrz R. D., 1989, IAU Circ., 4786, 1

Mata Sánchez D., Muñoz-Darias T., Casares J., Corral-Santana J. M., Shahbaz T., 2015, MNRAS, 454, 2199

McClintock J. E., Horne K., Remillard R. A., 1995, ApJ, 442, 358

Mikolajewska J., Zdziarski A. A., Ziolkowski J., Torres M. A. P., Casares J., 2022, ApJ, 930, 9

Miller-Jones J. C. A., Jonker P. G., Dhawan V., Brisken W., Rupen M. P., Nelemans G., Gallo E., 2009, ApJ, 706, L230

Mirabel I. F., Dhawan V., Mignani R. P., Rodrigues I., Guglielmetti F., 2001, Nature, 413, 139

Negoro H. et al., 2019, Astron. Telegram, 13256

Nowak M. A., Wilms J., 1999, ApJ, 522, 476

Orosz J. A. et al., 2001, ApJ, 555, 489

Orosz J. A., Steiner J. F., McClintock J. E., Torres M. A. P., Remillard R. A., Bailyn C. D., Miller J. M., 2011, ApJ, 730, 75

Piirola V., 1973, A&A, 27, 383

Piirola V., 1975, Ann. Acad. Sci. Fennicae, 418, 1

Piirola V., Berdyugin A., Berdyugina S., 2014, in Ramsay S. K., McLean I. S., Takami H., eds, Proc. SPIE Conf. Ser. Vol. 9147, Ground-based and Airborne Instrumentation for Astronomy V. SPIE, Bellingham, p. 914781 Piirola V. et al., 2020, A&A, 635, A46

Piirola V., Kosenkov I. A., Berdyugin A. V., Berdyugina S. V., Poutanen J., 2021, AJ, 161, 20

Pooley G. G., 2005, Astron. Telegram, 385

Poutanen J., Veledina A., 2014, Space Sci. Rev., 183, 61

Poutanen J. et al., 2022, Science, 375, 874

Remillard R. et al., 1998, IAU Circ., 6920, 1

Remillard R., Morgan E., Smith D., Smith E., 2000, IAU Circ., 7389, 2

Remillard R. Garcia M. Torres M. A. P. Steeghs D. 2005, Astron Telegram

Remillard R., Garcia M., Torres M. A. P., Steeghs D., 2005, Astron. Telegram, 384

Richter G. A., 1989, Inf. Bull. Var. Stars, 3362, 1

Rodriguez J. et al., 2015, A&A, 581, L9

Rupen M. P., Dhawan V., Mioduszewski A. J., 2005, Astron. Telegram, 387 Russell D. M., Shahbaz T., Lewis F., Gallo E., 2016, MNRAS, 463, 2680

Rybicki G. B., Lightman A. P., 1979, Radiative Processes in Astrophysics. John Wiley & Sons, Ltd, New York, USA

Salvesen G., Pokawanvit S., 2020, MNRAS, 495, 2179

Schultz J., Hakala P., Huovelin J., 2004, Baltic Astron., 13, 581

Shahbaz T., Dhillon V. S., Marsh T. R., Zurita C., Haswell C. A., Charles P. A., Hynes R. I., Casares J., 2003, MNRAS, 346, 1116

Shahbaz T., Russell D. M., Zurita C., Casares J., Corral-Santana J. M., Dhillon V. S., Marsh T. R., 2013, MNRAS, 434, 2696

Shahbaz T., Russell D. M., Covino S., Mooley K., Fender R. P., Rumsey C., 2016, MNRAS, 463, 1822

Simmons J. F. L., Stewart B. G., 1985, A&A, 142, 100

Sobolev V. V., 1963, A Treatise on Radiative Transfer. Van Nostrand, Princeton

Stiele H., Kong A. K. H., 2020, ApJ, 889, 142

Strader J., Aydi E., Sokolovsky K., Shishkovsky L., 2019, Astron. Telegram, 13260

Tanaka Y. T. et al., 2016, ApJ, 823, 35

Thompson A. R., Clark B. G., Wade C. M., Napier P. J., 1980, ApJS, 44, 151

Thorstensen J. R., 1987, ApJ, 312, 739

Tomsick J. A. et al., 2019, Astron. Telegram, 13270

Torres M. A. P., Callanan P. J., Garcia M. R., Zhao P., Laycock S., Kong A. K. H., 2004, ApJ, 612, 1026

Torres M. A. P., Casares J., Jiménez-Ibarra F., Álvarez-Hernández A., Muñoz-Darias T., Armas Padilla M., Jonker P. G., Heida M., 2020, ApJ, 893, L37 Udalski A., Kaluzny J., 1991, PASP, 103, 198

Uttley P., Casella P., 2014, Space Sci. Rev., 183, 453

Veledina A. et al., 2019, A&A, 623, A75

Wagner R. M., Foltz C. B., Shahbaz T., Casares J., Charles P. A., Starrfield S. G., Hewett P., 2001, ApJ, 556, 42

Wijnands R., Miller J. M., van der Klis M., 2002, MNRAS, 331, 60

Zhirkov K. et al., 2021, Astron. Telegram, 15014

Zurita C. et al., 2006, ApJ, 644, 432 Życki P. T., Done C., Smith D. A., 1999, MNRAS, 309, 561

This paper has been typeset from a TEX/LATEX file prepared by the author.

Ahlberg V., Kravtsov V., Poutanen J. Orbital variability of polarized X-ray radiation reflected from a companion star in X-ray binaries

Astronomy & Astrophysics, 2024; 688: A220



Orbital variability of polarized X-ray radiation reflected from a companion star in X-ray binaries

Varpu Ahlberg[®], Vadim Kravtsov[®], and Juri Poutanen[®]

Department of Physics and Astronomy, 20014 University of Turku, Finland e-mail: varpu.a.ahlberg@utu.fi

Received 26 March 2024 / Accepted 2 June 2024

ABSTRACT

The reflection of X-ray radiation produced near a compact object from its stellar companion contributes to the orbital variability of polarization in X-ray binaries. The X-rays are reflected mainly via Thomson scattering resulting in a high polarization. The orbital variability of the polarization strongly depends on the inclination and the orbital parameters allowing us to constrain them. To explore this phenomenon, we present analytical single-scattering models for the polarized reflection. We find that while diluted by the direct emission, the reflection can produce a polarization degree of about 1% in the case of a large reflection albedo. We fitted the orbital variations of the X-ray polarization observed by the Imaging X-ray Polarimetry Explorer from an accreting weakly magnetized neutron star "clocked burster" GS 1826-238 and found that the amplitude of the variations is too large to be primarily caused by the companion star. The polarized reflection is more significant if the compact object is obscured from the observer, and thus it should be more easily observable in certain high-inclination targets.

Key words. accretion, accretion disks – polarization – methods: analytical – stars: neutron – X-rays: binaries

1. Introduction

X-ray binaries (XRBs) comprise a compact object, a black hole or a neutron star, that accretes matter from a stellar companion. A fraction of the X-ray emission produced in the vicinity of a compact object is reflected from the companion star. This fraction is defined mostly by the ratio of the Roche lobe size to the separation, which is a function of the mass ratio (Eggleton 1983; Frank et al. 2002). Soft X-rays are mostly absorbed in the stellar atmosphere, but the harder X-rays are reflected through electron scattering, which incurs a high linear polarization on the reflected light. The orbital motion of the companion leads to a variation of the X-ray polarization degree and angle (Gnedin & Sunyaev 1974). In principle, this polarization may be used to constrain the orbital parameters of the XRBs.

Optical polarization has been used for decades as a tool to study orbital parameters, inclination, and orientation on the sky (Brown et al. 1978) in massive binary stars (Berdyugin et al. 2016, 2018; Abdul Qadir et al. 2023), exoplanets (Berdyugina et al. 2011; Madhusudhan & Burrows 2012), gamma-ray binaries (Kravtsov et al. 2020), as well as X-ray binaries (Kemp et al. 1978; Dolan & Tapia 1989b,a; Kravtsov et al. 2023). In the X-rays, polarimetry in the 2-8 keV band has recently been made possible with the launch in December 2021 of the Imaging X-ray Polarimetry Explorer (IXPE) (Weisskopf et al. 2022). The contribution of the companion star reflection is small, but it may be marginally detectable within the accuracy of IXPE. For example, low-mass X-ray binary GS 1826-238 exhibits weak but detectable orbital polarization variations (Rankin et al. 2024), which have been described using an optically thin electron-scattering model (Brown et al. 1978; Kravtsov et al. 2020). IXPE did not detect any orbital polarization variations in Cyg X-1, so the reflected component may be too faint to be observable (Krawczynski et al. 2022). Moreover, resolving the orbital polarization is difficult if the orbital period is long. The IXPE observations of LMC X-1 hinted at a variability of the polarization with the orbital period, but it was observed only for two and a half periods (Podgorný et al. 2023). Cyg X-3 has high polarization varying with the orbital phase, but produced by processes other than stellar reflection (Veledina et al. 2024).

The fraction of the incident light reflected by the star depends on the energy of the photons and the composition of the stellar atmosphere. For an atmosphere of cosmic abundances with low ionization, the photoionization absorption coefficient α_{ph} is approximately equal to the Thomson scattering coefficient $\alpha_{\rm T}$ at ~10 keV and reduces as $\propto E^{-3}$ with increasing energy (George & Fabian 1991). Below this threshold, most of the incoming radiation is absorbed and reprocessed to lower energies. At energies greater than 10 keV, the electron scattering dominates over absorption and most of the X-rays will be reflected (Basko et al. 1974; Matt 1993). If the reflected photons undergo only one scattering, their polarization degree (PD) is (Chandrasekhar 1960)

$$P = \frac{1 - \mu^2}{1 + \mu^2},\tag{1}$$

where μ is the cosine scattering angle. Single-scattered light can therefore be strongly polarized, but further scatterings reduce the PD. The number of scatterings depends on the single-scattering albedo $\lambda = \alpha_{\rm T}/(\alpha_{\rm T} + \alpha_{\rm ph})$. The reflection is thus well approximated with single scattering in the standard X-ray band 2-10 keV. In the hard X-rays, the larger albedo will lead to a greater reflected flux, yet the polarized flux will not increase as much due to multiple scatterings reducing the PD (e.g., Matt 1993; Poutanen et al. 1996). The scattering albedo in the soft X-rays is small for a normal stellar atmosphere, although it may be

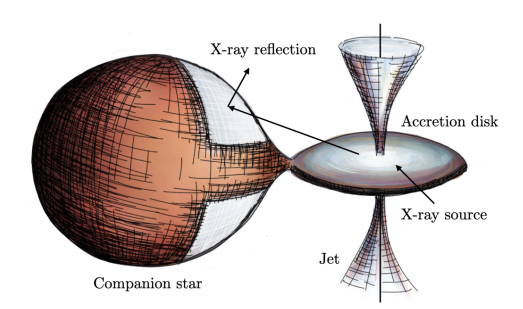


Fig. 1. Illustration of how X-rays emitted near the compact object are reflected from the binary companion in XRBs.

enhanced due to the effects of irradiation. Specifically, some of the energy absorbed by the companion is transformed into evaporative winds near the surface layers of the atmosphere (Blondin 1994). The outflowing gas is hot and highly ionized, and therefore absorption is negligible compared to scattering. The gas would have a significant Thomson optical depth, and its reflection albedo remains nearly constant in the soft X-rays (Basko et al. 1974). Different XRBs likely have different albedos, so the amplitude of the orbital polarization may vary from target to target.

In this paper, we present analytical single-scattering models for the X-ray stellar reflection in XRBs. In Sect. 2 we detail the geometry and polarization basis of our models. We describe the methods to compute polarized reflection under different approximations in Sect. 3. We move on to study how the models behave with different parameters in Sect. 4. We then apply the model to observations of an accreting neutron star GS 1826–238 in Sect. 5, and discuss the results in Sect. 6.

2. Model

2.1. Geometry

We considered an X-ray binary containing a point-like compact object in a circular orbit (see Fig. 1 for illustration). The compact object emission is assumed to be unpolarized and isotropic. We first modeled the reflection geometry as a spherical companion of radius r at a binary separation of d, as depicted in Fig. 2. In the case of the Roche lobe overflow, the shape of the star deviates from a sphere, and the shadow of the accretion disk covers the equator. We did not model the shadowing here, but we make calculations for the Roche lobe in Sect. 2.4.

We chose a coordinate system with the origin coinciding with the companion star and the z-axis aligned with the orbital axis $\hat{\Omega} = (0, 0, 1)$. The unit vector pointing from the center of the companion star toward the compact object lies on the x-axis:

$$\hat{d} = (1, 0, 0). \tag{2}$$

In these coordinates, the direction toward the observer rotates clockwise as a function of the orbital phase angle φ (shifted true anomaly):

$$\hat{\boldsymbol{o}} = (-\sin i \cos \varphi, \sin i \sin \varphi, \cos i), \tag{3}$$

where i is the inclination of the observer to the orbital axis. With this definition, the star is between the observer and the compact

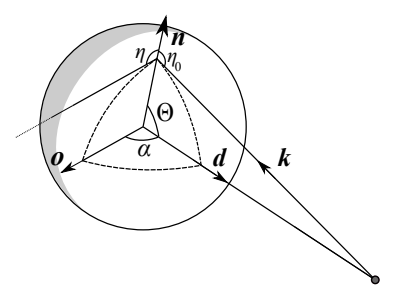


Fig. 2. Geometry of the reflection model. The light emitted by a point-like compact object along vector \hat{k} is intercepted by the binary companion and reflected toward the observer along vector \hat{o} .

object when $\varphi = 0$. The cosine of the phase angle (i.e. the angle between the observer direction and the vector pointing from the center of the companion star toward the compact object) is

$$\cos \alpha = \hat{\mathbf{d}} \cdot \hat{\mathbf{o}} = -\sin i \cos \varphi. \tag{4}$$

The stellar surface normal can be written as

$$\hat{\mathbf{n}} = (\sin\theta\cos\phi, \sin\theta\sin\phi, \cos\theta), \tag{5}$$

where θ and ϕ are the co-latitude and azimuthal angle. The cosine angle between the reflected photons propagating toward the observer and the surface normal is

$$\eta = \hat{\boldsymbol{o}} \cdot \hat{\boldsymbol{n}} = \cos i \cos \theta - \sin i \sin \theta \cos(\phi + \varphi). \tag{6}$$

The direction of the incident light, \hat{k} , can be calculated as a linear combination of vectors \hat{d} and \hat{n} . First, we define the angle between the surface normal and the orbital vector as

$$\cos\Theta = \hat{\mathbf{n}} \cdot \hat{\mathbf{d}} = \sin\theta\cos\phi. \tag{7}$$

Using the law of cosines, the distance between the compact object and the point on the surface is

$$k^2 = d^2 + r^2 - 2rd\cos\Theta.$$
 (8)

Vector \hat{k} can be expressed as

$$\hat{k} = \frac{r}{k}\hat{n} - \frac{d}{k}\hat{d},\tag{9}$$

which yields the cosine angle between the incident light and the surface normal

$$\eta_0 = -\hat{\boldsymbol{n}} \cdot \hat{\boldsymbol{k}} = \frac{d \cos \Theta - r}{k},\tag{10}$$

and the cosine of the scattering angle

$$\mu = \hat{\mathbf{k}} \cdot \hat{\mathbf{o}} = \frac{r\eta - d\cos\alpha}{k}.\tag{11}$$

A220, page 2 of 8

2.2. Visibility conditions

The visibility of the reflected light depends on the overlap between the stellar area visible to the observer and the area illuminated by the compact object. Firstly, the element of the stellar surface has to be visible from the compact object:

$$\eta_0 > 0, \tag{12}$$

which is satisfied when $\cos \Theta > r/d$. This limits the visible area

$$\arcsin\left(\frac{r}{d}\right) < \theta < \pi - \arcsin\left(\frac{r}{d}\right),$$
 (13)

$$-\arccos\left(\frac{r}{d\sin\theta}\right) < \phi < \arccos\left(\frac{r}{d\sin\theta}\right). \tag{14}$$

Secondly, the surface element must be visible to the observer as well:

$$\eta > 0. \tag{15}$$

The illuminated surface is completely invisible for α close to π

$$\cos \alpha < 0 \text{ and } \sin \alpha < r/d.$$
 (16)

The visible range of angles for the observer is

$$i - \pi/2 < \theta < i + \pi/2,\tag{17}$$

$$\arccos(\cot i \cot \theta) < \phi + \varphi < 2\pi - \arccos(\cot i \cot \theta).$$
 (18)

If $\theta < \pi/2 - i$, the surface is visible to the observer for all ϕ . The combination of the two visibility conditions can be complicated, as the visible ranges of ϕ can overlap in two separate intervals.

2.3 Polarized reflection

Linear polarization of the reflected radiation is fully described by the Stokes parameters I, Q, and U. The PD is $P = \sqrt{Q^2 + U^2}/I$ and the normalized Stokes parameters q = Q/I and u = U/I can be written as

$$q = P\cos(2\chi), \qquad u = P\sin(2\chi),$$
 (19)

where $\chi \equiv (1/2) \arctan(U/Q)$ is the polarization angle (PA). The angle depends on the choice of polarization basis, which we defined by the projection of the orbital axis on the plane of

$$\hat{\mathbf{e}}_1 = \frac{\hat{\mathbf{\Omega}} - \cos i \,\hat{\mathbf{o}}}{\sin i} = (\cos i \cos \varphi, -\cos i \sin \varphi, \sin i),\tag{20}$$

$$\hat{\mathbf{e}}_2 = \frac{\hat{\mathbf{o}} \times \hat{\mathbf{\Omega}}}{\sin i} = (\sin \varphi, \cos \varphi, 0). \tag{21}$$

The scattering plane can be expressed using the polarization pseudo-vector:

$$\hat{p} = \frac{\hat{o} \times \hat{k}}{|\hat{o} \times \hat{k}|}.\tag{22}$$

The PA is the angle between the polarization vector and the

$$\cos \chi = \hat{\boldsymbol{e}}_1 \cdot \hat{\boldsymbol{p}} = \frac{d \sin \varphi - r \sin \theta \sin(\phi + \varphi)}{k \sqrt{1 - \mu^2}},$$
 (23)

$$\chi = \hat{e}_2 \cdot \hat{p}$$

$$= \frac{r[\sin i \cos \theta + \cos i \sin \theta \cos(\phi + \varphi)] - d \cos i \cos \varphi}{k \sqrt{1 - u^2}}.$$
(2)

The PD after single scattering is determined by Eq. (1). If the compact object's intrinsic emission has a small PD, it does not considerably change the polarization of the reflection emission. Thus, a constant term corresponding to the intrinsic polarization can be added to the Stokes parameters to model its contribution.

2.4. Scattering from a star filling its Roche lobe

In some XRBs, the companion star loses its mass through Roche lobe overflow. The Roche lobe is described as the equipotential surface that includes the first Lagrange point (L1), which is a point along the x-axis where the gradient of the gravitational potential is zero. The dimensionless gravitational potential under synchronous rotation is (Leahy & Leahy 2015)

$$\psi = \frac{1}{\rho} + q_{\rm m} \left(\frac{1}{\sqrt{1 - 2\rho \sin \theta \cos \phi + \rho^2}} - \rho \sin \theta \cos \phi \right)$$

+
$$\frac{q_{\rm m} + 1}{2} \rho^2 \sin^2 \theta,$$
 (25)

where ρ is the radial distance from the center of the star in units of binary separation and $q_{\rm m} = M_{\rm x}/M_{\rm c}$ is the ratio of the compact object mass M_x and the companion mass M_c . Expressed using Cartesian coordinates, the gradient of the potential is

$$\frac{\mathrm{d}\psi}{\mathrm{d}x} = \frac{x}{\rho^3} - q_{\rm m} \left(\frac{1-x}{(1-2x+\rho^2)^{3/2}} - 1 \right) - (q_{\rm m}+1)x,\tag{26}$$

$$\frac{\mathrm{d}\psi}{\mathrm{d}v} = \frac{y}{\rho^3} + q_{\rm m} \frac{y}{(1 - 2x + \rho^2)^{3/2}} - (q_{\rm m} + 1)y,\tag{27}$$

$$\frac{d\psi}{dy} = \frac{y}{\rho^3} + q_m \frac{y}{(1 - 2x + \rho^2)^{3/2}} - (q_m + 1)y,$$

$$\frac{d\psi}{dz} = \frac{z}{\rho^3} + q_m \frac{z}{(1 - 2x + \rho^2)^{3/2}},$$
(28)

where $\rho = \sqrt{x^2 + y^2 + z^2}$. The position of the L1 point and the value of the potential there can be found from the condition $d\psi/dx = 0$ at y = z = 0 as a function of q_m , although it is a fifthorder polynomial and thus requires some numerical root-finding method. Finding the shape of the Roche lobe $\rho(\theta, \phi)$ where the potential is equal to that at L1 has to be done numerically as well. The surface normal of the Roche lobe, \hat{n}^* , is the unit vector of the gradient along the equipotential surface. Similar to the spherical star, the cosine scattering angles are $\eta = \hat{\mathbf{o}} \cdot \hat{\mathbf{n}}^*$, $\eta_0 = -\hat{\mathbf{k}} \cdot \hat{\mathbf{n}}^*$, and $\mu = \hat{k} \cdot \hat{o}$. The visibility conditions do not have a simple analytical form due to the complexity of this geometry.

3. Reflected flux from a stellar surface

3.1. Exact calculations

The radiative transfer equation for a plane-parallel atmosphere with absorption and Thomson scattering is (Chandrasekhar

$$\eta \frac{d\tilde{I}(\tau, \eta, \Phi)}{d\tau} = \frac{1}{\lambda} \tilde{I}(\tau, \eta, \Phi) - \tilde{S}(\tau, \eta, \Phi), \tag{29}$$

where λ is the single-scattering albedo, η is the cosine of the zenith angle, Φ is the azimuthal angle relative to the scattering plane, and $d\tau = -\alpha_T dz$ the vertical Thomson optical depth. Using the source function for Thomson/Rayleigh scattering and assuming unpolarized incident light, the Stokes vector of the single-scattered radiation is (see Veledina et al. 2024 and p.146 of Chandrasekhar 1960)

$$\tilde{I}_1(\eta, \Phi) = \frac{3}{16\pi} I_0 \lambda (1 + \mu^2) \begin{pmatrix} 1 \\ P\cos 2\chi \\ P\sin 2\chi \end{pmatrix} \frac{\eta_0}{\eta + \eta_0}, \tag{30}$$

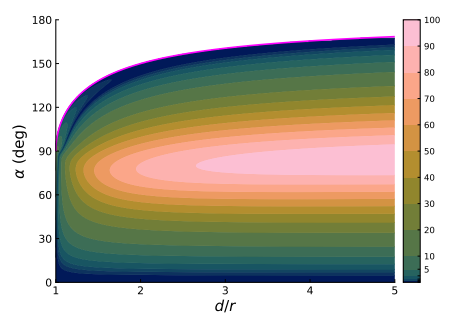


Fig. 3. PD (in percent) of light reflected from the surface of a spherical star as a function of the phase angle α and separation parameter d/r. The magenta line represents the eclipse limit given by Eq. (16), above which the reflected flux is zero (white area). To highlight the behavior near eclipses, each contour below 10% is half the PD of the previous one, down to 0.375%.

where I_0 is the flux of the incident light. In the isotropic case, $I_0 = L/(4\pi k^2)$, where L is the luminosity of the compact object. The total Stokes vector of the reflected light can be obtained by integrating over the surface of the star. In spherical coordinates, the surface element of a sphere at a constant radius is

$$dS = r^2 \sin \theta \, d\theta \, d\phi. \tag{31}$$

In the case of a nonspherical star, the element is

$$dS = r^2 \sqrt{\sin^2 \theta + \left(\frac{\sin \theta}{r} \frac{dr}{d\theta}\right)^2 + \left(\frac{1}{r} \frac{dr}{d\phi}\right)^2} d\theta d\phi.$$
 (32)

For a Roche lobe, we estimated the radius derivatives numerically. The reflected flux from the projection of a surface element

$$d\tilde{F}_{\rm r} = \frac{\eta \, dS}{D^2} \, \tilde{I}_1(\theta, \phi), \tag{33}$$

where D is the distance of the observer. Thus, the reflected flux (Stokes vector) from a spherical star is

$$\tilde{F}_{\rm r} = F_\star \frac{3\lambda}{16\pi} \int\limits_0^\pi r^2 \sin\theta \, {\rm d}\theta \int\limits_0^{2\pi} \frac{1+\mu^2}{k^2} \begin{pmatrix} 1 \\ P\cos2\chi \\ P\sin2\chi \end{pmatrix} \frac{\eta\eta_0}{\eta+\eta_0} {\rm d}\phi, \ (34)$$

where $F_{\star} = L/(4\pi D^2)$ is the direct flux of the compact object. This integral can be performed using standard quadrature methods. We used the visibility conditions to set the integral limits for the spherical star. For the Roche lobe geometry, we integrated over the entire surface but set the flux to zero when the visibility conditions were not met. Due to symmetry around the x-axis, the integrated PD of the spherical star reflection depends only on α and d/r, as is shown in Fig. 3. However, the asymmetric shape of the Roche lobe makes its PD depend on i and φ separately.

The observed Stokes vector is a sum of the reflected component and the direct unpolarized emission:

$$\tilde{F}_{\text{tot}} = F_{\star} \begin{pmatrix} 1 \\ 0 \\ 0 \end{pmatrix} + \tilde{F}_{r}. \tag{35}$$

The direct emission therefore dilutes the observed PD depending on the amount of reflected light. The observed PD is $P_{\rm obs} = F_r P/(F_r + F_\star)$. The PA is computed from the Q and U components of the Stokes vector \tilde{F}_t .

3.2. Large separation approximation

The reflected flux can be solved analytically if a very large binary separation is assumed. For small values of r/d, the direction of incident light is $\hat{k} \approx \hat{d}$. It follows that $\eta_0 \approx \cos \Theta$ and $\mu \approx -\cos \alpha$. The PD becomes

$$P = \frac{1 - \cos^2 \alpha}{1 + \cos^2 \alpha},\tag{36}$$

and the P

$$\sin \chi = -\frac{\cos i \cos \varphi}{\sin \alpha},\tag{37}$$

$$\cos \chi = \frac{\sin \varphi}{\sin \alpha}.\tag{38}$$

Under this approximation, the integral in Eq. (34) becomes analytically solvable (p. 192 in Sobolev 1975):

$$F_{\rm r} = \epsilon F_{\star} \frac{3\lambda}{8} (1 + \cos^2 \alpha) \Phi_{\rm LS}(\alpha), \tag{39}$$

$$\epsilon = \frac{1}{2} \left(1 - \sqrt{1 - \frac{r^2}{d^2}} \right),\tag{40}$$

$$\Phi_{LS}(\alpha) = 1 - \sin\frac{\alpha}{2} \tan\frac{\alpha}{2} \ln\left[\cot\frac{\alpha}{4}\right],\tag{41}$$

where ϵ is the fraction of the compact object flux intercepted by the star and Φ_{LS} is the Lommel-Seeliger phase function as described in Russell (1916). Assuming $F_r \ll F_\star$, the normalized Stokes q and u for the diluted reflection is

$$q = f_0 \left(\sin^2 \varphi - \cos^2 \varphi \cos^2 i \right) \Phi_{LS}(\alpha), \tag{42}$$

$$u = -f_0 \sin 2\varphi \cos i \ \Phi_{LS}(\alpha), \tag{43}$$

where $f_0 = \frac{3}{8}\lambda\epsilon$ is the flux normalization factor.

A different analytical approximation of scattering from a distant spherical object is the Rayleigh-Lambertian reflector. Using the Lambertian phase function, the reflected flux is (Russell 1016)

$$F_{\rm r} = \epsilon F_{\star} p \Phi_{\rm L}(\alpha), \tag{44}$$

$$\Phi_{L}(\alpha) = \frac{\sin \alpha + (\pi - \alpha)\cos \alpha}{\pi},$$
(45)

where p=2/3 is the geometrical albedo of a Lambertian disk. While the Lambertian phase function Φ_L assumes isotropic scattering which does not polarize the light, we used the above Thomson scattering formulae to calculate the polarization under this approximation.

3.3. Optically thin cloud

As a point of comparison, we also considered scattering from an orbiting optically thin cloud. If the cloud is distant, the PD and PA of the reflected radiation are identical to those determined in the large separation approximation. The reflected flux is (Kravtsov et al. 2020)

(35)
$$F_{\rm r} = \epsilon F_{\star} \frac{3}{8} (1 + \cos^2 \alpha),$$
 (46)

where ϵ is the fraction of scattered radiation. The distant cloud does not have a set size or shape, and is rather characterized by the number of scattering electrons. The density structure and shape of the cloud begin to matter if the cloud is closer to the

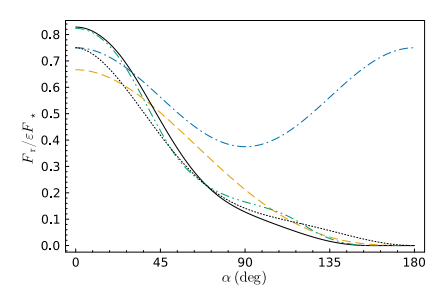


Fig. 4. Comparison between the phase function of the different models: Thomson scattering spherical star including the exact calculation (solid, black) and the large separation approximation (dotted, black), Lambertian reflector (dashed, orange), Thomson scattering cloud (dash-dotted, blue), and Thomson scattering from a Roche lobe (green, dash-double dotted). The binary separation parameter is d/r = 2.673 and the mass ratio $q_{\rm m} = 1.0$.

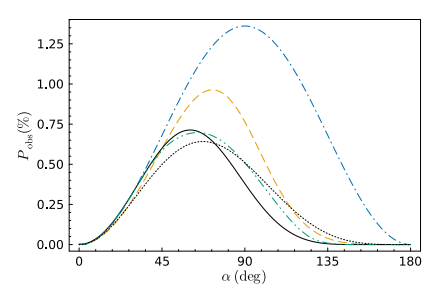


Fig. 5. Comparison of the diluted PD between the same models as Fig. 4

point source. Modeling such a cloud is beyond the scope of this work, especially as we did not use it to represent any physical feature in XRBs. The purpose of the model is to demonstrate the difference between optically thick and optically thin reflecting media.

4. Results

4.1. Comparison between models

We calculated the binary companion reflection using Eq. (34) for both the spherical and Roche lobe cases and compared it to the large separation approximation, Lambertian reflector, and the optically thin cloud. Although the Roche lobe reflection depends on both i and φ rather than just α , we compared it to the other models as a function of α by varying the inclination while keeping the orbital phase angle fixed. This produces slightly different results than with a fixed inclination, but it does not change the qualitative comparison. Additionally, as the size of the Roche lobe depends on the mass ratio $q_{\rm m}$ rather than d/r, we set the size of the spherical star so it corresponded to the radius of the Roche lobe along the y-axis. We find that this produces results more similar to the spherical star than using the equivalent spherical radius of the lobe's surface area. For both the cloud and the Roche lobe, we set ϵ equal to that of the spherical models.

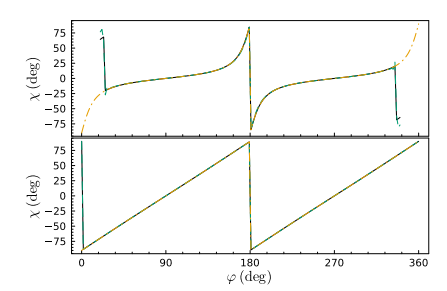


Fig. 6. PA as a function of orbital phase angle at inclinations of 80° (top) and 10° (bottom) for a Thomson scattering spherical star (black, solid) and one filling its Roche lobe (green, dashed), and a distant scatterer (orange, dash-dotted). The orbital separation and mass ratios are the same as in Fig. 4.

Figure 4 shows the ratio $F_r/(F_\star\epsilon)$ for all five cases for the conservative limit $\lambda=1$. The angular dependence of the reflected flux is similar between the Roche lobe and the spherical star. Both the large separation approximation and the optically thin cloud reflect 3/4 of the incoming flux at maximum, which is the classical result for Thomson scattering. The spherical and Roche lobe models reach a higher normalized flux because of the different geometry of the reflecting area. The Rayleigh-Lambert approximation differs significantly from all of the Thomson scattering cases since it uses a different law of reflection. Unlike all the other models, the optically thin cloud is symmetric around $\alpha=90^\circ$ as the observer always sees the full reflection.

The angular dependence of $P_{\rm obs}$ assuming $\lambda=1$ is shown in Fig. 5. The models act similarly under $\alpha \le 40^{\circ}$ but diverge as the angle increases. The spherical and Roche lobe models are the most different at $\alpha \sim 90^{\circ}$, thus the error of assuming a spherical geometry is most significant at low inclinations and at orbital phase angles of 90° and 270° . Overall, the spherical star is a good approximation of the Roche lobe as long as $i \ge 45^{\circ}$. The large separation approximation has a lower maximum PD and is skewed toward higher phase angles as the visibility is less limited. The Rayleigh-Lambert model is clearly different from the Thomson scattering stars outside of certain orbital phases. The PD of the optically thin cloud is much higher than the other models and is symmetric like its flux.

The PA is nearly the same for each model, as can be seen in Fig. 6. Unlike the PD, the PA depends separately on i and φ rather than just α , so we compared it over one orbital period at two different inclinations. It undergoes two full rotations each orbit with a different shape depending on the inclination. The only difference between the models is the presence of eclipses at high inclinations, with 90° jumps near the eclipse as the PD goes to zero. The jumps are a consequence of a narrow visible area limiting the scattering angles, making the Stokes Q and U average to zero at some orbital phase. This can be seen in Fig. 3 as a narrow contour of zero polarization near the $\sin \alpha < r/d$ eclipse limit. Besides the eclipse jumps, Eqs. (37) and (38) are an excellent approximation for the PA.

In conclusion, the limited visibility of the stellar surface in close binaries has a significant effect on the reflection. An optically thin reflector is clearly distinguishable from a star, especially as the polarized flux is much higher than in the other models. A star filling its Roche lobe can be effectively simplified as a sphere, albeit with some inaccuracy that increases if the

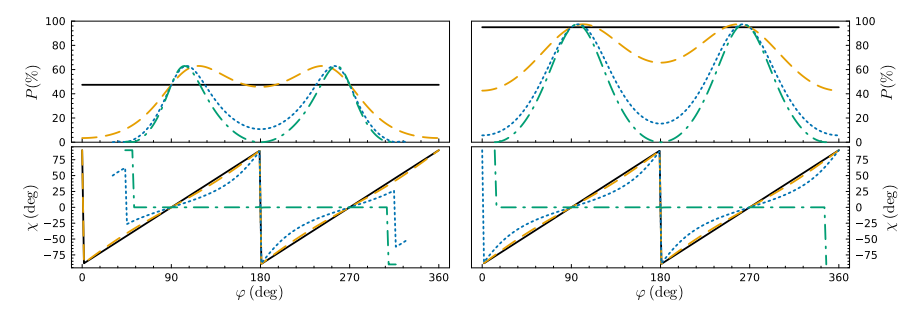


Fig. 7. Orbital polarization curves of the reflected emission for inclinations of $i = 0^{\circ}$ (solid black), 30° (dashed orange), 60° (blue dotted), and 90° (green dash-dotted). The orbital separation parameter is d/r = 1.5 (left) and 5.0 (right).

inclination is low. The large separation approximation is the most accurate of the analytical formulae, although it is noticeably different even at moderate separations. We continue our analysis only for the spherical star because of its mathematical simplicity.

4.2. Parameter study of the spherical reflector

We calculated orbital polarization curves of the reflected emission at different inclinations and orbital separations (Fig. 7). The variability is strongly dependent on the inclinations, at $i=0^\circ$, the PD remains constant, and at higher inclinations, it has an increasingly double-peaked profile. Besides the eclipsing behavior, the curve of the PA is entirely determined by the inclination, transforming from a linear profile to a more sinusoidal one as the inclination increases. At an inclination of exactly 90° , it remains constant over the orbit.

Decreasing the binary separation reduces the PD of the reflected light because the smaller visible area increases the range of scattering angles. At d/r = 5.0, the difference amounts to only a few percent lower polarization than at large separations, but at d/r = 1.5, it is lower by ~50%. The difference in geometry causes the maximum polarization to occur at smaller phase angles, and therefore at orbital phase angles closer to 180°. Additionally, the separation determines the length of the eclipses and the phase angle when the PA jumps. Otherwise, the separation has no noticeable impact on the PA, as evidenced by the accuracy of the large separation approximation.

Dilution of the reflected radiation by the direct emission reduces the PD of the observed light. As we only consider single scattering, the albedo λ acts as a simple coefficient for the amount of reflected flux. While at $\lambda \sim 1$ the light realistically undergoes multiple scatterings, we set it to unity in the following analysis to find an upper limit for the reflection. Figure 8 shows the diluted PD $P_{\rm obs}$ and its maximum at each d/r. Because the reflected flux and PD depend on the binary separation in opposite ways, the observed PD only goes up to a maximum of ~2% in the range $d/r \sim 1.2-1.6$. Compared to a Roche lobe, this separation corresponds to small mass ratios of $q_{\rm m} \sim 0.005$ -0.1. When $q_{\rm m} > 1$, the polarization is less than one percent. Accounting for the scattering albedo, the maximum at close separations is likely on the order of 0.1%-0.7%. The PD increases at extremely small separations due to the geometry of the visible area approaching a plane. However, this is an unphysical scenario.

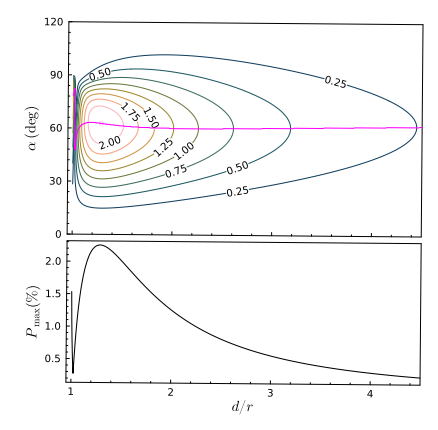


Fig. 8. Contours of constant PD (in percent) of the total radiation at the plane $d/r - \alpha$ (top). The location of the maximum PD for different d/r is shown with a magenta line and its dependence on d/r at the bottom panel.

5. Applications

We fitted our model to existing IXPE data of the orbital polarization in GS 1826–238. It features a weakly magnetized neutron star with near zero constant PD, making it ideal for the study of orbital polarization (Capitanio et al. 2023). A previous study of the IXPE data by Rankin et al. (2024) found that an optically thin reflection model describes the data better than assuming constant polarization. Optical observations of the binary show a binary separation of $d/r \gtrsim 3$, and so the companion star can only cover a fraction of $\epsilon \lesssim 3\%$ of the sky (Mescheryakov et al. 2011) as seen from the X-ray source. This sets an upper limit for the flux contributed by the stellar reflection alone, and the high flux fraction of $\delta \approx 2.7^{+1.9}_{-1.9}\%$ found by the Rankin et al. (2024) fit implies that the reflection in GS 1826–238 is likely very significant. We performed the fit using Eqs. (42) and (43) of the large-separation approximation due to its simplicity and the low accuracy of the data.

The orbital solution for GS 1826–238 is unknown, so we assumed a circular orbit and added a phase shift parameter ω

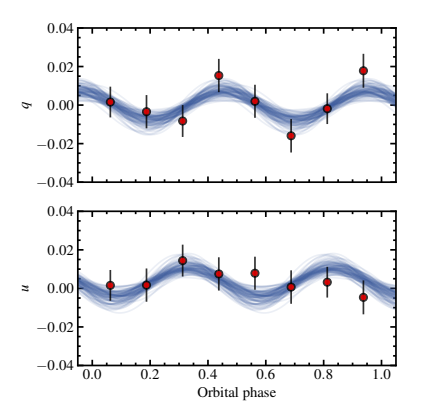


Fig. 9. Orbital variability of normalized Stokes parameters of GS 1826–238 (Rankin et al. 2024) (red circles with 1σ error bars). The solid blue lines show the large-separation reflection model given by Eqs. (42) and (43) for 100 samples from the posterior distribution.

to the orbital phase angle φ . The model has four parameters: the inclination i, the reflected flux normalization f_0 , the position angle of the orbital axis Ω , and the phase shift ω . The observed normalized Stokes parameters are related to the theoretically computed in Sect. 3 as :

$$q_{\text{obs}} = q\cos(2\Omega) - u\sin(2\Omega),$$
 (47)

$$u_{\text{obs}} = q\sin(2\Omega) + u\cos(2\Omega). \tag{48}$$

We employed Markov Chain Monte Carlo (MCMC) ensemble sampler implemented in emcee Python package (Foreman-Mackey et al. 2013) to minimize the χ^2 of the fit and to derive the posterior distributions for the model parameters. The best-fit model is presented in Fig. 9 and its posteriors in Fig. 10. The values of i, ω , and Ω are consistent with the results from the optically thin model fit of Rankin et al. (2024), so the difference between the models may not be apparent within the accuracy of current data. The optically thin fit is not sensitive for inclinations of $i \ge 120^{\circ}$, but our model fit shows a preference for inclinations close to 180°. Previously measured values for the inclination of GS 1826-238 are $i = 62^{\circ}5 \pm 5^{\circ}5$ (Mescheryakov et al. 2011) and $i = 69^{+2}_{-3}$ deg (Johnston et al. 2020) (note the degeneracy between inclinations i and $180^{\circ} - i$ in those studies), so the reflection model does not seem to improve the constraints on the inclination. The parameters ω and Ω are degenerate with one another and thus are difficult to constrain with no prior information. Our fit of the scattering fraction $\lambda\epsilon \sim 5\%$ is higher than the optically thin model by a factor of ~2, which is a consequence of the optically thin reflector predicting a much higher PD. The amplitude of the observed variations cannot easily be explained by the stellar reflection model, especially as the accretion disk shadow further reduces the reflected flux. The stellar reflection model produces sinusoidal variations of q and u only when the orbit is nearly edgeon, while the optically thin model is always sinusoidal. The fit preferring inclinations near 180° could indicate that the reflecting medium is optically thin, although the evidence for this is inconclusive.

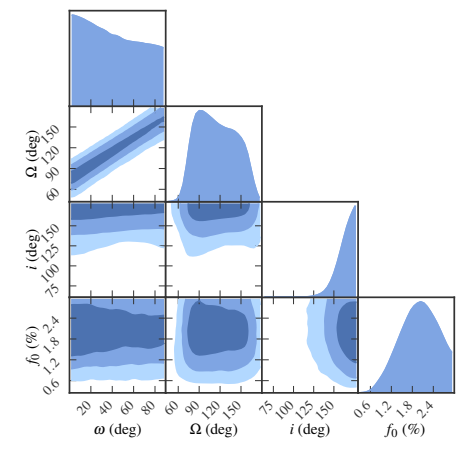


Fig. 10. Posterior distribution of the large-separation model parameters of the fit shown in Fig. 9. The contours are 1, 2, and 3σ .

6. Discussion

Polarized X-ray reflection from the companion star is rather weak when diluted by direct emission from the compact object. Even though the single-scattering albedo is larger in the hard X-rays, the observed PD will remain less than 1%. The reflection should be most prominent in high-mass XRBs, since the observed polarization $P_{\rm obs}$ peaks at separations corresponding to the mass ratio $q_{\rm m} < 1$. The dilution of the reflected light may be avoided if the direct emission from the compact source is blocked while the companion star is visible. Because the opening angle of XRB accretion disks is about 10° (de Jong et al. 1996), an observer inclination over ~80° can provide the necessary conditions for the eclipse of the central source. Alternatively, the direct emission can be blocked even at lower inclinations if the disk is warped.

A famous example of an XRB with a warped disk is the X-ray pulsar Her X-1, which is viewed nearly edge-on (Gerend & Boynton 1976; Petterson 1975). It has a 35-day superorbital period with two 10-d long low states, during which the compact object is obscured by the accretion disk (Scott et al. 2000). Similar disk obscuration is also seen in slightly lower inclination systems such as LMC X-4 and SMC X-1 (Inoue 2019; Ogilvie & Dubus 2001). However, all aforementioned targets are pulsars, whose direct emission is highly polarized (e.g., Doroshenko et al. 2022, 2023; Tsygankov et al. 2022, 2023; Forsblom et al. 2023; Suleimanov et al. 2023; Mushtukov et al. 2023) and variable on a time scale much shorter than the orbital period, making detection of orbital variations related to the reflection from the companion an extremely difficult task. Some XRBs such as SS 433 and Cyg X-3 have thick equatorial obscurers that block the direct emission even at lower inclinations (Fabrika 2004; Veledina et al. 2024), but the emission toward the star is also blocked. Orbital variations of X-ray polarization in Cyg X-3 are then inconsistent with the reflection from the companion but rather consistent with reflection from inhomogeneities in the stellar wind (Veledina et al. 2024).

Additionally, in dipping low-mass XRBs, the accretion flow obscures the compact object from the observer near the eclipse

(Díaz Trigo et al. 2006). However, the PD of the reflection would be low during this orbital phase, and the accretion disk corona can still be visible. IXPE observations of the dipping XRB 4U 1624–49 set an upper limit of 22% for the PD during dips (Saade et al. 2024). On the other hand, observations of a high-inclination weakly magnetized accreting neutron star GX 13+1 revealed extremely complex variations of the polarization on timescales much below the orbital period (Bobrikova et al. 2024), also making detection of polarized reflection from the companion in such targets difficult.

Our models do not account for the shadowing of the stellar surface by the accretion disk. The shadowing reduces the reflected flux and overall reduces the amplitude of the orbital variations. Consequently, our approximation is an upper limit for the variability. The shadowing effect is most significant in XRBs with low-mass companions due to the small size of the star relative to the disk. For a disk opening angle of 10° (de Jong et al. 1996) and separations of d/r = 5, 4, and 3, the shadow covers roughly 80%, 60%, and 40% of the illuminated surface, respectively. Depending on the exact geometry of the shadow it may not cover the area visible to the observer, especially if the disk is warped. The orbital polarization will therefore be complex for XRBs with precessing warped disks.

Although the availability of observational data is limited, the amplitudes of the observed variations can be compared with the theoretical model. Both Cyg X-1 and LMC X-1 have high-mass companions, and thus their binary separation is on the order of $d/r \sim 2$. The nondetection of orbital polarization variations in Cyg X-1 (Krawczynski et al. 2022) means that any variability must be smaller than the statistical noise, which is in line with our predictions. Although LMC X-1 was not observed over many orbital periods, the data are consistent with PD variations of a few percent (Podgorný et al. 2023). Assuming this detection is reliable, our stellar reflection model cannot realistically produce PDs this high. The X-ray light curve of the LMC X-1 is modulated by about 7%, which is consistent with electron scattering in the stellar wind, so the polarization is likely also dominated by wind scattering (Orosz et al. 2009). Our fit of the GS 1826-238 data similarly shows a need for an unexpectedly high reflected flux, so either the direct emission is partially obscured, the emission from the central source is anisotropic, or the polarization is dominated by some other component. This component can be associated with scattering off a nonaxisymmetric -disk, the bulge where the accretion stream hits the disk, or the wind. Understanding the nature of the variability of the polarization in this source requires more data.

7. Conclusions

We developed analytical models for the polarized X-ray reflection from the stellar companion in XRBs and performed fits to the existing data on the low-mass X-ray binary GS 1826–238. The quality of the data is not sufficient to constrain the orbital parameters, but we find that the observed amplitude of the variations of the Stokes parameters is surprisingly large. If diluted by the direct emission, the reflection from the companion's stellar surface cannot typically produce the observed PD of more than 1% (unless the source is anisotropic), making the detection difficult under most circumstances. The amplitude of the variability in both GS 1826–238 and LMC X-1 appears greater than what stellar reflection could produce. The polarized reflection is

expected to be more noticeable in XRBs where the direct emission is obscured, although many such targets are pulsars with highly variable compact object emission. Higher-quality data are required to determine the origin of the orbital polarization.

 $\label{lem:acknowledgements.} A cknowledgements. This research has been supported by the Academy of Finland grants 333112 (JP), 355672 (VA), and by Finnish Cultural Foundation (VK).$

Abdul Qadir, Y., Berdyugin, A. V., Piirola, V., Sakanoi, T., & Kagitani, M. 2023,

References

```
Basko, M. M., Sunyaev, R. A., & Titarchuk, L. G. 1974, A&A, 31, 249
Berdyugin, A., Piirola, V., Sadegi, S., et al. 2016, A&A, 591, A92
Berdyugin, A., Piirola, V., Sakanoi, T., Kagitani, M., & Yoneda, M. 2018, A&A,
Berdyugina, S. V., Berdyugin, A. V., Fluri, D. M., & Piirola, V. 2011, ApJ, 728,
Blondin, J. M. 1994, ApJ, 435, 756
Bobrikova, A., Forsblom, S. V., Di Marco, A., et al. 2024, A&A, 688, A170
Brown, J. C., McLean, I. S., & Emslie, A. G. 1978, A&A, 68, 415
Capitanio, F., Fabiani, S., Gnarini, A., et al. 2023, ApJ, 943, 129
Chandrasekhar, S. 1960, Radiative Transfer (New York: Dover)
de Jong, J. A., van Paradijs, J., & Augusteijn, T. 1996, A&A, 314, 484
Díaz Trigo, M., Parmar, A. N., Boirin, L., Méndez, M., & Kaastra, J. S. 2006,
Dolan, J. F., & Tapia, S. 1989a, PASP, 101, 1135
Dolan, J. F., & Tapia, S. 1989b, ApJ, 344, 830
Doroshenko, V., Poutanen, J., Tsygankov, S. S., et al. 2022, Nat. Astron., 6, 1433
Doroshenko, V., Poutanen, J., Heyl, J., et al. 2023, A&A, 677, A57
Eggleton, P. P. 1983, ApJ, 268, 368
Fabrika, S. 2004, Astrophys. Space. Phys. Rev., 12, 1
Foreman-Mackey, D., Hogg, D. W., Lang, D., & Goodman, J. 2013, PASP, 125,
Forsblom, S. V., Poutanen, J., Tsygankov, S. S., et al. 2023, ApJ, 947, L20
Frank, J., King, A., & Raine, D. J. 2002, Accretion Power in Astrophysics
   (Cambridge: Cambridge University Press)
George, I. M., & Fabian, A. C. 1991, MNRAS, 249, 352
Gerend, D., & Boynton, P. E. 1976, ApJ, 209, 562
Gnedin, I. N., & Sunyaev, R. A. 1974, A&A, 36, 379
Inoue, H. 2019, PASJ, 71, 36
Johnston, Z., Heger, A., & Galloway, D. K. 2020, MNRAS, 494, 4576
Kemp, J. C., Barbour, M. S., Herman, L. C., & Rudy, R. J. 1978, ApJ, 220,
Kravtsov, V., Berdyugin, A. V., Piirola, V., et al. 2020, A&A, 643, A170
 Kravtsov, V., Veledina, A., Berdyugin, A. V., et al. 2023, A&A, 678, A58
Krawczynski, H., Muleri, F., Dovčiak, M., et al. 2022, Science, 378, 650
Leahy, D. A., & Leahy, J. C. 2015, Comput. Astrophys. Cosmol., 2, 4
Madhusudhan, N., & Burrows, A. 2012, ApJ, 747, 25
Matt, G. 1993, MNRAS, 260, 663
Mescheryakov, A. V., Revnivtsev, M. G., & Filippova, E. V. 2011, Astron. Lett.,
Mushtukov, A. A., Tsygankov, S. S., Poutanen, J., et al. 2023, MNRAS, 524,
Ogilvie, G. I., & Dubus, G. 2001, MNRAS, 320, 485
Orosz, J. A., Steeghs, D., McClintock, J. E., et al. 2009, ApJ, 697, 573
Petterson, J. A. 1975, ApJ, 201, L61
Podgorný, J., Marra, L., Muleri, F., et al. 2023, MNRAS, 526, 5964
Poutanen, J., Nagendra, K. N., & Svensson, R. 1996, MNRAS, 283, 892
Rankin, J., Kravtsov, V., Muleri, F., et al. 2024, ApJ, 962, 34
Russell, H. N. 1916, ApJ, 43, 173
Saade, M. L., Kaaret, P., Gnarini, A., et al. 2024, ApJ, 963, 133
Scott, D. M., Leahy, D. A., & Wilson, R. B. 2000, ApJ, 539, 392
Sobolev, V. V. 1975, Light Scattering in Planetary Atmospheres (Oxford:
   Pergamon Press)
Suleimanov, V. F., Forsblom, S. V., Tsygankov, S. S., et al. 2023, A&A, 678,
Tsygankov, S. S., Doroshenko, V., Poutanen, J., et al. 2022, ApJ, 941, L14
Tsygankov, S. S., Doroshenko, V., Mushtukov, A. A., et al. 2023, A&A, 675,
Veledina, A., Muleri, F., Poutanen, J., et al. 2024, Nat. Astron., 8, 1031
Weisskopf, M. C., Soffitta, P., Baldini, L., et al. 2022, JATIS, 8, 026002
```

Rankin J., Kravtsov V., Muleri F., Poutanen J., Marin F., Capitanio F., Matt G., Costa E., Di Marco A., Fabiani S., La Monaca F., Marra L., Soffitta P. X-ray polarimetry as a tool to constrain orbital parameters in X-ray binaries

The Astrophysical Journal, 2024; 962: 34



OPEN ACCESS



X-Ray Polarimetry as a Tool to Constrain Orbital Parameters in X-Ray Binaries

John Rankin¹, Vadim Kravtsov², Fabio Muleri¹, Juri Poutanen², Frédéric Marin³, Fiamma Capitanio¹, Giorgio Matt⁴, Enrico Costa¹, Alessandro Di Marco¹, Sergio Fabiani¹, Fabio La Monaca^{1,5,6}, Lorenzo Marra⁴, and Paolo Soffitta¹

INAF Istituto di Astrofisica e Planetologia Spaziali, Via del Fosso del Cavaliere 100, I-00133 Roma, Italy
 Department of Physics and Astronomy, University of Turku, Fi-20014 Turku, Finland
 Université de Strasbourg, CNRS, Observatoire Astronomique de Strasbourg, UMR 7550, F-67000 Strasbourg, France
 Dipartimento di Matematica e Fisica, Università degli Studi Roma Tre, Via della Vasca Navale 84, I-00146 Roma, Italy
 Dipartimento di Fisica, Università degli Studi di Roma "Tor Vergata," Via della Ricerca Scientifica I, I-00133 Roma, Italy
 Dipartimento di Fisica, Università degli Studi di Roma "La Sapienza," Piazzale Aldo Moro 5, I-00185 Roma, Italy
 Received 2023 November 7; revised 2023 December 22; accepted 2023 December 27; published 2024 February 5

Abstract

X-ray binary systems consist of a companion star and a compact object in close orbit. Thanks to their copious X-ray emission, these objects have been studied in detail using X-ray spectroscopy and timing. The inclination of these systems is a major uncertainty in the determination of the mass of the compact object using optical spectroscopic methods. In this paper, we present a new method to constrain the inclination of X-ray binaries, which is based on the modeling of the polarization of X-rays photons produced by a compact source and scattered off the companion star. We describe our method and explore the potential of this technique in the specific case of the low-mass X-ray binary GS 1826–238 observed by the Imaging X-ray Polarimetry Explorer observatory.

Unified Astronomy Thesaurus concepts: Polarimetry (1278); X-ray binary stars (1811); Low-mass x-ray binary stars (939); High mass x-ray binary stars (733); Binary stars (154); Orbit determination (1175); Inclination (780)

1. Introduction

X-ray binary systems are among the brightest celestial objects in the X-rays. They are powered by mass transfer from a companion star to a compact object, either a white dwarf, neutron star or a black hole, which orbits at a short distance. Their high luminosity allowed the discovery and the detailed study of these systems since the dawn of X-ray astronomy. To achieve this, spectroscopy and timing were critical tools.

One of the most interesting parameters of these systems is the mass of the compact object, which, for example, can constrain the equation of state of ultra-dense matter in neutron stars (Miller et al. 2020) or clarify the origin of intermediate-mass black holes which are observed as sources of gravitational waves (Mehta et al. 2022). However, apart from very special systems like double pulsars, measuring the mass in X-ray binaries is challenging because these systems currently cannot be spatially resolved. In some cases, the radial velocity can be measured both for the companion star through optical observations and for the compact object with, for example, X-ray pulsations. Even in those conditions, one can only derive the ratio of the mass of two objects; determining the individual masses requires solving the mass function, which depends on the orbital inclination of the system.

The inclination of the orbit can be constrained when the source shows eclipses or dips, which can be due to obscuration of the central X-ray source by the companion; however, this requires the system to be nearly edge-on. Another possibility is in systems that accrete via Roche lobe, where the shape of the

Original content from this work may be used under the terms of the Creative Commons Attribution 4.0 licence. Any further distribution of this work must maintain attribution to the author(s) and the title of the work, journal citation and DOI.

companion star can be significantly distorted due to the Rochelobe geometry; in this case, the size of the surface visible to the observer changes with the orbital phase in an inclination-dependent way, creating a modulation in the optical-light emission (Orosz & Bailyn 1997).

In addition to the importance of fixing the parameters of the binary system, the orbital inclination is also of interest per se. For example, it can be compared with the orientation of the accretion disk if the latter is known from other means, e.g., optical polarimetry. This allows one to verify if these two are aligned or not, with important constraints on the geometry of the mass transfer.

In this paper, we investigate the possibility of determining the orbital inclination, and potentially other orbital parameters, by measuring the polarization of the X-ray photons generated in the vicinity of the compact object (e.g., from the accretion disk, corona and/or spreading/boundary layer in the case of a neutron star) and then scattered off the companion-star outer envelopes. It has been speculated for some time that the effect should be detectable as a polarization ~1% (Basko et al. 1974; Rees 1975), but measuring polarization in the X-rays is notoriously challenging. In fact, before the launch of the NASA/ASI Imaging X-ray Polarimetry Explorer (IXPE) mission (Soffitta et al. 2021; Weisskopf et al. 2022), only very few detections of X-ray polarization had been made.

The approach discussed here has been attempted at other wavelengths, e.g., at optical wavelengths (Kravtsov et al. 2020). Optical polarimetric observations, however, have some uncertainties due to the high contamination from interstellar dust polarization. Furthermore, the emission in the vicinity of the compact source is much lower at optical wavelengths than in the X-rays and, in low-mass X-ray binaries (where the mass

of the companion is <1 solar mass), the orbital variability is lost in the variability of the much brighter accretion disk.

In this paper, we look for this polarization signal in the IXPE observation of GS 1826–238, which is a low-mass X-ray binary hosting a weakly magnetized neutron star. This is a ideal candidate for our study: Capitanio et al. (2023) studied the polarization of the source itself, due to the accretion geometry of the disk/corona, finding it to be unpolarized at high significance. As a consequence, any phase-resolved polarization we observe is due to orbital effects—and the short orbital period (~2.2 hr; Meshcheryakov et al. 2010) allows us to average intrinsic source variations over several orbits, even during relatively short observations.

This paper is structured as follows. We first describe the orbital polarization model in Section 2, and then present the expected polarization as a function of the orbital phase in Section 3. In Section 4, we apply this to the GS 1826–238 system. Finally, in Section 5, we present our conclusions.

2. Modeling Polarization Induced by Orbital Scattering

To quantitatively investigate the information that can be obtained by X-ray polarization, we developed a simple model which predicts the polarization as a function of the orbital parameters. We modeled the orbital motion of the compact object and companion star with the Keplerian TWOSTARS code that comes with Carroll & Ostlie (2006), which we ported into PYTHON. This code computes the orbits using the Kepler equation, in which the orbital distance as a function of the orbital plane longitude λ is given by

$$r(\lambda) = \frac{a(1 - e^2)}{1 + e\cos(\lambda - \lambda_p)},\tag{1}$$

where a is the semimajor axis of the orbit and λ_p the longitude of periastron. The orbit is described in a reference system such that the z-axis points to the celestial north, the y-axis west, and the x-axis toward the observer; the orbital angular momentum is inclined to the line-of-sight at an angle i. The reference system is represented from the side in Figure 1 (bottom), and from the observer's point of view in Figure 1 (top).

The polarization due to scattering is computed as in Appendix A of Kravtsov et al. (2020), where elastic Thomson scattering of photons is assumed to occur on the companion star. The shape of the observed normalized Stokes q and u profiles is determined by the geometry of the orbit (inclination, eccentricity e, and the orientation of the orbit on the sky), while the amplitude depends on the fraction of scattered radiation f_{sc} , which in turn depends on the total number of electrons in the cloud N_e and the binary separation r as $f_{sc} = N_e \sigma T/(4\pi r^2)$, where σ_T is the Thomson cross section. Electron temperature does not affect the polarization because it is relatively low in the stellar atmosphere so that the scattering can be considered in the Thomson regime. In this approach the polarization is given by

$$P = \frac{3}{8} f_{\rm sc} \sin^2 \theta,\tag{2}$$

where θ is the scattering angle (shown in Figure 1).

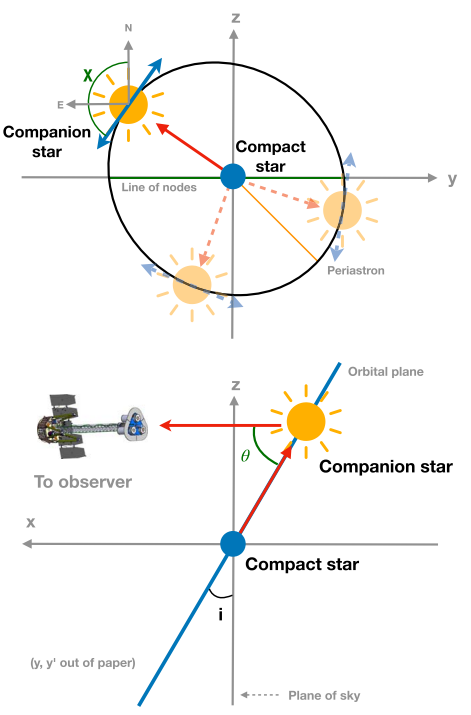


Figure 1. Representation of the geometry of the orbital model (in a reference system centered on the compact object such that the z-axis points to the celestial north, the y-axis west, and the x-axis toward the observer). Top: view seen from the observer's point of view. The central compact object is the blue central circle, while the orange companion star orbits it. The radiation emitted from the compact object is reflected by the companion star, and is this way polarized. In Compton scattering the direction of the scattered photons is orthogonal to the scattering plane; the blue lines identify such a direction for a distant observer, corresponding to the direction of polarization. The polarization angle is given by x. Bottom: reference system used to represent orbits. The polarization degree depends on the scattering angle \(\theta \).

3. Polarization as a Function of Orbital Phase

3.1. Polarization for Different Orbital Inclinations

We show four scenarios in Figure 2 representing a face-on, an inclined, an edge-on, and a clockwise face-on orbit. In all cases the polarization degree is lower than 1%, but the variation of either the polarization degree, angle or both depends on the orbit parameters. In particular:

- 1. Face-on orbit (left column of the figure): the polarization angle varies with the orbital phase, while the polarization degree is constant because the scattering angle θ is constant.
- 2. Intermediate inclinations (in the center of the figure): for these inclinations the minimum of the polarization degree is higher than in edge-on orbits, but the maximum is the same. The direction of the orbital motion, counterclockwise (i.e., i < 90°) or clockwise (i.e., i > 90°) as

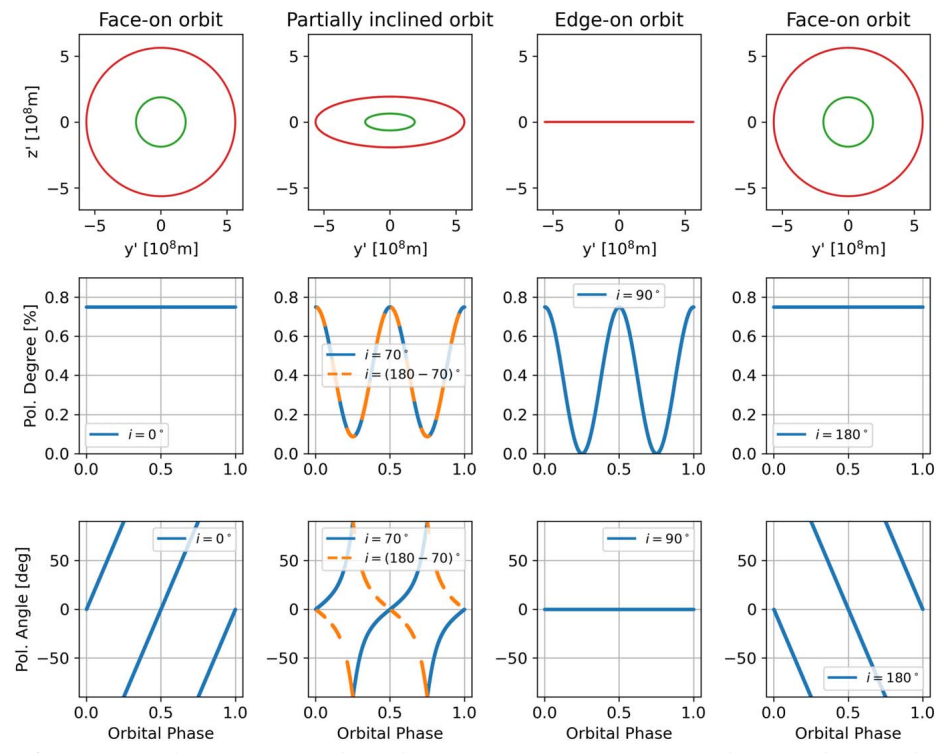


Figure 2. Polarization derived from the orbital model as a function of the orbital phase. The top row shows the projection of the orbital configuration seen from the observer's point of view, while two lower rows show the polarization degree and angle. In these examples, to avoid discontinuities in the polarization angle, the argument of periapsis is set to $\omega = 0^\circ$ and the longitude of the ascending node is set to $\Omega = 0^\circ$?: the scattering fraction is set to $f_{sc} = 0.02$ and the eccentricity is set to e = 0 for graphical simplicity. Left: face-on orbit. In this case θ is constant and so the polarization degree is also constant, while the polarization angle depends on the orbital phase. Center left: inclinations of 70° and $(180 - 70)^\circ$. The first case is counterclockwise and the second is clockwise. Center right: edge-on orbit. In this case the polarization degree depends on the orbital phase, while the polarization angle is constant. Right: face-on orbit but counterclockwise with respect to that on the left column ($e = 180^\circ$).

seen from Earth, causes opposite trends in the polarization angle.

3. Edge-on orbit (right column of the figure): the polarization degree varies between 0 and its maximum depending on the orbital phase, while the polarization angle is constant.

Linear polarization is often represented not as polarization degree and angle, but through the normalized Stokes parameters q and u (Trippe 2014; Kislat et al. 2015), which have the advantage of being statistically independent. Because these are the parameters used in the rest of this paper, Figure 3 represents the same configurations as Figure 2 but with the Stokes parameters. We see that a change in the sense of rotation causes an inversion in u but not in q.

3.2. Variations of Other Orbital Parameters

Because low-mass X-ray binaries are very old, the orbit has stabilized as a circular orbit (Lecar et al. 1976), so that we can set the eccentricity to e=0; the remaining parameters that

influence the trend of polarization with orbital phase are the argument of periapsis ω and the longitude of ascending node Ω . Because e=0, ω produces only a phase shift in the trend of polarization with orbital phase. Figure 4 shows instead the polarization trend with orbital phase for different Ω : The polarization degree is not sensitive to Ω , while the effect on q and u is more evident—varying Ω causes the variations with phase to be more visible in one parameter or in the other.

4. Searching for Orbital Polarization in the GS 1826-238 System

4.1. IXPE Observation of GS 1826-238

The IXPE observatory (Weisskopf et al. 2022) consists of three identical X-ray mirror modules, with at their focus three identical X-ray polarization-sensitive gas pixel detectors (Baldini et al. 2021; Soffitta et al. 2021). These detectors measure the energy, position, time, and linear polarization of the incident X-rays, in the 2–8 keV energy range.

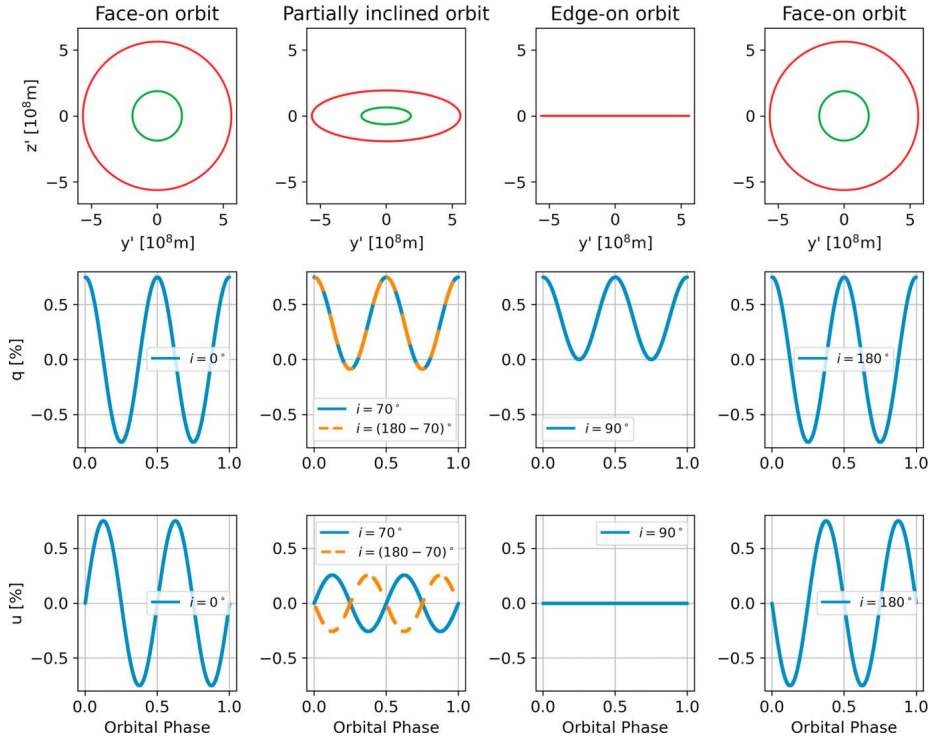


Figure 3. Same as Figure 2 but for the normalized Stokes parameters.

The IXPE observation of GS 1826–238 lasted for $\sim 90 \, \mathrm{ks}$ and was taken on 2022 March 29–31. The orbital-averaged results have already been analyzed by Capitanio et al. (2023); here, we focus on the analysis of the variation of polarization along the orbit.

Data files, reduced by the standard IXPE pipeline running at the Science Operations Center in NASA/MSFC, were downloaded from the IXPE public archive at HEASARC (obs id: 01002801 v.03). Reduced data are corrected for temporal gain variations, which are monitored during the observation with inflight calibration sources (Ferrazzoli et al. 2020), and for the response to unpolarized radiation (Rankin et al. 2022). Event-by-event Stokes parameters are calculated following Kislat et al. (2015) and computed using the weighted scheme described by Di Marco et al. (2022); they are provided to the user in a reference frame projected on the sky.

We analyzed these data files using IXPEOBSSIM v30.6.4 (Baldini et al. 2022), HEASOFT v6.32.1 (Nasa High Energy Astrophysics Science Archive Research Center (HEA-SARC) 2014), and XSPEC v12.13.1 (Arnaud 1996). To exclude the background, we selected a circular region of radius 115"

around the source using the SAOIMAGEDS9 software (Joye & Mandel 2003). We used the barycorr FTOOL in HEASOFT to convert photon arrival times to the solar system barycenter.

We divided the observation in different orbital phase bins, each event being assigned to the appropriate bin by the xpphase tool of IXPEOBSSIM. We set the folding frequency to that corresponding to the orbital period of 2.2494 hr (found by Meshcheryakov et al. 2010). The derivatives of the folding frequency were set to 0. We then obtained the binned spectra for Stokes parameters I, Q, and U using the xpbin tool of IXPEOBSSIM.

We obtained the normalized Stokes parameters q=Q/I and u=U/I using XSPEC. We defined the user-defined polarization model stokesconst, in which the q and u Stokes parameters are fit as constants as a function of energy; compared to polconst, this has the advantage of not having the shift in polarization angle between 90° and -90° . We fit the data in the 2–8 keV band using the spectral model used by Capitanio et al. (2023) multiplied by stokesconst: tbabs*(diskbb+comptt)*stokesconst; the only parameters left free to vary were q and u. Figure 5 shows an example spectral fit. The dependencies of Stokes parameters q and u on orbital phase are shown in Figure 6.

⁷ https://heasarc.gsfc.nasa.gov/docs/ixpe/archive/

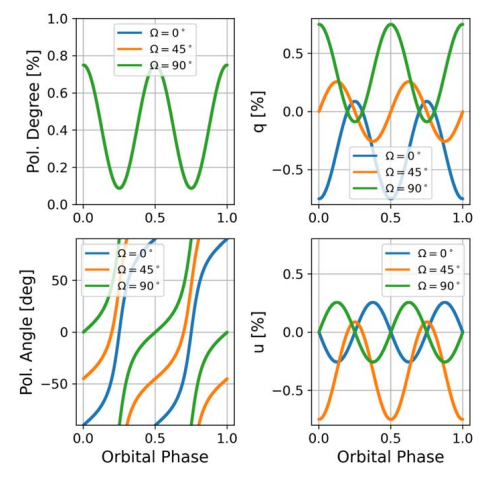


Figure 4. Polarization degree, angle, and Stokes parameters as a function of orbital phase for different longitudes of ascending node Ω . The other parameters are set to $i=70^\circ$ and $\omega=0^\circ$. The change of Ω is in fact a standard rotation of the Stokes parameters by the rotation matrix with the argument equal to 2Ω .

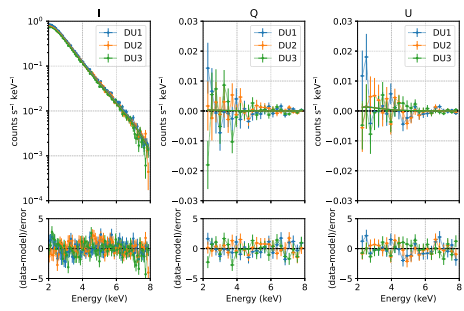


Figure 5. Example XSPEC fits of the l, Q, and U Stokes parameters in the phase bin 5 (the others are similar). Blue, red, and green crosses correspond to the IXPE detector units (DUs) 1, 2, and 3, respectively. As also reported in Capitanio et al. (2023), the observation was carried out with the mirrors slightly offset with respect to the nominal position. This caused some uncertainties in the response functions which are yet to be modeled, and contributes to the small residuals present in the fit, without affecting the measured polarization (Capitanio et al. 2023).

Compared to the analysis by Capitanio et al. (2023), our analysis uses the same data divided into eight phase bins. As a consequence, we expect a $\sqrt{8}$ reduction in sensitivity in each bin; the actual reduction is 10%-15% smaller because the analysis in this paper uses the weighting scheme by Di Marco et al. (2022), while Capitanio et al. (2023) do not. Because the polarization angle rotates in the different time bins, when doing a phase-averaged analysis (as done by Capitanio et al. 2023) the polarization of the different bins cancels out. The analysis carried out by Capitanio et al. (2023) investigated the structure of the corona (close to the neutron star), while our analysis,

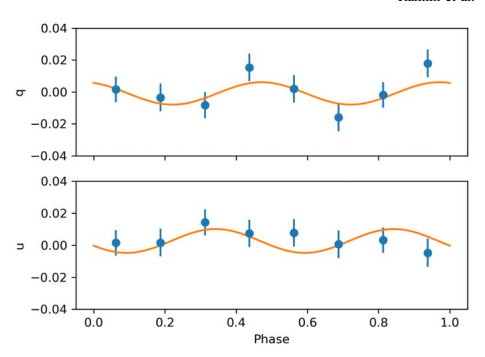


Figure 6. Orbital dependence of the normalized Stokes parameters q and u for 6S 1826–238 and the best-fit model described in Section 2. The error bars are 1σ . The best fit has $\chi^2=8.7$ for 12 degrees of freedom (dof), while a fit with a constant gives $\chi^2=15.9$ for 14 dof. An Akaike information criterion test gives a value of ALC=2261 for the orbital model and ALC=5392 for the constant fit, indicating that the fit with our model is more significant than with a constant

being resolved in phase with the orbital period, is sensitive to orbital phenomena on a much larger scale.

4.2. Fitting Polarization as a Function of the Orbital Phase

We fit the folded data to the orbital model described in Section 2; the q and u dependencies were fitted simultaneously, keeping as free parameters the inclination i, ω , and Ω . We minimized the χ^2 of the fit and derived the posterior probability distributions for the parameters of the model with the nested sampling Monte Carlo algorithm MLFRIENDS (Buchner 2016, 2019) using the ULTRANEST package (Buchner 2021). Figure 7 shows in Figure 6. The numerical values of the fitted parameters and their uncertainties are reported in Table 1. The orbital inclination is $132^{+\frac{47}{24}}$ deg, which is inside the interval from 90° to 180° , indicating that the stars rotate in the clockwise direction on the sky.

The uncertainties obtained above (Table 1) do not correspond to the actual confidence intervals; in particular, the inclination is biased toward higher values (Wolinski & Dolan 1994). To estimate the correct intervals, following the same procedure as Kraytsov et al. (2023), we modeled orbital variations of the Stokes parameters for inclinations in the range from 90° to 180°, with a step of 5°, for the same phases of the observations as in the data. Next, we added Gaussian noise to these points with the same σ as the data and, after that, we fit the model back to the simulated data. The result is a relation between the real inclination i and that estimated from the formal fit (i'), shown in Figure 8. From the simulations we get a critical inclination of about 120°, implying that we are only sensitive to inclinations in the range from 90° to 110°, while any fit of an inclination value greater than the critical inclination will result in an inclination of about 120°. The value of inclination we obtain above from the fit is close to this critical inclination, indicating that we have weak constraints on the inclination: Its value could likely be higher than found from

⁸ https://johannesbuchner.github.io/UltraNest/

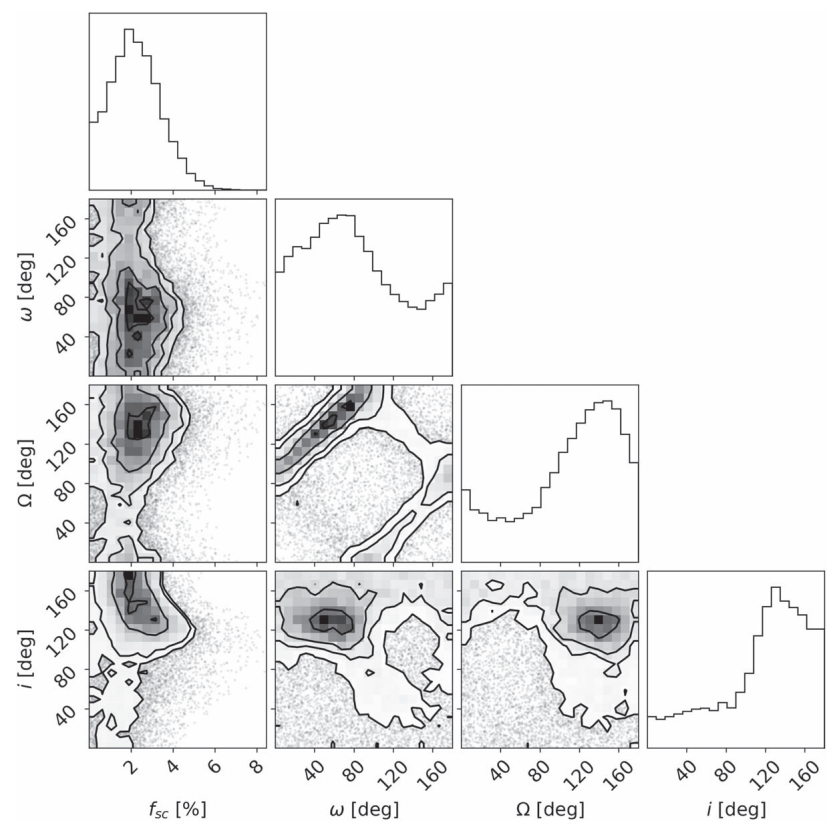


Figure 7. Posterior probability distribution of the reflection model parameters: the scattering fraction f_{sc} , the argument of periapsis ω , the longitude of ascending node Ω , and the inclination i from the fitted model; ω and Ω are partially degenerate because the orbit is not edge-on. The contour levels are 0.5, 1, 1.5, and 2σ .

Table 1
Best-fit Parameters for the Reflection Model

Parameter	Units	Value
f_{sc}	(%)	$2.7^{+1.0}_{-1.2}$
i	(deg)	132^{+47}_{-24}
ω	(deg)	57+42
Ω	(deg)	144^{+34}_{-45}

Note. Uncertainties are at 68% confidence level (1σ) .

the confidence interval of Table 1, covering the entire interval up to 180° .

The large estimated range of the orbital inclination with respect to the observer, if one allows for the indetermination of the direction of motion, is consistent with the previous estimates of Johnston et al. (2020), who found an inclination of 69^{+2}_{-3} deg by modeling multi-epoch X-ray bursts, and of Mescheryakov et al. (2011), who found an inclination of $62.5^{\circ} \pm 5.5^{\circ}$ by looking at modulations in the optical flux.

5. Conclusion

We presented a method to study the orbits of X-ray binaries using X-ray polarization, which is based on the study of the X-ray photons scattered off the companion star. A basic model is built to estimate the polarization as a function of the orbital phase; this trend depends on the orbital inclination and on other orbital parameters.

We searched for this orbital polarization trend in GS 1826 $-238,\,a$ low-mass X-ray binary system which was observed by IXPE with a short pointing in 2022. The statistical uncertainty on the constraints we find when fitting the model is very large, but the results are not incompatible with an inclination exceeding $90^{\circ}.$

Future longer observations of GS 1826–238 could bring better statistics to constrain the orbital parameters. Observations of other X-ray binary systems are also planned, and other detections are possible and expected.

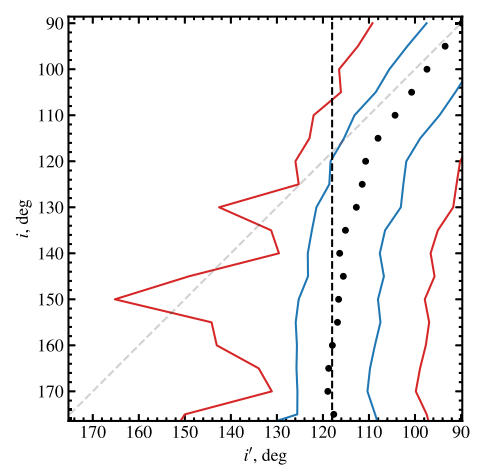


Figure 8. Relation between the real inclination (i) and the inclination obtained from the fit (i'), shown with black circles. The blue and red lines are the 1σ and 2σ confidence intervals. The dashed vertical line shows the critical inclination of about 120°

Acknowledgments

IXPE is a joint US and Italian mission. The US contribution is supported by the National Aeronautics and Space Administration (NASA) and led and managed by its Marshall Space Flight Center (MSFC), with industry partner Ball Aerospace (contract NNM15AA18C). The Italian contribution is supported by the Italian Space Agency (Agenzia Spaziale Italiana, ASI) through contract ASI-OHBI-2022-13-I.0, agreements ASI-INAF-2022-19-HH.0 and ASI-INFN-2017.13-H0, and its Space Science Data Center (SSDC) with agreements ASI-INAF-2022-14-HH.0 and ASI-INFN 2021-43-HH.0, and by the Istituto Nazionale di Astrofisica (INAF) and the Istituto Nazionale di Fisica Nucleare (INFN) in Italy. This research used data products provided by the IXPE Team (MSFC, SSDC, INAF, and INFN) and distributed with additional software tools by the High-Energy Astrophysics Science Archive Research Center (HEASARC), at NASA Goddard Space Flight Center (GSFC). V.K. acknowledges support from the Finnish Cultural Foundation. J.P. thanks the Academy of Finland grant No. 333112 for support.

Facility: IXPE

Software: IXPEOBSSIM (Baldini et al. 2022), XSPEC (Arnaud 1996).

ORCID iDs

John Rankin https://orcid.org/0000-0002-9774-0560 Vadim Kravtsov https://orcid.org/0000-0002-7502-3173 Fabio Muleri https://orcid.org/0000-0003-3331-3794 Juri Poutanen https://orcid.org/0000-0002-0983-0049 Frédéric Marin https://orcid.org/0000-0003-4952-0835 Fiamma Capitanio https://orcid.org/0000-0002-6384-3027 Giorgio Matt 6 https://orcid.org/0000-0002-2152-0916 Enrico Costa 6 https://orcid.org/0000-0003-4925-8523 Alessandro Di Marco https://orcid.org/0000-0003-

Sergio Fabiani https://orcid.org/0000-0003-1533-0283 Fabio La Monaca https://orcid.org/0000-0001-8916-4156 Lorenzo Marra https://orcid.org/0009-0001-4644-194X Paolo Soffitta https://orcid.org/0000-0002-7781-4104

References

Arnaud, K. A. 1996, in ASP Conf. Ser., 101, Astronomical Data Analysis Software and Systems V, ed. G. H. Jacoby & J. Barnes (San Francisco, CA:

Baldini, L., Barbanera, M., Bellazzini, R., et al. 2021, APh, 133, 102628 Baldini, L., Bucciantini, N., Di Lalla, N., et al. 2022, 567X, 19, 101194
Basko, M. M., Sunyaev, R. A., & Titarchuk, L. G. 1974, A&A, 31, 249 Buchner, J. 2016, § &C. 26, 383

Buchner, J. 2019, P, 131, 108005

Buchner, J. 2021, JOSS, 6, 3001

Capitanio, F., Fabiani, S., Gnarini, A., et al. 2023, ApJ, 943, 129 Carroll, B. W., & Ostlie, D. A. 2006, An Introduction to Modern Astrophysics

and Cosmology (2nd ed.; San Francisco, CA: Pearson) Di Marco, A., Costa, E., Muleri, F., et al. 2022, AJ, 163, 170 Ferrazzoli, R., Muleri, F., Lefevre, C., et al. 2020, JATIS, 6, 048002 Johnston, Z., Heger, A., & Galloway, D. K. 2020, MNRAS, 494, 4576 Joye, W. A., & Mandel, E. 2003, in ASP Conf. Ser. 295, Astronomical Data

Analysis Software and Systems XII, ed. H. E. Payne, R. I. Jedrzejewski, & R. N. Hook (San Francisco, CA: ASP), 489 Kislat, F., Clark, B., Beilicke, M., & Krawczynski, H. 2015, APh, 68, 45

Kravtsov, V., Berdyugin, A. V., Piirola, V., et al. 2020, A&A, 643, A170 Kravtsov, V., Veledina, A., Berdyugin, A. V., et al. 2023, A&A, 678, A50 Lecar, M., Wheeler, J. C., & McKee, C. F. 1976, ApJ, 205, 556 Mehta, A. K., Buonanno, A., Gair, J., et al. 2022, ApJ, 924, 39 Mescheryakov, A. V., Revnivtsev, M. G., & Filippova, E. V. 2011, AstL,

Meshcheryakov, A. V., Revnivtsev, M. G., Pavlinsky, M. N., Khamitov, I., & Bikmaev, I. F. 2010, AstL, 36, 738

Miller, M. C., Chirenti, C., & Lamb, F. K. 2020, ApJ, 888, 12 Nasa High Energy Astrophysics Science Archive Research Center (HEASARC) 2014 HEAsoft: Unified Release of FTOOLS and XANADU, Astrophysics

Source Code Library, ascl:1408.004 Orosz, J. A., & Bailyn, C. D. 1997, ApJ, 477, 876 Rankin, J., Muleri, F., Tennant, A. F., et al. 2022, AJ, 163, 39

Rees, M. J. 1975, MNRAS, 171, 457 Soffitta, P., Baldini, L., Bellazzini, R., et al. 2021, AJ, 162, 208

Trippe, S. 2014, JKAS, 47, 15 Weisskorf, M. C., Soffitta, P., Baldini, L., et al. 2022, JATIS, 8, 026002

Wolinski, K. G., & Dolan, J. F. 1994, MNRAS, 267, 5

Poutanen J., Veledina A., Berdyugin A.V., Berdyugina S.V., Jermak H., Jonker P.G., Kajava J.J.E., Kosenkov I.A., Kravtsov V., Piirola V., Shrestha M., Torres M.A.P., Tsygankov S.S. Black hole spin-orbit misalignment in the x-ray binary MAXI J1820+070

Science, 2022; 375: 874



BLACK HOLES

Black hole spin-orbit misalignment in the x-ray binary MAXI J1820+070

Juri Poutanen^{1,2,3}*, Alexandra Veledina^{1,3,2}, Andrei V. Berdyugin¹, Svetlana V. Berdyugina⁴, Helen Jermak⁵, Peter G. Jonker^{6,7}, Jari J. E. Kajava^{1,8}, Ilia A. Kosenkov¹, Vadim Kravtsov¹, Vilppu Piirola¹, Manisha Shrestha^{5,9}, Manuel A. P. Torres^{10,11}, Sergey S. Tsygankov^{1,2}

The observational signatures of black holes in x-ray binary systems depend on their masses, spins, accretion rate, and the misalignment angle between the black hole spin and the orbital angular momentum. We present optical polarimetric observations of the black hole x-ray binary MAXI J1820+070, from which we constrain the position angle of the binary orbital. Combining this with previous determinations of the relativistic jet orientation, which traces the black hole spin, and the inclination of the orbit, we determine a lower limit of 40° on the spin-orbit misalignment angle. The misalignment must originate from either the binary evolution or black hole formation stages. If other x-ray binaries have similarly large misalignments, these would bias measurements of black hole masses and spins from x-ray observations.

lack holes can be characterized with just two parameters: mass and spin. When a black hole resides in a binary system, accreting material from a companion donor star through the accretion disk there are additional parameters that determine its observational signatures: the mass accretion rate and the misalignment angle between the black hole spin and the orbital axis. Standard methods to measure black hole spin from x-ray observations—iron line spectroscopy (1) or modeling of the accretion disk spectrum (2)-assume that the misalignment angle is small. Conversely, the standard interpretation of low-frequency quasi-periodic oscillations in x-ray and optical observations of black hole x-ray binaries as precession of the accretion disk (3-5) requires the assumption that the misalignment angle is non-negligible. Substantial misalignment is theoretically predicted for x-ray binaries that received high velocities during formation (6). The misalignment angle must be inherited from the formation process, because it can only decrease when the black hole is accreting (7). Gravitational wave observations of merging black holes have detected signatures of orbital precession (8), indicating nonzero misalignment in

Department of Physics and Astronomy, Fi-20014 University of Turku, Finland. *Space Research Institute (IKI) of the Russian Academy of Sciences, 117997 Moscow, Russia. *Nordic Institute for Theoretical Physics (Nordita), KTH Royal Institute for Theoretical Physics (Nordita), KTH Royal Institute of Technology and Stockholm University, SF-10691 Stockholm, Sweden. *4Leibniz-Institut fur Sonnenphysik, 79104 Freiburg, Germany. *Astrophysics and Research Institute, Liverpool John Moores University, L3 SRF Liverpool, UK. *Department of Astrophysics, Institute for Mathematics, Astrophysics and Particle Physics (IMAPP), Radboud University, NL-6500 GL Nijmegen, Netherlands. *Space Research, NL-2333, CA Leiden, Netherlands. *Gentro de Astrobiología, Villanueva de la Cañada, *Se8692 Madrid, Spain. *Department of Physics and Astronomy, University of Derver, Derver, CO 80208, USA. **Instituto de Astrofisica de Canarias, F-38205 La Laguna, Tenerife, Spain. **Departamento de Astrofisica, Universidad de la Laguna, E-38206 La Laguna, Tenerife, Spain. **Oreorsponding author. Email: ¿irri.poutanne@ixi.pri.poutanne@ixi.poutanne.

these systems (9), though they might not be representative of the wider population.

Measuring the misalignment angle in x-ray binaries requires determining the threedimensional orientation of the black hole spin and orbital axis. Accreting black holes often show relativistic jets, which are launched along an axis determined by the black hole spin direction (10). The jet inclination angle can be directly obtained in some cases from radio observations (11), whereas the jet position angle can be measured using either radio or x-ray imaging. Combining these two angles allows the black hole spin orientation to be determined. Orbital parameters such as period and orbital inclination can be determined using spectroscopic measurements of radial velocities of the donor star taken during quiescence, the stage at which accretion to the black hole is reduced and optical emission is not dominated by the accretion disk, through orbital modulation of the optical photometry and using constraints from the presence or absence of x-ray and optical disk eclipses (12).

The black hole x-ray binary MAXI J1820+070 was discovered as a transient x-ray source on 11 March 2018 (13). X-ray quasi-periodic oscillations detected shortly after this discovery were observed for >100 days (14). Ejections of material traveling at relativistic velocities have been observed from this source in both radio and x-rays, indicating that the jet inclination (measured from the line of sight) is $i_{\rm iet} =$ 63°±3° and the position angle (measured on the plane of the sky from north to east) is $\theta_{\text{iet}} = 25.^{\circ}1\pm1.^{\circ}4$ (15-17). Both angles were determined to be stable over the observed duration of the outburst. The orbital inclination has been constrained to the range $66^{\circ} < i_{
m orb} < 81^{\circ}$ by the lack of x-ray eclipses and the detection of grazing optical eclipses (12). Determination of the orientation of the orbital axis requires one further parameter, the orbital position angle θ_{orb} .

We monitored MAXI J1820+070 in the optical B, V, and R photometric bands using double image polarimeters (18, 19) during the 2018 outburst and quiescence. We obtained the source intrinsic linear polarization by subtracting the foreground interstellar polarization, measured from nearby field stars, During the outburst, when the relativistic jets were detected at radio frequencies, the intrinsic linear polarization degree (PD) in the V and R bands reached 0.5% at a polarization angle [(PA), also measured from north to east)] of 23° to 24°, which coincides with the jet position angle within the uncertainties (20, 21). After the source faded in the x-rays, the PD increased by a factor of 5 to 10 and the PA changed by $40^{\circ}\pm4^{\circ}$ to $-17^{\circ}\pm4^{\circ}$ (Fig. 1 and table S1) (22). This increase in PD is most prominent in the B band, which also has the highest PD in the range 1.5 to 5%, whereas the R-band polarization changes from 0.4 to 2%. The PA is most precisely determined in the B band, which also shows the least variability, with the mean being $\langle PA \rangle = -19.^{\circ}7\pm1.^{\circ}2.$

We identify three properties of the quiescent-state polarization: (i) It is strongest in the blue part of the optical, with approximate dependence on frequency vas PD(v) \simeq v³ (Fig. 2 and table S1); (ii) the PD remains high in the range 0.5 to 5% and the PA is stable; and (iii) the PA undergoes apparently stochastic variations with an amplitude of <10° with no dependence on the orbital phase (23). These properties constrain the mechanism of the polarized emission. We modeled broadband photometric data obtained

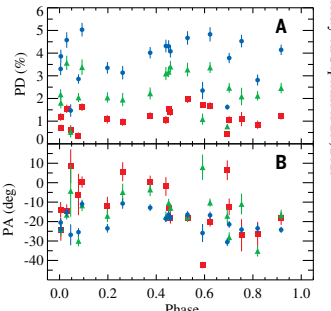


Fig. 1. Observed optical polarization properties of MAXI J1820+070. (A) Intrinsic PD and (B) PA of MAXI J1820+070 (during quiescence are shown as a function of orbital phase (using a published ephemeris) (23). The intrinsic values were obtained from the observed ones by subtracting the foreground interstellar polarization, which is measured from nearby field stars. Blue circles, green triangles, and red squares correspond to the B, V, and R bands, respectively, with error bars showing the 68% confidence levels. Polarization is strongest in the B band and weakest in the R band, although the angle does not change substantially.

with the Liverpool Telescope and the Swift Ultraviolet and Optical Telescope (UVOT) together with the polarized fluxes (Fig. 2). We decomposed the total spectral energy distribution into three components: a companion star (contributing ~25% to the R-band flux) (24), an accretion disk with inner temperature $T_d \approx 6200$ K and inner radius $R_d \approx 6 \times 10^{10}$ cm, and an additional ultraviolet (UV) component with blackbody temperature $T_{\rm bb} \approx 15,000$ K and radius $R_{\rm bb} \approx 9 \times 10^9$ cm (table S4). The properties of the polarized flux are consistent with being produced by the UV component with constant PD of 5 to 8%.

The jet cannot be the source of the polarized emission because its optically thin synchrotron spectrum is red, which is inconsistent with the observed blue spectrum of polarized light. Moreover, the PA is offset by ~40° from the jet position angle. The absence of detectable orbital variations in the PA excludes a hot spot origin. An optically thick accretion disk is excluded by the high PD and blue spectrum. A potential source of the polarized emission is scattering of the accretion disk's radiation in the hot, optically thin, geometrically thick accretion flow close to the disk's inner radius (22, 25), which may also be re-

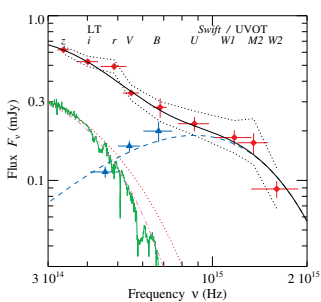


Fig. 2. Spectral energy distribution. The average spectral energy distribution (SED) of MAXI 11820+070 (red diamonds) as observed with the Liverpool Telescope (LT) and Swift UVOT in July 2020 and corrected for reddening, with color excess E(B-V) = 0.29. The photometric bands are indicated at the top of the figure. The black dotted lines give the lower and upper limits on the flux for lower and higher extinction with F(B - V) =0.25 and 0.325, respectively. The polarized flux divided by the best-fitting model polarization degree P_{UV} : 0.055 (i.e., multiplied by a factor of ~18) is indicated by blue triangles. Error bars show 68% confidence levels. The solid black line gives the total model flux consisting of the companion star modeled as a blackbody (pink dot-dashed line), accretion disk (red dotted line), and a hot blackbody (blue dashed line). The spectrum of a K7 star (24) is shown for comparison (solid green line).

sponsible for the observed UV excess. This mechanism would produce polarization parallel to the meridional plane, i.e., the plane formed by the orbital axis and the direction toward the observer. Another possibility is dust scattering, thought to be responsible for the blue polarized spectra observed from accretion disks around some supermassive black holes (26). The presence of dust in quiescent-state black hole x-ray binaries has been inferred from the detection of the mid-IR excess in two systems (27). If dust is located within a flattened envelope, in the wind around the accretion disk, or in a circumbinary disk, the resulting polarization vector would also be parallel to the meridional plane. However, if dust forms an extended, approximately spherical structure at a high elevation above the accretion disk, the polarization would be perpendicular to the meridional plane. We consider the latter scenario to be implausible, as a nearly spherical envelope cannot produce the high observed PD. A dust scattering mechanism would not explain the UV excess because the disk does not emit in that range and hence there are no photons to be scattered by the dust.

Independent of the spectral modeling and geometry of the emission, the stability of the PA (most evident in the B band, Fig. 1) over the orbital phase suggests that the polarization is related to the orbital axis, either parallel or perpendicular to it. Hence, the observed PA provides information about the position angle of the orbital axis. The misalignment angle β can be determined from

$$\cos \beta = \cos i_{\rm bh} \cos i_{\rm orb} + \\ \sin i_{\rm bh} \sin i_{\rm orb} \cos \Delta$$
 (1

where $i_{\rm bh}$ is the inclination of the black hole spin vector (measured from the line of sight) and $\Delta = \theta_{bh} - \theta_{orb}$ is the difference between the position angles of the black hole spin vector θ_{hh} and the orbital angular momentum θ_{orb} (the geometry is illustrated in Fig. 3). If the black hole spin vector is directed along the southern approaching jet, then its inclination is $i_{
m bh}=i_{
m jet}=63^{
m o}\pm3^{
m o}$ and its position angle is $\theta_{bh} = 180^{\circ} + \theta_{jet} = 205.^{\circ}1\pm1.^{\circ}4$ (15–17). The smallest misalignment, $\beta \approx 42^{\circ}$, is achieved when the orbital spin is also directed south at $\theta_{orb} = \langle PA \rangle + 180^{\circ} = 160.^{\circ}3\pm1.^{\circ}2$ (because the PA has an ambiguity of 180°) at the inclination $i_{\text{orb}} \approx 73^{\circ}$. The probability distribution for β in this case is shown in Fig. 4. The radial velocity measurements (12) do not differentiate between orbital inclinations $i_{
m orb}$ and $180^{
m o}-i_{
m orb}$ so there is a second solution with $i_{\rm orb} \approx 107^{\rm o}$ and $\beta \approx 63^{\rm o}$. If either the orbital angular momentum or the black hole spin is instead directed to the north, the black hole rotation is then retrograde, resulting in $\beta \approx 117^{\circ}$ or 138° for the same two solutions for the orbital inclination as above.

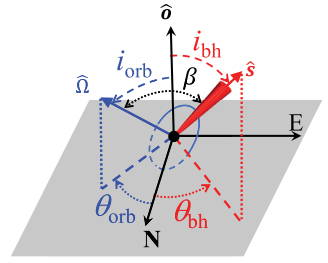


Fig. 3. Geometry of the system from the observer's perspective. The gray plane is the plane of the sky, labelled with north and east axes, perpendicular to the line of sight toward the observer \hat{o} . The angles between the line of sight and the vectors of the orbital angular momentum $\hat{\Omega}$ and and the black hole spin \hat{s} are the inclinations i_{arb} and i_{bh} . The corresponding position angles θ_{orb} and θ_{bh} are the azimuthal angles projected onto the sky, measured from north to east. The misalignment angle β is defined as the angle between \hat{s} and $\hat{\Omega}$. The red cone indicates the jet and the blue ellipse indicates the companion star orbit around the black hole, which is at the coordinate center.

If the polarization vector is perpendicular to the meridional plane, the orbital position angle can take values $\theta_{\rm orb} = \langle PA \rangle + 90^{\circ}$ or $\langle PA \rangle + 270^{\circ}$. This geometrical arrangement leads to nearly identical values for β because the difference between jet position angle and $\langle PA \rangle$ is ${\sim}45^{\circ}$. All possible cases for the orientations of the black hole and orbital spins, the resulting values for β , and the azimuthal angle of the black hole spin in the orbital plane are listed in table S5. Corresponding probability distributions are shown in figs. S4 and S5.

The difference of $\approx 45^{\circ}$ between the jet position angle and the PA indicates $\geq 40^{\circ}$ misalignment between the black hole spin and the orbital angular momentum. This result is independent of modeling or geometric ambiguities because it relies only on the observed difference between the polarization angle and jet position angle.

During outbursts, when material reaches the black hole, this misalignment affects the innermost regions of the accretion disk. For a nonzero spin, particles moving around the black hole—in orbits tilted with respect to the black hole equatorial plane—undergo precession at a rate that decreases with radius (3). Hence, a tilted disk is subject to twist and warp. A high misalignment adds complications to the models of quasi-periodic oscillations observed in black hole x-ray binaries, which rely on precession of the inner parts of the accretion flow, implying that the whole

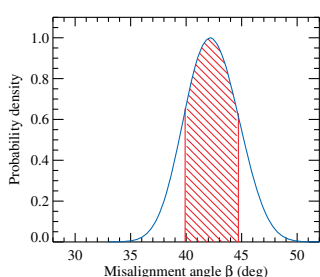


Fig. 4. Probability distribution function for the misalignment angle. The distribution normalized to the peak value is shown for the smallest misalignment angle possible. This case corresponds to the black hole spin directed along the southern approaching jet and the orbital spin being directed south at position angle $\theta_{\text{orb}} = \langle \text{PA} \rangle + 180^{\circ}$ and inclination $i_{\text{orb}} \approx 73^{\circ}$. The red hatched region corresponds to the 68% confidence interval (i.e., between 16th and 84th percentiles of the posterior probability distribution). Distributions of β for the other seven possible combinations of θ_{orb} , i_{orb} , and ibh are shown in fig. S4.

flow is misaligned by 2β from the orbital axis in some phases (3). For $\beta \sim 40^{\circ}$, the inner parts of the accretion disk would need to become almost perpendicular to its outer parts. Most models assume smaller misalignment angles. typically $\beta \sim 10^{\circ}$ to 20° (3, 4, 5) although highly inclined possibilities with $\beta \sim 45^{\circ}$ to 65° have sometimes been considered (28).

High misalignment has previously been suggested on the basis of observations of the gamma-ray light curves produced by the jet in Cyg X-3 (29), and differences between orbital and jet inclination angles are ~15° in GRO J1655-40 (7) and ~50° in V4641 Sgr (30) though the latter is highly uncertain. Misalignment has also been theorized on the basis of the inferred high kick velocities of x-ray binaries acquired during formation (6). For the black hole x-ray binary MAXI J1820+070, the high misalignment was identified only after obtaining the constraints on the position angle of the orbital angular momentum θ_{orb} . Without information on the binary plane orientation, we would have obtained only a lower limit on the misalignment angle in MAXI J1820+070 of ≥5° because the orbital inclination is only marginally different from the jet inclination.

Our results demonstrate the need to treat the misalignment angle as a free parameter when measuring black hole masses and spins. Assuming that the black hole spin and the orbital angular momentum are aligned introduces a systematic bias on measurements (12, 15, 31). A large misalignment angle is expected to drive precession of the binary orbital plane, altering the gravitational waves emitted during a subsequent merger event (9). Evidence for orbital precession has been found from population properties of black hole mergers observed using gravitational waves (8).

REFERENCES AND NOTES

- C. S. Reynolds, Space Sci. Rev. 183, 277–294 (2014). J. E. McClintock, R. Narayan, J. F. Steiner, Space Sci. Rev. 183,
- 295–322 (2014).
 P. C. Fragile, O. M. Blaes, P. Anninos, J. D. Salmonson,
- Astrophys. J. 668, 417–429 (2007).

 A. Ingram, C. Done, P. C. Fragile, Mon. Not. R. Astron. Soc. 397,
- I 101-I 105 (2009) eledina, J. Poutanen, A. Ingram, Astrophys. J. 778, 165
- P. Atri et al., Mon. Not. R. Astron. Soc. 489, 3116–3134 (2019)
- T. J. Maccarone, Mon. Not. R. Astron. Soc. 336, 1371-1376 (2002)
- Abbott et al., Astrophys. J. Lett. 913, L7 (2021).

 A. Apostolatos, C. Cutler, G. J. Sussman, K. S. Thorne Phys. Rev. D 49, 6274-6297 (1994).
- C. McKinney, A. Tchekhovskoy, R. D. Blandford, Science 339, 49-52 (2013).
- I. F. Mirabel, L. F. Rodríguez, Annu. Rev. Astron. Astrophys. 37,
- I. T. Miladel, L. F. Roungdez, Autha. Rev. Astrol. Astrofras. 3 409–443 (1999).
 M. A. P. Torres et al., Astrophys. J. Lett. 893, L37 (2020).
 T. Kawamuro et al., MAXI/GSC detection of a probable new X-ray transient MAXI J1820+070. The Astronomer's Telegram
- no. 11399 (2018).
- H. Stiele, A. K. H. Kong, Astrophys. J. 889, 142 (2020).
 P. Atri et al., Mon. Not. R. Astron. Soc. 493, L81–L86 (2020).
 J. S. Bright et al., Nat. Astron. 4, 697–703 (2020).
 J. M. Espinssee et al., Astrophys. J. Lett. 895, 131 (2020).
 V. Piirola, A. Berdyugin, S. Berdyugina, "DIPOL-2: a double
- image high precision polarimeter" in Proc. SPIE 9147, Ground-based and Airborne Instrumentation for Astronomy V (Society of Photo-Optical Instrumentation Engineers, 2014).
- p. 91478I; doi: 10.1117/12.2055923

 19. V. Piirola, I. A. Kosenkov, A. V. Berdyugin, S. V. Berdyugina,
- J. Poutanen, Astron. J. 161, 20 (2021).
 A. Veledina et al., Astron. Astrophys. 623, A75 (2019).
 I. A. Kosenkov et al., Mon. Not. R. Astron. Soc. 496, L96–L100
- (2020)
- Materials and methods are available as supplementary materi
 M. A. P. Torres et al., Astrophys. J. Lett. 882, L21 (2019).
 A. J. Pickles, Publ. Astron. Soc. Pac. 110, 863–878 (1998).
- 25. R. Naravan, J. E. McClintock, I. Yi. Astrophys. J. 457, 821 (1996). 26. W. Webb, M. Malkan, G. Schmidt, C. Impey, Astrophys. J. 419.
- 494 (1993).
- 27. M. P. Muno. J. Mauerhan, Astrophys. J. 648, L135–L138

- 28. M. Liska et al., Mon. Not. R. Astron. Soc. 507, 983-990 (2021) 29. A. A. Zdziarski et al., Mon. Not. R. Astron. Soc. 479, 4399-4415
- (2018).
 J. A. Orosz et al., Astrophys. J. 555, 489–503 (2001).
- X. Zhao et al., Astrophys. J. 916, 108 (2021).
 A. V. Berdyugin et al., Zenodo (2021); doi: 10.5281/zenodo
- 33 J. Poutanen Zenodo (2022): doi: 10.5281/zenodo.5837857

ACKNOWLEDGMENTS

We thank K. Belczynski and A. Zdziarski for comments and suggestions. A.V. thanks the International Space Science Institute (ISSI) in Bern, Switzerland, for providing the environment for stimulating discussions. Our findings are based on observations made with the Nordic Optical Telescope (NOT), owned in collaboratio by the University of Turku and Aarhus University, and operated jointly by Aarhus University, the University of Turku, and the University of Oslo, representing Denmark, Finland, and Norway, the University of Iceland and Stockholm University at the Observatorio de Roque de los Muchachos, La Palma, Spain, of the Instituto de Astrofisica de Canarias. We thank the NOT staff for their excellent support. DIPol-UF is a joint effort between University of Turku (Finland) and Leibniz Institute for Solar Physics (Germany). The Liverpool Telescope is operated on the island of La Palma by Liverpool John Moores University in the Spanish Observatorio del Roque de los Muchachos of the Instituto de Astrofisica de Canarias financial support from the UK Science and Technology Facilities Council. Funding: A.V. acknowledges support from the Academy of Finland grant 309308. J.P., A.V., V.K., and S.S.T. received funding from Russian Science Foundation grant 20-12-00364. I.A.K. and V.K. thank the Magnus Ehrnrooth Foundation for support. S.V.B. acknowledges support from ERC Advanced Grant HotMol ERC-2011-AdG-291659. M.A.P.T. acknowledges support from the State Research Agency (AEI) of the Spanish Ministry of Science, Innovation and Universities (MCIU) and the European Regional Development Fund (FEDER) under grant AYA2017-83216-P and a Ramón y Cajal Fellowship (RYC-2015-17854) Author contributions: LP and AV initiated the project rformed modeling, and led writing of the text. A.V.B., V.P. and I.A.K. planned and performed the polarimetric observation: H.J., M.S., and M.A.P.T. planned and executed observations using the Liverpool Telescope and V.K. reduced the photometric data. LLE K obtained the Swift observations and analyzed the data together with S.S.T., P.G.J., and S.V.B. contributed to the interpretation of the results. All authors provided input and comments on the manuscript. Competing interests: We declare no competing interests. Data and materials availability: The raw DIPol-UF data are available at Zenodo (32). The Liverpool Telescope data are available from https://telescope.livjm.ac.uk/ DataProd/ under proposal ID JO20A01. The Swift data are available at https://heasarc.gsfc.nasa.gov/cgi-bin/W3Browse/ swift.pl under Observation IDs 000106272**, with ** being 19 to 22 and 24 to 26. Our software for computing the probability distribution of the misalignment angle and for modelling polarization properties of the hot accretion flow is available at enodo (33). The parameters of our SED model are listed in table S4 and our derived geometrical parameters are in table S5

SUPPLEMENTARY MATERIALS

ence.org/doi/10.1126/science.abl4679 Materials and Methods Figs. S1 to S5 Tables S1 to S5 References (34-74)

15 July 2021: accepted 21 January 2022 10.1126/science.abl4679



Supplementary Materials for

Black hole spin-orbit misalignment in the x-ray binary MAXI J1820+070

Juri Poutanen et al.

Corresponding author: Juri Poutanen, juri.poutanen@utu.fi

Science **375**, 874 (2022) DOI: 10.1126/science.abl4679

The PDF file includes:

Materials and Methods Figs. S1 to S5 Tables S1 to S5 References

Materials and Methods

DIPol-UF/NOT observations

We have performed polarimetric observations of the black hole x-ray binary MAXI J1820+070 (13, 34, 35) both during the bright stages of the outburst in 2018 as well as in the quiescence. The data during the outburst (20, 21) were obtained with the Double Image Polarimeter-2 (DIPol-2) polarimeter (18) mounted on the Tohoku 60-cm telescope (T60) at Haleakala observatory, Hawaii. During the quiescence MAXI J1820+070 was observed with the DIPol Ultra Fast (DIPol-UF) (19) at the 2.56-m Nordic Optical Telescope (NOT) in July 2019, April and July 2020, and July 2021 (Table S1) (32). Both polarimeters have similar design: incoming light passes through a modulator (superachromatic halfwavelength plate, HWP), it is then split by the plane-parallel calcite plate into two orthogonally polarized rays (ordinary and extraordinary) and further is reflected by two dichroic beam splitters to produce o- and e-images on three charge-coupled devices (CCDs) simultaneously in the B,V,R bands. This design optically eliminates the sky polarization at the registration stage (even if it is variable), reaching up to 10^{-5} polarization precision (18, 19, 36). The instrumental polarization is below 10^{-4} level and can be accounted for using zero-polarization standards (19) but is negligible for our study. The zero point of the PA was determined by observing high polarization standards HD 161056 and HD 204827 (19).

For each independent measurement of linear polarization, four sequential images with the HWP rotated by 22° 5 in each step are obtained. Each measurement cycle consists of 16 images recorded simultaneously by three CCDs for one full rotation of the HWP modulator $(0^\circ-360^\circ)$ giving four independent measurements of the normalized Stokes parameters (q,u) in the B,V, and R bands. This algorithm helps eliminate effects arising from dust particles on the retarder, nonparallelism of rotating components, etc. The images produced by DIPol-UF require standard CCD calibrations (36).

The average normalized Stokes parameters (q,u) are then obtained from 16 to 40 individual measurements using a 2σ weighting algorithm (19,37). The typical duration of an observational window where the data were averaged was one hour. The polarization produced by the interstellar medium (ISM) has been estimated from numerous (more than 400) observations of sample of field stars (stars #2, 3, 6, 7, 9 from fig. 9 of ref. (20)), which are close in distance to the target as indicated by their parallaxes (38). These normalized Stokes parameters $(q_{\rm ISM}, u_{\rm ISM})$ were subtracted from the measured values of the normalized Stokes parameters to obtain the intrinsic polarization information of the source $(q_{\rm intr}, u_{\rm intr})$. We then define the complex linear polarization quantity as $\mathcal{P} = q_{\rm intr} + iu_{\rm intr}$. Intrinsic polarization degree (PD) P and polarization angle (PA) θ are then obtained from the formulae.

$$P = |\mathcal{P}| = \sqrt{q_{\rm intr}^2 + u_{\rm intr}^2}, \quad \theta = \frac{1}{2}\arg(\mathcal{P}). \tag{S1}$$

Because our PD measurements typically have significance 5– 10σ , the bias in the measured PD is negligible and the uncertainty in PD ΔP is the same as the uncertainty on individual Stokes parameters. The uncertainty of the PA is estimated as

 $\Delta\theta = \Delta P/(2P)$ (39). The intrinsic PD and PA computed following this procedure are reported in Table **S1**.

Polarization observed during quiescence shows no clear dependence on the orbital phase (Fig. 2), apart from some spread of the points in close orbital phases. The PD has a blue spectrum depending on frequency ν as $\propto \nu^3$, which is inconsistent with the red spectra expected from a jet or accretion disk. The PA is very stable in the B-band, where the PD is the highest and the relative uncertainty is smallest. Therefore, we computed the average PA in that band as a inverse-variance weighted mean of individual PAs. Since the deviations of individual measurements exceed the measurement uncertainties, the standard error of the weighted mean was corrected for overdispersion by the square root of the reduced χ^2 , resulting in $\langle PA \rangle = -19.7 \pm 1.2$. We also computed the mean and its uncertainty using a bootstrap (sampling with replacement) method (40) arriving at an identical value. The mean PA in the V- and R-bands have similar values, but larger uncertainties (Table S1).

Using the images from DIPol-UF we also measured photometry of MAXI J1820+070 relative to two nearby stars (#1 and 2 from table 2 in ref. (20)). Absolute photometry during July 2020 observations was obtained using simultaneous observations by the Liverpool Telescope (LT), see Fig. S1 and Table S2. The flux of MAXI J1820+070 in all bands is anti-correlated with the PD (Fig. S1). This anti-correlation together with the spectral dependence of the PD can be interpreted as an interplay between two components: one, polarized, with contribution growing towards blue and another, unpolarized or, possibly, weakly polarized, variable component dominating the flux in the red. Following the spectral decomposition (Fig. 2), the UV component produces only 20% of the total flux in the R band. This makes PA measurements of the UV component less reliable in this band. Stronger variations of the PA in ${\cal R}$ may be caused by the presence of a red and polarized at a level of 0.1-0.3% component, whose PA is different from that of the UV component. Such red and polarized component, with the PA consistent with the jet position angle, has been observed during the outburst (Table S1).

Liverpool Telescope observations

Photometric observations in the optical band were performed using the optical imaging component of the Infrared-Optical suite of instruments (IO:O) with the Sloan Digital Sky Survey (SDSS) i'r'z', Bessel V and B filters on the LT (41) on La Palma, Spain. The object was observed during four nights from 2020 July 20 to 24, i.e. Modified Julian Dates (MJD) 59050–59054. LT image reduction was provided by the basic IO:O pipeline (42). As the photometric standards, we used four stars with known Panoramic Survey Telescope and Rapid Response System (PS1) point spread function magnitudes. To convert PS1 magnitudes to SDSS and Johnson-Cousins magnitudes we used equation (6) and table 6 from ref. (43). To obtain fluxes of the object from its magnitudes we used standard zero-points for SDSS and Johnson-Cousins systems (44, 45). The fluxes and their uncertainties are presented in Table S3.

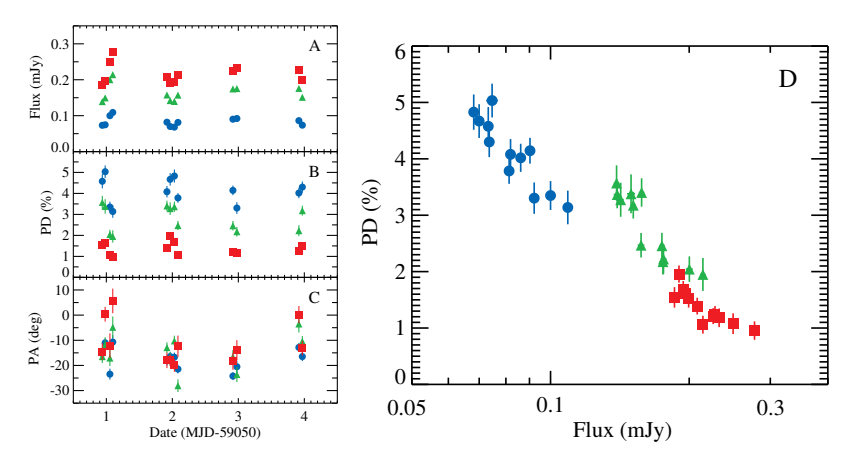


Figure S1: Variation of flux and polarization. (A) The dependence of the observed flux (not corrected for reddening), (B) intrinsic source PD and (C) PA on time during the July 2020 observations of MAXI J1820+070 with DIPol-UF in three filters: B (blue circles), V (green triangles), and R (red squares). (D) Dependence of the PD on flux in the same three filters. An anticorrelation is evident.

Table S1: Intrinsic polarization of MAXI J1820+070. The intrinsic values of the PD and PA derived from observations of MAXI J1820+070 during the outburst with DIPol-2 (20, 21) and during quiescence with DIPol-UF at NOT. Uncertainties are 1 σ . The Stokes parameters have been corrected for the interstellar polarization. The dates for observations during quiescence correspond to the middle of observing windows of a typical duration of one hour.

Date	В		1	V	R		
(MJD)	PD (%)	PA (deg)	PD (%)	PA (deg)	PD (%)	PA (deg)	
			Outburst				
58195-58222	0.28 ± 0.01	9.2 ± 1.0	0.36 ± 0.01	22.9 ± 1.0	0.30 ± 0.01	29.0 ± 0.9	
58223-58234	0.34 ± 0.02	8.8 ± 1.4	0.51 ± 0.02	23.4 ± 1.4	0.53 ± 0.02	23.9 ± 1.1	
58312-58344	0.16 ± 0.01	-15.8 ± 1.6	0.15 ± 0.01	13.4 ± 2.3	0.02 ± 0.01	39.1 ± 11.0	
58406-58428	0.06 ± 0.04	-3.0 ± 15.4	0.13 ± 0.06	2.8 ± 12.4	0.09 ± 0.04	44.8 ± 12.5	
			Quiescence				
58686.93	3.86 ± 0.29	-23.8 ± 2.1	1.81 ± 0.24	-23.8 ± 3.8	0.70 ± 0.14	-24.1 ± 5.7	
58688.01	2.35 ± 0.38	-25.9 ± 4.7	1.09 ± 0.25	8.0 ± 6.5	1.70 ± 0.10	-42.4 ± 1.7	
58961.15	1.47 ± 0.28	-26.8 ± 5.4	0.52 ± 0.24	-4.2 ± 13.3	0.63 ± 0.19	8.5 ± 8.7	
58964.16	4.31 ± 0.28	-18.5 ± 1.8	3.10 ± 0.29	-17.5 ± 2.7	1.05 ± 0.18	-2.0 ± 4.8	
58965.11	2.81 ± 0.24	-23.5 ± 2.5	2.12 ± 0.21	-35.1 ± 2.9	0.84 ± 0.18	-26.3 ± 6.2	
58967.12	4.53 ± 0.28	-24.1 ± 1.8	2.09 ± 0.39	-11.0 ± 5.3	1.09 ± 0.31	-27.0 ± 8.3	
59050.94	4.58 ± 0.34	-15.3 ± 2.1	3.57 ± 0.31	-16.5 ± 2.5	1.54 ± 0.18	-14.5 ± 3.4	
59050.98	5.03 ± 0.30	-11.0 ± 1.7	3.38 ± 0.34	-11.7 ± 2.9	1.62 ± 0.16	0.3 ± 2.9	
59051.05	3.35 ± 0.26	-23.5 ± 2.2	2.04 ± 0.23	-17.1 ± 3.2	1.08 ± 0.18	-12.1 ± 4.9	
59051.10	3.14 ± 0.30	-10.7 ± 2.7	1.95 ± 0.29	-4.8 ± 4.3	0.95 ± 0.16	5.6 ± 4.9	
59051.92	4.08 ± 0.27	-18.1 ± 1.9	3.40 ± 0.25	-12.9 ± 2.1	1.39 ± 0.15	-18.0 ± 3.1	
59051.97	4.67 ± 0.30	-16.5 ± 1.8	3.27 ± 0.30	-17.5 ± 2.6	1.96 ± 0.15	-17.9 ± 2.2	
59052.03	4.83 ± 0.31	-16.7 ± 1.9	3.37 ± 0.24	-10.3 ± 2.1	1.68 ± 0.15	-20.0 ± 2.6	
59052.09	3.78 ± 0.23	-21.5 ± 1.7	2.47 ± 0.22	-28.0 ± 2.5	1.06 ± 0.16	-12.4 ± 4.3	
59052.92	4.14 ± 0.23	-24.2 ± 1.6	2.46 ± 0.23	-16.6 ± 2.7	1.21 ± 0.14	-18.4 ± 3.3	
59052.98	3.30 ± 0.28	-20.5 ± 2.4	2.18 ± 0.23	-23.6 ± 3.0	1.18 ± 0.17	-14.0 ± 4.0	
59053.92	4.02 ± 0.25	-12.8 ± 1.8	2.22 ± 0.26	-3.5 ± 3.4	1.24 ± 0.15	0.2 ± 3.4	
59053.97	4.30 ± 0.27	-16.5 ± 1.8	3.18 ± 0.24	-10.4 ± 2.1	1.51 ± 0.15	-13.1 ± 2.9	
59400.99	1.62 ± 0.12	-30.5 ± 2.0	0.77 ± 0.10	-17.1 ± 3.9	0.41 ± 0.07	6.4 ± 5.1	
59401.94	2.86 ± 0.21	-25.4 ± 2.1	2.04 ± 0.20	-29.9 ± 2.8	0.36 ± 0.14	-6.1 ± 10.7	
59051-59054	4.00 ± 0.19	-17.5 ± 1.3	2.65 ± 0.19	-14.7 ± 1.9	1.32 ± 0.08	-12.8 ± 2.3	
58686-59402	3.18 ± 0.22	-19.7 ± 1.2	1.89 ± 0.19	-16.8 ± 1.9	0.94 ± 0.11	-18.6 ± 3.3	
			Interstellar polarizat	tion			
58195-59054	0.81 ± 0.03	64.0 ± 1.1	0.71 ± 0.03	68.4 ± 1.2	0.60 ± 0.02	64.4 ± 0.8	

Table S2: Observed flux of MAXI J1820+070. Mean fluxes and their 1σ uncertainties derived from observations of MAXI J1820+070 during quiescence in July 2020 with DIPol-UF at NOT.

Date		Flux (mJy)	
Date		riux (mjy)	
(MJD)	B	V	R
59050.94	0.0732 ± 0.0014	0.1391 ± 0.0019	0.1858 ± 0.0020
59050.98	0.0747 ± 0.0022	0.1495 ± 0.0030	0.1966 ± 0.0029
59051.05	0.1000 ± 0.0022	0.2002 ± 0.0034	0.2491 ± 0.0035
59051.10	0.1090 ± 0.0018	0.2142 ± 0.0030	0.2772 ± 0.0028
59051.92	0.0819 ± 0.0015	0.1577 ± 0.0021	0.2082 ± 0.0023
59051.97	0.0700 ± 0.0014	0.1420 ± 0.0022	0.1901 ± 0.0022
59052.03	0.0681 ± 0.0015	0.1395 ± 0.0024	0.1941 ± 0.0025
59052.09	0.0813 ± 0.0018	0.1572 ± 0.0026	0.2142 ± 0.0027
59052.92	0.0902 ± 0.0015	0.1745 ± 0.0023	0.2255 ± 0.0023
59052.98	0.0922 ± 0.0021	0.1754 ± 0.0031	0.2323 ± 0.0031
59053.92	0.0861 ± 0.0017	0.1759 ± 0.0027	0.2275 ± 0.0028
59053.97	0.0736 ± 0.0013	0.1512 ± 0.0020	0.1995 ± 0.0020

Swift/UVOT observations

The Neil Gehrels Swift Observatory (Swift) (46) observed MAXI J1820+070 in the low state with the X-ray Telescope (XRT) and Ultraviolet/Optical Telescope (UVOT) instruments (partly quasi-simultaneously with DIPol-UF/NOT) between 2020 July 20 - September 6. All the XRT data were taken in the photon counting mode with about 9 ks of total exposure. An averaged spectrum was extracted using the online tools (47) provided by the UK Swift Science Data Centre. The spectrum was rebinned to have at least 1 count per energy channel in order to apply W-statistic (48, 49). The data were fitted with a model consisting of a power law modified by the interstellar absorption TBABS*POWERLAW in the 0.5-10 keV band using the XSPEC package (50). Fixing the hydrogen column density to $N_{\rm H}=1.6\times10^{21}\,{\rm cm^{-2}}$ (51) we obtained a power-law photon index $\Gamma = 1.62 \pm 0.24$ with W-statistics of 42.7 for 46 degrees of freedom. We find flux corrected for absorption of $(3.3 \pm 0.7) \times 10^{-13} \, \mathrm{erg} \, \mathrm{cm}^{-2} \, \mathrm{s}^{-1}$ in the 0.5–10 keV energy range.

The UVOT data were processed with the UVOTPRODUCT tool (52-54). We used a 5" source aperture around the known position of MAXI J1820+070 (38), and a circular source-free 10" background aperture about 40" east of it. After comparing the magnitudes obtained between July 20 - September 6 to other quiescence data taken when the x-ray counting rate was low, we found that during this period MAXI J1820+070 was roughly 0.5-1 magnitude fainter in all the UV filters than in the data taken in 2019 or earlier in 2020. The same trend was observed in the V-band and, to a lesser extent, in the R-band. Therefore, we decided to stack all the 2020 July 20-September 6 UVOT data together to obtain time averaged fluxes in the u, uvw1, uvm2 and uvw2 filters for the spectral energy distribution (SED). Conversion of the background corrected count rates obtained from the UVOTPRODUCT to the fluxes is non-trivial, as it depends on the assumed spectral shape (53). Therefore, for reliable estimate of the fluxes we performed direct spectral fitting with a broad-band SED model using the XSPEC package (Fig. 2).

Decomposition of the broadband spectrum

The broad-band average spectrum obtained with the LT and Swift/UVOT is shown in Fig. 2. The spectrum was corrected for

reddening using model of ref. (55) with extinction $A_V=0.89$ (corresponding to the color excess E(B-V)=0.29) obtained from the hydrogen column density $N_{\rm H}=(0.16\pm0.02)\times10^{22}{\rm cm}^{-2}$ (51) using transformation $A_V=5.59\,{\rm N_H}/10^{22}{\rm cm}^{-2}$ (56). The optical/infrared SED obtained with the LT is very red and can be described by a joined contribution of companion star and multicolor accretion disk, but the UVOT data show a UV excess. The excess is also seen in the non-dereddened data and is not an artefact of dereddening procedure. A similar excess has been detected previously in quiescent-state observations of the black hole x-ray binary A 0620–00 (57), but its nature remained a mystery.

The blue PD spectrum differs from the red (even after correcting for the reddening) spectrum of the infrared to UV continuum. This rules out accretion disk as the source of polarized light. We infer that the component producing the UV excess is responsible for polarization. To extract the average shape of the polarized component, we calculated the polarized fluxes as

$$(PF)_k = P_k F_k, \tag{S2}$$

where k is the index corresponding to one of the BVR-bands, P_k is the average PD and F_k is the average flux in this band. If PD of the polarized component is wavelength-independent, then the computed PF directly replicates its total spectral shape, with the normalization being smaller by the polarization fraction. The average PD was computed from the average Stokes parameters ($q_{\rm intr}, u_{\rm intr}$) obtained in 12 individual measurements in July 2020 during quiescence with DIPol-UF (Table S1). Because absolute photometry with DIPol-UF is not very reliable, the average flux was obtained from the LT observations. The averages were computed as a inverse-variance weighted mean of individual measurements and their standard errors were corrected for overdispersion by the square root of the reduced χ^2 .

Published spectroscopy obtained during quiescence indicates a K-type spectral type for the companion star, which contributed about 20% to the flux in the r-band (12, 22). The average observed r-band flux during the spectroscopy was about 0.33 mJy, higher than the average flux of 0.24 mJy in our LT observations. Thus, the contribution of the companion star to the r-band flux rose to 27%. The radius of the companion star, which fills its Roche lobe, can be established from the measured orbital period $P_{\rm orb}=0.68549\pm0.00001$ d, projected rotational

Table S3: Log of observations with the Liverpool Telescope. The observed fluxes of MAXI J1820+070 and their 1σ uncertainties in various filters.

Date	Filter	Exposure	Flux	Date	Filter	Exposure	Flux
(MJD)		(s)	(mJy)	(MJD)		(s)	(mJy)
59050.92075	i	100	0.2700 ± 0.0014	59052.92842	z	100	0.3944 ± 0.0033
59050.92213	i	100	0.2468 ± 0.0015	59052.92980	z	100	0.4037 ± 0.0033
59050.92350	i	100	0.2482 ± 0.0015	59052.93193	V	200	0.1605 ± 0.0011
59050.92505	z	100	0.3990 ± 0.0028	59052.93463	B	200	0.0974 ± 0.0007
59050.92642	z	100	0.4093 ± 0.0029	59052.93637	r	40	0.3063 ± 0.0018
59050.92780	z	100	0.3733 ± 0.0029	59052.93705	r	40	0.2142 ± 0.0018
59050.93052	V	300	0.1440 ± 0.0009	59053.92120	i	100	0.3071 ± 0.0017
59051.01279	i	100	0.3321 ± 0.0014	59053.92257	i	100	0.3600 ± 0.0018
59051.01417	i	100	0.3075 ± 0.0014	59053.92395	i	100	0.3450 ± 0.0018
59051.01554	i	100	0.3164 ± 0.0014	59053.92550	z	100	0.3917 ± 0.0033
59051.01709	z	100	0.4208 ± 0.0027	59053.92687	z	100	0.3598 ± 0.0033
59051.01846	z	100	0.5048 ± 0.0028	59053.92825	z	100	0.3736 ± 0.0034
59051.01984	z	100	0.4703 ± 0.0027	59053.93038	V	200	0.1369 ± 0.0011
59051.02254	B	300	0.1263 ± 0.0005	59053.93308	B	200	0.0762 ± 0.0007
59051.09342	i	100	0.3476 ± 0.0016	59053.93482	r	40	0.2281 ± 0.0019
59051.09479	i	100	0.3489 ± 0.0016	59053.93550	r	40	0.2174 ± 0.0019
59051.09617	i	100	0.3809 ± 0.0015	59053.95474	i	100	0.2752 ± 0.0016
59051.09771	z	100	0.4877 ± 0.0032	59053.95612	i	100	0.2927 ± 0.0016
59051.09909	z	100	0.4963 ± 0.0033	59053.95750	i	100	0.2633 ± 0.0017
59051.10047	z	100	0.4706 ± 0.0033	59053.95904	z	100	0.3587 ± 0.0032
59051.10168	r	40	0.2339 ± 0.0019	59053.96042	z	100	0.3824 ± 0.0030
59051.10236	r	40	0.2592 ± 0.0018	59053.96180	z	100	0.4097 ± 0.0033
59051.92206	i	100	0.3003 ± 0.0015	59053.96393	V	200	0.1467 ± 0.0010
59051.92343	i	100	0.2982 ± 0.0015	59053.96663	B	200	0.0799 ± 0.0007
59051.92481	i	100	0.2860 ± 0.0015	59053.97116	i	100	0.3032 ± 0.0042
59052.01060	i	100	0.2838 ± 0.0016	59053.97254	i	100	0.3390 ± 0.0016
59052.01197	i	100	0.2693 ± 0.0015	59053.97391	i	100	0.3308 ± 0.0016
59052.01335	i	100	0.2501 ± 0.0016	59053.97546	z	100	0.4278 ± 0.0032
59052.09336	i	100	0.2979 ± 0.0015	59053.97684	z	100	0.4017 ± 0.0032
59052.09474	i	100	0.2800 ± 0.0016	59053.97821	z	100	0.4193 ± 0.0031
59052.09611	i	100	0.2974 ± 0.0015	59053.98035	V	200	0.1535 ± 0.0010
59052.92275	i	100	0.3161 ± 0.0017	59053.98305	B	200	0.0601 ± 0.0007
59052.92412	i	100	0.3058 ± 0.0016	59053.98479	r	40	0.2427 ± 0.0017
59052.92550	i	100	0.3048 ± 0.0017	59053.98546	r	40	0.2100 ± 0.0017
59052,92705	z	100	0.3686 ± 0.0034				

Table S4: Best-fitting parameters of the SED model. Distance of 2.96 kpc (15) and inclination $i_{\rm orb}=73^{\circ}$ (12) are assumed. The temperature and the radius of the blackbody approximating the SED of the stellar companion were fixed.

Parameter	Value	Units
$T_{\rm in}$	6200^{+1400}_{-1100}	K
$R_{\rm in}$	$(5.6^{+2.7}_{-1.8}) \times 10^{10}$	cm
$T_{ m bb}$	14900^{+2300}_{-1400}	K
$R_{ m bb}$	$(8.9^{+2.3}_{-2.1}) \times 10^9$	cm
T_*	4000	K
R_*	8.3×10^{10}	cm
P_{UV}	$0.055^{+0.023}_{-0.011}$	

velocity $v_{\rm rot}\sin i_{\rm orb}=84\pm5~{\rm km~s^{-1}},$ and orbital inclination $i_{\rm orb}=73^\circ\pm6^\circ$ (12)

$$R_{\rm c} = \frac{P_{\rm orb}(v_{\rm rot}\sin i_{\rm orb})}{2\pi\sin i_{\rm orb}} = (8.3\pm0.6)\times10^{10}~{\rm cm}. \tag{S3}$$

A moderately evolved late-type star of spectral class K7 can satisfy the constraint on radius and contribute about 27% to the r-band flux. A star with higher temperature overpredicts the companion star contribution in the r-band. For the fitting purposes, we approximate the stellar spectrum (24) by the blackbody with $T_*=4000$ K and $R_*=R_{\rm c}=8.3\times10^{10}$ cm (see Fig. 2).

Using XSPEC v.12.11 (50), we modelled the total SED from LT and Swift/UVOT and, jointly, the three points of the PF. The total spectrum is described by the model REDDEN (BBODYRAD1+DISKBB+ BBODYRAD2). The REDDEN model describes interstellar extinction (55). Component BBODYRAD1 corresponds to the spectrum of the stellar companion, modeled as a blackbody of fixed temperature T_* and radius R_* . The DISKBB corresponds to the multicolor accretion disk. It has two free parameters: normalization, which is related to the inner radius $R_{\rm in}$, and temperature at that radius $T_{\rm in}$. Component BBODYRAD₂ corresponds to the UV excess that is modeled by a blackbody with two free parameters: temperature $T_{\rm bb}$ and radius $R_{\rm bb}$. The PFis modeled by the reddened second blackbody multiplied by the polarization fraction P_{UV} . Blackbody and disk normalizations were converted to radii assuming the distance to the source of 2.96 kpc as determined by the radio parallax (15) and disk inclination $i_{orb} = 73^{\circ}$ (12).

The best-fitting model parameters with the corresponding uncertainties are listed in Table S4. We find the accretion disk temperature of about 6200 K, which is very close to that expected for the disk in quiescence (58). The inner radius of the disk $R_{\rm in} \approx 6 \times 10^{10}$ cm, which is 30% smaller than the estimate of the circularization radius for the measured $P_{\rm orb}$ and companion-to-black hole mass ratio $q=0.072\pm0.012$ (12). The outer radius has to be at least 2–3 times larger to avoid underpredicting the red part of the spectrum. This is consistent with the expectation that the accretion disk size does not exceed the tidal radius of about 2.4×10^{11} cm (58).

The temperature of the additional blackbody is $T_{\rm bb} \sim 15,000$ K and the characteristic size $R_{\rm bb} \sim 9 \times 10^9$ cm. This reproduces the shape of the polarized flux SED and the UV excess. The PD of this component is $P_{\rm UV} = 0.055^{+0.023}_{-0.011}$, corresponding to 5–8% intrinsic PD (on average) of the polarized component. The broad-band SED and the best-fitting spectral components are

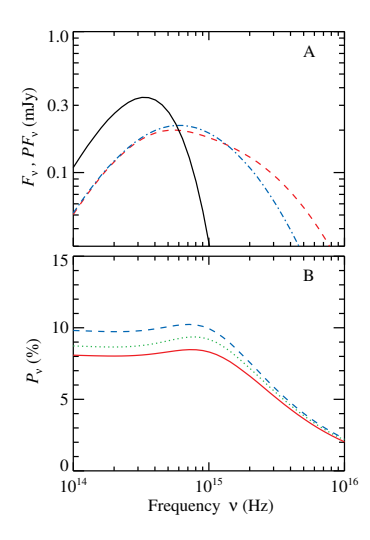


Figure S2: Polarization properties of the hot accretion flow model. (A) Flux from the spectral components: blackbody ($T_{\rm in} = 6200$ K, black solid line) and first Compton scattering of these photons by hot medium (red dashed line) with $kT_{\rm e}=200~{\rm keV}$ and scale-height given by parameter $\cos \alpha_{\rm crit} = 0.5$, and spectrum of the polarized flux of the first scattering component (blue dot-dashed line) that has been scaled up to match the low-energy part of the intensity spectrum (divided by the PD at low energies). This shows that the polarized flux has the same shape as the scattered component flux, justifying our joint model fitting of the UV flux together with the polarized flux (shown in Fig. 2). Only results for inclination of $i_{\rm orb}=73^{\circ}$ are shown, as the dependence on the inclination in its allowed range is minor. (B) PD of the scattered component as a function of frequency is shown for different inclinations $i_{\rm orb} = 81^{\circ}$ (blue dashed line), 73° (green dotted) and 66° (red solid). PD for energies below the peak of the scattered component is nearly frequency-independent. The observed strong dependence of the PD on frequency is caused by the dilution of the polarized scattered radiation by the unpolarized accretion disk.

shown in Fig. 2. The computed values of PF were divided by the constant $P_{\rm UV}$ to demonstrate the fit with the UV excess component

For lower and higher values of the color excess of 0.25 and 0.325, corresponding to the 1σ uncertainties in $N_{\rm H}$, the best-fitting spectral parameters change. The lower E(B-V) leads to the 8% smaller disk temperature $T_{\rm in}$ and 13% larger inner radius $R_{\rm in}$, 8% smaller blackbody temperature $T_{\rm bb}$ and 3% larger radius $R_{\rm bb}$. For the higher E(B-V), the effect is opposite: $T_{\rm in}$ is 7% larger, $R_{\rm in}$ is 9% smaller, $T_{\rm bb}$ is 7% larger and $R_{\rm bb}$ is smaller by 3%. This uncertainty does not affect any of our conclusions.

The source of polarized light and the nature of the spectral components

In this section we seek to answer two questions: what is the nature of the UV excess and what is the source of polarized radiation? The accretion disk itself cannot be the source of the

UV emission, because in quiescence its temperature is lower as we see from the red optical spectrum. Another possibility is a hotspot (or hot line), the place where the accretion stream hits the disk. This component could be responsible for the UV excess. However, whether it can also be the source of polarization is questionable. The high temperature of this component implies that the matter is ionized. The PD from the optically thick electron-scattering dominated atmosphere (59,60) depends on the cosine of the viewing angle $\mu=\cos i_{\rm orb}$ approximately as $11.7\%\times(1-\mu)/(1+3.582\mu)$ (61). For inclination angles permitted by the absence of eclipses (12), $i_{\rm orb}<81^\circ$, the expected PD is $\lesssim6\%$. A high implied PD, $P_{\rm UV}\approx5-8\%$, is barely consistent with that.

On the other hand, high PD can be produced by synchrotron radiation in the ordered magnetic field. The blue spectrum indicates that we might see the optically thick part of this radiation, with the possible transition to optically thin part at $\nu \gtrsim 10^{15}$ Hz. Self-absorption becomes important at the turn-over frequency (62–64), $\nu_{\rm t}\approx 3\times 10^{15}B_{6}^{\frac{p+2}{p+4}}(\tau_{\rm t}\gamma_{\rm t}^p)^{\frac{2}{p+4}},$ where B_{6} is the magnetic field in units of 10^6 G, $\tau_{\rm t}$ is the Thomson optical depth of electrons emitting at the turn-over frequency, $\gamma_{\rm t}$ is their Lorentz factor and p is the index of the power-law distribution of electron number density on the Lorentz factor γ , $dn_{\rm e}/d\gamma \propto \gamma^{-p}$. For the observed $\nu_{\rm t} \approx 10^{15}$ Hz, this requires highly opaque source with $\tau_{\rm t} \gamma_{\rm t}^p \sim 1$ and/or high magnetic field with $B_6 \sim 1$, which would be expected in the bright hard state, but inconsistent with the relevant values for the source in (near-)quiescence, when both optical depth and the magnetic field drop by 2 to 4 orders of magnitude (65). The highest theoretically possible PD below the self-absorption frequency (66) of $P_{\rm max} = 3/(6p+13) \sim 10\%$ requires highly ordered - and constant - magnetic field during two years, July 2019-July 2021. Hence, we find the synchrotron radiation to be an implausible source of the observed polarized

Substantial polarization could instead be produced by electron scattering of radiation in an optically thin slab if the seed photons are injected along the slab plane (67). The PD= $(1-\mu^2)/(3-\mu^2)$ reaches 33% edge-on and is a weak function of orbital inclination (for $i_{\rm orb} \gtrsim 66^\circ$, i.e. $\mu \lesssim 0.41$, the PD is larger than $\sim 30\%$). Scattering in the Thomson regime means that the scattered radiation does not gain a systematic shift in energy with respect to the incident continuum, and hence the peak of the spectrum of the polarized component directly probes the characteristic energy and spectral shape of the incident radiation. Hence, the source of the incident light should have narrow, blackbody-like shape, with characteristic temperature $T \sim 15,000$ K. Because this temperature is much higher than the disk inner temperature, and the polarization angle is independent of orbital phase, the location and physical properties of such a component are unclear.

The additional polarized component may instead arise from Compton up-scattering of soft photons by hot electrons, which is related to a systematic shift in energy. A hot, geometrically thick accretion flow can exist in low-luminosity black hole binaries and active galactic nuclei (25,65). Alternatively, a hot layer (corona) atop of the cold disk, heated by the unwinding stream of matter, could be present. In both cases, the hot medium is expected to be optically thin, and may Compton up-scatter the photons coming from the cold accretion disk. We calculate the

spectra and polarization properties of Compton scattering using iterative scattering method (68). We assume the spectrum of incident, non-polarized photons is a blackbody with temperature equal to the disk inner temperature $T_{\rm in} = 6200$ K. For these seed photons, to explain the peak of the first scattering order at $\sim 10^{15}$ Hz (as demanded by the spectral decomposition), we need to have electrons with temperature of about 200 keV. For such a high temperature, the PD is expected to drop with respect to the maximal, Thomson-regime PD by a factor of 3 (69). In the case of inner hot flow, only the photons travelling at inclinations α to the disk normal that are larger than some critical value $\alpha_{\rm crit}$ can interact with the hot matter. This limiting angle is related to the scale-height H of the hot medium $\cot \alpha_{\rm crit} \sim (H/R_{\rm in})$. Increasing the flow scale-height leads to a drop of PD. In Fig. ${\bf S2}$ we show the resulting flux, polarized flux and PD spectra at different viewing angles $i_{\rm orb}=66^{\circ}, 73^{\circ}$ and 81° . In this case the polarization is parallel to the disk normal. We find that the PD of scattered radiation is nearly independent of the photon frequency up to its peak at $\nu \sim 10^{15}$ Hz and therefore the spectral shape of the flux and PF of the scattered component are nearly identical in the optical band.

For the slab-corona geometry, an appropriate parameter determining PD is the Thomson optical depth of the hot slab $\tau_{\rm T}.$ Only for $\tau_{\rm T}\gtrsim0.5$ a substantial polarization exceeding 5% can be produced and the dominant electric-field oscillations are perpendicular to the projection of the disk normal. However, Comptonization in a slab of $\tau_{\rm T}=0.1$ and electron temperature $kT_{\rm e}=200$ keV overproduces the observed x-ray flux. This would imply that a more probable model that is more consistent with the observed spectral energy distribution and polarization properties is scattering of the disk radiation in the inner hot flow. Such a geometry favors the measured PA being parallel to the orbital axis.

Finally, the blue PD spectrum could be produced by dust scattering of the accretion disk radiation. This process is thought to be responsible for similarly blue polarization spectra observed from supermassive black holes in Seyfert galaxies and quasars (26, 70–74). The dust would likely be located in a flattened envelope (equatorial wedge) around the accretion disk (73), where it is shielded from the inner disk radiation, or in a circumbinary disk (27). In this case, the polarization vector lies in the meridional plane. If instead the dust has a more spherical distribution, the PD is expected to be smaller and the polarization to be perpendicular to the meridional plane. The dust scattering model, however, does not explain the UV excess.

Geometry

Here we define the coordinate systems and derive the formulae to compute the misalignment angle between the black hole spin and the orbital angular momentum, and the azimuthal angle of the black hole spin projection in the orbital plane. We consider a Cartesian system with the x-y plane coinciding with the orbital plane. Thus the unit vector of the orbital angular momentum is $\hat{\Omega}=(0,0,1)$. We choose the direction to an observer to lie in the x-z plane at inclination angle i_{orb} as measured from the orbital axis (see Fig. S3 for geometry), so the observer unit vector is

$$\hat{\boldsymbol{o}} = (\sin i_{\text{orb}}, 0, \cos i_{\text{orb}}). \tag{S4}$$

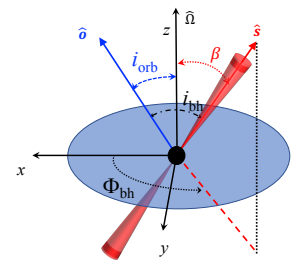


Figure S3: Geometry of the system from the point of view of the binary. The orbital plane here coincides with the x-y plane of the Cartesian system with the orbital axis being along the z-axis. The observer is situated in the x-z plane at inclination angle i_{orb} as measured from the orbital axis. The black hole spin is directed at angle β from the z-axis at azimuthal angle $\Phi_{\rm bh}$ as measured from the x-axis in the counter-clockwise direction in the x-y plane as viewed from the top. The red cones indicate the jet, and the blue disk indicates the binary orbit. Fig. 3 shows the same geometry from the observer's perspective.

We assume that the black hole spin is directed at an angle β from the z-axis at azimuthal angle $\Phi_{\rm bh}$, which is measured from the x-axis in the counter-clockwise direction in the x-y plane as viewed from the top. The unit vector of the black hole spin is

$$\hat{s} = (\sin \beta \cos \Phi_{bh}, \sin \beta \sin \Phi_{bh}, \cos \beta).$$
 (S5)

We define the polarization basis with the unit vector \hat{e}_1 directed on the sky in the direction of the projection of the orbital spin, vector \hat{e}_2 being directed to the left on the sky, and the third vector coincides with the observer direction:

$$\begin{split} \hat{\boldsymbol{e}}_1 &= \frac{\hat{\boldsymbol{\Omega}} - \cos i_{\text{orb}} \,\hat{\boldsymbol{o}}}{\sin i_{\text{orb}}} = (-\cos i_{\text{orb}}, 0, \sin i_{\text{orb}}), \\ \hat{\boldsymbol{e}}_2 &= (0, -1, 0), \end{split} \tag{S6}$$

In this vector basis, the black hole and the orbital spin vectors can be represented as

$$\hat{s} = (\sin i_{\rm bh} \cos \Delta, \sin i_{\rm bh} \sin \Delta, \cos i_{\rm bh}),$$
 (S7)

$$\hat{\mathbf{\Omega}} = (\sin i_{\text{orb}}, 0, \cos i_{\text{orb}}), \tag{S8}$$

where $\Delta=\theta_{\rm bh}-\theta_{\rm orb}$ is the difference in position angles of the black hole and the orbital spins. The misalignment angle β between the black hole and the orbital axis is then given by the scalar product:

$$\cos \beta = \hat{\Omega} \cdot \hat{s} = \cos i_{\text{bh}} \cos i_{\text{orb}} + \sin i_{\text{bh}} \sin i_{\text{orb}} \cos \Delta.$$
 (S9)

The direction cosines of the black hole spin vector \hat{s} in polarization basis are

$$\begin{split} \hat{\boldsymbol{s}} \cdot \hat{\boldsymbol{e}}_1 &= \sin i_{\rm bh} \cos \Delta = \cos \beta \sin i_{\rm orb} - \sin \beta \cos i_{\rm orb} \cos \Phi_{\rm bh}, \\ \hat{\boldsymbol{s}} \cdot \hat{\boldsymbol{e}}_2 &= \sin i_{\rm bh} \sin \Delta = -\sin \beta \sin \Phi_{\rm bh}, \end{split}$$

$$\hat{\boldsymbol{s}} \cdot \hat{\boldsymbol{e}}_3 = \cos i_{\text{bh}} = \cos \beta \cos i_{\text{orb}} + \sin \beta \sin i_{\text{orb}} \cos \Phi_{\text{bh}},$$

Figure S4: Probability distribution function for the misalignment angle. Distributions normalized to the peak values are shown for the eight different cases presented in Table S5.

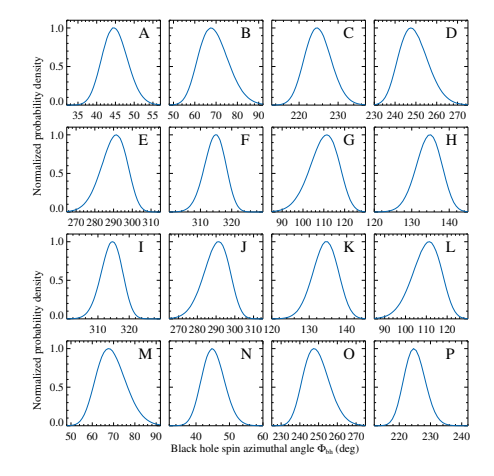


Figure S5: Probability distribution function for the black hole spin azimuthal angle. Distributions normalized to the peak values are shown for the 16 different cases (A-P) presented in Table S5.

allowing us to obtain the azimuthal angle of the black hole spin:

$$\begin{split} \cos\Phi_{\rm bh} &= \frac{\sin i_{\rm orb}\cos i_{\rm bh} - \cos i_{\rm orb}\sin i_{\rm bh}\cos\Delta}{\sin\beta},\\ \sin\Phi_{\rm bh} &= -\frac{\sin i_{\rm bh}\sin\Delta}{\sin\beta}. \end{split} \tag{S11}$$

We assume that the black hole spin is aligned with the jet. If the spin is directed along the southern approaching jet, then its inclination $i_{\rm bh}=i_{\rm jet}=63^\circ\pm3^\circ$ and its position angle is $\theta_{\rm bh}=180^\circ+\theta_{\rm jet}=205^\circ1\pm1^\circ24$ (15–17). If, on the other hand, the black hole spin points along the northern receding jet, then $i_{\rm bh}=180^\circ-i_{\rm jet}=117^\circ\pm3^\circ$ and its position angle is $\theta_{\rm bh}=\theta_{\rm jet}=25^\circ.1\pm1^\circ.4$.

The polarimetric data provide us with the average polarization angle $\langle PA \rangle = -19^\circ.7 \pm 1^\circ.2$, which carries information about orientation of the orbital axis on the sky. If dominant oscillations of the electric field lie in the meridional plane formed by the or-

Table S5: Geometrical parameters. Geometrical parameters for the 16 possible cases identified by letters A-P of relative orientation of the orbital and the black hole spins.

	$i_{ m bh}$		$i_{\rm iet} = 63^{\circ} \pm 3^{\circ}$				$180^{\circ} - i_{\text{jet}} = 117^{\circ} \pm 3^{\circ}$			
	$\theta_{ m bh}$		$\theta_{\rm jet} + 180^{\circ} = 205^{\circ}1 \pm 1^{\circ}4$				$\theta_{\rm jet} = 25^{\circ}.1 \pm 1^{\circ}.4$			
	$i_{ m orb}$		$73^{\circ} \pm 6^{\circ}$		$107^{\circ} \pm 6^{\circ}$		$73^{\circ} \pm 6^{\circ}$		$107^{\circ} \pm 6^{\circ}$	
		Pol	arization parall	el to	the meridional p	lane				
$\theta_{orb} = \langle PA \rangle$	β (deg)		117.3 ± 4.3 45.2 ± 3.4	ъ	137.6 ± 2.4	C	62.7 ± 4.3 225.2 ± 3.4	D	42.4 ± 2.4	
$=-19^{\circ}7 \pm 1^{\circ}2$	$\Phi_{\rm bh}$ (deg)	А	45.2 ± 3.4	ь	69.7 ± 7.0	C	225.2 ± 3.4	D	249.0 ± 7.0	
	Q (dag)		49.4 ± 9.4		69.7 ± 4.2		1276 ± 24		1179 ± 49	
$\theta_{ m orb} = \langle { m PA} \rangle + 180^{\circ}$	Φ _{kk} (deg)	Е	42.4 ± 2.4 289.8 ± 7.0	F	62.7 ± 4.3 314.8 ± 3.4	G	137.6 ± 2.4 110.3 ± 7.0	Н	117.3 ± 4.3 134.8 ± 3.4	
	- BH (8)									
Polarization perpendicular to the meridional plane										
0 /DA\.000	β (deg)		117.0 ± 4.3		137.2 ± 2.4	- 1/	63.0 ± 4.3		42.8 ± 2.4	
$\theta_{\rm orb} = \langle {\rm PA} \rangle {+} 90^{\circ}$	β (deg) $\Phi_{\rm bh}$ (deg)	1	117.0 ± 4.3 314.5 ± 3.4	J	290.3 ± 6.9	K	63.0 ± 4.3 134.5 ± 3.4	L	42.8 ± 2.4 110.3 ± 6.9	
$\theta_{ m orb} = \langle { m PA} \rangle {+} 270^{\circ}$	β (deg)	М	42.8 ± 2.4	N	63.0 ± 4.3	0	137.3 ± 2.4 249.7 ± 6.9	Р	117.0 ± 4.3	
$v_{\rm orb} = \langle rA/\pm 2/0 \rangle$	β (deg) $\Phi_{\rm bh}$ (deg)	IVI	69.7 ± 6.9	14	45.5 ± 3.4	U	249.7 ± 6.9	г	225.5 ± 3.4	

bital spin and photon propagation direction, the position angle of the orbital spin can be either $\theta_{\rm orb} = \langle {\rm PA} \rangle$ or $\langle {\rm PA} \rangle + 180^\circ$. The electric field oscillations can also be perpendicular to the meridional plane, then the orbital spin position angle is $\langle {\rm PA} \rangle + 90^\circ$ or $\langle {\rm PA} \rangle + 270^\circ$. Furthermore, the radial velocity measurements are not able to differentiate between inclinations $i_{\rm orb}$ and $180^\circ - i_{\rm orb}$. The possible combinations result in 16 different geometrical arrangements of the black hole and orbital spins that satisfy the observational constraints. These 16 cases can be reduced to eight different values for the misalignment angle β : four for misalignment less than 90° and four for misalignment between 90° and 180° for the retrograde rotation of the black hole (Table S5).

The probability distribution for the orbital inclination $i_{\rm orb}$ was assumed to be a Gaussian with the peak at 73° with 1σ error of 6° and a cutoff at 81° (12, 22). For an alternative case of inclination exceeding 90°, the distribution mirror reflected relative to 90° is considered. Other parameters are assumed to follow a Gaussian distribution with corresponding 1σ errors. Using Monte-Carlo simulations (33), we obtain the probability distributions for β and $\Phi_{\rm bh}$ using Equations (S9) and (S11), respectively. Their mean and standard deviation are given in Table S5. In Fig. S4 we show the posterior probability distribution for β for the eight different cases from Table S5. The probability distributions for $\Phi_{\rm bh}$ for the 16 cases from Table S5 are shown in Fig. S5.

References and Notes

- C. S. Reynolds, Measuring Black Hole Spin Using X-Ray Reflection Spectroscopy. Space Sci. Rev. 183, 277 (2014). doi:10.1007/s11214-013-0006-6
- J. E. McClintock, R. Narayan, J. F. Steiner, Black Hole Spin via Continuum Fitting and the Role of Spin in Powering Transient Jets. Space Sci. Rev. 183, 295 (2014). doi:10.1007/s11214-013-0003-9
- P. C. Fragile, O. M. Blaes, P. Anninos, J. D. Salmonson, Global general relativistic magnetohydrodynamic simulation of a tilted black hole accretion disk. *Astrophys. J.* 668, 417 (2007). doi:10.1086/521092

- A. Ingram, C. Done, P. C. Fragile, Low-frequency quasiperiodic oscillations spectra and Lense-Thirring precession. *Mon. Not. R. Astron. Soc.* 397, L101 (2009). doi:10.1111/j.1745-3933.2009.00693.x
- A. Veledina, J. Poutanen, A. Ingram, A unified Lense-Thirring precession model for optical and X-ray quasiperiodic oscillations in black hole binaries. *Astrophys. J.* 778, 165 (2013). doi:10.1088/0004-637X/778/2/165
- P. Atri, et al., Potential kick velocity distribution of black hole X-ray binaries and implications for natal kicks. Mon. Not. R. Astron. Soc. 489, 3116 (2019). doi:10.1093/mnras/stz2335
- T. J. Maccarone, On the misalignment of jets in microquasars. Mon. Not. R. Astron. Soc. 336, 1371 (2002). doi:10.1046/j.1365-8711.2002.05876.x
- R. Abbott, et al., Population properties of compact objects from the second LIGO-Virgo gravitational-wave transient catalog. Astrophys. J. Lett. 913, L7 (2021). doi:0.3847/2041-8213/abe949
- T. A. Apostolatos, C. Cutler, G. J. Sussman, K. S. Thorne, Spin-induced orbital precession and its modulation of the gravitational waveforms from merging binaries. *Phys. Rev.* D 49, 6274 (1994). doi:10.1103/PhysRevD.49.6274
- J. C. McKinney, A. Tchekhovskoy, R. D. Blandford, Alignment of Magnetized Accretion Disks and Relativistic Jets with Spinning Black Holes. *Science* 339, 49 (2013). doi:10.1126/science.1230811
- I. F. Mirabel, L. F. Rodríguez, Sources of Relativistic Jets in the Galaxy. *Ann. Rev. Astron. Astrophys.* 37, 409 (1999). doi:10.1146/annurev.astro.37.1.409
- M. A. P. Torres, et al., The binary mass ratio in the black hole transient MAXI J1820+070. Astrophys. J. Lett. 893, L37 (2020). doi:10.3847/2041-8213/ab863a
- T. Kawamuro, et al., MAXI/GSC detection of a probable new X-ray transient MAXI J1820+070. The Astronomer's Telegram 11399 (2018).

- 14. H. Stiele, A. K. H. Kong, A Timing Study of MAXI 28. M. Liska, et al., Disc tearing and Bardeen-Petterson align-J1820+070 Based on Swift/XRT and NICER Monitoring in 2018/19. Astrophys. J. 889, 142 (2020). doi:10.3847/1538-4357/ab64ef
- 15. P. Atri, et al., A radio parallax to the black hole X-ray binary MAXI J1820+070. Mon. Not. R. Astron. Soc. 493, L81 (2020). doi:10.1093/mnrasl/slaa010
- 16. J. S. Bright, et al., An extremely powerful long-lived superluminal ejection from the black hole MAXI J1820+070. Nature Astronomy 4, 697 (2020). doi:10.1038/s41550-020-1023-5
- 17. M. Espinasse, et al., Relativistic X-ray jets from the black hole X-ray binary MAXI J1820+070. Astrophys. J. Lett. 895, L31 (2020). doi:10.3847/2041-8213/ab88b6
- 18. V. Piirola, A. Berdyugin, S. Berdyugina, DIPOL-2: a double image high precision polarimeter. Ground-based and Airborne Instrumentation for Astronomy V (2014), vol. 9147 of Proc. of Society of Photo-Optical Instrumentation Engineers, p. 91478I. doi:10.1117/12.2055923
- 19. V. Piirola, I. A. Kosenkov, A. V. Berdyugin, S. V. Berdyugina, J. Poutanen, Double Image Polarimeter-Ultra Fast: simultaneous three-color (BVR) polarimeter with electronmultiplying charge-coupled devices. Astron. J. 161, 20 (2021). doi:10.3847/1538-3881/abc74f
- 20. A. Veledina, et al., Evolving optical polarisation of the black hole X-ray binary MAXI J1820+070. Astron. & Astrophys. 623, A75 (2019). doi:10.1051/0004-6361/201834140
- 21. I. A. Kosenkov, et al., Disc and wind in black hole X-ray binary MAXI J1820+070 observed through polarized light during its 2018 outburst. Mon. Not. R. Astron. Soc. 496, L96 (2020). doi:10.1093/mnrasl/slaa096
- 22. M. A. P. Torres, et al., Dynamical confirmation of a black hole in MAXI J1820+070. Astrophys. J. Lett. 882, L21 (2019). doi:10.3847/2041-8213/ab39df
- 23. Materials and methods are available as supplementary mate-
- 24. A. J. Pickles, A stellar spectral flux library: 1150-25000 Å. Pub. Astron. Soc. Pacific 110, 863 (1998). doi:10.1086/316197
- 25. R. Narayan, J. E. McClintock, I. Yi, A new model for black hole soft X-ray transients in quiescence. Astrophys. J. 457, 821 (1996). doi:10.1086/176777
- 26. W. Webb, M. Malkan, G. Schmidt, C. Impey, The wavelength dependence of polarization of active galaxies and quasars. Astrophys. J. 419, 494 (1993). doi:10.1086/173503
- 27. M. P. Muno, J. Mauerhan, Mid-Infrared Emission from Dust around Quiescent Low-Mass X-Ray Binaries. Astrophys. J. Lett. 648, L135 (2006). doi:10.1086/507990

- ment in GRMHD simulations of highly tilted thin accretion discs. Mon. Not. R. Astron. Soc. 507, 983 (2021). doi:10.1093/mnras/staa099
- 29. A. A. Zdziarski, et al., A comprehensive study of high-energy gamma-ray and radio emission from Cyg X-3. Mon. Not. R. Astron. Soc. 479, 4399 (2018). doi:10.1093/mnras/stv1618
- 30. J. A. Orosz, et al., A black hole in the superluminal source SAX J1819.3-2525 (V4641 Sgr). Astrophys. J. 555, 489 (2001). doi:10.1086/321442
- 31. X. Zhao, et al., Estimating the Black Hole Spin for the X-Ray Binary MAXI J1820+070. Astrophys. J. 916, 108 (2021). doi:10.3847/1538-4357/ac07a9
- 32. A. V. Berdyugin et al., Optical polarimetric observations of low-mass X-ray black hole binary MAXI J1820+070 during 2019-2021. Zenodo (2021); doi:10.5281/zenodo.5767397 doi:10.5281/zenodo.5767397
- 33. J. Poutanen, Modeling polarization properties of X-ray black hole binary MAXI J1820+070. Zenodo (2022); doi:10.5281/zenodo.5837857 doi:10.5281/zenodo.5837857
- 34. D. Denisenko, Optical follow-up of MAXI J1820+070 and possible identity with ASASSN-18ey. The Astronomer's Telegram 11400 (2018).
- 35. M. A. Tucker, et al., ASASSN-18ey: The rise of a new black hole X-ray binary. Astrophys. J. Lett. 867, L9 (2018). doi:10.3847/2041-8213/aae88a
- 36. A. Berdyugin, V. Piirola, J. Poutanen, Optical polarimetry: methods, instruments and calibration techniques. Astronomical Polarisation from the Infrared to Gamma Rays, R. Mignani, A. Shearer, A. Słowikowska, S. Zane, eds. (Springer Nature, Cambridge, 2019), vol. 460 of Astrophysics and Space Science Library, pp. 33-65. doi:10.1007/978-3-030-19715-5_3
- 37. I. A. Kosenkov, et al., High-precision optical polarimetry of the accreting black hole V404 Cyg during the 2015 June outburst. Mon. Not. R. Astron. Soc. 468, 4362 (2017). doi:10.1093/mnras/stx779
- 38. Gaia Collaboration, et al., Gaia Data Release 2. Summary of the contents and survey properties. Astron. & Astrophys. 616, A1 (2018). doi:10.1051/0004-6361/201833051
- 39. K. Serkowski, Polarization of starlight. Advances in Astronomy and Astrophysics 1, 289 (1962). doi:10.1016/B978-1-4831-9919-1.50009-1
- 40. B. Efron, Bootstrap Methods: Another Look at the Jackknife. The Annals of Statistics 7, 1 (1979). doi:10.1214/aos/1176344552
- 41. I. A. Steele, et al., The Liverpool Telescope: performance and first results. Ground-based Telescopes, J. Oschmann, Jacobus M., eds. (2004), vol. 5489 of Proc. of Society

- of Photo-Optical Instrumentation Engineers, pp. 679-692. 57. C. S. Froning, et al., Multiwavelength observations of doi:10.1117/12.551456
- 42. https://telescope.livjm.ac.uk/TelInst/ Inst/IOO
- 43. J. L. Tonry, et al., The Pan-STARRS1 photometric system. Astrophys. J. 750, 99 (2012). doi:10.1088/0004-637X/750/2/99
- 44. M. Fukugita, et al., The Sloan Digital Sky Survey Photometric System. Astron. J. 111, 1748 (1996). doi:10.1086/117915
- 45. M. S. Bessell, UBVRI photometry II: the Cousins VRI system, its temperature and absolute flux calibration, and relevance for two-dimensional photometry. Pub. Astron. Soc. Pacific 91, 589 (1979). doi:10.1086/130542
- 46. N. Gehrels, et al., The Swift gamma-ray burst mission. Astrophys. J. 611, 1005 (2004). doi:10.1086/422091
- 47. P. A. Evans, et al., Methods and results of an automatic analysis of a complete sample of Swift-XRT observations of GRBs. Mon. Not. R. Astron. Soc. 397, 1177 (2009). doi:10.1111/j.1365-2966.2009.14913.x
- 48. K. Wachter, R. Leach, E. Kellogg, Parameter estimation in X-ray astronomy using maximum likelihood. Astrophys. J. 230, 274 (1979). doi:10.1086/157084
- 49. https://heasarc.gsfc.nasa.gov/xanadu/ xspec/manual/XSappendixStatistics.html
- 50. K. A. Arnaud, XSPEC: the first ten years. Astronomical Data Analysis Software and Systems V, G. H. Jacoby, J. Barnes, eds. (ASP, San Francisco, 1996), vol. 101 of Astronomical Society Pacific Conf. Ser., pp. 17-20.
- 51. P. Bharali, J. Chauhan, K. Boruah, Broad-band spectral study of X-ray transient MAXI J1820+070 using Swift/XRT and NuSTAR. Mon. Not. R. Astron. Soc. 487, 5946 (2019). doi:10.1093/mnras/stz1686
- 52. A. A. Breeveld, et al., An Updated Ultraviolet Calibration for the Swift/UVOT. Gamma Ray Bursts 2010, J. E. McEnery, J. L. Racusin, N. Gehrels, eds. (AIP, Melville, NY, 2011), vol. 1358 of American Institute of Physics Conf. Ser., pp. 373-376. doi:10.1063/1.3621807
- 53. P. J. Brown, A. Breeveld, P. W. A. Roming, M. Siegel, Interpreting flux from broadband photometry. Astron. J. 152, 102 (2016). doi:10.3847/0004-6256/152/4/102
- 54. https://www.swift.ac.uk/analysis/uvot/
- 55. J. A. Cardelli, G. C. Clayton, J. S. Mathis, The relationship between infrared, optical, and ultraviolet extinction. Astrophys. J. 345, 245 (1989). doi:10.1086/167900
- 56. P. Predehl, J. H. M. M. Schmitt, X-raying the interstellar medium: ROSAT observations of dust scattering halos. Astron. & Astrophys. 293, 889 (1995).

- A0620-00 in quiescence. Astrophys. J. 743, 26 (2011). doi:10.1088/0004-637X/743/1/26
- 58. J. Frank, A. King, D. J. Raine, Accretion Power in Astrophysics: Third Edition (Cambridge University Press, Cambridge, UK, 2002).
- 59. S. Chandrasekhar, Radiative Transfer (Dover, New York,
- 60. V. V. Sobolev, A Treatise on Radiative Transfer (Van Nostrand, Princeton, 1963).
- 61. K. Viironen, J. Poutanen, Light curves and polarization of accretion- and nuclear-powered millisecond pulsars. Astron. & Astrophys. 426, 985 (2004). doi:10.1051/0004-6361:20041084
- 62. G. B. Rybicki, A. P. Lightman, Radiative Processes in Astrophysics (Wiley, New York, 1979).
- 63. G. Wardziński, A. A. Zdziarski, Effects of non-thermal tails in Maxwellian electron distributions on synchrotron and Compton processes. Mon. Not. R. Astron. Soc. 325, 963 (2001). doi:10.1046/j.1365-8711.2001.04387.x
- 64. A. Veledina, J. Poutanen, I. Vurm, Hot accretion flow in black hole binaries: a link connecting X-rays to the infrared. Mon. Not. R. Astron. Soc. 430, 3196 (2013). doi:10.1093/mnras/stt124
- 65. F. Yuan, R. Narayan, Hot accretion flows around black holes. Ann. Rev. Astron. Astrophys. 52, 529 (2014). doi:10.1146/annurev-astro-082812-141003
- 66. V. L. Ginzburg, S. I. Syrovatskii, Developments in the theory of synchrotron radiation and its reabsorption. Ann. Rev. Astron. Astrophys. 7, 375 (1969). doi:10.1146/annurev.aa.07.090169.002111
- 67. R. A. Sunyaev, L. G. Titarchuk, Comptonization of lowfrequency radiation in accretion disks: angular distribution and polarization of hard radiation. Astron. & Astrophys. 143, 374 (1985).
- 68. J. Poutanen, R. Svensson, The two-phase pair corona model for active galactic nuclei and X-ray binaries: how to obtain exact solutions. Astrophys. J. 470, 249 (1996). doi:10.1086/177865
- 69. J. Poutanen, Relativistic jets in blazars: polarization of radiation. Astrophys. J. Suppl. Ser. 92, 607 (1994). doi:10.1086/192024
- 70. G. Berriman, The origin of the optical polarizations of Seyfert 1 galaxies. Astrophys. J. 345, 713 (1989). doi:10.1086/167944
- 71. C. Brindle, et al., An optical and near-infrared polarization survey of Seyfert and broad-line radio galaxies. II. The wavelengh dependence of polarization. Mon. Not. R. Astron. Soc. 244, 604 (1990).

- J. S. Miller, R. W. Goodrich, W. G. Mathews, Multidirectional views of the active nucleus of NGC 1068. *Astrophys. J.* 378, 47 (1991). doi:10.1086/170406
- R. W. Goodrich, J. S. Miller, Spectropolarimetry of highpolarization Seyfert 1 galaxies: geometry and kinematics of the scattering regions. *Astrophys. J.* 434, 82 (1994). doi:10.1086/174706
- M. Kishimoto, et al., The characteristic blue spectra of accretion disks in quasars as uncovered in the infrared. Nature 454, 492 (2008). doi:10.1038/nature07114





ISBN 978-952-02-0452-5 (PRINT) ISBN 978-952-02-0453-2 (PDF) ISSN 0082-7002 (PRINT) ISSN 2343-3175 (ONLINE)